University of Southampton

Faculty of Natural & Environmental Sciences

# Lithium – Sulfur Batteries: An Investigation into the Electrolyte and the Intermediate Polysulfide Species Within

By

James William Dibden

Supervisors

Dr. Nuria Garcia-Araez

Prof. John R. Owen

Advisor

Prof. Andrew L. Hector

Thesis for the degree of Doctor of Philosophy

August 2017

UNIVERSITY OF SOUTHAMPTON

ABSTRACT

FACULTY OF NATURAL AND ENVIRONMENTAL SCIENCES

Chemistry

Doctor of Philosophy

# Lithium-Sulfur Batteries: An Investigation into the Electrolyte and the Polysulfide Species Within

By James William Dibden

The lithium-sulfur (Li-S) battery is one of the most promising candidates in next-generation energy storage, offering high theoretical specific capacities through the use of inexpensive and environmentally benign positive electrode materials. However, full commercialisation has been prevented by several technical challenges, most notably polysulfide shuttling. Despite significant scientific interest in recent years, the mechanism of the discharge and charge processes is still poorly understood. Whilst it is known that a variety of different processes occur between electrochemically active species during cycling, the identity of the polysulfides species remains unknown. Additionally, the polysulfide concentrations at different stages of discharge and charge, as well as their thermodynamic and kinetic properties are still poorly understood.

In this project, the significance of cell design on the cycling performance of a Li-S battery is highlighted. The reproducibility of a selected cell design and the effect of lithium nitrate as an electrolyte additive is investigated. To obtain a thorough understanding of the electrolyte system used throughout this report (LiTFSI in DOL), various electrolytes containing different concentrations of the electrolyte salt are prepared and analysed. Using a Walden plot, it is revealed that at high salt concentrations, this electrolyte system begins to exhibit properties similar to that of an ionic liquid. Additionally, employing high salt concentrations improves the cycling performance of the Li-S battery. Two methods have been developed to quantitatively determine the total ‘sulfur’ content of an electrolyte containing polysulfides, as well as its average oxidation state. These techniques have enabled production of the first experimental ternary phase diagram for the Li-S battery. Finally, the galvanostatic intermittent titration technique (GITT) method is quantitatively analysed using a model redox system to assess its ability to determine the diffusion coefficient of the redox system. This study offers a unique assessment of the ability to use GITT to study the mass transport of polysulfide intermediates within a Li-S battery.

# List of Contents

# Academic Thesis: Declaration Of Authorship

I, James William Dibden

declare that this thesis and the work presented in it are my own and has been generated by me as the result of my own original research.

Lithium-Sulfur Batteries: An Investigation into the Electrolyte and the Polysulfide Species Within

I confirm that:

1. This work was done wholly or mainly while in candidature for a research degree at this University;
2. Where any part of this thesis has previously been submitted for a degree or any other qualification at this University or any other institution, this has been clearly stated;
3. Where I have consulted the published work of others, this is always clearly attributed;
4. Where I have quoted from the work of others, the source is always given. With the exception of such quotations, this thesis is entirely my own work;
5. I have acknowledged all main sources of help;
6. Where the thesis is based on work done by myself jointly with others, I have made clear exactly what was done by others and what I have contributed myself;
7. Either none of this work has been published before submission, or parts of this work have been published as:

    - S. M. Al-Mahmoud, J. W. Dibden, J. R. Owen, G. Denuault and N. Garcia-Araez, *J. Power Sources*, 2016, **306**, 323-328.
    - J. W. Dibden, J. W. Smith, N. Zhou, N. Garcia-Araez and J. R. Owen, *Chem. Commun.*, 2016, **52**, 12885-12888.
    - J. W. Dibden, N. Meddings, J. R. Owen and N. Garcia-Araez, *ChemElectroChem*, 2017, DOI: 10.1002/celc.201701004
    - R. Raccichini, J. W. Dibden, A. Brew, J. R. Owen and N. Garcia-Araez, *J. Phys. Chem. B*, 2017, DOI: 10.1021/acs.jpcb.7b09614.

Signed: ……

Date: ……

# Acknowledgements

I would like to thank both of my academic supervisors Dr Nuria Garcia-Araez and Professor John Owen for their continued support and guidance throughout my studies. I feel privileged to have been offered the opportunity to work with them both and they have provided me with invaluable research experience, which will enable me to continue my scientific career with enthusiasm and confidence.

I would like to thank the past and present members of John Owen and Nuria Garcia-Araez research group for their help in the lab, scientific discussions and social activities, including 'cakey Thursdays', crossword puzzles, five-a-side football, cricket, group meals and occasional Friday drinks. In particular, I would like to thank Dr Jacob Locke, Dr Noramon Intaranont, Dr Luyi Yang, Dr Saddam Al-Mahmoud, Dr James Frith, Dr Michael Palmer, Dr William Richardson, Thomas Homewood, Nina Meddings, Daniel Wright, Liam Furness, Dr Rinaldo Raccichini and Dr Vivek Padmanabhan.

I would like to thank my industrial sponsor Oxis Energy Limited, with whom I have thoroughly enjoyed collaborating, undertaking placements and contributing to the rise of the mighty 'Oxis Yellow Sox' who made it all the way to the Culham Science Centre intercompany softball tournament finals. In particular, I would like to thank Dr David Ainsworth, Dr Steve Rowlands, Dr Jacob Locke (again!), Ashley Cooke, Lisset Urrutia, Agata Swiatek and Martin Clegg for their support during my placements at Oxis.

Finally, I would like to offer a huge thanks to my parents Peter and Eira, my girlfriend Samantha and other friends/family members, who have always provided support and encouragement in all aspects of my life, without them this would not have been possible.

I would like to also acknowledge the University of Southampton, the Engineering and Physical Sciences Research Council (EPSRC) and once again Oxis Energy Limited for funding my PhD (CASE Studentship: EP/M50662X/1).

# Abbreviations and Units

## General Abbreviations

| | |
|---|---|
| AB | acetylene black |
| ACN | acetonitrile |
| BHT | butylated hydroxytoluene |
| CV | cyclic voltammogram |
| DFT | density functional theory |
| DME | 1,2-dimethoxyethane |
| DoD | depth of discharge |
| DOL | 1,3-dioxolane |
| DSC | differential scanning calorimetry |
| EIS | electrochemical impedance spectroscopy |
| ESR | electron spin resonance |
| EtV | ethyl viologen |
| Fc | ferrocene |
| $Fc^+$ | ferrocenium |
| FEP | fluorinated ethylene propylene |
| *et al.* | *et alii* (Latin: and others) |
| GITT | galvanostatic intermittent titration technique |
| HFE | hydrofluoroether |
| HPLC | high-performance liquid chromatography |
| IEA | International Energy Agency |
| IPCC | Intergovernmental Panel on Climate Change |
| LICGC | lithium-ion conducting glass ceramic |
| Li-S | lithium-sulfur |
| $LiS_n$ | lithium polysulfide of chain length *n* |
| LiTFSI | bis(trifluoromethane)sulfonamide lithium salt |
| MAS | magic angle spinning |
| MeTf | methyl trifluoromethane sulfonate |
| NMR | nuclear magnetic resonance |
| OCP/OCV | open-circuit potential/open-circuit voltage |
| OECD | Organisation for Economic Cooperation and Development |
| OTf | triflate |
| PFA | polyfluoroalkoxy alkane |
| PTFE | polytetrafluoroethylene |
| PVdF | polyvinylidene fluoride |
| RBF | round-bottom flask |
| SEI | solid electrolyte interface |
| SEM | scanning electron microscopy |
| SHE | standard hydrogen electrode |
| TEGDME | tetraethylene glycol dimethyl ether (tetraglyme) |
| $T^M$ | transition metal |
| UV-vis | ultraviolet-visible |

| | |
|---|---|
| XANES | x-ray absorption near-edge spectroscopy |
| XRD | x-ray diffraction |

Mathematical Abbreviations

| | |
|---|---|
| A | electrode area or absorbance |
| $a_i$ | activity of species *i* |
| C | Walden product |
| $c$ | concentration or speed of light ($3 \times 10^8$ m $s^{-1}$) |
| $c_0$ | initial concentration |
| $c^*$ | concentration in the bulk solution |
| $c_{(x = 0, t)}$ | concentration at electrode/electrolyte interface at specified time |
| $D$ | diffusion coefficient |
| $e^-$ | electron |
| $E$ | potential |
| $E_{1/2}$ | half-wave potential |
| $E^\circ$ | standard electrode potential |
| $E_e$ | equilibrium potential |
| $E_e^{0'}$ | formal potential |
| $E_{pa}$ | potential of the oxidation/anodic peak current |
| $E_{pc}$ | potential of the reduction/cathodic peak current |
| $E_s$ | steady-state voltage potential |
| $E_{\tau/4}$ | quarter-wave potential |
| $E_t$ | current pulse potential |
| $F$ | Faraday's constant (96485 C $mol^{-1}$) |
| $h$ | Planck constant ($6.626 \times 10^{-34}$ J s) |
| $i$ | current |
| $I$ | current density or intensity of the sample cuvette |
| $I_0$ | intensity of the reference cuvette |
| $i_p$ | peak current |
| $I_{pa}$ | oxidation/anodic peak current |
| $I_{pc}$ | reduction/cathodic peak current |
| $k^0$ | standard heterogeneous rate constant |
| $k_m$ | mass transfer rate constant |
| $k_s$ | electron transfer rate constant |
| $K_\sigma$ | stress constant |
| $K_\gamma$ | strain constant |
| $l$ | path length |
| $L$ | distance between phase boundaries |
| $m$ | number of moles or average oxidation state in $S^{m-}$ |
| $M$ | torque or molar ratio |
| $n$ | number of electrons involved in an electrode reaction or polysulfide chain length in $Li_2S_n$ |
| O | oxidised species |

| | |
|---|---|
| $q/Q$ | charge |
| R | reduced species |
| $R$ | resistance or ideal gas constant (8.314 J $K^{-1}$ $mol^{-1}$) |
| $R_{ct}$ | charge transfer resistance |
| $R_u$ | uncompensated resistance |
| $S^{m-}$ | average oxidation state of the dissolved sulfur containing species ($0 \leq m \leq 2$) |
| $[S]_T^{mix.}$ | prepared concentration of the total dissolved sulfur species assuming full dissolution of solids into polysulfide electrolyte solution |
| $[S]_T^{sol.}$ | analysed concentration of the total dissolved sulfur species in filtered polysulfide electrolyte solution |
| $[S^{2-}]$ | analysed concentration of 'dissolved sulfide' in filtered polysulfide electrolyte solution |
| $T$ | Temperature |
| $t$ | time |
| V | voltage |
| $V$ | volume |
| wt% | percentage by mass |
| $x_i$ | mole fraction of species $i$ |
| $x$ | distance into the electrolyte from the electrode/electrolyte interface |
| | |
| $\alpha$ | transfer coefficient |
| $\gamma$ | Walden exponent ($0 \leq \gamma \leq 1$) |
| $\dot{\gamma}$ | shear rate |
| $\Delta$ | change in |
| $\varepsilon$ | molar extinction coefficient |
| $\eta$ | dynamic viscosity |
| $\kappa$ | conductivity |
| $\Lambda$ | equivalent (or molar) conductivity |
| $v$ | scan rate |
| $\rho$ | resistivity or density |
| $\sigma$ | shear stress |
| $\tau$ | transition time or duration of current pulse |
| $\Omega$ | motor angular velocity |
| Ø | diameter |

Units

Prefixes to units: P = peta ($10^{15}$), M = mega ($10^6$), k = kilo ($10^3$), d = deci ($10^{-1}$), c = centi ($10^{-2}$), m = milli ($10^{-3}$), μ = micro ($10^{-6}$), n = nano ($10^{-9}$) and p = pico ($10^{-12}$).

| | |
|---|---|
| A | ampere |
| g | gram |
| $g_S$ | gram of sulfur |
| h | hour |

| | |
|---|---|
| J | joule |
| K | kelvin |
| L | litre |
| $L_{electrolyte}$ | litre of electrolyte |
| $L_{solvent}$ | litre of solvent |
| m | metre |
| M | molar (mol $dm^{-3}$) |
| min | minute |
| mpg | miles per gallon |
| Pa | pascal |
| ppm | parts per million |
| s | second |
| S | siemens |
| t | tonne |
| toe | tonne of oil equivalent |
| V | volt |
| W | watt |
| Ω | ohm |

# 1 – Introduction

## 1.1 – World Energy Consumption, Climate Change and Renewable Energy Sources

The International Energy Agency (IEA) estimates that in 2013, the total world energy consumption had reached 9,301 megatonne of oil equivalent (Mtoe) or 108 PW h, approximately double the consumption of 40 years previously in 1973, estimated at 4667 Mtoe or 54 PW h (Figure 1.1.1).[1] Energy consumption continues to grow, despite energy saving schemes and improved efficiency in the way energy is used, e.g. average fuel economy (cars) has doubled over the same 40 year period from 14 mpg in 1975 to 29 mpg in 2014. The increase in world energy consumption is a result of several factors, including industrialisation, increasing wealth in emerging markets (particularly China and India, containing 37% of the total world population) and globalisation, where transportation accounts for the majority of liquid fuel consumption worldwide.

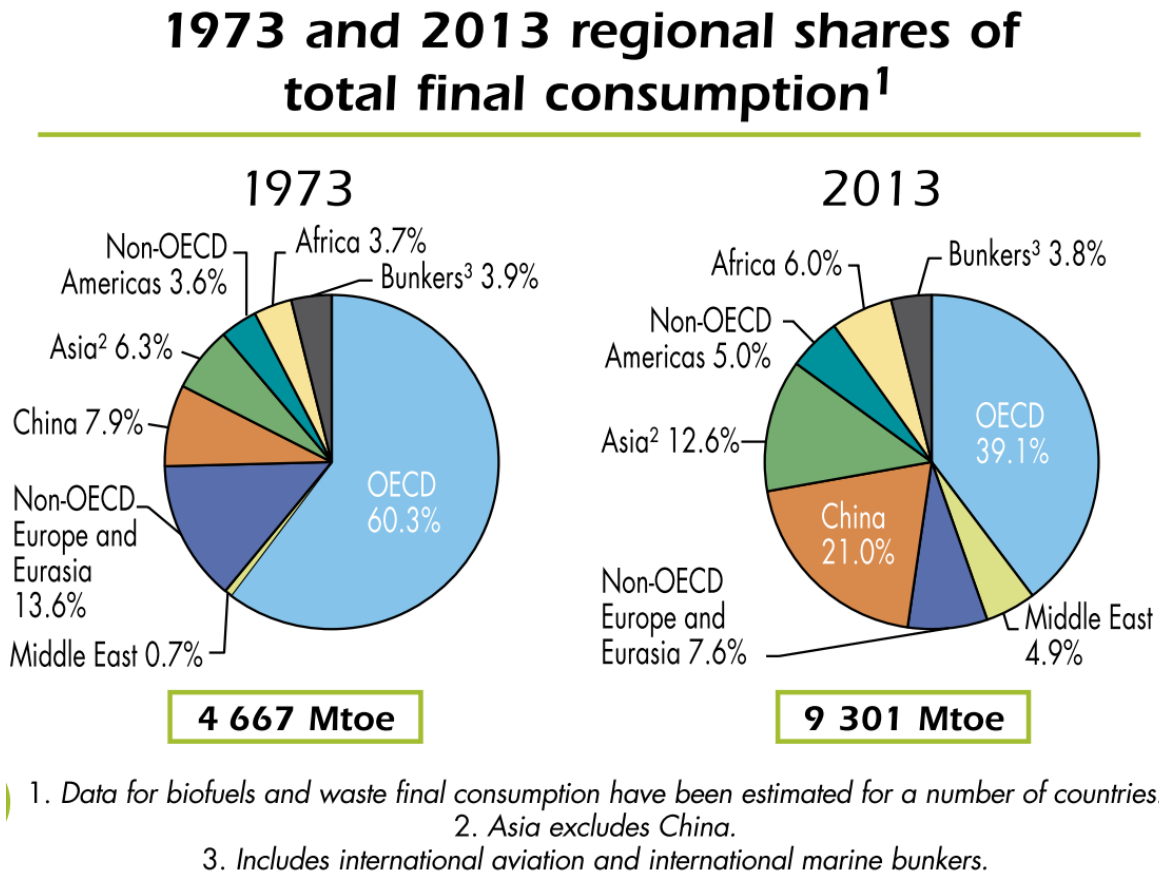


**Figure 1.1.1 –** Comparison of total final energy consumption worldwide between 1973 and 2013 by regional shares. OECD stands for Organisation for Economic Cooperation and Development and consists of 35 member countries.[1] © OECD/IEA 2015 *Key World Energy Statistics*, IEA Publishing,. Licence: www.iea.org/t&c

The majority of the energy consumed comes from non-renewable sources such as oil, coal and natural gas. Burning fossil fuels is not only unsustainable but the greenhouse gasses produced are detrimental to the environment and a direct cause of global warming.[2] Such greenhouse gasses include carbon dioxide, methane and nitrous oxide and since the Industrial Revolution (assume year 1750), human activity has produced a 40% increase in the atmospheric concentration of carbon dioxide, from 280 ppm in 1750, to 400 ppm in 2015. The rise in energy consumption will continue despite efforts to curtail the growth, therefore an alternative long term approach is required. Renewable and clean energy sources that do not produce greenhouse gasses, such as solar power and wind, could provide the energy needed but these energy sources are only intermittent and require electrical energy storage to be successful.

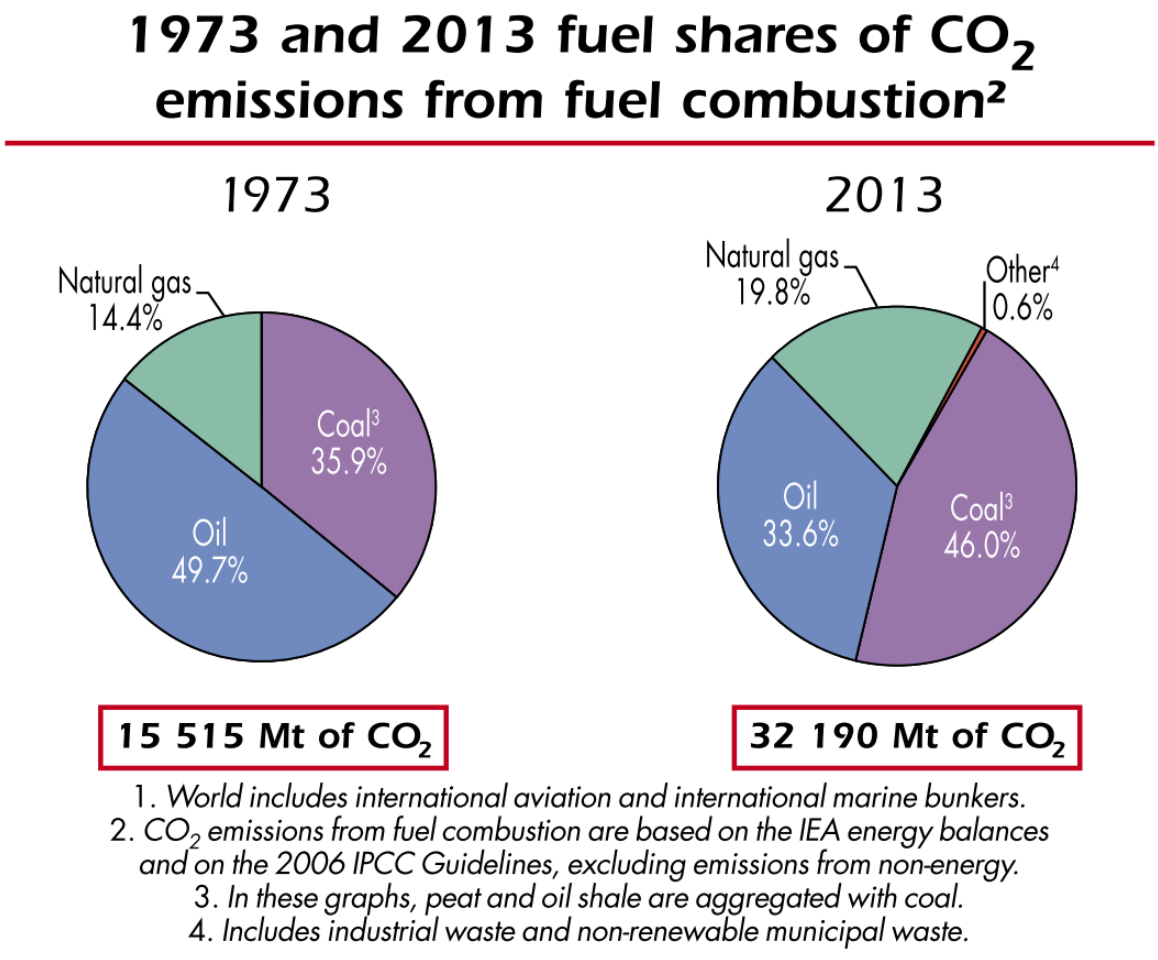


**Figure 1.1.2 –** Comparison of $CO_2$ emissions worldwide between 1973 and 2013 by fuel type. IPCC stands for Intergovernmental Panel on Climate Change.[1] © OECD/IEA 2015 *Key World Energy Statistics*, IEA Publishing,. Licence: www.iea.org/t&c

## 1.2 – Electrical Energy Storage

Electrical energy storage is the process of converting electrical energy obtained from a power network into a form which can be stored and converted back into electrical energy when needed.[3] Electrical energy storage is required for a large variety of applications.[4] Portable electronic devices, such as cell phones and laptops are some of the most obvious. Other applications include transportation, such as electric vehicles, load-levelling and storage of electricity generated from renewable sources, such as wind and solar power. There are several different kinds of electrical energy storage systems, which can be classified according to the forms of energy used. These are electrochemical, chemical, electrical, thermal and mechanical.

- **Electrochemical:** Secondary batteries (lead acid, NiCd, Li and NaS) and flow batteries (redox flow and hybrid flow)
- **Chemical:** Hydrogen (electrolyser and fuel cell)
- **Electrical:** Double-layer capacitor and superconducting magnetic coil
- **Thermal:** Sensible heat storage (molten salt)
- **Mechanical:** Pumped hydro, compressed air, flywheel

Each of the aforementioned systems possesses advantages and disadvantages, which makes it either more or less suited to a particular application. For example, double-layer capacitors possess high specific power (2000-5000 W / kg) and high power density (20,000-30,000 W / $m^3$), require low maintenance, have long life with the ability to perform tens of thousands of cycles and are able to be charged and discharged very quickly.[5] However, the technology is hindered by low specific energy (2-5 W h / kg) and low energy density (10,000 W h / $m^3$), high cost ($ 9500 / kW h) and high self-discharge.[6] This makes double-layer capacitors well suited for use in short-term energy storage applications where a large amount of power is needed for a relatively short time with many cycles. However, double-layer capacitors may not be suited to longer-term energy storage applications such as the sole energy storage system in electric vehicles or electronic mobile devices, which require higher energy density, lower costs and lower self-discharge. Secondary batteries would be much better suited to these applications given the high energy density, high efficiency, low self-discharge and good cycle life, giving a few thousand cycles. This report focuses on electrochemical energy storage and in particular lithium-sulfur secondary batteries.

## 1.3 – Electrochemical Energy Storage using Batteries

Batteries are one the most commonly used electrical energy storage devices and are used to convert stored chemical energy into electrical energy on demand when needed.[5, 7] A commercial battery is a device composed of one or more electrochemical cells each of which is composed of two electrodes connected by an ionically conducting material called an electrolyte (Figure 1.3.1).[8] Each electrode has a different chemical potential which is dictated by the chemistry that occurs. In battery systems, the electrode with the more negative chemical potential is known as the negative electrode and the electrode with the more positive chemical potential is known as the positive electrode. For a charged cell, when the electrodes are connected through an external circuit, electrons spontaneously flow from the negative electrode to the positive electrode, generating current to perform work. To maintain charge balance between the two electrodes, ions are able flow through the electrolyte from one electrode to the other.

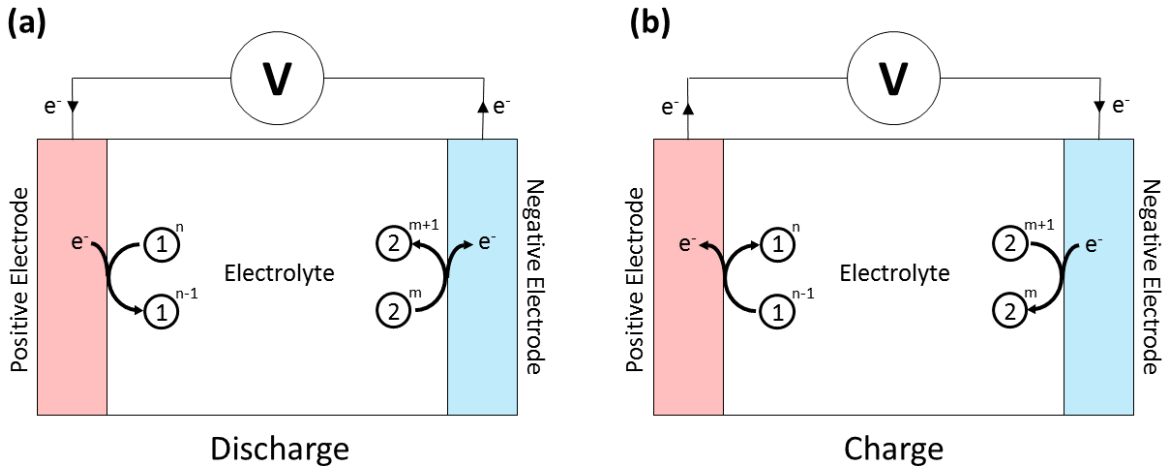


**Figure 1.3.1 –** Generalised schematic diagram of a battery cell during (a) discharge and (b) charge. During discharge, species 1 is reduced at the positive electrode and species 2 is oxidised at the negative electrode. During charge, species 1 is re-oxidised at the positive electrode and species 2 is re-reduced at the negative electrode. Note that the components are not drawn to scale.

There are two types of battery; single discharge primary batteries, and rechargeable secondary batteries. In order to recharge secondary batteries, two techniques are commonly used; constant-current and constant-voltage. During constant-current charging, a current of opposite sign to the discharge current is applied to the battery, whilst the potential 'response' is measured and once a potential limit is reached, charging stops. During constant-voltage charging, a voltage is applied that is larger than the discharge voltage,

whilst the current 'response' is measured and once a current limit is reached, charging stops. Some batteries, such as the modern lithium-ion battery, use a combination of the two charging techniques, in order to improve cycle life.[9-11] The multiple electrochemical cells in batteries are connected in series and/or in parallel to give the required voltage and capacity, respectively.[12] The amount of electrical energy stored in a battery can be expressed in terms of specific energy (W h $kg^{-1}$) or energy density (W h $L^{-1}$) and is a function of both the cell potential (V) and its specific capacity (A h $kg^{-1}$, Equation 1.3.1).[13]

$$Energy = \int_0^{\Delta t} IV(t)dt = \int_0^{Q} V(q)dq$$

**Equation 1.3.1 –** Calculating electrical energy as a function of either time (*t*) or charge (*q*)

Both the cell potential and its capacity are directly linked to the chemistry of the system, which varies depending on the battery technology. Some examples of such battery technologies include lead-acid, nickel-cadmium, nickel-metal hydride and lithium-ion. Currently, lithium-ion batteries dominate the consumer electronic markets and are particularly popular in portable electronic devices.[14] However, for sustainable electric vehicle applications, it is essential that batteries with higher energy densities are developed to enable vehicles to travel longer distances (over 500 kilometres) on a single discharge.[15, 16]

### 1.3.1 – Lithium-Ion Batteries

Sony first commercialised the lithium-ion battery in 1991 and it is known as 'lithium-ion' due to the movement of $Li^+$ ions between the graphite ($Li_xC_6$) negative electrode and a layered-oxide ($Li_{1-x}T^MO_2$) positive electrode, where $T^M$ is a transition metal such as cobalt, nickel or manganese (Figure 1.3.2).[8, 17, 18] Silicon and tin based negative electrodes have also been developed.[7, 19, 20] The materials used in both electrodes are known as insertion materials as they allow the reversible insertion of $Li^+$ ions. The electrolyte is usually composed of a lithium salt dissolved in one or more organic solvents, such as lithium hexafluorophosphate ($LiPF_6$) dissolved in a mixture of ethylene carbonate and diethyl carbonate.[21] Li-ion batteries are prepared in a discharged state using $LiT^MO_2$, and must be charged before use.

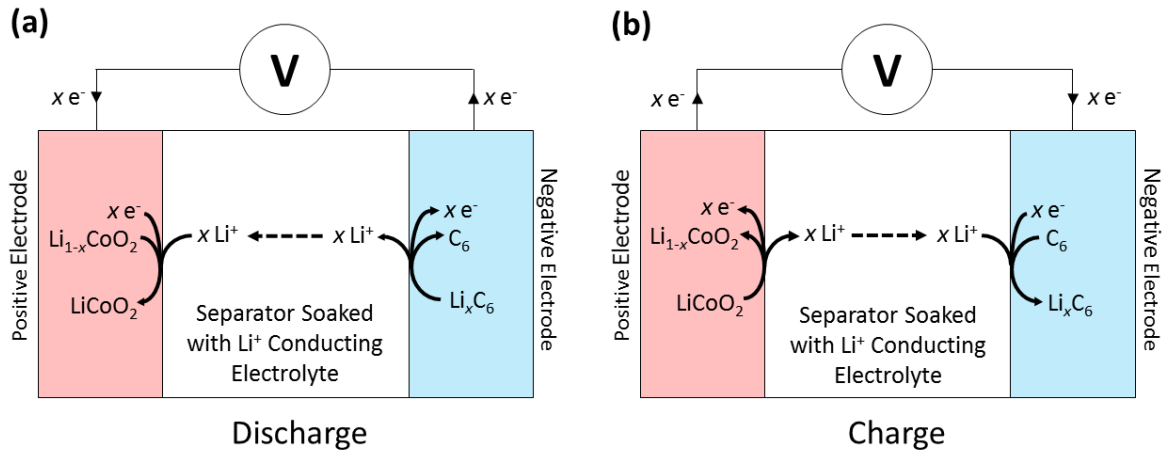


**Figure 1.3.2 –** Generalised schematic diagram of a Li-ion cell using a $LiCoO_2$ positive electrode and $Li_xC_6$ negative electrode during (a) discharge and (b) charge. Note that the components are not drawn to scale.

Li-ion batteries capable of over 30,000 safe discharge/charge cycles have been demonstrated, equivalent to many years of operation.[7, 22] However, secondary batteries with much larger energy densities than is currently possible with Li-ion batteries are required, whilst retaining the cycle life, safety, rate of charge/discharge and affordability. Lithium-sulfur and lithium-air batteries are two promising technologies capable of much larger energy densities than that currently obtainable by Li-ion, however each possesses unique technical challenges that have prevented their commercialisation.

### 1.3.2 – Lithium-Air Batteries

Often referred to as the lithium-oxygen battery, as oxygen is the 'oxidant', the lithium-air battery is composed of a lithium metal negative electrode, a conductive porous positive electrode, usually consisting of a matrix of carbon into which oxygen can diffuse, and an electrolyte, which can be either aqueous or non-aqueous.[16] On discharge, the lithium metal negative electrode is oxidised and $Li^+$ ions are released into the electrolyte.[23] Oxygen from the atmosphere diffuses into the positive electrode and dissolves into the electrolyte within the pores. The dissolved oxygen is then reduced at the electrode surface forming oxides that combine with $Li^+$ ions, which have migrated to the positive electrode from the negative electrode (Figure 1.3.3).

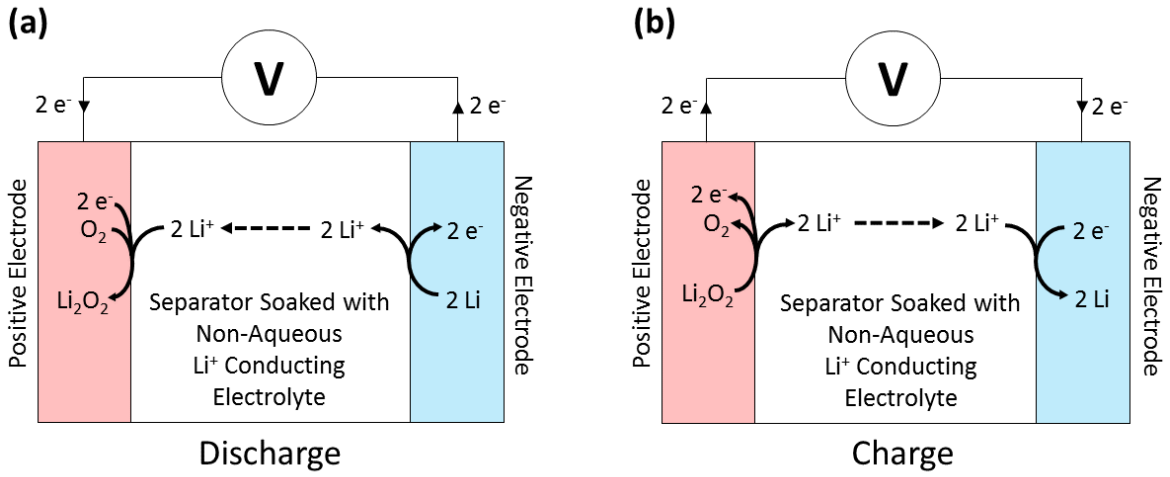


**Figure 1.3.3 –** Generalised schematic diagram of a Li-air cell using a non-aqueous electrolyte during (a) discharge and (b) charge. Note that the components are not drawn to scale.

When using non-aqueous electrolytes, $O_2^{2-}$ is formed on discharge, which when combined with $Li^+$ from the electrolyte forms $Li_2O_2$ (Equation 1.3.2a).[24] On charging, the peroxide decomposes back to oxygen. It has been reported that the cells can be discharged further to give $Li_2O$, which would increase the energy stored (twice the lithium per oxygen), however the decomposition of $Li_2O$ on charging is difficult, reducing the cell performance (Equation 1.3.2b).[16, 25] When using aqueous electrolytes, $OH^-$ is formed on discharge, which combines with $Li^+$ to form LiOH at the positive electrode (Equation 1.3.2c). On charging, the hydroxide is oxidised to give oxygen and water.

(a) $2\ Li^+ + O_2 + 2\ e^- \rightleftharpoons Li_2O_2$

(b) $Li_2O_2 + 2\ Li^+ + 2\ e^- \rightleftharpoons 2\ Li_2O$

(c) $2\ Li^+ + ½\ O_2 + H_2O + 2\ e^- \rightleftharpoons 2\ LiOH$

**Equation 1.3.2 –** Oxygen reduction reactions in lithium-air batteries (a) reduction to lithium peroxide in non-aqueous electrolyte, (b) subsequent reduction to lithium oxide in non-aqueous electrolyte and (c) reduction to lithium hydroxide in aqueous electrolyte.

When based on lithium alone, the lithium-air cell has a theoretical specific energy of 11,586 W h $kg^{-1}$, although since all metal-air cells gain mass through the reaction with oxygen during discharge, the mass of oxygen should also be included. Therefore, a more accurate value for the theoretical specific energy is 3,505 W h $kg^{-1}$, when the discharge

product is $Li_2O_2$.[16, 23] Although lithium-air batteries look promising for the future, the technology is some way from commercialisation and has several major and fundamental challenges to overcome, including electrolyte degradation, small practical capacity, poor cyclability and high overcharge potential.[26]

### 1.3.3 – Sodium-Sulfur Batteries

The sodium-sulfur battery consists of a molten sodium negative electrode, a molten sulfur positive electrode and β''-alumina solid electrolyte.[27] Unlike the lithium based batteries, the sodium-sulfur battery operates at high temperatures of 270 to 350 °C.[28-30] At these elevated temperatures the active electrode materials, sodium and sulfur, are molten and the $Na^+$ conducting membrane between the two electrodes, β''-alumina, exhibits increased conductivity.[31] On discharge, the molten sodium is oxidised and $Na^+$ ions migrate through the solid electrolyte to the molten sulfur positive electrode. The sulfur is reduced to polysulfide species and combine with $Na^+$ ions, which have migrated to the positive electrode from the negative electrode (Figure 1.3.4).

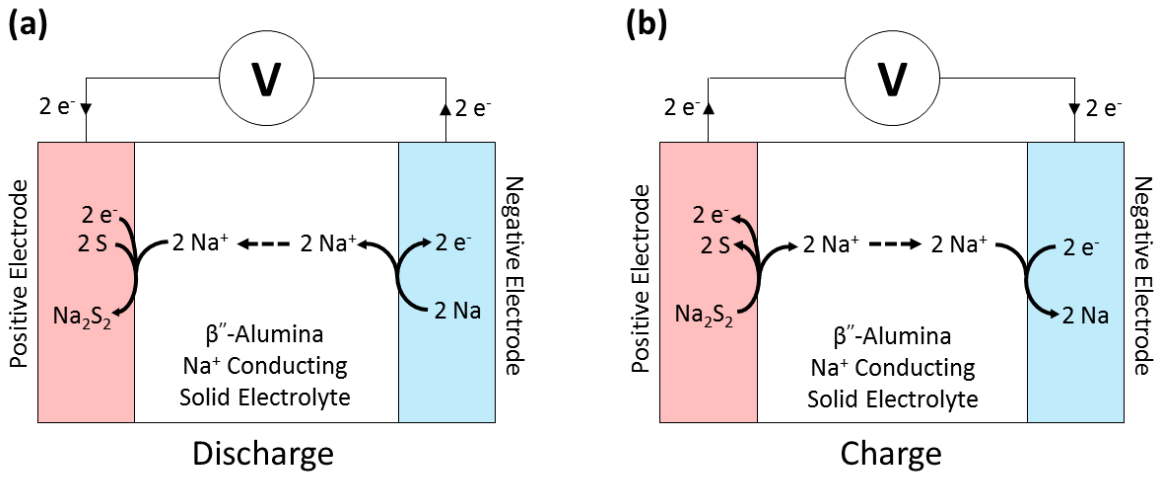


**Figure 1.3.4 –** Generalised schematic diagram of a Na-S cell using a molten sulfur positive electrode and a molten sodium negative electrode during (a) discharge and (b) charge. Note that the components are not drawn to scale.

There are several advantages to using sodium as a negative electrode, including its high abundance, low cost and suitable redox potential ($E^{\circ}_{(Na^+/Na)}$ = -2.71 vs. SHE, or +0.3 V vs. $Li/Li^+$) making it in many ways a suitable replacement to lithium, which has

increased in price due to the huge demand on supplies.[29, 32] Furthermore, using sulfur as a positive electrode has many advantages attributed to its low cost, high capacity and low toxicity. Although sodium-sulfur batteries have been successful in applications such as load-levelling, where energy density is not so important, the high operating temperatures, safety issues and difficulty obtaining high capacities through incomplete reduction of sulfur have prevented sodium-sulfur being incorporated into portable electronics and electric vehicles.

## 1.4 – Lithium-Sulfur Batteries

Research into the field of lithium-sulfur (Li-S) batteries first began over 50 years ago when Herbet and Ulam first used elemental sulfur as a positive electrode material in electric dry cells and storage batteries.[33] Specific characteristics of sulfur make it an attractive material to use in positive electrodes. It is highly abundant and produced as a by-product from oil refineries. Over 60 million tons of sulfur are produced annually, the majority of which is produced through a process known as hydrodesulfurization, which is used to remove sulfur from natural gas and refined petroleum products.[34] However, existing applications have a limited demand for sulfur and there is a huge surplus produced annually (on the order of 7 million tons). As a result sulfur is cheap, estimated at \$4 $kg^{-1}$ for small scale industrial production, which could be further reduced in future sulfur positive electrode mass production to as low as \$0.6 $kg^{-1}$.[35] This is far cheaper than the metal cobalt oxides currently used in the Li-ion technology, which is priced at over \$23 $kg^{-1}$ (nickel manganese cobalt oxide, NMC333).[36] Furthermore, sulfur is non-toxic, making it a favourable material for use in terms of large scale production processes as well as consumer safety. In addition to the sulfur positive electrode being cheap, environmentally friendly and non-toxic, when coupled with lithium, the Li-S battery offers a high theoretical specific capacity (1672 mA h $g^{-1}$), high theoretical specific energy (2600 W h $kg^{-1}$) and high theoretical energy density (2800 W h $L^{-1}$).[15, 37-39] These notably high values of capacity and energy are based on complete conversion of sulfur ($S_8$) to lithium sulfide ($Li_2S$, Equation 1.4.1). Theoretically, the Li-S battery has the potential to produce specific energies up to five times greater than those obtainable for current Li-ion batteries.[40-43] For a packaged Li-S battery, the practical specific energy could reach 400 to 600 W h $kg^{-1}$, which is approximately two or three times higher than that of current commercial Li-ion batteries.[44]

$$S_8 + 16\ Li^+ + 16\ e^- \rightleftharpoons 8\ Li_2S$$

**Equation 1.4.1 –** Overall redox couple in a Li-S cell

A complete Li-S battery is composed of a variety of cell components, including a sulfur positive electrode, a separator, a non-aqueous electrolyte and a lithium negative electrode. The sulfur positive electrode is usually prepared using sulfur; a conductive additive, such as carbon; and a binder, such as polytetrafluoroethylene (PTFE) or

polyvinylidene fluoride (PVdF). The separators are usually composed of expanded polypropylene and the electrolyte is comprised of a lithium salt, commonly bis(trifluoromethane)sulfonamide lithium salt (LiTFSI) dissolved in a mixture of organic solvents such as tetraglyme (TEGDME), 1,3-dioxolane (DOL) or 1,2-dimethoxyethane (DME). The lithium negative electrode is prepared directly from lithium metal. Illustrated below is a schematic of an example Li-S cell during discharge and charge (Figure 1.4.1). However, it should be noted that the reduction of $S_8$ to $Li_2S$ is a multistep process that occurs *via* the formation of several intermediate polysulfide species (discussed further in Chapter 1.4.2).

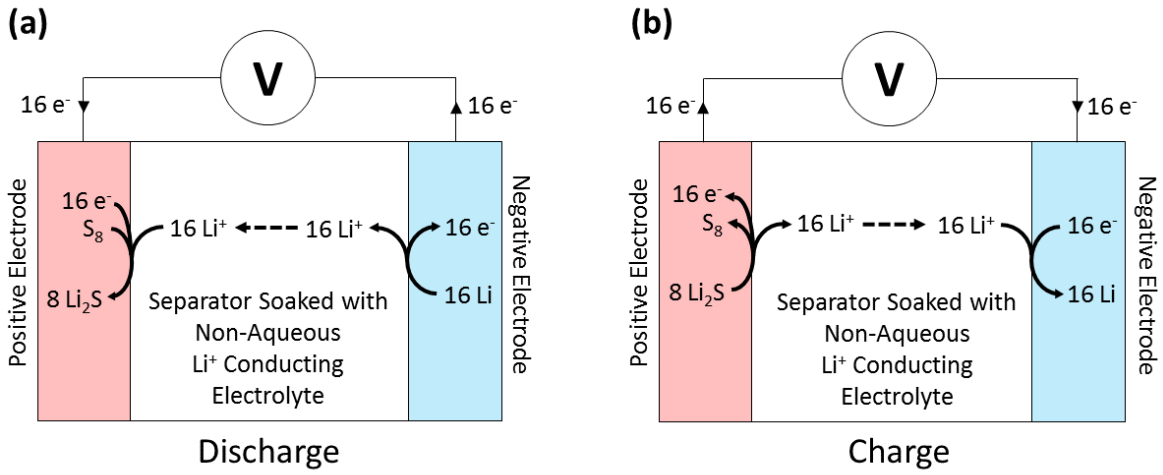


**Figure 1.4.1 –** Generalised schematic diagram of a Li-S cell during (a) discharge and (b) charge. Note that the components are not drawn to scale.

In order to realise this high theoretical capacity and develop electrochemical storage devices that can meet the future needs of electric vehicles, portable electronic devices and storage of electricity generated from renewable sources, there are several technical challenges that must be addressed.[37-41, 45] These technical challenges, which include self-discharge, low coulombic efficiency and poor cyclability, have been outlined in Section 1.4.3. Each of these issues can be attributed to specific aspects of the Li-S cell chemistry and in order find solutions to overcome these challenges, a thorough understanding of the discharge and charge mechanisms is required. There has been significant focus on the fundamentals of Li-S cells in the literature (discussed in Section 1.4.4), however due to the severely complicated nature of the polysulfide intermediates and their sensitivity to their surroundings, no discharge and charge mechanism has been universally accepted.

### 1.4.1 – A Brief Note on Terminology

In this report, the term positive electrode is used to represent the sulfur electrode and the term negative electrode is used to represent the lithium electrode, in order to avoid any obscurity when referring to each electrode. This is due to the terms anode and cathode referring to the flow of current into and out of a polarised electrical device respectively, and depending on whether the cell is charging or discharging, an electrode will change from the cathode to the anode and *vice versa*. It is also important to note that in battery research, the positive and negative electrodes are defined by comparing the redox potentials of the redox reactions occurring at each electrode. The electrode with the more positive redox potential is defined as the positive electrode and the electrode with the more negative redox potential is defined as the negative electrode. For example, in a Li-S battery the redox reaction at the sulfur electrode ($S^0_{(s)} + 2\ Li^+ + 2\ e^- \rightleftharpoons Li_2S_{(s)}$) has a nominal redox potential of -0.8 V vs. SHE, whereas the lithium electrode ($Li^+ + e^- \rightleftharpoons Li$) has a nominal redox potential of -3.0 V vs. SHE and since the sulfur electrode redox reaction possesses the more positive redox potential, it is known as the positive electrode and the lithium electrode is known the negative electrode. Due to the low redox potential of the lithium redox reaction, it is commonly used and defined as a negative electrode in other battery systems. This nomenclature contradicts that used in traditional electrochemistry, where the term positive electrode is synonymous with anode and the term negative electrode is synonymous with cathode, however these terms would be ambiguous for secondary battery systems. In addition, the terms 'specific energy' is used to represent energy per unit mass and 'energy density' is used to represent energy per unit volume. This allows the terms gravimetric energy density and volumetric energy density commonly used in the literature to be avoided, since density more precisely relates to a property per unit volume, not per unit mass. Lastly, it should be noted that during this report, values of potential (or voltage) should be assumed to be measured against a lithium reference electrode (i.e. vs. $Li/Li^+$) unless specifically stated otherwise.

### 1.4.2 – General Mechanism of Discharge and Charge

The mechanism by which Li-S cells discharge and charge remains unclear, although its elucidation has been a subject of interest to many researchers for some time.[46] It is known that both the complete reduction of sulfur ($S_8$) to lithium sulfide ($Li_2S$) and its

reverse oxidation, occur *via* a multistep reaction pathway. Unlike the Li-ion battery, the discharge/charge reactions do not occur in the solid state but rather electron transfer occurs between the carbon framework of the positive electrode interface and the various sulfur species dissolved in the electrolyte, which gives a characteristic discharge profile (Figures 1.4.2 and 1.4.3). In Li-S batteries, carbon is required as a conductive additive due to the insulating nature of sulfur (discussed further in Section 1.4.3). The unique properties of the lithium polysulfide intermediates make them particularly difficult to analyse. For example, the polysulfides are unstable as solids and only observed in solution (dissolved in aqueous or non-aqueous media), with the possible exception of solid $Li_2S_2$, the existence of which has been widely debated.[47-54] The polysulfides are moisture sensitive, reacting with protons ($H^+$) to form hydrogen sulfide ($H_2S$) gas, which is both toxic and volatile. Furthermore, lithium polysulfide species are known to comproportionate and disproportionate to form an equilibria of various polysulfides, the composition of which depends on their thermodynamic stability in that specific environment.[55-58]

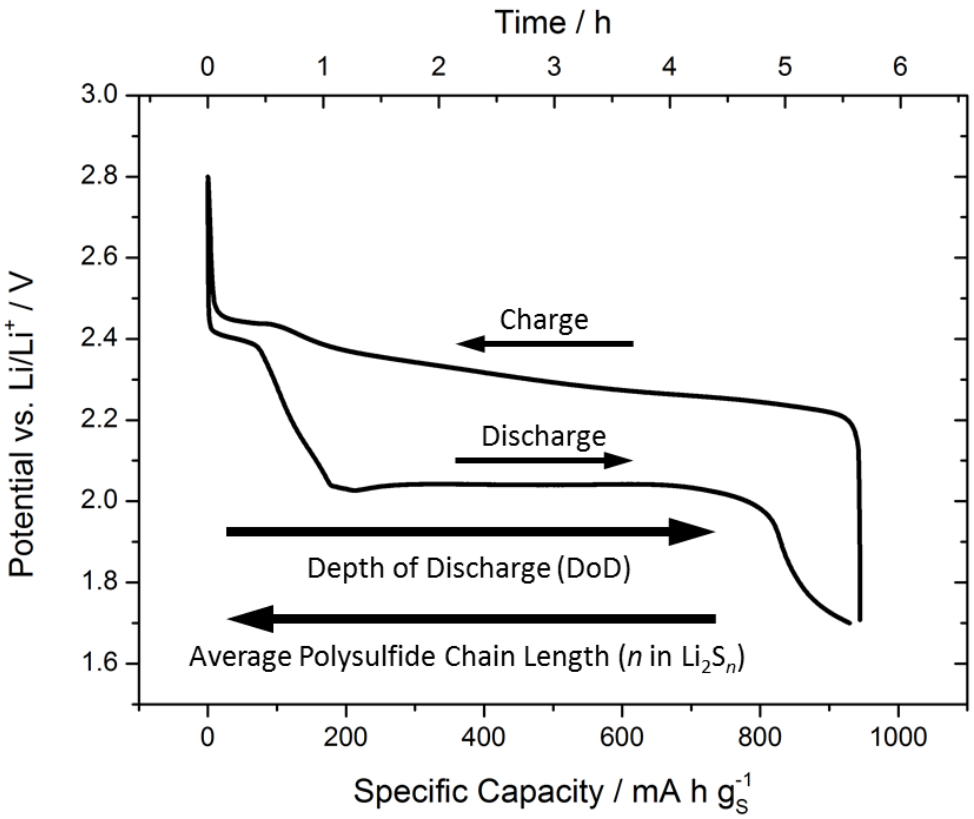


**Figure 1.4.2 –** A typical discharge/charge curve for a Li-S cell when plotting potential vs. capacity (or time). Note that the two discharge plateaux are characteristic of Li-S cells.

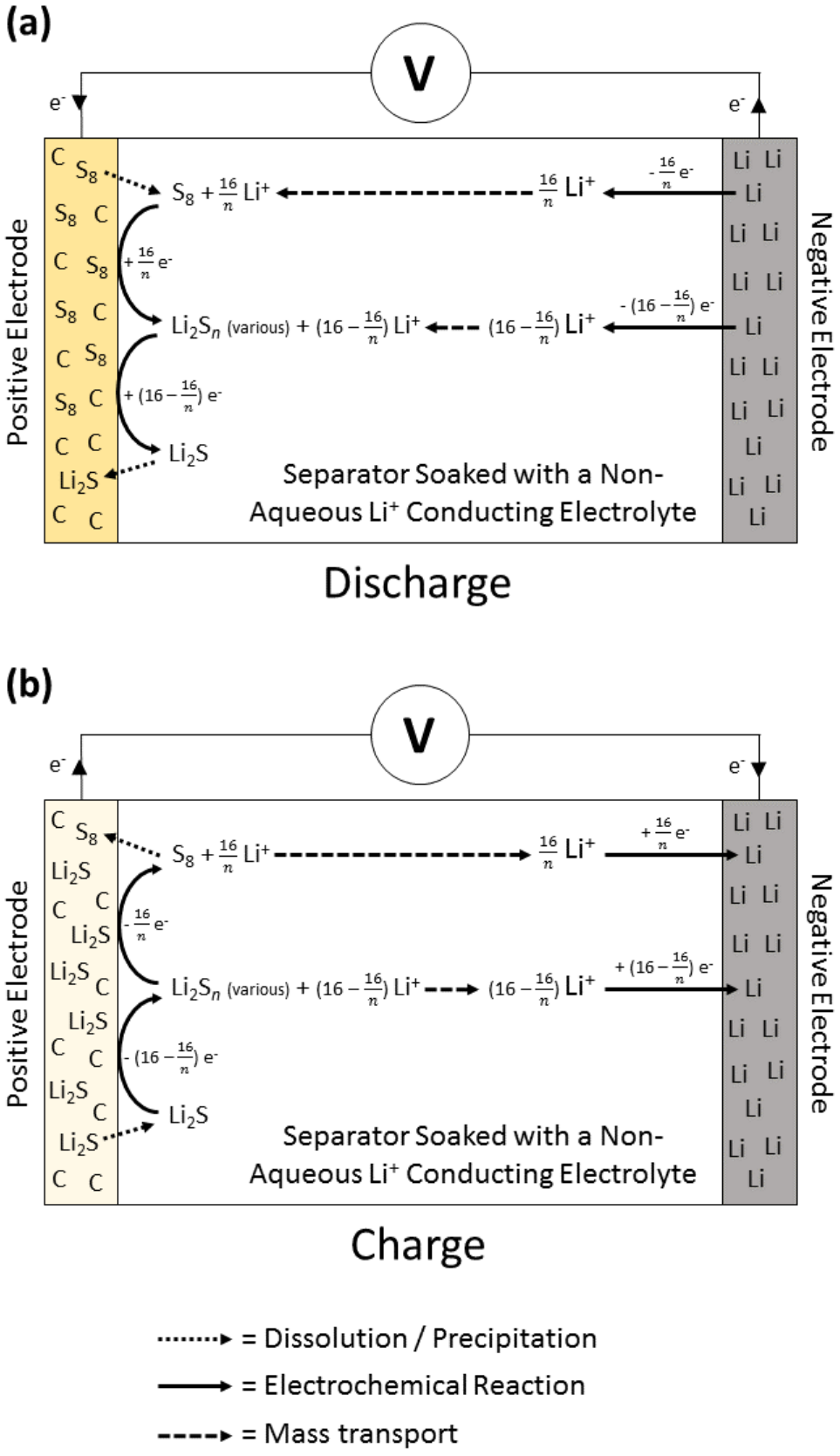


**Figure 1.4.3 –** General mechanism of a Li-S cell during (a) discharge and (b) charge, where $Li_2S_n$ (various) represents multiple polysulfide species with an average chain length of *n*. These polysulfides are formed *via* several electrochemical and chemical processes. Note that the components are not drawn to scale.

### 1.4.3 – Technical Challenges

Li-S batteries show great promise, however several technical challenges have prevented full commercialisation. Although significant progress has been made in these areas, they remain problematic and a better understanding of the mechanism by which Li-S batteries discharge and charge, as well as a thorough understanding of the thermodynamic and kinetic properties of the Li-S system would help in developing new and effective strategies for tackling these issues. Some of the key technical challenges, along with potential solutions, are discussed in this chapter.

Whilst using sulfur as a positive electrode material offers many advantages, an important disadvantage is its insulating nature with the conductivity of sulfur reported to be approximately $10^{-30}$ S $cm^{-1}$.[37, 40, 45] As a result, conductive additives, such as acetylene black or other forms of carbon, are required in order to improve the electrical conductivity of the positive electrode. However, this additional material reduces both the specific energy and energy density of the Li-S cell and so a compromise must be made between improving the electrical conductivity of the positive electrode and maintaining suitably high energy storage. Another key issue comes from the lithium polysulfide intermediates formed during cycling, which are highly soluble in electrolytes prepared using dioxolane and glyme-based solvents. The ability of the polysulfides to freely travel between the positive electrode and negative electrode leads to the well described 'shuttle mechanism' (Figure 1.4.4).[37, 38, 40, 41, 45, 59, 60]

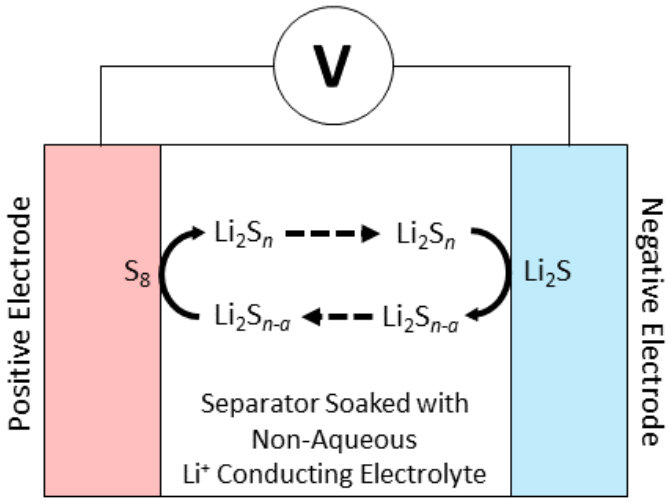


**Figure 1.4.4 –** Generalised schematic diagram of the 'shuttle mechanism', where $Li_2S_n$ represents high-order (or long chain) polysulfide species and $Li_2S_{n-a}$ represents low-order (or short chain) polysulfide species. Note that the components are not drawn to scale and the reaction has not be drawn stoichiometrically.

In this mechanism, the high-order polysulfides (e.g. $Li_2S_8$ or $Li_2S_6$) diffuse through the separator and reach the lithium negative electrode where they are reduced to insoluble $Li_2S$, which deposits on the lithium negative electrode. After coating the lithium negative electrode, high-order soluble polysulfide species react with the fully reduced and insoluble $Li_2S$ to form low-order polysulfide species (e.g. $Li_2S_4$ or $Li_2S_3$), which are also highly soluble. The concentration of these species increases close to the negative electrode which causes them to diffuse back to the positive electrode where they are re-oxidised back into high-order soluble polysulfide species and the process repeats itself. The shuttle mechanism has strongly hindered Li-S battery performance and it has been a leading factor in preventing full commercialisation of the technology. These parasitic reactions are known to consume the active sulfur species, corrode of the lithium negative electrode and polarise the lithium negative electrode through deposition of insoluble $Li_2S$.[37, 38] Furthermore, rapid capacity fading during extended cycling and poor Coulombic efficiency of Li-S cells have been attributed to this shuttling behaviour.[45] Lithium nitrate ($LiNO_3$) is a common electrolyte additive used to protect the lithium metal negative electrode through the formation of a solid electrolyte interface (SEI) and has been shown to prevent the shuttle mechanism and lithium dendrite formation.[42, 61, 62] Additionally, Li-S cells show high self-discharge behaviour, which can also be attributed to shuttling behaviour. After charging, the sulfur and the polysulfides slowly dissolve into the electrolyte even whilst the cell is resting.[45] Due to the concentration gradient, the active material then gradually diffuses to the negative electrode where it is reduced to low-order polysulfides, giving a reduced open-circuit potential and discharge capacity. Mikhaylik *et al.* observed that on increasing the storage time of Li-S cells from several hours to several days, the resulting discharge profiles showed that the upper discharge plateau capacity had decayed.[60] However, it was observed that the lower discharge plateau capacity was stable for several weeks.

Other technical challenges include the precipitation of insoluble $Li_2S$ on the positive electrode after complete discharge of the Li-S cell, which forms insoluble agglomerates.[41] These become electrochemically inaccessible, leading to the loss of active material at the positive electrode and the build-up of passivating layers, which results in capacity fading. Furthermore, the formation of dendritic or ‘mossy’ lithium remains a common problem among lithium-battery technologies where a lithium metal negative

electrode is employed.[61] It is caused by the stripping and plating of lithium during cycling and is a major safety concern. Uncontrolled growth of lithium dendrites may result in contact with the positive electrode, inducing a short circuit that leads to the generation of heat and rapid volume expansion. Furthermore, lithium dendrite formation results in poor Coulombic efficiency and cycle life. This is caused by dendrites breaking from the lithium surface, giving 'dead lithium', which is unusable in subsequent cycles and enhances electrolyte breakdown. Fortunately, the problem of dendrite formation is not as serious in Li-S batteries as it is in other lithium-metal based batteries as the intermediate lithium polysulfides react with and break down the lithium dendrites.[42]

Despite the fact that the exact composition of the polysulfide intermediates present in the electrolyte during cycling remains unclear, it is well reported that their properties can be 'managed' by tailoring the Li-S cell components. For example, positive electrode design has been used to trap polysulfides in order to prevent dissolution into the bulk electrolyte, which ensures high local concentrations of polysulfides at the positive electrode surface and prevents shuttling.[63] This was demonstrated by both Ji *et al.* who used 'nanostructured polymer-modified mesoporous carbon-sulfur composite' and Wang *et al.* using 'graphene-wrapped sulfur particles'.[64, 65] In a different approach, the electrolyte has been modified to reduce polysulfide solubility, either by changing the solvent used or by increasing the electrolyte salt concentration and exploiting the 'common-ion' effect.[46, 66, 67] Cuisinier *et al.* illustrated this using 'non-solvents' (LiTFSI dissolved in acetonitrile and hydrofluoroether) and Suo *et al.* using 'solvent-in-salt' electrolytes.[66, 67] Furthermore, ion selective membranes have also been used, which allow the lithium cations ($Li^+$) to pass but repel the polysulfide anions ($S_n^{2-}$) and prevent the polysulfide species shuttling to the lithium negative electrode.[39] This was demonstrated by Huang *et al.* who used the sulfonate groups ($-SO_3^-$) of Nafion to allow $Li^+$ to permeate through the separator but not polysulfides.[39]

Once again, despite the significant progress that has been made in these areas, the issues remain problematic and a better understanding of the mechanism by which Li-S batteries discharge and charge is required. In addition to managing the properties of the polysulfide intermediates, many researchers have attempted to identify the individual polysulfide species that exist. However, before evaluating these results, several limitations

in these methods should be noted. Firstly, any proposed species observed experimentally will be specific to the system used in that experiment and may or may not exist in other systems. In other words, certain polysulfide species will be more or less stable depending on the system adopted and in particular, the electrolyte system used will be important in influencing this. Secondly, the experimental conditions, such as cycling rate, will influence the species observed. Whether thermodynamic or kinetic conditions are applied will influence which species are observed at each stage of charge and discharge. Lastly, the methods of identifying the polysulfide species will have limitations, making complete observation of all polysulfide species difficult. These limitations are discussed on case-by-case basis.

### 1.4.4 – Techniques used in Previous Mechanistic Studies

Due to the rising interest in Li-S battery research, several approaches have been taken to aid the mechanistic understanding of Li-S battery discharge and charge. This understanding is important in order to overcome the fundamental challenges associated with Li-S batteries and enable full commercialisation of the technology. The majority of these studies focus on the identification of the intermediate polysulfide species, using various methods of spectroscopy, some of which are performed *in situ* and/or *in operando*. In this section, some of these mechanistic studies have been briefly described in order to illustrate the broad range of different techniques that have been used, as well as the variation in the interpretation of the mechanisms of discharge and charge.

Barchasz *et al.* used several spectroscopic techniques, including ultraviolet-visible (UV-vis) spectroscopy, high-performance liquid chromatography (HPLC) and electron spin resonance (ESR) spectroscopy to identify intermediate polysulfide species dissolved in electrolyte.[56] They hypothesised that $S_8^{2-}$ and $S_6^{2-}$ dianions are produced during the first reduction process, which disproportionate to give $S_5^{2-}$ and $S_3^{\bullet-}$ species. Then in the second reduction process, $S_6^{2-}$ and $S_3^{\bullet-}$ are reduced to $S_4^{2-}$ and $S_3^{2-}$. Then in the final reduction process, $S_3^{-}$, $S_2^{2-}$ and $S^{2-}$ are formed and these tend to precipitate in the electrolyte. As discussed in the article, it is not possible to isolate individual polysulfide species making it difficult to completely characterise the polysulfide system using UV-vis spectroscopy alone, particularly given each polysulfide species can be responsible for several absorption

bands, which are observed at similar values of wavelength. To achieve characterisation by UV-vis spectroscopy, values from other literature sources were used and an assumption was made that the polysulfide absorption energy decreases with increasing polysulfide chain length. In order to support the analysis of the UV-vis spectroscopic data, HPLC was used as it can separate the different polysulfide species by their respective chain lengths, where the retention time is increased with chain length. However, in order to perform the HPLC, the polysulfide species must be methylated using methyl trifluoromethane sulfonate (MeTf) to stabilise the species and prevent further com-/disproportionation reactions. A buffer solution (pH = 7) of 1 M $Na_3PO_4/Na_2HPO_4/NaH_2PO_4$ was added at the same time as the MeTf to prevent the formation of protons ($H^+$), which could react with polysulfides, altering their composition. Furthermore, HPLC cannot be used to detect $S^{2-}$ as $Li_2S$ is practically insoluble. ESR was used to detect the $S_3^{\bullet-}$, however ESR is limited to the detection of radical species.

Cuisinier *et al.* used *operando* X-ray absorption near-edge spectroscopy (XANES) to monitor sulfur speciation on the positive electrode of a Li-S battery.[68] They hypothesised that during discharge, $S_8^{2-}$ rapidly disproportionates to $S_6^{2-}$ and $S_8^0$ and a stable equilibrium is formed between $S_8^0$, $S_6^{2-}$ and $S_4^{2-}$. However, it should be noted that for such a disproportionation reaction to occur, a minimum of four $S_8^{2-}$ molecules would be required and therefore, such a reaction is only likely to occur if very high concentrations of $S_8^{2-}$ are present. For the most part, this process agrees with Barchasz *et al.* who also concluded that the dominating species during the first discharge process were $S_8^0$, $S_6^{2-}$ and $S_4^{2-}$, where $S_8^{2-}$ disproportionates to $S_6^{2-}$ and $S_8^0$. Cuisinier *et al.* hypothesised that the concentrations of $S_8^0$, $S_6^{2-}$ and $S_4^{2-}$ remain fairly constant throughout much of the second plateau until the formation of $Li_2S$, when the concentration of $Li_2S$ increases at the expense of the polysulfides. The charge mechanism differs from the discharge mechanism in that $Li_2S$ is slowly consumed throughout most of the charge process. This comprehensive study gives a great insight into the polysulfide speciation during discharge and charge, however similarly to UV-vis data, any reference spectra prepared will contain a mixture of polysulfide species making peak identification difficult. Furthermore, synchrotron radiation and a specific cell design are required to obtain XANES data, limiting the availability of the technique.

Waluś *et al.* used *operando* X-ray diffraction (XRD) to identify solid precipitate formation during cycling.[69] XRD is only able to observe solid, crystalline materials, which in the Li-S battery limits detection to solid $S_8^0$ and $Li_2S$. They observed that during discharge, crystalline $Li_2S$ was detected on the positive electrode at the beginning of the second plateau, which indicates that $Li_2S$ solid is present throughout the entire second plateau. This contradicts other reports, including those by Barchasz *et al.* and Cuisinier *et al.*, which suggest that solid $Li_2S$ only forms at the end of the second plateau. Whilst studies using XRD are able to give valuable information on the mechanism, they are unable to give any insight into the nature of the polysulfide species present. Furthermore, a specific cell design is required to obtain *in situ* XRD data and *ex situ* results could be misleading given the phase transitions that can occur whilst resting.

Wu *et al.* used *in situ* Raman spectroscopy to identify soluble polysulfide species formed during cycling.[48] They hypothesised that during the first reduction step (2.4 V), long chain polysulfides species ($S_8^{2-}$) were formed from $S_8^0$ ring opening and during the second reduction step (2.3 V), short chain polysulfide species ($S_4^{2-}$, $S_4^-$, $S_3^{\bullet-}$ and $S_2O_4^{2-}$) were formed. They also concluded that the short chain polysulfides completely decomposed at 1.6 V and by fitting the appearance and disappearance of bands to a pseudo first order reaction, they were able to calculate the rate constant for these processes, which showed that the $S_8^0$ disappearance and polysulfide appearance occur at the same rate. Furthermore, they illustrated that adding carbon disulfide ($CS_2$) to the electrolyte, changed the sulfur reduction mechanism by preventing the formation of short chain polysulfide species. Similarly to the other spectroscopic techniques discussed, analysing the Raman data for polysulfide species is challenging as it relies on using previous literature values and density functional theory (DFT) calculations to characterise the observed peaks. Furthermore, the vibrational frequencies of the different polysulfide species are solvent dependant.

Huff *et al.* used $^6$Li and $^{33}$S magic angle spinning (MAS) nuclear magnetic resonance (NMR) spectroscopy to identify the discharge products on Li-S battery positive electrodes coupled with $^7$Li and $^1$H NMR spectroscopy.[70] They described that the chemical shifts ($^{33}$S) of the longer chain, soluble polysulfides formed at the beginning of discharge were indistinguishable from each other, however it was possible to identify the insoluble

$Li_2S$, which they detected only at the end of discharge (1.5 V). This contradicts the results from the XRD study of Waluś *et al.*, who observed that $Li_2S$ was formed at the beginning of the second plateau. Furthermore, this study was performed on electrodes *ex situ* and so the species detected may not be representative of those present whilst the cell is in operation. Another notable technique used to study the mechanism of discharge and charge includes using *operando* optical imaging of the temporal and spatial distribution of soluble polysulfides in Li-S batteries, by Sun *et al.*[71]

The aforementioned studies are just some examples of literature that has focused on improving the mechanistic understanding of Li-S battery discharge and charge. These examples were chosen to illustrate the variety of different techniques that have been adopted, as well as the variety of results that have been obtained, whether supporting or conflicting. However, there is plenty more literature that employs these techniques, as well as others, helping to elucidate the mechanism of Li-S battery discharge and charge.[72-82] These results, among others, have been nicely summarised by Wild *et al.*, who have completely reviewed the current mechanistic understanding of Li-S battery discharge and charge from the perspective of both experimental studies and physical modelling.[83] They have also managed to highlight the important limitations of such studies and proposed a simplified model for the Li-S mechanism.

The reviewed studies have illustrated that the mechanism of the Li-S battery is complex and it is likely that both thermodynamic and kinetic factors play important roles in both the discharge and charge processes. However, before attempting to understand the associated kinetics, it is important that the thermodynamic equilibria of the system are well understood. To do this, the Li-S battery can be considered to possess three components, the equilibrium of which controls the composition and concentration of the polysulfides dissolved in the electrolyte. The proposed components are $S_8$, $Li_2S$ and electrolyte, since any polysulfide electrolyte solution can be described as a mixture of these three components (Equation 1.4.2).

$$Li_2S_{n\,(solv.)} \rightleftharpoons \frac{(n-1)}{8} S_{8\,(s)} + Li_2S_{(s)} + \text{electrolyte (e.g. LiTFSI in DOL)}$$

**Equation 1.4.2 –** An illustration that any polysulfide electrolyte solution can be described as a mixture of the three components sulfur ($S_8$), lithium sulfide ($Li_2S$) and electrolyte (e.g. LiTFSI in DOL).

By presenting these components in the form of a ternary phase diagram, it should be possible to not only predict the composition and concentration of the polysulfide species dissolved in the electrolyte, but also to make predictions on the formation of solid products and to provide a deeper understanding of the characteristic discharge and charge voltage profiles. Furthermore, a ternary phase diagram would enable electrolyte systems to be designed more efficiently, tailoring their properties to the application for which the battery is required. Whilst a ternary phase diagram is limited to providing a purely thermodynamic understanding of the Li-S mechanism of discharge and charge, which should provide a good approximation for slow cycling rates, it provides an essential starting point to study the kinetics of the system at faster cycling rates.

## 1.5 – Ternary Phase Diagram

A ternary plot is used to graphically depict the ratios of three variables, which sum to a constant (usually 1.0 or 100%), as positions on an equilateral triangle. In physical chemistry, among other scientific fields, it is used to show the composition of three component systems. In these plots, the three variables must sum to a constant and hence only two variables must be stated to describe the ternary composition.[84] This means that two dimensions must be used to represent the composition on a complete phase diagram. Including the two component variables, other external variables that must be considered include temperature and pressure. To construct a complete phase diagram would require four-dimensional space, so in most cases the pressure of the system is assumed to be constant (normally atmospheric). To represent fully a ternary phase diagram with temperature as a variable, a three dimensional model (commonly termed as space model) would be required. In this work, the temperature of the system is considered constant (room temperature) and so only a two dimensional model is required.

### 1.5.1 – Gibbs' Phase Rule

Proposed by Josiah Willard Gibbs in 1878,[85] the Gibbs' phase rule typically applies to non-reactive multi-component heterogeneous systems, which are in thermodynamic equilibrium with each other. Knowing the number of components and phases present, it is possible to determine the degrees of freedom associated with each phase and whether the composition of the saturated electrolyte solution will change given small variations in the amount of each component present (Equation 1.5.1).

$$\text{Freedom} = \text{Components} - \text{Phases}$$

**Equation 1.5.1 –** Gibbs' Phase Rule for determining the degrees of freedom at fixed temperature and pressure.

This can be applied to a Li-S battery to describe the $S_8$-$Li_2S$-electrolyte system. Despite the fact that $Li_2S$ and $S_8$ react to form polysulfides, the Gibbs' phase rule can still be applied assuming that both $Li_2S$ and $S_8$ are the only two solids present and the polysulfide species are dissolved (Equation 1.5.2). This is analogous to the $S_8$ and $Li_2S$

species dissolving into the electrolyte and precipitating back out. However, the fact that $S_8$ and $Li_2S$ are poorly soluble (< 100 mM) but the polysulfide species produced are very soluble (> 5 M) leads to the addition of one solid improving the solubility of the other. This has been discussed further in section 1.5.4.

$$Li_2S_{(s)} + \frac{(n-1)}{8} S_{8\,(s)} \rightarrow Li_2S_{n\,(solv.)}$$

**Equation 1.5.2 –** Reaction of solid $Li_2S$ and solid $S_8$ to give dissolved $Li_2S_n$

### 1.5.2 – Three Component Systems Composed of Two Solids and One Liquid

Various ternary systems exist as three liquid systems, or systems containing two solids and one liquid. An example of the latter is given in Figure 1.5.1, which describes a ternary system of water and two salts, potassium chloride (KCl) and sodium chloride (NaCl). At the top of the phase diagram there is a one-phase region (coloured white) where everything dissolves and only the solution is present. To the left and right of the phase diagram there are two two-phase regions (coloured blue and green) consisting of one solid and the solution, which is saturated with respect to the solid species. To the bottom of the phase diagram there is a three-phase region (coloured red), where both solids are present as well as the solution, which is saturated with respect to both solids.

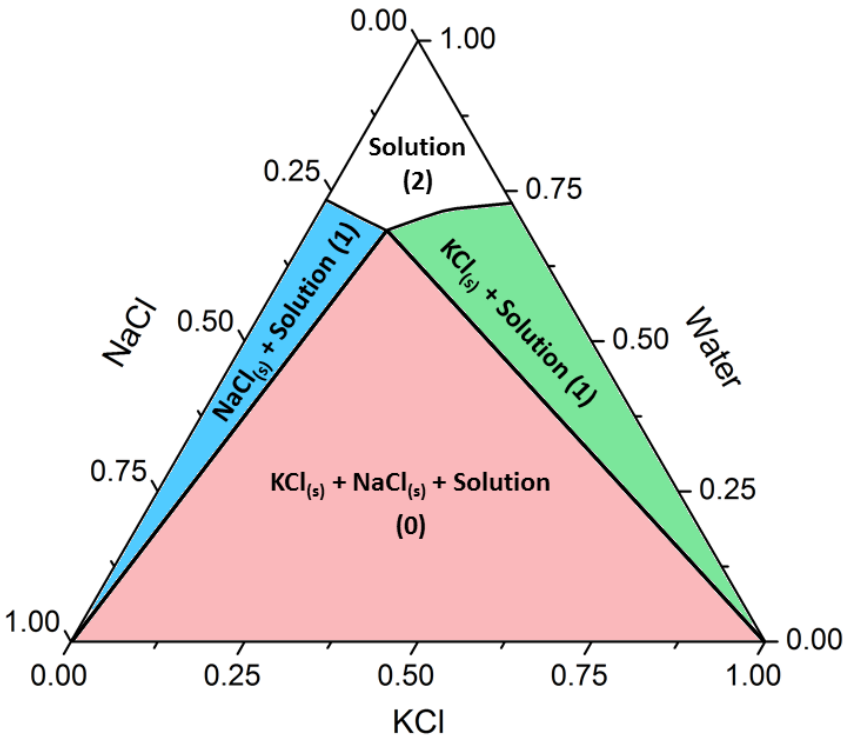


**Figure 1.5.1 –** A ternary phase diagram for KCl, NaCl and water, temperature at 298 K and pressure at 1 bar. The degrees of freedom associated with each phase is given in brackets. The values used to sketch this phase diagram were taken from the National Research Council.[86]

For each of the described phase regions the degrees of freedom, calculated using Gibb's Phase Rule (Equation 1.5.1), have been indicated in brackets. For example, the three-phase region has no degrees of freedom (i.e. zero), because the number of components is three (NaCl, KCl and water) as it is for all phase regions in this system and the number of phases is three ($KCl_{(s)}$, $NaCl_{(s)}$ and solution), which varies depending on the phase region. Since the three-phase region has zero degrees of freedom, small changes in the quantity of each component used (assuming the prepared mixture remains in the boundaries of the three-phase region) will not affect the salt concentration or composition dissolved in the solution, i.e. only in this region is the solution saturated with respect to both salt components (NaCl and KCl). In any of the other phase regions (either two phase or one phase), the calculated degrees of freedom are greater than zero, hence changing the quantity of each component used (except for the saturated solid) will affect the salt concentration and composition dissolved in solution, i.e. the solution is not saturated with respect to both solids. This also assumes very fast reaction kinetics, where the system is effectively always at thermodynamic equilibrium.

In this phase diagram, where we have two solid components and one liquid component, moving vertically from the top to the bottom of the phase diagram can be considered analogous to increasing the concentration of salt added to the mixtures. Whilst in the one-phase region, where both salt components fully dissolve, the exact salt concentration and composition dissolved in solution will be known. However, in either of the other phase regions (two- or three-phase), the salt concentration and composition dissolved in the solution will be unknown, unless a method is used to analyse either the dissolved salt solutions or remaining salt precipitate.

The Li-S system can be modelled in a similar way, assuming that there are three components present in the form of two solids and a liquid. The two solids are $S_8$ (fully charged species) and $Li_2S$ (fully discharged species) and the liquid would be the electrolyte. Such a phase diagram would be extremely useful in predicting the dissolution and precipitation of $S_8$ and $Li_2S$ and it would enable the concentration and composition of polysulfide species dissolved in the electrolyte to be calculated. Furthermore, it would be a great insight into the Li-S battery mechanism of discharge and charge to observe how the appearance of such a ternary phase diagram would change when varying parameters, such as sulfur loading, electrolyte volume and solvent system.

### 1.5.3 – Current Lithium-Sulfur Battery Phase Diagrams

Despite great interest in the Li-S battery technology and numerous mechanistic studies, there has been little research on a representative ternary phase diagram. There is only one known example, proposed by See *et al.* who used a ternary phase diagram to explain their experimental observation from an $^7$Li NMR study that solid $Li_2S$ formation occurs near the beginning of the first plateau (Figure 1.5.2).[49] This observation is contradictory to several previous XRD studies, which all reported either detecting solid $Li_2S$ after the first reduction plateau, or not at all. However, this study utilised *in situ* $^7$Li NMR, which can detect very small quantities of solid regardless of crystallinity and particle size, unlike XRD which requires a minimum particle size and crystallinity to enable detection. Therefore, it is suggested that perhaps during those XRD studies, solid $Li_2S$ may have been formed much earlier than was detected, since the initial solid $Li_2S$ formed may have been small amorphous particles. The sulfur-lithium-electrolyte ternary

phase diagram suggested by See *et al.* (Figure 1.5.2) has very similar features to the NaCl-KCl-water ternary phase diagram (Figure 1.5.1) described in Section 1.5.2. Both phase diagrams are three component systems, containing two solids and one liquid and both possess four distinct phase regions; one one-phase region (coloured orange), two two-phase regions (coloured white with red tie lines) and one three-phase region (coloured blue).

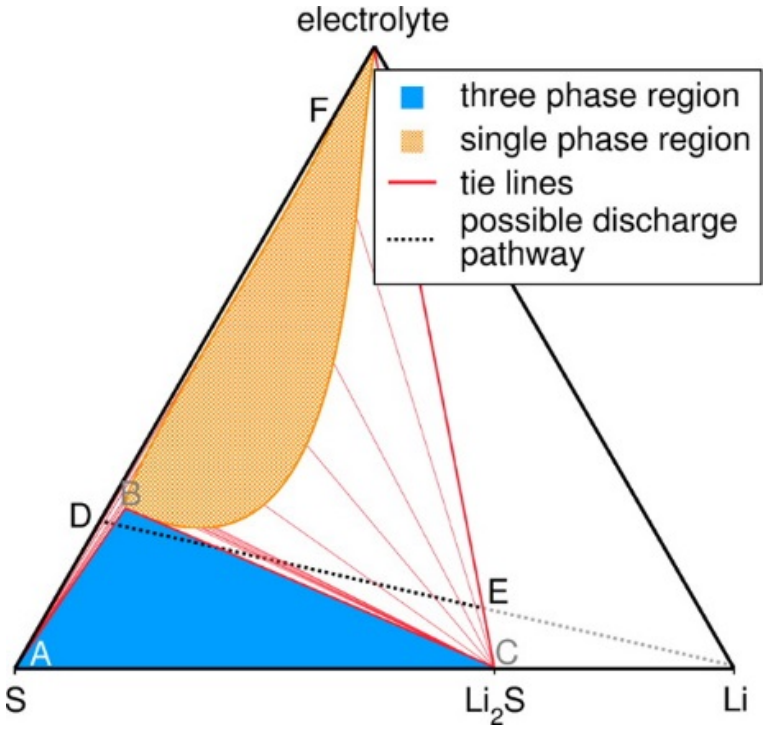


**Figure 1.5.2 –** Phase diagram of Li-S cell suggested by See *et al.*, reprinted from Ref.[49] Copyright © 2014 American Chemical Society. Permission to reproduce figure not required as the article is open access and published under a Creative Commons Attribution (CC-BY) License.

In the one-phase region (orange) everything dissolves giving polysulfides dissolved in electrolyte; in the left-hand side two-phase region (white with red tie lines) there is solid $S_8$ and polysulfides dissolved in electrolyte; in the right-hand side two-phase region (also white with red tie lines) there is solid $Li_2S$ and polysulfides dissolved in electrolyte; and in the three-phase region (blue) there is solid $S_8$, solid $Li_2S$ and polysulfides dissolved in electrolyte. At the top vertex labelled 'electrolyte', only electrolyte is present without any active material (i.e. $S_8$ or $Li_2S$) but on moving from this vertex down towards the bottom binary sulfur-$Li_2S$ axis, the amount of active material present increases, which is synonymous with increasing the sulfur-to-electrolyte ratio in a Li-S cell. The binary sulfur-

electrolyte axis on the left-hand side represents a system that only contains sulfur and electrolyte, as is the case in a fully charged Li-S cell, whereas the binary $Li_2S$-electrolyte axis represents a system that only contains $Li_2S$ and electrolyte, as is the case in a fully discharged Li-S cell. Therefore, during the discharge of a Li-S cell, the composition of the system is expected to change from a position on the left-hand side of the diagram to a position closer to the right-hand side and *vice versa* during charge. Li-S cells prepared with low sulfur-to-electrolyte ratios (e.g. coin cells with an excess of electrolyte) would possess discharge/charge pathways close to the top of the phase diagram, whereas Li-S cells prepared with high sulfur-to-electrolyte ratios (e.g. commercial pouch cells) would possess discharge/charge pathways closer to the bottom of the phase diagram.

See *et al.* have labelled a possible discharge pathway (Figure 1.5.2, dashed black line linking point D to point E) on the phase diagram, which rationalises the results obtained using $^7$Li NMR.[49] It is suggested that before discharging the cell, the composition at the positive electrode – electrolyte interface sits on the binary sulfur-electrolyte axis (point D). They point out that for high sulfur to electrolyte ratios at the positive electrode surface, the initial composition will lie close to pure sulfur. It is then suggested that assuming local equilibrium, the line will quickly pass through the three-phase region, at which point solid $Li_2S$ will form and coexist with both solid $S_8$ and dissolved polysulfides in electrolyte, hence the detection of solid $Li_2S$ early in the first plateau by $^7$Li NMR. They state that on passing through the three-phase region, the formation of solid $Li_2S$ will likely occur on pre-existing $S_8$ particle surfaces, forming a '$Li_2S$/S core-shell morphology'. This is supported by the measured linear increase in $Li_2S$ formation, suggesting a surface reaction that does not rely on solid-state Li diffusion. It is then reported that the positive electrode – electrolyte interface exits the three-phase region, indicating electrochemical passivation of the $S_8$ due to $Li_2S$ deposition, and enters the two-phase region where $Li_2S$ formation continues *via* the reduction of polysulfides dissolved in the electrolyte. The discharge then comes to an end as the composition at the positive electrode – electrolyte interface reaches the binary $Li_2S$-electrolyte axis (point E).

See *et al.* then continue to describe how the suggested phase diagram can be used to explain the shape of the measured discharge profile (Figure 1.5.3).[49] They state that the potential will exhibit a plateau when either passing through the three-phase region, which

is consistent with Gibbs' Phase Rule, or the variation in composition is parallel to a tie line in the two-phase region. They predict that otherwise, whilst in the two-phase region, the potential will slope with the gradient defined by the density of the tie lines. They report that the first plateau observed is consistent with the three-phase region and the initial dip in potential before the first plateau can be associated with the polarisation required to overcome the nucleation barrier to form solid $Li_2S$. After the first plateau, the potential drops, which has been attributed to passage through dense tie lines between $Li_2S$ and a very stable dissolved polysulfide. Then the next plateau has been attributed to passing through the two-phase region with a low density of tie lines.

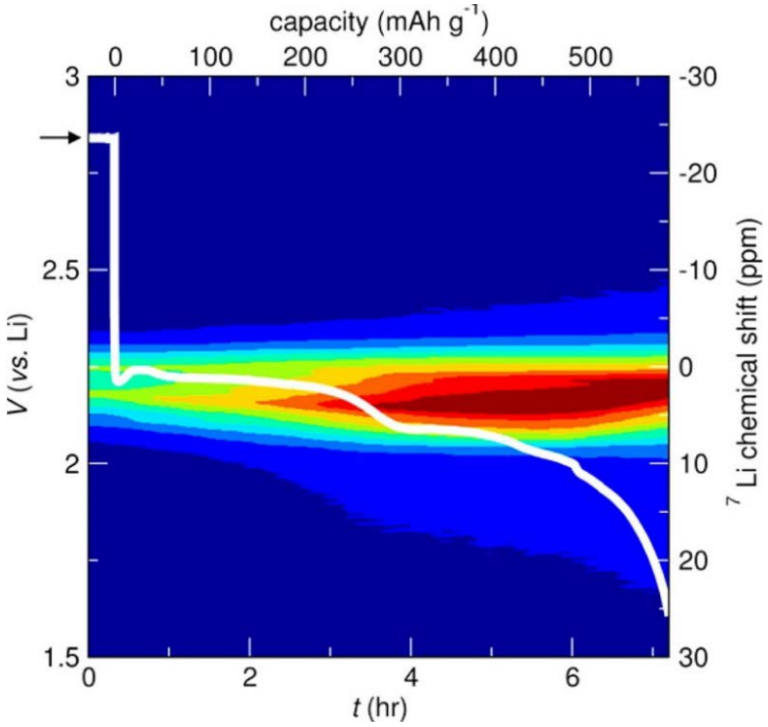


**Figure 1.5.3 –** Li-S bag cell discharge profile with the $^7$Li NMR signal overlaid, C/20 rate using 1 M LiTFSI in DOL/DME electrolyte by See *et al.*, reprinted from Ref.[49] Copyright © 2014 American Chemical Society. Permission to reproduce figure not required as the article is open access and published under a Creative Commons Attribution (CC-BY) License.

See *et al.* then continue to explain that despite the proposed three-phase region being consistent with nearly all observations, it is indeed inconsistent with the observed linear increase in dissolved $Li^+$ formation determined by $^7$Li NMR. This is because on passing through the three-phase region, the dissolved polysulfide concentration and composition in the electrolyte close to the positive electrode surface should remain

constant as predicted by Gibbs' Phase Rule. They attribute this contradiction to inhomogeneity in the polysulfide composition/concentration throughout the cell as a whole, i.e. the whole cell is not in equilibrium. Hence as the polysulfide species diffuse away from the positive electrode surface, polysulfides need to be formed at the positive electrode – electrolyte interface, along with solid $Li_2S$, in order to maintain the constant polysulfide concentration at the positive electrode surface, which in turn increases the overall $Li^+$ concentration in the electrolyte.

This innovative study is the first to suggest a ternary phase diagram for the Li-S battery and use it to explain the mechanism of discharge. They nicely describe the features of the phase diagram and illustrate how it can be used to explain the Li-S battery discharge profile. However, it should be noted that this phase diagram has been qualitatively drawn to explain the results obtained from the $^7Li$ NMR study. In the literature, there is yet to be a ternary phase diagram for the Li-S battery that has been produced using quantitatively determined values. To do this would require quantitative analysis of the polysulfides dissolved in the electrolyte, in terms of concentration and composition. Determining such parameters quantitatively is not trivial and would require novel analytical techniques to be developed. This was one of the major aims of this work, to develop quantitative analytical methods for determining parameters that will enable the production of the first experimentally determined ternary phase diagram for the Li-S battery.

### 1.5.4 – Proposition of Ternary Phase Diagram

Li-S batteries discharge *via* the transformation of solid $S_8$ to solid $Li_2S$ *via* the formation of several polysulfide species that have only been observed in solution. Similar to the sulfur-lithium-electrolyte ternary phase diagram proposed by See *et al.*,[49] it should be possible to predict the general form that such a ternary phase diagram for Li-S batteries would take (Figure 1.5.4).

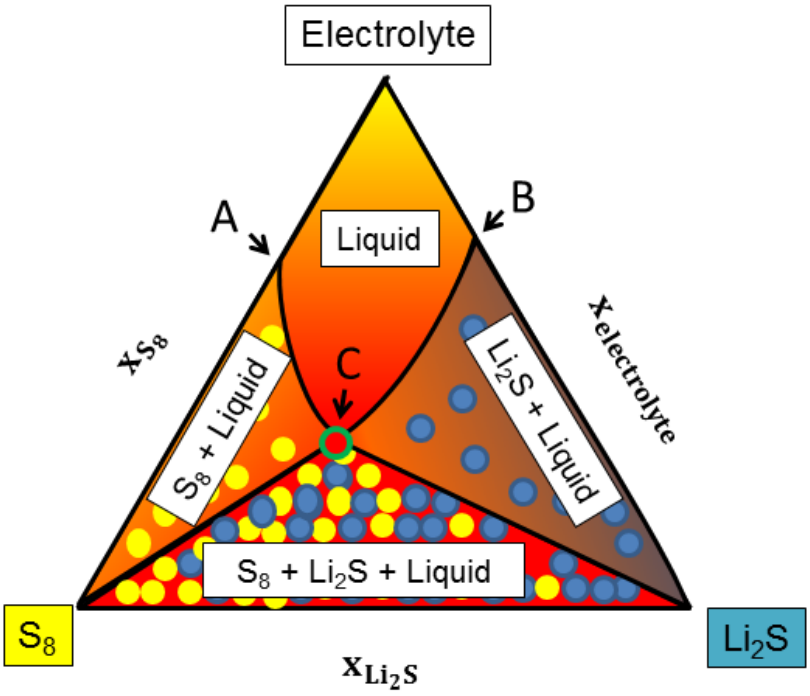


**Figure 1.5.4 –** General form of the ternary phase diagram for a $S_8$-$Li_2S$-electrolyte system.[87]

In the generalised form of the ternary phase diagram, there are still four different phase regions. At the top of the diagram, we have the one-phase region, where everything dissolves in the electrolyte. At either side of the phase diagram, there are two two-phase regions. On the left-hand side, the two-phase region consists of solid $S_8$ and polysulfides dissolved in electrolyte, i.e. the electrolyte is saturated with respect to $S_8$. On the right-hand side, the two-phase region consists of solid $Li_2S$ and polysulfides dissolved in electrolyte, i.e. the electrolyte is saturated with respect to $Li_2S$. Along the $S_8$-electrolyte binary axis, point A represents the saturation concentration for $S_8$ dissolved in electrolyte and along the $Li_2S$-electrolyte binary axis, point B represents the saturation concentration for $Li_2S$ dissolved in electrolyte. Starting from point A, it can be seen that the one-phase/two-phase boundary follows a downward curve, which illustrates how adding $Li_2S$ in solution, effectively increases the solubility of $S_8$ by reacting with it to form polysulfides, which are far more soluble than either solid component $S_8$ or $Li_2S$. Similarly starting from point B, it can be seen that the one-phase/two-phase boundary follows a downward curve, which illustrates how adding $S_8$ in solution, effectively increases the solubility of $Li_2S$ due to the reaction to form polysulfides. These two one-phase/two-phase boundaries meet at point C, which is the congruent solution composition, which is analogous to the eutectic point in the binary $S_8$-$Li_2S$ phase diagram with respect to temperature. At this point, the electrolyte is

saturated with respect to both $S_8$ and $Li_2S$, i.e. it is in equilibrium with both of the solid components. Therefore, this point corresponds to the maximum concentration of all the polysulfide species in a given electrolyte at a given temperature and pressure. This point will possess a specific polysulfide concentration and composition, which will remain constant throughout the entire three-phase region. The axes of the ternary phase diagram are known as binary axes and these are labelled with the binary mole fraction ($x_i$) of each component. The bottom $S_8$-$Li_2S$ binary axis is related to the stoichiometry of the polysulfides ($Li_2S_n$, Equation 1.5.3).

$$x_{Li_2S} = \frac{[Li_2S]}{[S] + [Li_2S]} = \frac{1}{n}$$

**Equation 1.5.3 –** Binary mole fraction of $Li_2S$ ($x_{Li_2S}$) where *n* is the average theoretical chain length $Li_2S_n$.

According to Gibbs' Phase Rule, the one-phase region where everything dissolves will possess two degrees of freedom, the two two-phase regions will possess one degree of freedom and the three-phase region will possess zero degrees of freedom (Figure 1.5.5).

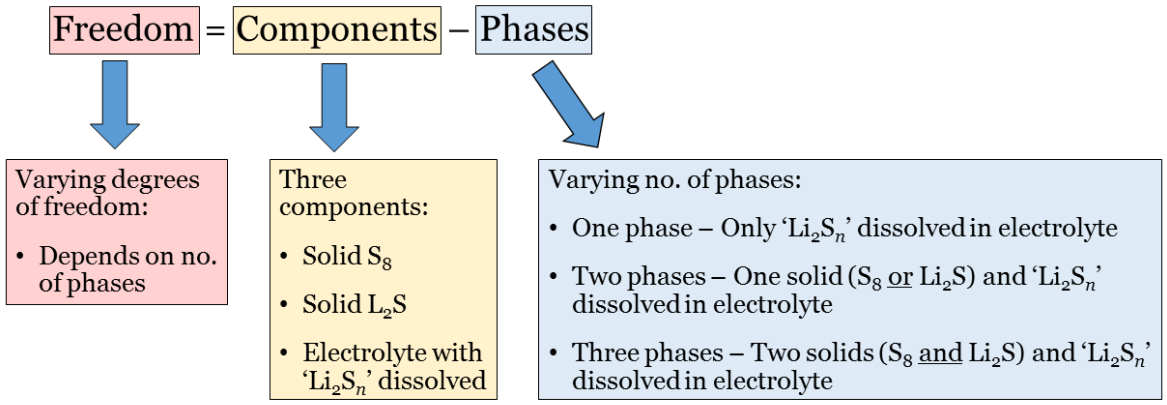


**Figure 1.5.5 –** Calculating the degrees of freedom using Gibbs' Phase Rule, assuming constant pressure and temperature.

An experimentally determined ternary phase diagram of the $S_8$-$Li_2S$-electrolyte system would be a practical tool to determine the solution composition and formation of solids ($S_8$ and $Li_2S$) in Li-S batteries. It could be used to predict the appearance of the discharge and charge voltage profiles as a function of $S_8$ to electrolyte ratio and the onset potential of precipitation and dissolution reactions. High energy Li-S batteries should

operate with the highest $S_8$ to electrolyte ratio possible, which means that both solid $S_8$ and solid $Li_2S$ will be present during most of the cell discharge and charge, i.e. the cell will operate primarily in the three-phase region. In this case, it is predicted that only one voltage plateau will be observed, instead of the characteristic two voltage plateau that are commonly reported. However, it should be noted that the ternary phase diagram is a purely thermodynamic treatment based on the equilibrium between the three components (solid $S_8$, solid $Li_2S$ and electrolyte). In addition to this, we do not consider the existence of any other solid species such as $Li_2S_2$, which has been often cited as a reaction intermediate despite the fact that a crystal structure has yet to be published.

Furthermore, polysulfides do not exist in the solid state and hence the term 'solubility' of polysulfides should be clarified. In this instance, the term 'solubility' simply refers to the polysulfide saturation concentration in the chosen electrolyte system. Unlike traditional solubility, precipitation and dissolution of the polysulfide species does not occur, rather polysulfides are formed in solution through comproportionation and disproportionation reactions from dissolved $S_8$ and $Li_2S$ (Equation 1.5.4). The dissolved polysulfide $Li_2S_n$ represents the average composition for various polysulfides, where the average chain length is *n*. Once the saturation concentration of the polysulfides has been reached (i.e. the solubility limit), then the $S_8$ and/or $Li_2S$ precipitate out of solution.

$$Li_2S_{(s)} + \frac{(n-1)}{8} S_{8\,(s)} \rightarrow Li_2S_{n\,(solv.)}$$

**Equation 1.5.4 –** Reaction of solid $Li_2S$ and solid $S_8$ to give dissolved $Li_2S_n$

## 1.6 – Aims and Objectives

Despite many significant advances in the field of Li-S batteries, full commercialisation has not yet been possible as technical challenges have restricted its practical applications. In order to overcome these challenges, it is important to comprehensively understand the mechanism of the discharge and charge processes. The primary focus of this research project, has been to develop various techniques to characterise the electrolytes used in Li-S batteries, as well as the polysulfide species dissolved within them. Utilising these techniques should improve the fundamental understanding of the Li-S battery discharge and charge mechanisms and offer greater insight into the role that the electrolyte plays on this mechanism. In addition to this, these techniques should enable high performance electrolytes to be chosen more effectively.

In this report, there are four main sections:

1. **Cell design –** A Li-S cell design that affords good cycling performance in terms of both specific capacity and cycle life, as well as offering high reproducibility was chosen and $LiNO_3$ was investigated as an electrolyte additive.
2. **Electrolyte salt concentration –** A model electrolyte system of LiTFSI dissolved in 1,3-dioxolane (DOL) was used to investigate the effects of varying the electrolyte salt concentration on electrolyte density, conductivity, viscosity, polysulfide solubility, thermal phase transitions, cycling performance (Swagelok and coin cell setup) and lithium corrosion.
3. **Ternary phase diagram –** Techniques were developed to quantitatively determine both the concentration and composition of polysulfide species present in electrolyte solutions, enabling the production of the first experimental $S_8$-$Li_2S$-electrolyte ternary phase diagram.
4. **Galvanostatic intermittent titration technique (GITT) –** Thorough analysis of the GITT technique has been performed using a model reversible redox system. The advantages and limitations of this techniques are presented, alongside its ability to determine the diffusion coefficient of a species dissolved in electrolyte. A conclusion is made on the techniques ability to analyse the mass transport of species within the Li-S battery during cycling.

## 1.7 – References


1. Key World Energy Statistics 2015, https://www.iea.org/publications/freepublications/publication).

2. D. J. C. MacKay, *Sustainable Energy: Without the Hot Air*, UIT, 2009.

3. H. S. Chen, T. N. Cong, W. Yang, C. Q. Tan, Y. L. Li and Y. L. Ding, *Prog. Nat. Sci.*, 2009, **19**, 291-312.

4. M. S. Whittingham, *MRS Bull.*, 2008, **33**, 411-419.

5. F. Díaz-González, A. Sumper, O. Gomis-Bellmunt and R. Villafáfila-Robles, *Renew. Sust. Energ. Rev.*, 2012, **16**, 2154-2171.

6. H. Ibrahim, A. Ilinca and J. Perron, *Renew. Sust. Energ. Rev.*, 2008, **12**, 1221-1250.

7. J. B. Goodenough and K.-S. Park, *J. Am. Chem. Soc.*, 2013, **135**, 1167-1176.

8. M. Armand and J. M. Tarascon, *Nature*, 2008, **451**, 652-657.

9. S. S. Zhang, *J. Power Sources*, 2006, **161**, 1385-1391.

10. S. S. Zhang, K. Xu and T. R. Jow, *J. Power Sources*, 2006, **160**, 1349-1354.

11. J. Li, E. Murphy, J. Winnick and P. A. Kohl, *J. Power Sources*, 2001, **102**, 302-309.

12. J. M. Tarascon and M. Armand, *Nature*, 2001, **414**, 359-367.

13. Y. Wang and Y. Xia, *Nat Chem*, 2013, **5**, 445-447.

14. J. Hun-Gi, J. Hassoun, P. Jin-Bum, S. Yang-Kook and B. Scrosati, *Nat. Chem.*, 2012, **4**, 579-585.

15. A. Manthiram, Y. Fu and Y.-S. Su, *Acc. Chem. Res.*, 2012, **46**, 1125-1134.

16. P. G. Bruce, S. A. Freunberger, L. J. Hardwick and J. M. Tarascon, *Nat. Mater.*, 2012, **11**, 19-29.

17. A. R. Armstrong and P. G. Bruce, *Nature*, 1996, **381**, 499-500.

18. Y. Nishi, *J. Power Sources*, 2001, **100**, 101-106.

19. C. K. Chan, H. Peng, G. Liu, K. McIlwrath, X. F. Zhang, R. A. Huggins and Y. Cui, *Nat Nano*, 2008, **3**, 31-35.

20. Y. Idota, T. Kubota, A. Matsufuji, Y. Maekawa and T. Miyasaka, *Science*, 1997, **276**, 1395.

21. A. S. Arico, P. Bruce, B. Scrosati, J.-M. Tarascon and W. van Schalkwijk, *Nat Mater*, 2005, **4**, 366-377.

22. K. Zaghib, M. Dontigny, A. Guerfi, P. Charest, I. Rodrigues, A. Mauger and C. M. Julien, *J. Power Sources*, 2011, **196**, 3949-3954.

23. N.-S. Choi, Z. Chen, S. A. Freunberger, X. Ji, Y.-K. Sun, K. Amine, G. Yushin, L. F. Nazar, J. Cho and P. G. Bruce, *Angew. Chem. Int. Ed.*, 2012, **51**, 9994-10024.

24. G. Girishkumar, B. McCloskey, A. C. Luntz, S. Swanson and W. Wilcke, *J. Phys. Chem. Lett.*, 2010, **1**, 2193-2203.

25. S. S. Zhang, D. Foster and J. Read, *J. Power Sources*, 2010, **195**, 1235-1240.

26. H. D. Lim, H. Song, J. Kim, H. Gwon, Y. Bae, K. Y. Park, J. Hong, H. Kim, T. Kim, Y. H. Kim, X. Lepro, R. Ovalle-Robles, R. H. Baughman and K. Kang, *Angewandte Chemie-International Edition*, 2014, **53**, 3926-3931.

27. F. Cheng, J. Liang, Z. Tao and J. Chen, *Adv. Mater.*, 2011, **23**, 1695-1715.

28. B. Dunn, H. Kamath and J. M. Tarascon, *Science*, 2011, **334**, 928-935.

29. B. L. Ellis and L. F. Nazar, *Curr. Opin. Solid State Mater. Sci.*, 2012, **16**, 168-177.

30. X. Lu, G. Xia, J. P. Lemmon and Z. Yang, *J. Power Sources*, 2010, **195**, 2431-2442.

31. J. Liu, J.-G. Zhang, Z. Yang, J. P. Lemmon, C. Imhoff, G. L. Graff, L. Li, J. Hu, C. Wang, J. Xiao, G. Xia, V. V. Viswanathan, S. Baskaran, V. Sprenkle, X. Li, Y. Shao and B. Schwenzer, *Adv. Funct. Mater.*, 2013, **23**, 929-946.

32. K. B. Hueso, M. Armand and T. Rojo, *Energ. Environ. Sci.*, 2013, **6**, 734-749.

33. *US Pat.*, US3043896, 1962.

34. W. J. Chung, J. J. Griebel, E. T. Kim, H. Yoon, A. G. Simmonds, H. J. Ji, P. T. Dirlam, R. S. Glass, J. J. Wie, N. A. Nguyen, B. W. Guralnick, J. Park, SomogyiÁrpád, P. Theato, M. E. Mackay, Y.-E. Sung, K. Char and J. Pyun, *Nat Chem*, 2013, **5**, 518-524.

35. M. Hagen, S. Dörfler, P. Fanz, T. Berger, R. Speck, J. Tübke, H. Althues, M. J. Hoffmann, C. Scherr and S. Kaskel, *J. Power Sources*, 2013, **224**, 260-268.

36. S. Ahmed, P. A. Nelson, K. G. Gallagher, N. Susarla and D. W. Dees, *J. Power Sources*, 2017, **342**, 733-740.

37. G. Y. Xu, B. Ding, J. Pan, P. Nie, L. F. Shen and X. G. Zhang, *J. Mater. Chem. A*, 2014, **2**, 12662-12676.

38. S. S. Zhang, *J. Power Sources*, 2013, **231**, 153-162.

39. J. Q. Huang, Q. Zhang, H. J. Peng, X. Y. Liu, W. Z. Qian and F. Wei, *Energ. Environ. Sci.*, 2014, **7**, 347-353.

40. S. Evers and L. F. Nazar, *Acc. Chem. Res.*, 2013, **46**, 1135-1143.

41. X. L. Ji and L. F. Nazar, *J. Mater. Chem.*, 2010, **20**, 9821-9826.

42. G. Ma, Z. Wen, M. Wu, C. Shen, Q. Wang, J. Jin and X. Wu, *Chem. Commun.*, 2014, **50**, 14209-14212.

43. Q. W. Tang, Z. Q. Shan, L. Wang, X. Qin, K. L. Zhu, J. H. Tian and X. S. Liu, *J. Power Sources*, 2014, **246**, 253-259.

44. Y.-X. Yin, S. Xin, Y.-G. Guo and L.-J. Wan, *Angew. Chem. Int. Ed.*, 2013, **52**, 13186-13200.

45. A. Manthiram, Y. Fu, S.-H. Chung, C. Zu and Y.-S. Su, *Chem. Rev.*, 2014, **114**, 11751-11787.

46. K. Ueno, J. W. Park, A. Yamazaki, T. Mandai, N. Tachikawa, K. Dokko and M. Watanabe, *J. Phys. Chem. C*, 2013, **117**, 20509-20516.

47. M. Marinescu, T. Zhang and G. J. Offer, *PCCP*, 2016, **18**, 584-593.

48. H.-L. Wu, L. A. Huff and A. A. Gewirth, *ACS Appl. Mater. Inter.*, 2014, **7**, 1709-1719.

49. K. A. See, M. Leskes, J. M. Griffin, S. Britto, P. D. Matthews, A. Emly, A. Van der Ven, D. S. Wright, A. J. Morris, C. P. Grey and R. Seshadri, *J. Am. Chem. Soc.*, 2014, **136**, 16368-16377.

50. M. R. Busche, P. Adelhelm, H. Sommer, H. Schneider, K. Leitner and J. Janek, *J. Power Sources*, 2014, **259**, 289-299.

51. Y.-S. Su, Y. Fu, T. Cochell and A. Manthiram, *Nat. Commun.*, 2013, **4**.

52. P. Partovi-Azar, T. D. Kuhne and P. Kaghazchi, *PCCP*, 2015, **17**, 22009-22014.

53. G. Yang, S. Shi, J. Yang and Y. Ma, *J. Mater. Chem. A*, 2015, **3**, 8865-8869.

54. Z. Feng, C. Kim, A. Vijh, M. Armand, K. H. Bevan and K. Zaghib, *J. Power Sources*, 2014, **272**, 518-521.

55. D. Zheng, X. R. Zhang, C. Li, M. E. McKinnon, R. G. Sadok, D. Y. Qu, X. Q. Yu, H. S. Lee, X. Q. Yang and D. Y. Qu, *J. Electrochem. Soc.*, 2015, **162**, A203-A206.

56. C. Barchasz, F. Molton, C. Duboc, J.-C. Leprêtre, S. Patoux and F. Alloin, *Anal. Chem.*, 2012, **84**, 3973-3980.

57. D.-H. Han, B.-S. Kim, S.-J. Choi, Y. Jung, J. Kwak and S.-M. Park, *J. Electrochem. Soc.*, 2004, **151**, E283-E290.

58. S.-I. Tobishima, H. Yamamoto and M. Matsuda, *Electrochim. Acta*, 1997, **42**, 1019-1029.

59. S. Z. Xiong, K. Xie, Y. Diao and X. B. Hong, *J. Power Sources*, 2014, **246**, 840-845.

60. Y. V. Mikhaylik and J. R. Akridge, *J. Electrochem. Soc.*, 2004, **151**, A1969-A1976.

61. W. Li, H. Yao, K. Yan, G. Zheng, Z. Liang, Y. M. Chiang and Y. Cui, *Nat. Commun.*, 2015, **6**, 7436.

62. J. Bruckner, S. Thieme, H. T. Grossmann, S. Dorfler, H. Althues and S. Kaskel, *J. Power Sources*, 2014, **268**, 82-87.

63. A. Manthiram, S.-H. Chung and C. Zu, *Adv. Mater.*, 2015, **27**, 1980-2006.

64. X. Ji, K. T. Lee and L. F. Nazar, *Nat Mater*, 2009, **8**, 500-506.

65. H. Wang, Y. Yang, Y. Liang, J. T. Robinson, Y. Li, A. Jackson, Y. Cui and H. Dai, *Nano Lett.*, 2011, **11**, 2644-2647.

66. L. Suo, Y.-S. Hu, H. Li, M. Armand and L. Chen, *Nat. Commun.*, 2013, **4**, 1481.

67. M. Cuisinier, P. E. Cabelguen, B. D. Adams, A. Garsuch, M. Balasubramanian and L. F. Nazar, *Energ. Environ. Sci.*, 2014, **7**, 2697-2705.

68. M. Cuisinier, P. E. Cabelguen, S. Evers, G. He, M. Kolbeck, A. Garsuch, T. Bolin, M. Balasubramanian and L. F. Nazar, *J. Phys. Chem. Lett.*, 2013, **4**, 3227-3232.

69. S. Walus, C. Barchasz, J. F. Colin, J. F. Martin, E. Elkaim, J. C. Lepretre and F. Alloin, *Chem. Commun.*, 2013, **49**, 7899-7901.

70. L. A. Huff, J. L. Rapp, J. A. Baughman, P. L. Rinaldi and A. A. Gewirth, *Surf. Sci.*, 2015, **631**, 295-300.

71. Y. Sun, Z. W. Seh, W. Li, H. Yao, G. Zheng and Y. Cui, *Nano Energy*, 2015, **11**, 579-586.

72. N. A. Cañas, D. N. Fronczek, N. Wagner, A. Latz and K. A. Friedrich, *J. Phys. Chem. C*, 2014, **118**, 12106-12114.

73. M. A. Lowe, J. Gao and H. D. Abruna, *RSC Advances*, 2014, **4**, 18347-18353.

74. M. U. M. Patel, I. Arčon, G. Aquilanti, L. Stievano, G. Mali and R. Dominko, *ChemPhysChem*, 2014, **15**, 894-904.

75. M. Vijayakumar, N. Govind, E. Walter, S. D. Burton, A. Shukla, A. Devaraj, J. Xiao, J. Liu, C. Wang, A. Karim and S. Thevuthasan, *PCCP*, 2014, **16**, 10923-10932.

76. K. H. Wujcik, J. Velasco-Velez, C. H. Wu, T. Pascal, A. A. Teran, M. A. Marcus, J. Cabana, J. Guo, D. Prendergast, M. Salmeron and N. P. Balsara, *J. Electrochem. Soc.*, 2014, **161**, A1100-A1106.

77. R. Xu, I. Belharouak, X. Zhang, R. Chamoun, C. Yu, Y. Ren, A. Nie, R. Shahbazian-Yassar, J. Lu, J. C. M. Li and K. Amine, *ACS Appl. Mater. Inter.*, 2014, **6**, 21938-21945.

78. T. A. Pascal, C. D. Pemmaraju and D. Prendergast, *PCCP*, 2015, **17**, 7743-7753.

79. H. Marceau, C.-S. Kim, A. Paolella, S. Ladouceur, M. Lagacé, M. Chaker, A. Vijh, A. Guerfi, C. M. Julien, A. Mauger, M. Armand, P. Hovington and K. Zaghib, *J. Power Sources*, 2016, **319**, 247-254.

80. D. Zheng, X. Zhang, J. Wang, D. Qu, X. Yang and D. Qu, *J. Power Sources*, 2016, **301**, 312-316.

81. Q. Zou and Y.-C. Lu, *J. Phys. Chem. Lett.*, 2016, **7**, 1518-1525.

82. M. U. M. Patel, R. Demir-Cakan, M. Morcrette, J. M. Tarascon, M. Gaberscek and R. Dominko, *ChemSusChem*, 2013, **6**, 1177-1181.

83. M. Wild, L. O'Neill, T. Zhang, R. Purkayastha, G. Minton, M. Marinescu and G. J. Offer, *Energ. Environ. Sci.*, 2015, **8**, 3477-3494.

84. F. C. Campbell, *Phase Diagrams: Understanding the Basics*, ASM International, 2012.

85. J. W. Gibbs, *American Journal of Science*, 1878, **Series 3 Vol. 16**, 441-458.

86. N. R. Council, E. W. Washburn, C. J. West, I. c. o. s. unions, C. Hull and N. A. o. Sciences, *International Critical Tables of Numerical Data, Physics, Chemistry and Technology*, National Research Council, 1928.

87. J. W. Dibden, J. W. Smith, N. Zhou, N. Garcia-Araez and J. R. Owen, *Chem. Commun.*, 2016, **52**, 12885-12888.

# 2 – Experimental Procedures and Techniques

## 2.1 – General Experimental Procedures

In this section, the general experimental procedures that are used throughout this report have been described. Any experimental procedures or details that are specific to one particular chapter have been described in the experimental details section of that specific chapter. Unless specifically stated otherwise, all chemicals were used as received from their respective suppliers.

### 2.1.1 – Electrolyte Preparation

The electrolyte salts used in this report were bis(trifluoromethane)sulfonimide lithium salt (LiTFSI, 99.95%, Sigma-Aldrich) and lithium nitrate ($LiNO_3$, 99.99%, Sigma-Aldrich), which were both dried under vacuum (< 0.2 mbar) at 130 °C for at least 48 hours before use. After drying, the LiTFSI and $LiNO_3$ were stored in an argon-filled glovebox (oxygen and water content < 5 ppm) until use. Two solvents were used for electrolyte preparation, 1,3-dioxolane (DOL) and tetraethylene glycol dimethyl ether (TEGDME). DOL (99.8%, anhydrous, ~75 ppm butylated hydroxytoluene (BHT) as inhibitor, Sigma-Aldrich) was taken into the argon-filled glovebox (oxygen and water content < 5 ppm) on receiving and stored in the glovebox until use. TEGDME (≥ 99%, Sigma-Aldrich) was dried under vacuum at 90 °C for at least 72 hours, whilst stirring. After drying, the TEGDME was stored in an argon-filled glovebox (oxygen and water content < 5 ppm) until use. Unless stated otherwise, all electrolytes were prepared in an argon-filled glovebox (oxygen and water content < 5 ppm). The appropriate mass of LiTFSI was dissolved into the desired solvent or solvent mixture. Electrolytes were generally used within one month of preparation, unless a redox additive was used (e.g. $FcBF_4$), in which case the electrolytes were prepared as needed and used within a week. Throughout this report, the concentration is described in terms of molarity (M = mol $L^{-1}_{electrolyte}$) unless specifically stated otherwise. In the other cases, a form of 'molality' is used, which measures moles per litre of solvent added (mol $L^{-1}_{solvent}$). This method was used in Section 4.3.1 only, in order to compare results to data reported in the literature.

### 2.1.2 – Separator Preparation

Several different types of separator have been used throughout this report, including glass-fibre separators, polypropylene separators and lithium-ion conducting glass-ceramic. Glass-fibre separators (Whatman®, glass microfiber filters, grades GF/F and GF/C) were punched into appropriate sizes and dried under vacuum (< 0.2 mbar) at 130 °C overnight. After drying, the glass-fibre separators were stored in an argon-filled glovebox (oxygen and water content < 5 ppm) until use. The polypropylene separators (Toray T20) were punched into appropriate sizes and dried under vacuum (< 0.2 mbar) at room temperature overnight. After drying, the polypropylene separators were stored in an argon-filled glovebox (oxygen and water content < 5 ppm) until use. The lithium-ion conducting glass ceramic discs (LICGC™, Ohara Corporation, Ø = 1 inch) were dried under vacuum at 80 °C overnight. After drying, the LICGC separators were stored in an argon-filled glovebox (oxygen and water content < 5 ppm) until use.

## 2.2 – Cell Designs

Various test cell designs have been used during this project. For clarification, each cell design has been illustrated in this section and the individual components described. Any cell modifications specific to a certain chapter will be discussed in the experimental details section of that specific chapter. All cells were assembled in an argon-filled glovebox (oxygen and water content < 5 ppm) before taking outside of the glovebox for electrochemical testing, unless stated otherwise.

### 2.2.1 – Swagelok® Cell

In this report, two sizes of Swagelok cell have been used (Figure 2.2.1), where the inner diameter of the stainless steel body is either 1 inch or ½ inch in size. The 1 inch cell was used in preference to the ½ inch cell, when a piece of lithium-ion conducting glass ceramic (LICGC™, Ohara Corporation) needed to be incorporated into the cell, as the LICGC was only available as discs with a diameter of 1 inch. LICGC allows good conductivity of lithium ions ($Li^+$ conductivity is $1 \times 10^{-4}$ S $cm^{-1}$, at room temperature) but inhibits the movement of other species, such as polysulfides. This allows the two electrodes in the Swagelok cell to be isolated, preventing any unwanted side reactions with the lithium metal electrode. For the 1 inch cell, the ferrules were made from polytetrafluoroethylene (PTFE) and for the ½ inch cell, the ferrules were made from polyfluoroalkoxy alkane (PFA). To prepare the cell for construction, the Swagelok cell components (Figure 2.2.1, excluding the electrodes, separators and electrolyte) were dried in an oven at 80°C for several hours before the first half of the cell was pre-assembled (outside of the argon filled glove box). The back and front ferrules were placed onto one of the stainless steel rods and this was placed just under half way into the body of the metal Swagelok cell, which had been lined with a sheet of fluorinated ethylene propylene (FEP, thickness 0.127 mm, RS components). The role of the FEP sheet was to isolate the stainless steel body from the stainless steel current collectors and prevent short circuiting. The end cap of the Swagelok cell was then screwed on to secure the rod in place. This pre-assembled half of the Swagelok cell, along with all other components (excluding the electrodes, separators and electrolyte) were then dried in an oven at 80°C for several hours more before taking into the argon-filled glovebox (oxygen and water content < 5 ppm).

Once inside the glovebox, the cell components were allowed to cool to the ambient temperature of the glovebox before completing cell construction. Once the electrodes, separators and electrolyte had been added, the stainless steel current collector cap was placed into the body of the cell, followed by the stainless steel spring (used to maintain stack pressure) and the other stainless steel rod with the front and back ferrules in place. Finally, the cell end was screwed onto the cell body to seal the cell.

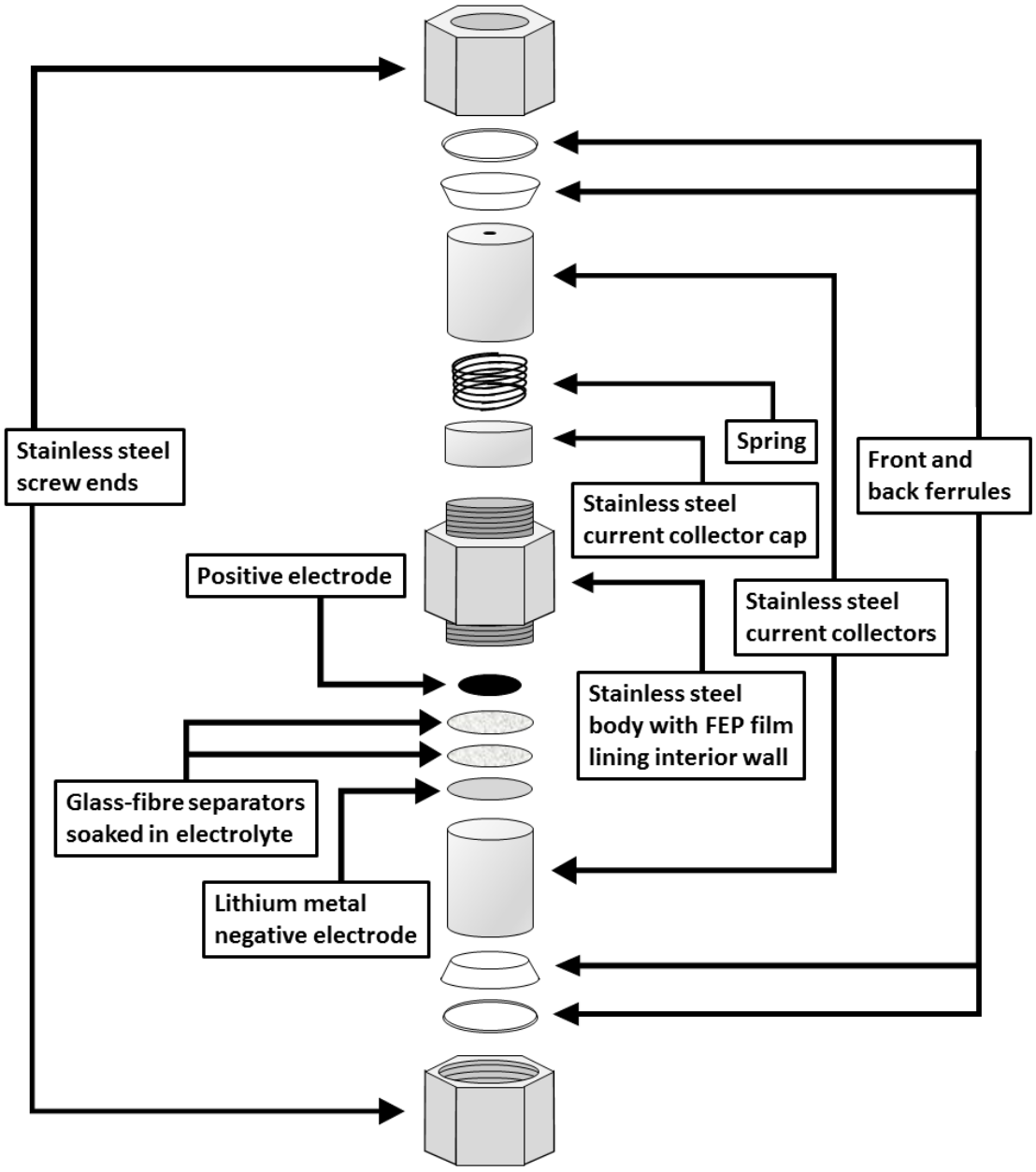


**Figure 2.2.1 –** Schematic of the Swagelok® cell used throughout the report, which was always constructed from the bottom up. Although, the order of the electrodes, separators and electrolyte was varied.

### 2.2.2 – Nylon Cell

Similarly to the Swagelok cell, the first half of the cell was pre-assembled (outside of the argon filled glove box) by screwing the bottom stainless steel current collector onto the Nylon body of the cell. This pre-assembled half of the Nylon cell, along with all other components (excluding the electrodes, separators and electrolyte) were then dried in an oven at 80°C for several hours more before taking into the argon-filled glovebox (oxygen and water content < 5 ppm). Once inside the glovebox, the cell components were allowed to cool to the ambient temperature of the glovebox before completing cell construction. Once the electrodes, separators and electrolyte had been added, the stainless steel cap was placed inside the body of the cell, followed by the stainless steel spring (used to maintain stack pressure) and the other stainless steel current collector, which was screwed onto the Nylon body, using screws and a small hex key, to seal the cell.

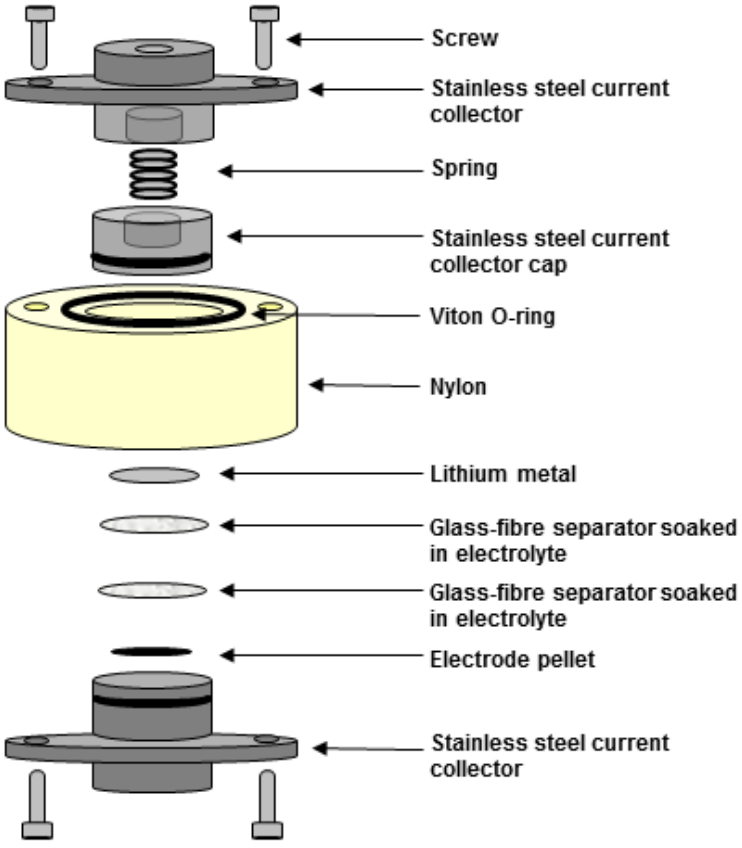


**Figure 2.2.2 –** Schematic of the Nylon cell used in Chapter 3, which was always constructed from the bottom up. Schematic originally drawn by Saddam Al-Mahmoud.

### 2.2.3 – Metal Cell

Unlike the Swagelok and Nylon cells, there was no pre-assembly of the cell (outside of the argon filled glove box). Instead, all components (excluding the electrodes, separators and electrolyte) were simply dried in an oven at 80°C for several hours before taking into the argon-filled glovebox (oxygen and water content < 5 ppm). Once inside the glovebox, the cell components were allowed to cool to the ambient temperature of the glovebox before beginning cell construction. The spring (used to maintain stack pressure) was placed into the stainless steel base, followed by the stainless steel cap. Then once the electrodes, separators and electrolyte had been placed on top of the stainless steel cap, the stainless steel lid was gently placed on top and screwed into place by hand.

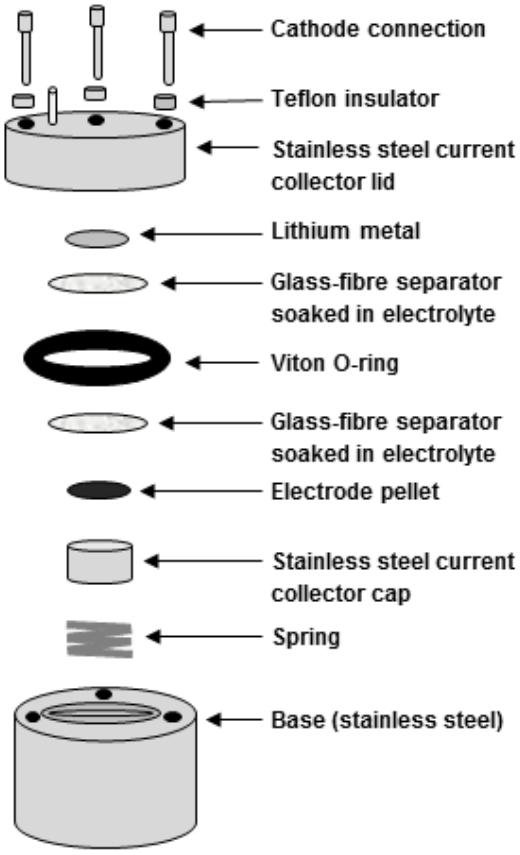


**Figure 2.2.3 –** Schematic of the metal cell used in Chapter 3, which was always constructed from the bottom up. Schematic originally drawn by Saddam Al-Mahmoud.

### 2.2.4 – Coin Cell

The coin cell components (stainless steel caps, bases/cups, plastic sealing rings and stainless steel spacers were dried and placed into an argon-filled glovebox (oxygen and water content < 5 ppm) for storage before use. The plastic sealing ring was first placed inside the stainless steel base. Then once the electrodes, separators and electrolyte had been placed inside the base, the spacer was added, followed by the spring (used to maintain stack pressure) and finally the cap. The coin cell was then sealed using crimper.

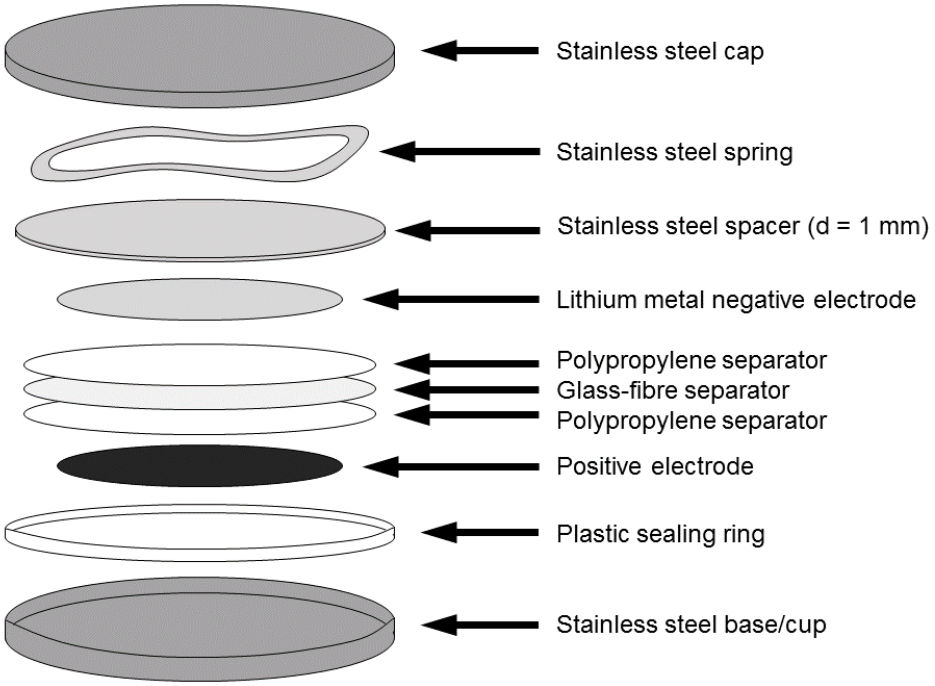


**Figure 2.2.4 –** Schematic of a coin cell used in Chapter 4, which was always constructed from the bottom up.

### 2.2.5 – Glass U-Cell

The glass U-cell, consists of two compartments that are separated by a porous glass frit (Figure 2.2.5). This allows a redox species dissolved in electrolyte to be analysed in the working electrode compartment without reacting directly with the lithium metal in the counter/reference electrode compartment. The glass U-cell, Suba-seals® and counter electrode (not including lithium metal) were dried in an oven at 80 °C overnight before transferring into an argon-filled glovebox (oxygen and water content < 5 ppm). The components were allowed to cool to the ambient temperature of the glovebox before beginning cell construction.

The carbon working electrode (glassy carbon rod encased in glass giving a disc shaped electrode, Ø = 3 mm, Alfa Aesar) was mechanically polished using alumina suspensions (3 μm and 0.5 μm) for 10 minutes per alumina size. After each polish, the electrode was thoroughly washed with deionised water to ensure that no alumina remained. The electrode was then allowed to dry in an oven at 80 °C overnight, before being taken into the glovebox. Once all the components were inside the argon-filled glovebox, the Suba-seals were placed into the side arms of the cell to seal. A strip of lithium (lithium foil battery grade, Rockwood Lithium) pressed onto the stainless steel gauze was used as the counter/reference electrode. Using an auto-pipette, electrolyte containing a redox species (4 mL) was placed into the working electrode compartment and electrolyte without the redox species (4 mL) was placed into counter/reference electrode compartment. The electrodes were then placed into their respective compartments before the ground glass joint was sealed using grease to prevent air leaking into the cell once taken outside of the glovebox.

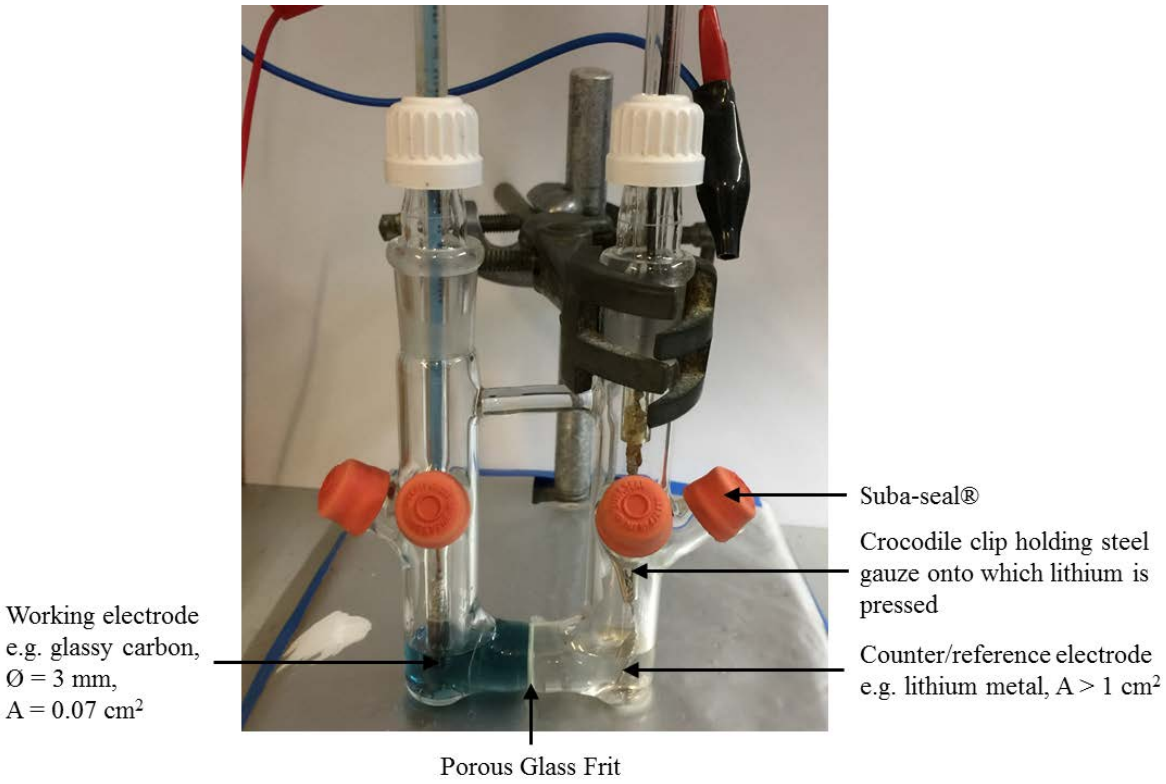


**Figure 2.2.5 –** Schematic of the U-cell used in Chapter 6.

## 2.3 – Experimental Techniques

### 2.3.1 – Cyclic Voltammetry

Cyclic voltammetry is a commonly used electrochemical technique that is particularly useful as an initial investigation of an electrochemical system, as each experiment can be performed quickly and the results can be qualitatively analysed. During cyclic voltammetry, the potential of the working electrode is ramped linearly with time (Figure 2.3.1), until a potential limit is reached. Unlike linear sweep voltammetry, the potential of the working electrode is then ramped in the opposite direction until another potential limit is reached. The potential of the working electrode may then be ramped in the opposite direction to the first potential limit and so on. This cycling may repeated as many times as required between the two defined potential limits. Whilst the potential is ramped, the current response is measured and it is generally the current (*i*) or current density (*I*) that is plotted against potential (*E*). However, it should be noted that the potential axis could equally be labelled as a time axis, since potential and time share a linear relationship (Figure 2.3.2). The potential limits must be carefully selected so that the desired electrochemical process occurs within the potential range. The rate at which the potential is ramped is known as the scan rate (*v*).

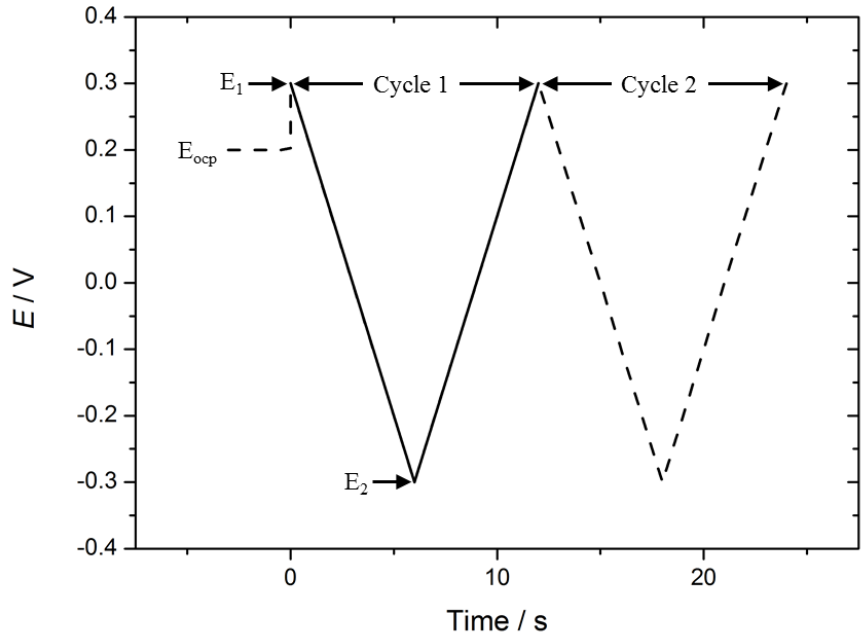


**Figure 2.3.1 –** Potential-time profile of a cyclic voltammogram. In this simulated example, the potential of the working electrode is ramped between two potential limits, $E_{start}$ (0.3 V) and $E_{end}$ (-0.3 V). A scan rate of 100 mV $s^{-1}$ is used and the open circuit potential ($E_{ocp}$) is measured at 0.2 V.

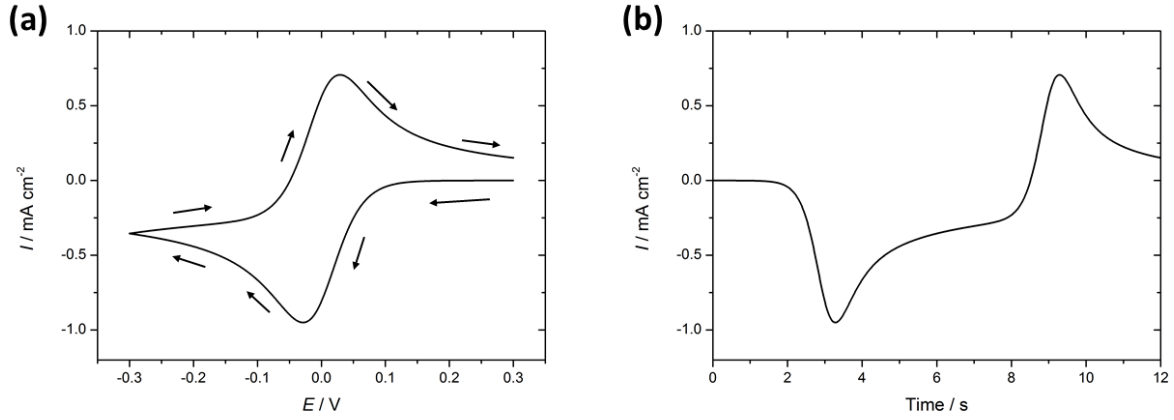


**Figure 2.3.2 –** Simulated cyclic voltammograms with (a) the current density plotted against potential and (b) the current density plotted against time. Simulated using DigiElch. For reaction O + e = R: $E_e^\circ$ = 0 V, $\alpha$ = 0.5, $k_s = 10^4$ cm $s^{-1}$, $D_O = 5 \times 10^{-6}$ $cm^2$ $s^{-1}$, $D_R = 5 \times 10^{-6}$ $cm^2$ $s^{-1}$, $c_O$ = 5 mM. Simulation parameters: $E_{start}$ = 0.3 V, $E_{end}$ = -0.3 V, $v$ = 100 mV $s^{-1}$, electrode geometry = planar, electrode area = 0.071 $cm^2$ (Ø = 3 mm), diffusion = semi-infinite 1D, pre-equilibrium = disabled.

Under non-steady-state conditions, such as those employed when using stationary macro-sized electrodes, a peak will be observed on the cyclic voltammogram (CV) for each electrochemical reaction occurring. To analyse these peaks, it is important to consider that even the simplest electrochemical reaction is a multistep process that consists of both mass transport and electron transfer. For example, a simple one-electron reduction where both reactant and product dissolve into the electrolyte must consist of at least three steps (Equation 2.3.1):

$$O_{bulk} \xrightarrow{\text{mass transport}} O_{interface}$$

$$O_{interface} + e^- \xrightarrow{\text{electron transfer}} R_{interface}$$

$$R_{interface} \xrightarrow{\text{mass transport}} R_{bulk}$$

**Equation 2.3.1 –** A simple one-electron reduction process converting oxidised species (O) into reduced species (R).

For a system where O is the only species present, sweeping from a potential at which no reaction occurs to one where O is reduced to R gives the CV in Figure 2.3.3, which can be understood by considering the concentration profiles of the species O and R (Figure 2.3.3).

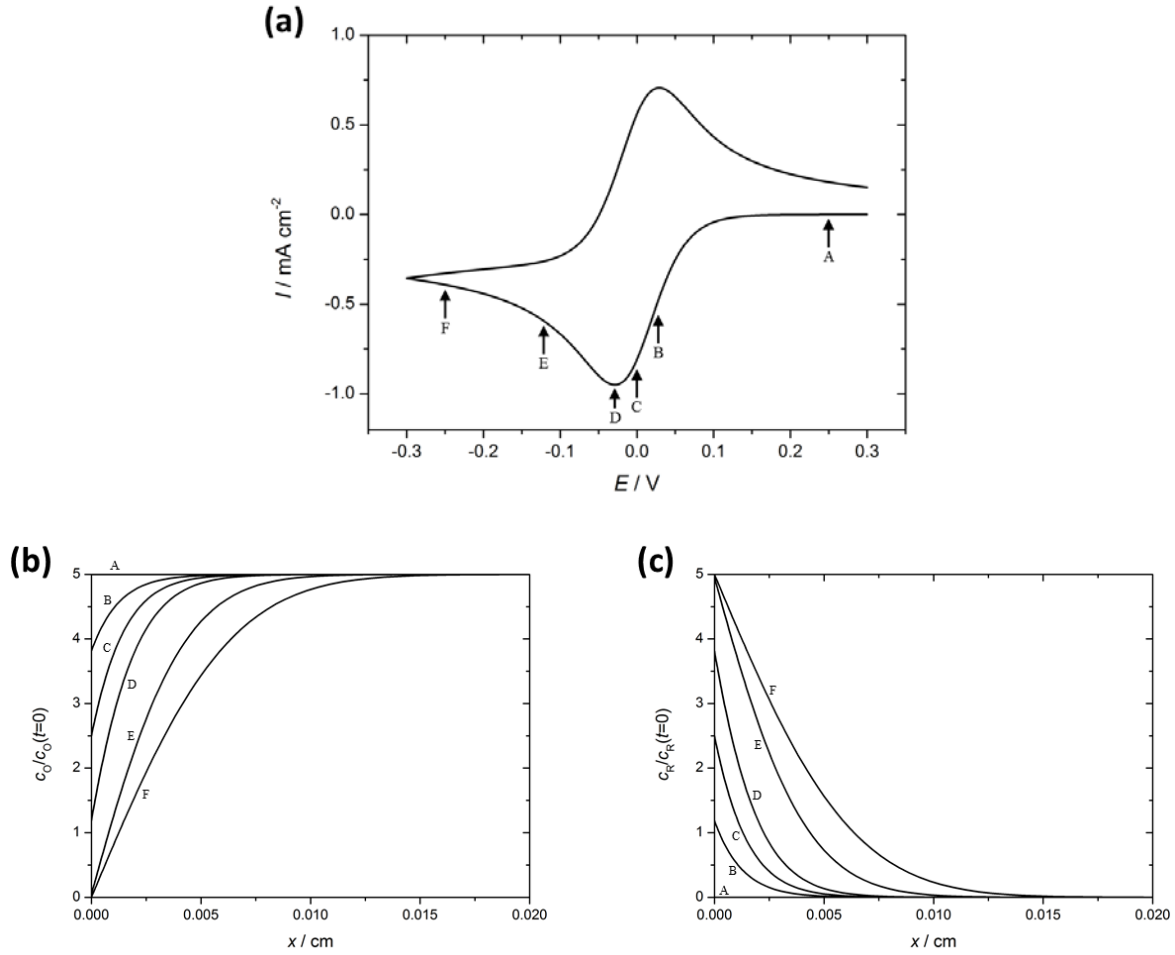


**Figure 2.3.3 –** Simulated (a) cyclic voltammogram with the current density plotted against potential, (b) the concentration profile of O close to the surface of the electrode and (c) the concentration profile of R close to the surface of the electrode. Simulated using DigiElch. For reaction O + e = R: $E_e^\circ$ = 0 V, $\alpha$ = 0.5, $k_s = 10^4$ cm s$^{-1}$, $D_O$ = 5 x 10$^{-6}$ cm$^2$ s$^{-1}$, $D_R$ = 5 x 10$^{-6}$ cm$^2$ s$^{-1}$, $c_O$ = 5 mM. Simulation parameters: $E_{start}$ = 0.3 V, $E_{end}$ = -0.3 V, ν = 100 mV s$^{-1}$, electrode geometry = planar, electrode area = 0.071 cm$^2$ (Ø = 3 mm), diffusion = semi-infinite 1D, pre-equilibrium = disabled.

During non-steady-state diffusion, two changes occur simultaneously, which have opposite effects on the current density and produce the characteristic shape of the CV. Firstly, the concentration of O close to the electrode surface starts to decrease rapidly and non-steady-state diffusion occurs. This increasing flux in response to the steepening concentration profile causes the current density to increase. Secondly, the non-steady-state

diffusion causes the concentration profile to expand into the solution. This expanding concentration profile, reduces the steepness of the concentration profile and reduces the current density. At some point, the flux of O and the current density will pass through a maximum values and then start to decrease. Both of these effects occur simultaneously, until the concentration at the electrode surface reaches zero, at which point the concentration profile can only expand into the solution. The peak current density can be calculated using the method illustrated in Figure 2.3.4. If only one species is present initially (such as the forward scan from + 0.3 V to – 0.3 V, in Figure 2.3.4), the current density starts at zero and the peak current density can be read from the CV, using zero as the baseline. However, if both species are present (such as the reverse scan from – 0.3 V to + 0.3 V, in Figure 2.3.4), then a baseline must be extrapolated from the 'steady-state current' of the reverse peak. This is then used to determine the peak current density.

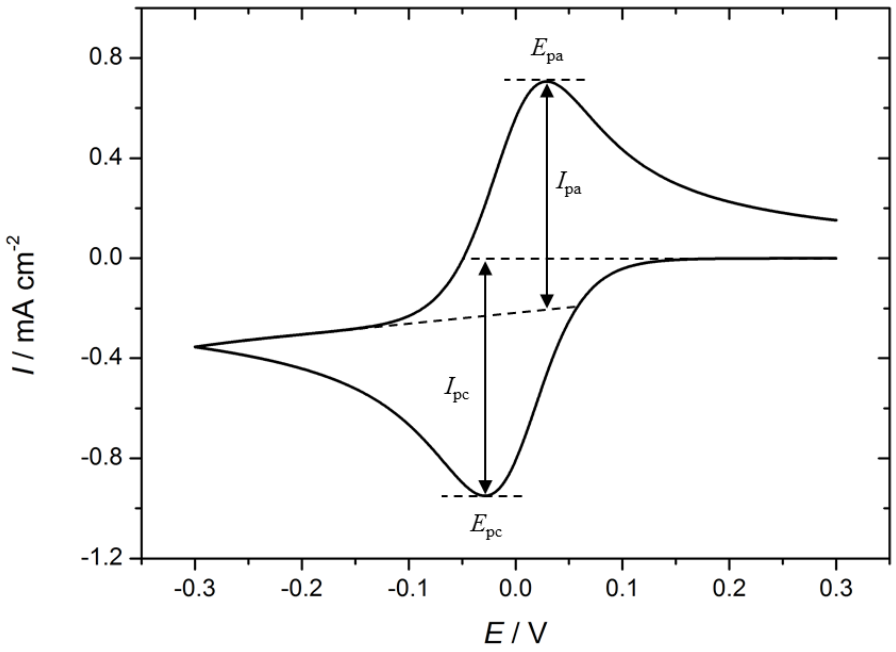


**Figure 2.3.4 –** Determining the peak current densities ($I_{pc}$ = reduction/cathodic and $I_{pa}$ = oxidation/anodic) using correctly drawn base lines and identifying the potential of the peaks ($E_{pc}$ = reduction/cathodic and $E_{pa}$ = oxidation/anodic).

In order to calculate the number of moles that have been reduced or oxidised, the charge associated with each process must be calculated. The charge is calculated by determining the area under the curve of the CV and dividing by the scan rate (Figure 2.3.5 and Equation 2.3.2). The calculated charge can then be used to estimate the number of moles reacted (Equation 2.3.3).

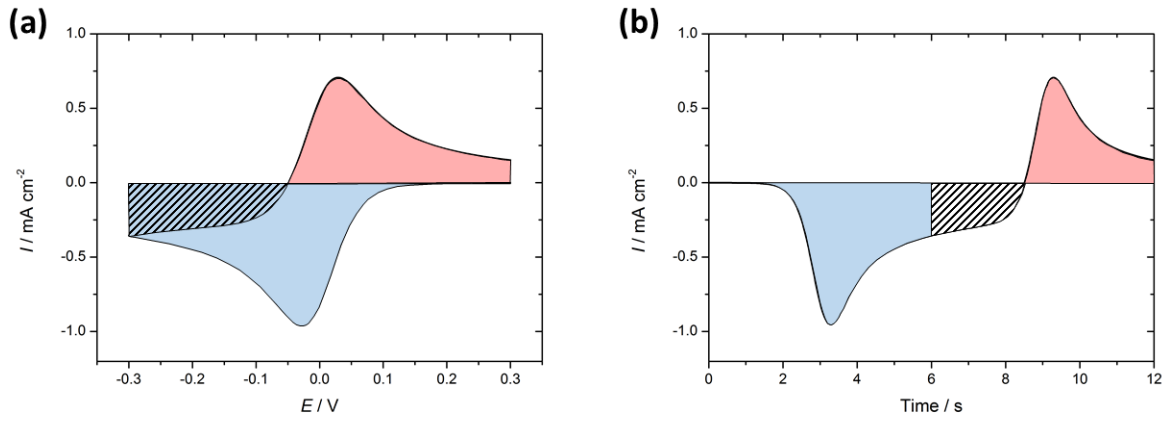


**Figure 2.3.5 –** Calculating the charge associated with the reduction (**blue** and **black stripes**) and the oxidation (**red**) for simulated cyclic voltammograms with (a) the current density plotted against potential and (b) the current density plotted against time.

$$\text{(a)} \qquad Q = \frac{\int_{E_1}^{E_2} i \, \mathrm{d}E}{\nu}$$

$$\text{(b)} \qquad Q = \int_{t_1}^{t_2} i \, \mathrm{d}t$$

**Equation 2.3.2 –** Calculating the charge (*Q)* from (a) the CV by integrating the current (*i*) with respect to potential (*E*) and then dividing by scan rate (*v*) or (b) the measurements of current as time changes by integrating *i* with respect to time (*t*).

$$m = \frac{Q}{nF}$$

**Equation 2.3.3 –** Calculating the number of moles (*m*) reacted using the calculated value of charge (*Q)*, where *n* = number of electrons involved in redox process and *F* = Faraday constant (96485 C $mol^{-1}$).

In electrochemistry, a reaction can be described as either ‘reversible’ or ‘irreversible’, terms that are used to describe whether or not the electron-transfer reaction at the electrode surface is in thermodynamic equilibrium.[1] In the case of a reversible electrode reaction, the electron-transfer step is inherently fast (i.e. faster than mass transport) and remains in equilibrium, which enables the surface concentrations to be calculated using the Nernst equation (Equation 2.3.4).

$$E_{\mathrm{e}} = E_{\mathrm{e}}^{0} + \frac{2.3RT}{nF}\log\frac{c_{\mathrm{O}}}{c_{\mathrm{R}}}$$

**Equation 2.3.4 –** Nernst equation, assuming activities can be substituted with concentrations e.g. $c_{\mathrm{O}} = a_{\mathrm{O}}$, where $E_{\mathrm{e}}$ = equilibrium potential, $E_{\mathrm{e}}^{0}$ = standard potential, $R$ = ideal gas constant (8.314 J $K^{-1}$ $mol^{-1}$) and $T$ = temperature in K.

No overpotential is required to obtain any rate in reversible electrode processes. In the case of an irreversible electrode reaction, the electron-transfer step is slow (i.e. slower than mass transport) and not in equilibrium, hence the surface concentrations are calculated using kinetic equations. Furthermore, overpotential is required to drive the reaction at a particular rate in irreversible electrode processes. If the reaction observed at the working electrode is reversible (i.e. the reaction is limited by mass transport), then cyclic voltammetry can be used to determine the diffusion coefficient ($D$). This can be calculated by measuring the peak currents ($i_{\mathrm{p}}$) and applying the Randles-Sevcik equation assuming the experiment is undertaken at 25 °C (Equation 2.3.5).

$$i_{\mathrm{p}} = (2.69 \times 10^{5}) n^{3/2} A c^{*} D^{1/2} v^{1/2}$$

**Equation 2.3.5 –** Randles-Sevcik equation, where $i_{\mathrm{p}}$ is the peak current in A, $n$ is the number of electrons involved in the electrode reaction, $A$ is the electrode area in $cm^2$, $c^*$ is the solution species concentration in the bulk solution in mol $cm^{-3}$, $D$ is the diffusion coefficient in $cm^2$ $s^{-1}$ and $v$ is the scan rate in V $s^{-1}$.

In the other case of irreversible electron transfer (i.e. reaction is limited by electron transfer), the Randles-Sevcik equation is no longer applicable. The shapes of the cyclic voltammograms can indicate whether a reaction shows reversible or irreversible electron transfer. In the reversible electron transfer case, the peak-to-peak separation should be close to 59 mV / $n$, which should remain constant regardless of scan rate. However, distortions such as $iR$ drop may affect this, increasing the peak-to-peak separation on increasing scan rate. In the irreversible electron transfer case, the overpotential required will become larger as the current increases and hence a peak for an oxidation will shift to a more positive value and become more drawn out along the potential axis compared to the reversible case. In the same way, a peak for reduction will also shift to a more negative value and become more drawn out. This means that the oxidation and reduction peaks will move apart as well as becoming less steep. Furthermore, increasing the scan rate also causes the peak separation to become larger.

### 2.3.2 – Galvanostatic Cycling

Constant current chronopotentiometry, more commonly known as galvanostatic cycling within battery research is used to simulate the charge and discharge conditions experienced by a battery. During galvanostatic cycling, a constant current pulse is applied to the working electrode whilst the potential is measured. This continues until either a potential or time limit is reached (Figure 2.3.6).

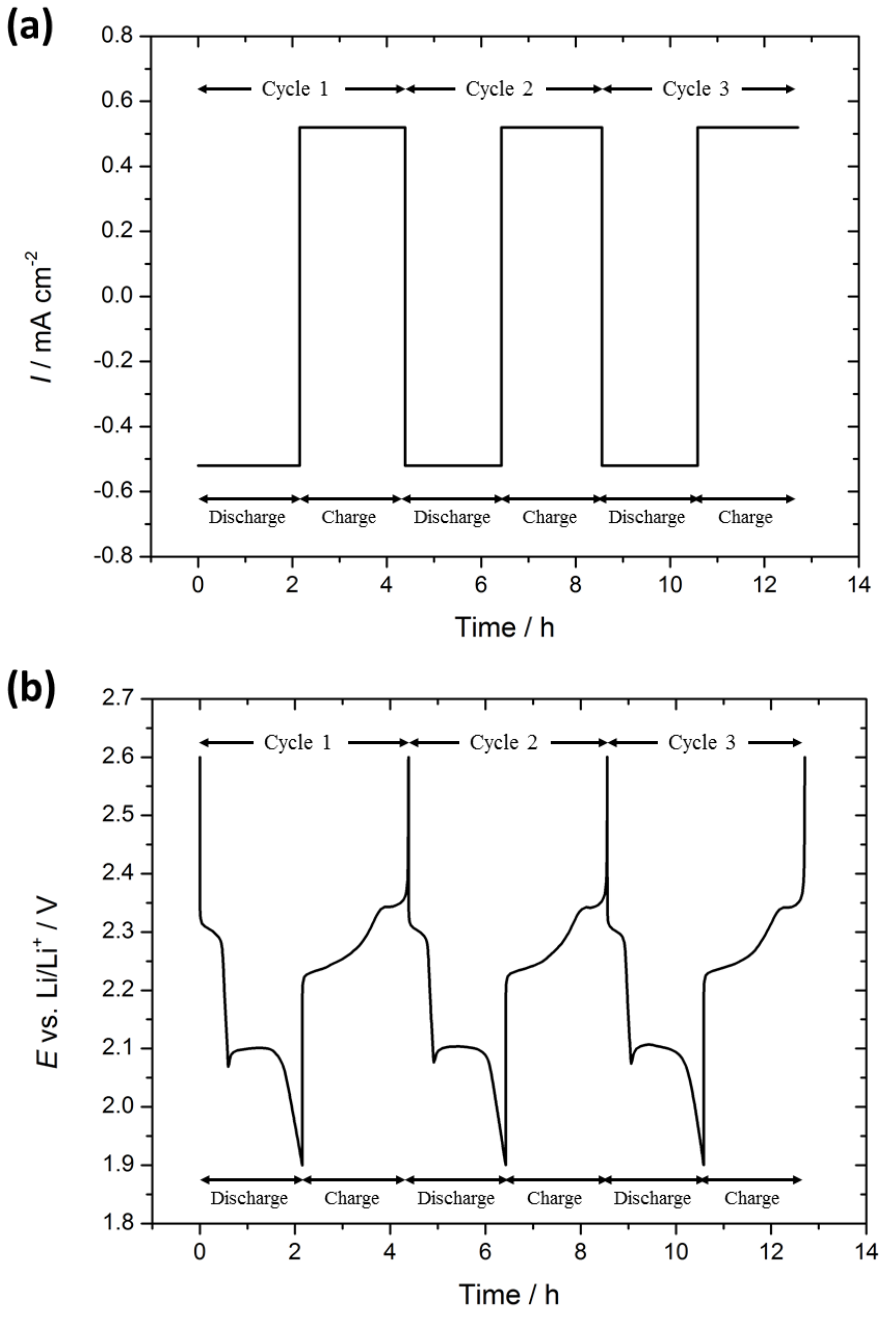


**Figure 2.3.6 –** In this example, (a) the current is fixed at a constant value of –/+ 0.52 mA $cm^{-2}$ and (b) the potential response measured. Once a potential limit, set here at 1.9 and 2.6 V, has been reached then the direction of the current is reversed.

Limiting the time of the constant current pulse allows the total charge to be controlled. For a battery, the sign of the current applied will dictate whether the battery is being charged or discharged. Usually for battery systems, the acquired data is presented as a plot of potential verses specific capacity, where the units of specific capacity are given in mA h $g^{-1}$ (Figure 2.3.7).

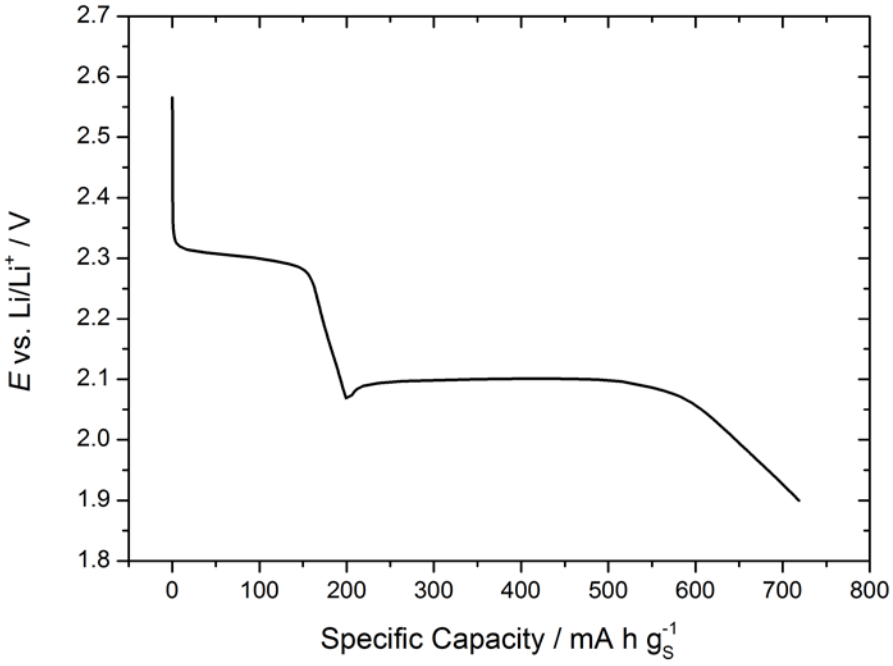


**Figure 2.3.7 –** A discharge profile for a Li-S cell where the specific discharge capacity reached 719 mA h $g_S^{-1}$ during this cycle.

If suitable potential limits are selected and the magnitude of the applied constant current pulse is sufficiently small, then it should be possible to completely reduce or oxidise the active species. A sufficiently small current is required to ensure that there is enough time for the active species to diffuse to the electrode surface from the bulk. In this way, only once the active species is completely exhausted will the concentration at the electrode surface reach zero. At this point, the potential will change quickly until the potential limit is reached. In addition to the small current, performing complete electrolysis would require all the active species in the system to be electrochemically accessible and assumes no other complications, such as electrode passivation. If a large constant current pulse is applied, then there will not be enough time for the active species to diffuse from the bulk to the electrode surface. This will cause the concentration of active species at the electrode surface to reach zero before the concentration in the bulk is exhausted. Therefore,

the potential will change and reach the potential limit before complete electrolysis has occurred. This is because the diffusion of the active species is too slow for the applied current. The relationship between current, time and diffusion is described by the Sand equation (Equation 2.3.6).[2]

$$\frac{i\tau^{1/2}}{c_{\mathrm{O}}^{*}} = \frac{nFAD_{\mathrm{O}}^{1/2}\pi^{1/2}}{2}$$

**Equation 2.3.6 –** The Sand Equation, where $i$ = current in A, $\tau$ = transition time in s, $c_O^*$ = bulk concentration of the oxidised species in mol cm$^{-3}$, $n$ = number of electrons involved in redox process, $F$ = Faraday constant (96485 C mol$^{-1}$), $A$ = area in cm$^2$ and $D_O$ = diffusion coefficient of the oxidised species in cm$^2$ s$^{-1}$.

Using the Sand equation, it is possible to model the potential response over time during galvanostatic cycling for both reversible and irreversible systems (Equations 2.3.7 and 2.3.8, respectively).[2]

$$E = E_{\tau/4} + \frac{RT}{nF}\ln\frac{\tau^{1/2} - t^{1/2}}{t^{1/2}}$$

**Equation 2.3.7 –** Determining the potential for reversible (Nernstian) systems, where $E$ = potential in V, $E_{\tau/4}$ = quarter-wave potential in V, $R$ = ideal gas constant (8.314 J K$^{-1}$ mol$^{-1}$), $T$ = temperature in K, $n$ = number of electrons involved in redox process, $F$ = Faraday constant (96485 C mol$^{-1}$), $\tau$ = transition time in s and $t$ = time in s.

$$E = E^{0\prime} + \frac{RT}{\alpha F}\ln\left[\frac{2k^0}{(\pi D_{\mathrm{O}})^{1/2}}\right] + \frac{RT}{\alpha F}\ln\left[\tau^{1/2} - t^{1/2}\right]$$

**Equation 2.3.8 –** Determining the potential for totally irreversible systems, where $E$ = potential in V, $E^{0'}$ = formal potential in V, $R$ = ideal gas constant (8.314 J K$^{-1}$ mol$^{-1}$), $T$ = temperature in K, $\alpha$ = transfer coefficient, $F$ = Faraday constant (96485 C mol$^{-1}$), $k^0$ = standard heterogeneous rate constant in cm s$^{-1}$, $D_O$ = diffusion coefficient of the oxidised species in cm$^2$ s$^{-1}$, $\tau$ = transition time in s and $t$ = time in s.

The quarter-wave potential ($E_{\tau/4}$) is the chronopotentiometric equivalent of the voltammetric half-wave potential ($E_{1/2}$, Equation 2.3.9). In order to assess the reversibility of the system, one can plot $E$ vs. log $[(\tau^{1/2} - t^{1/2})/t^{1/2}]$ and if the plot is linear and possesses a slope of $59/n$ mV, then the system can be considered to be reversible.[2]

$$E_{\tau/4} = E^{0\prime} - \frac{RT}{2nF}\ln\frac{D_O}{D_R}$$

**Equation 2.3.9 –** Determining the quarter-wave potential ($E_{\tau/4}$), where $E^{0'}$ = formal potential in V, $R$ = ideal gas constant (8.314 J $K^{-1}$ $mol^{-1}$), $T$ = temperature in K, $n$ = number of electrons involved in redox process, $F$ = Faraday constant (96485 C $mol^{-1}$), $D_O$ = diffusion coefficient of the oxidised species in $cm^2$ $s^{-1}$ and $D_R$ = diffusion coefficient of the reduced species in $cm^2$ $s^{-1}$.

### 2.3.3 – Galvanostatic Intermittent Titration Technique (GITT)

GITT can be used to obtain the diffusion coefficient of an active material present at a one-phase insertion electrode, as well as other useful thermodynamic and kinetic information.[3-6] First introduced by Weppner and Huggins in 1977, the technique involves a series of current pulses, each followed by a relaxation period where no current passes through the cell (Figure 2.3.8).[3] The applied current is positive or negative depending on whether the cell is being charged or discharged respectively.

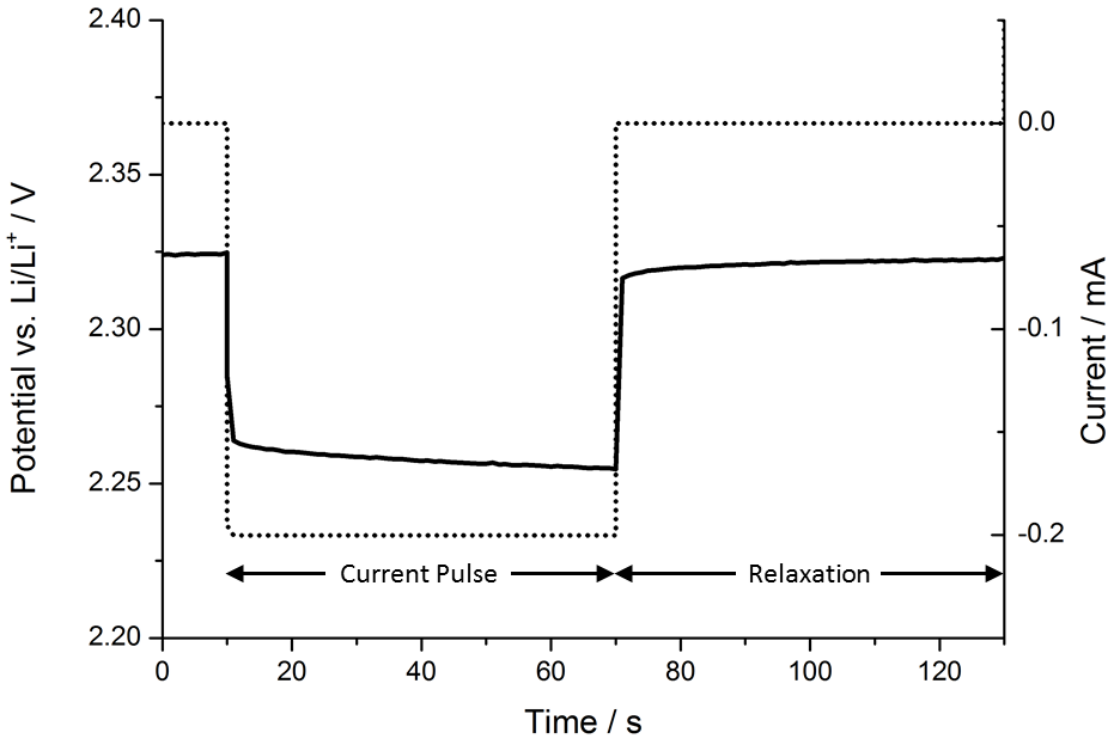


**Figure 2.3.8 –** Example GITT measurement showing a negative current pulse ($i$ = -0.2 mA) for 60 s followed by a relaxation period for 60 s (— Potential, ····· Current).

During a negative current pulse, the cell potential quickly decreases to a value proportional to the *IR* drop, where the resistance ($R$) is the sum of the uncompensated

resistance ($R_u$) and the charge transfer resistance ($R_{ct}$). The potential then starts to decrease at a slower rate due to the reduction of the redox species close to the electrode surface. During the relaxation period, the potential quickly increases to a value proportional to the *IR* drop and then slowly increases until the concentration of the redox species close to the electrode surface reaches equilibrium, where d$E$/d$t$ = 0. The next current pulse is applied and the process is repeated until the battery is fully discharged. The opposite occurs using a positive current i.e. charging the cell. If a sufficiently small current is used and the change in steady-state potential ($\Delta E_s$) over a single current pulse is small, then d$E$/d$c$ may be considered constant and linear. Furthermore, if short time intervals for the current pulses are employed and plotting $E$ versus $\sqrt{t}$ shows a straight line over the entire time period of current flux, then the following equation can be used (Equation 2.3.10)[7]:

$$D = \frac{4L^2}{\pi\tau}\left(\frac{\Delta E_s}{\Delta E_t}\right)^2 \qquad \left(t \ll \frac{L^2}{D}\right)$$

**Equation 2.3.10 –** Simplified equation for determining the diffusion coefficient ($D$), where $L$ is the distance between where the electrochemical redox process occurs and the impermeable phase boundary (in this case, the distance between the electrode surface and the LICGC separator), $\tau$ is the duration of the current pulse, $\Delta E_s$ is the change in steady-state potential over a single current pulse and $\Delta E_t$ is the total change in potential during the current pulse, excluding *IR* drop. See Figure 2.3.9 for an illustration of how the parameters $\Delta E_s$ and $\Delta E_t$ are determined.

This equation was first derived by Weppner and Huggins in 1979.[7] Under galvanostatic conditions, the initial and boundary conditions are as follows (Equation 2.3.11).

$$\text{(a)} \qquad c = c_0 \quad 0 \le x \le L, \quad t = 0$$

$$\text{(b)} \quad -D\frac{\partial c}{\partial x} = \frac{i}{nFA} \quad x = 0, \quad t > 0$$

$$\text{(c)} \qquad \frac{\partial c}{\partial x} = 0 \quad x = L, \quad t \ge 0$$

**Equation 2.3.11 –** Initial and boundary conditions where $c$ is the local concentration of species A, $c_0$ is the initial uniform concentration at the planar electrode corresponding to an equilibrium potential $E_e$, $x$ is the distance into the electrolyte from the electrolyte/electrode interface, $i$ is current, $n$ is number of electrons involved in the electrode reaction, $F$ is the Faraday constant 96485 C mol$^{-1}$, $A$ is the cross-sectional area of the electrode surface and $t$ is time.

GITT assumes one-dimensional diffusion and so the chemical diffusion process in the electrolyte is described by Fick's second law (Equation 2.3.12).

$$\frac{\partial c}{\partial t} = D\frac{\partial^2 c}{\partial x^2}$$

**Equation 2.3.12 –** Fick's second law of diffusion

Fick's second law is then solved with the initial and boundary conditions (Equations 2.3.11). This leads to the following equation, known to as the Sand equation, which for small values of time ($t \ll L^2/D$) can be applied (Equation 2.3.13). The full solutions can be found elsewhere.[7, 8]

$$c_\mathrm{t} - c_0 = \frac{2i\sqrt{t}}{nFA\sqrt{D\pi}} \quad if\ t \ll \frac{L^2}{D}$$

**Equation 2.3.13 –** The Sand equation, where $c_\mathrm{t}$ is the concentration at the electrode/electrolyte interface ($x = 0$) where time = t.

Differentiating the equation with respect to the square root of time (Equation 2.3.14).

$$\frac{dc_\mathrm{t}}{d\sqrt{t}} = \frac{2i}{nFA\sqrt{D\pi}} \quad if\ t \ll L^2/D$$

**Equation 2.3.14 –** The Sand equation differentiated with respect to the square root of time.

The Sand equation could be used to determine the chemical diffusion coefficient ($D$) if the time variation of the surface concentration ($c_\mathrm{t}$) were known. However, this is not usually directly measurable. Experimentally, the variation of potential (d$E$) is measured with time ($t$). In order to relate the variation of potential (d$E$) with the variation of the surface concentration (d$c_\mathrm{t}$), it can be assumed that the potential change ($\Delta E$) is proportional to the concentration change ($\Delta c$) and the proportionality constant can be obtained for the measured change in potential at the end of the relaxation ($\Delta E_\mathrm{s}$, Equation 2.3.15).

$$\frac{dE}{dc_t} = \frac{\Delta E_s}{\Delta c} \quad if\ \Delta c\ is\ small$$

**Equation 2.3.15 –** Change in potential with respect to concentration, where $\Delta E_s$ is the change in steady-state potential over a single current pulse and $\Delta c$ is the change in concentration.

$$Where \quad no.of\ moles = \frac{Q}{nF}; \quad V = LA \quad and \quad Q = i\tau$$

$$\Delta c = \frac{no.of\ moles}{V} = \frac{(Q/nF)}{LA} = \frac{i\tau}{nF\ LA}$$

**Equation 2.3.16 –** Solving the change in concentration, where $V$ is volume where diffusion can take place, $Q$ is the charge and $\tau$ is the duration of the current pulse.

Combining equations 2.3.14, 2.3.15 and 2.3.16, it is possible to determine the change in potential with respect to the square root of time ($dE/d\sqrt{t}$) and therefore, the slope of the plot $E$ vs. $\sqrt{t}$ allows the determination of the diffusion coefficient (Equation 2.3.17).

$$if\ t \ll L^2/D\ and\ \Delta c\ is\ small \begin{cases} \dfrac{dE}{d\sqrt{t}} = \dfrac{dc_t}{d\sqrt{t}}\ x\ \dfrac{dE}{dc_t} = \dfrac{2i}{nFA\sqrt{D\pi}}\ x\ \dfrac{\Delta E_s\ nF\ LA}{i\tau} = \dfrac{2L\ \Delta E_s}{\tau\sqrt{D\pi}} \\ slope = \dfrac{2L\ \Delta E_s}{\tau\sqrt{D\pi}} \\ \sqrt{D} = \dfrac{2L\ \Delta E_s}{\tau\sqrt{\pi}\ slope} \\ D = \dfrac{4L^2\ {\Delta E_s}^2}{\tau^2\ slope^2\ \pi} \end{cases}$$

**Equation 2.3.17 –** Determining the diffusion coefficient ($D$) from the slope of plotting potential ($E$) against the square root of time ($\sqrt{t}$) at short times. This can be obtained by measuring the potential as a function of time during a constant current pulse.

If a sufficiently small current and short time period is applied so that the transient potential response is a linear function of the square root of time, then $dE/d\sqrt{t}$ can be assumed equal to $\Delta E_t/\sqrt{\tau}$. This enables Equation 2.3.17 to be further simplified giving the final equation used to determine the diffusion coefficient from raw GITT data (Equation 2.3.10, Equation 2.3.18 and Figure 2.3.9).

$$if\ \tau \ll L^2/D\ and\ \Delta c\ is\ small \begin{cases} \dfrac{dE}{d\sqrt{t}}\ or\ slope = \dfrac{\Delta E_\mathrm{t}}{\sqrt{\tau}} = \dfrac{2L\ \Delta E_\mathrm{s}}{\tau\sqrt{D\pi}} \\ \sqrt{D} = \dfrac{2L\ \Delta E_\mathrm{s}\ \sqrt{\tau}}{\tau\ \Delta E_\mathrm{t}\ \sqrt{\pi}} = \dfrac{2L\ \Delta E_\mathrm{s}}{\Delta E_\mathrm{t}\ \sqrt{\pi\tau}} \\ D = \dfrac{4L^2\ {\Delta E_\mathrm{s}}^2}{\pi\tau\ {\Delta E_\mathrm{t}}^2} = \dfrac{4L^2}{\pi\tau}\left(\dfrac{\Delta E_\mathrm{s}}{\Delta E_\mathrm{t}}\right)^2 \end{cases}$$

**Equation 2.3.18 –** Application of small currents and short time period allows the simplification of Equation 2.3.17, where $\Delta E_\mathrm{t}$ is the total change in potential during the current pulse.

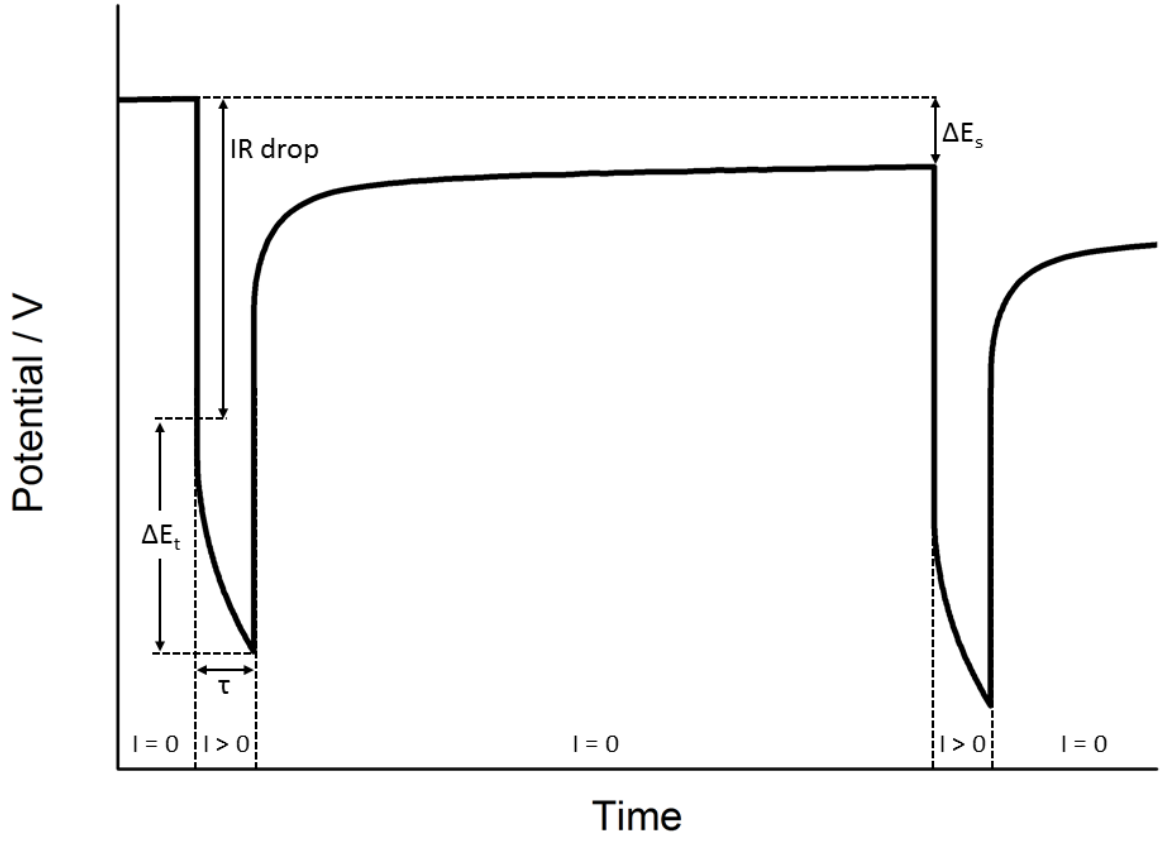


**Figure 2.3.9 –** Example GITT measurement showing how to determine the various parameters ($\Delta E_s$, $\Delta E_t$ and $\tau$) for use in Equation 2.3.10.

The current is related to the concentration gradient at the electrode-electrolyte interface (Equation 2.3.19).

$$i = -AnFD\left(\frac{\partial c}{\partial x}\right)_{x=0}$$

**Equation 2.3.19 –** Current is determined by the concentration gradient at the electrode surface and *vice versa*. During galvanostatic techniques, the concentration gradient at the electrode remains constant during the current pulse.

In GITT, a series of constant current pulses are applied, which implies that the concentration gradient at the electrode-electrolyte interface is also constant during each current pulse. This coupled with the boundary condition describing that the concentration gradient at the non-reactive surface (in this work, a LICGC separator) is zero at all times ($x = L$, Equation 2.3.11c), then the concentration profiles of species A with time can be described in the Figure 2.3.10.

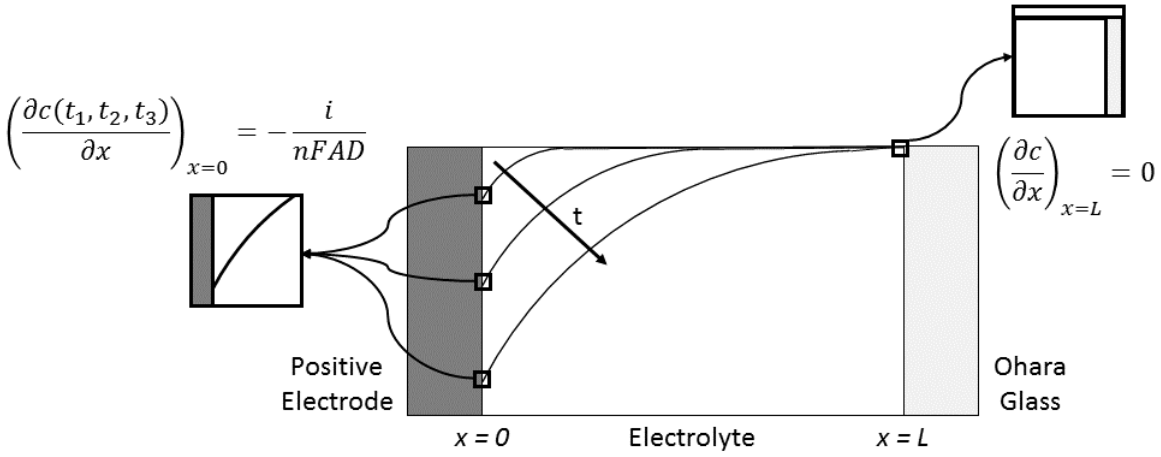


**Figure 2.3.10 –** Concentration profiles of a starting redox species as time increases noting in particular that at the electrode-electrolyte interface ($x = 0$) the concentration gradient is constant with increasing time and at the LICGC-electrolyte interface ($x = L$) the concentration gradient is always 0. Note that the components are not drawn to scale.

The slope of the plot $E$ vs. $\sqrt{t}$ is only linear if a sufficiently small current pulse time interval is applied ($\tau \ll L^2/D$). In Figure 2.3.10, it can be seen that if the current pulse time interval exceeds a certain time limit, the concentration of the redox species at the electrode-electrolyte interface ($x = 0$) will reach zero, causing the potential to change until another redox process occurs. If this were to happen, then $E$ vs. $\sqrt{\tau}$ would not be linear and Equation 2.3.10 would no longer be applicable. In this report, all GITT measurements were made using LICGC separator to prevent any redox species shuttling from the positive electrode to the negative electrode and reacting directly with the lithium metal.

### 2.3.4 – Measuring Conductivity (Electrolytic and Electrical)

The conductivity of a material can be generally described as its ability to transmit matter (e.g. ions) or energy (e.g. heat, electricity or sound). Therefore, there are several types of conductivity, including ionic conductivity (solid-state), electrolytic conductivity, thermal conductivity, electrical conductivity and hydraulic conductivity to name a few. In this report, only electrolytic conductivity and electrical conductivity will be discussed, both of which have units of S $m^{-1}$ (or mS $cm^{-1}$).

Electrolytic conductivity describes the ability of an electrolyte solution to conduct electricity. Unlike electrical conductivity, electrolytic conductivity is associated with the movement of ions through a solution and conduction increases with increasing temperature. To determine the electrolytic conductivity of a solution, the resistance is measured between two flat electrodes separated by a fixed distance (Figure 2.3.11).

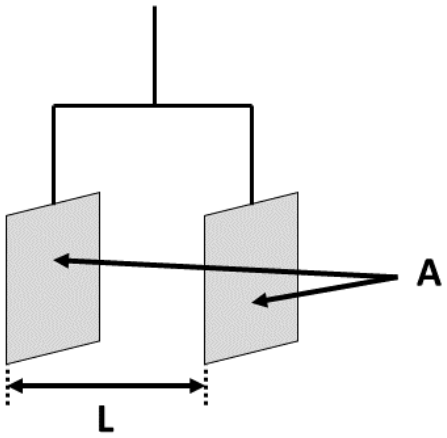


**Figure 2.3.11 –** Schematic of a conductivity meter illustrating the two parallel plate electrodes with identical cross-sectional areas (*A*) and separated by a specific distance (*l*).

Similar to electrochemical impedance spectroscopy (EIS), either an alternating current or potential is applied between the plates and the potential or current response is measured. Using Ohm's law, it is possible to determine the resistance and hence conductivity (Equation 2.3.20). The use of an alternating current/potential rather than direct current/potential avoids any unwanted electrolysis.

$$\kappa = \frac{1}{\rho} = \frac{l}{RA}$$

**Equation 2.3.20 –** Determining the conductivity of a solution from the measured resistance between two parallel plate electrodes, where $\kappa$ = conductivity in S $m^{-1}$, $\rho$ = resistivity in Ω m, $l$ = distance between electrodes in m, $R$ = resistance in Ω and $A$ = cross-sectional area of the electrodes in $m^2$.

Practically however, the conductivity meter is usually calibrated by using solutions of known resistivity, which means that the quantities of $l$ and $A$ do not need to be known precisely. This allows a cell constant ($K$) to be calculated, which can be used to determine the conductivity (Equation 2.3.21).

$$\text{(a)} \qquad K = \frac{R_{\text{cal.}}}{\rho_{\text{cal.}}}$$

$$\text{(b)} \qquad \kappa = \frac{1}{\rho} = \frac{K}{R}$$

**Equation 2.3.21 –** (a) Determining cell constant of the conductivity meter through measuring the resistance of a calibration solution with known resistivity, where $K$ = cell constant in $m^{-1}$, $R_{cal.}$ = measured resistance of calibration solution in Ω and $\rho_{cal.}$ = known resistivity of calibration solution in Ω m. (b) Determining the conductivity of a solution from the measured resistance using the cell constant, where $\kappa$ = conductivity in S $m^{-1}$, $\rho$ = resistivity in Ω m, $K$ = cell constant in $m^{-1}$ and $R$ = measured resistance in Ω.

### 2.3.5 – Rheometry

Rheology can be described as the study of flow and deformation of materials. Rheometers are used to measure the way in which a material (usually a liquid, suspension or slurry) flows or deforms in response to an applied external force or stress. There are two types of rheometer; rotational or shear rheometers that control the applied shear stress or shear strain and extensional rheometers that apply extensional stress or extensional shear. In this report, only rotational and shear rheometry is discussed and it has been used to determine the dynamic viscosity ($\eta$), also known as shear viscosity, of various electrolytes. Rheometers work by either controlling the torque (shear stress) and measuring the angular velocity (shear rate), or *vice versa*, controlling the angular velocity (shear rate) and measuring the torque (shear stress). Since the shear stress can be calculated from the torque, and the shear rate calculated from the angular velocity (directly controlled by the motor), it is possible to calculate the dynamic viscosity using Newton's law of viscosity (Equation 2.3.22).

$$\text{(a)} \qquad \sigma = MK_{\sigma}$$

$$\text{(b)} \qquad \dot{\gamma} = \Omega\, K_{\gamma}$$

$$\text{(c)} \qquad \eta = \frac{\sigma}{\dot{\gamma}}$$

**Equation 2.3.22 –** (a) Determining the shear stress from the torque, where $\sigma$ = shear stress in Pa, $M$ = torque in N m and $K_{\sigma}$ = stress constant in $m^{-3}$. (b) Determining the shear rate from the motor angular velocity, where $\dot{\gamma}$ = shear rate in $s^{-1}$, $\Omega$ = motor angular velocity in rad $s^{-1}$ and $K_{\gamma}$ = strain constant (unitless). (c) Newton's law of viscosity, where $\eta$ = dynamic viscosity in Pa s, $\sigma$ = shear stress in Pa and $\dot{\gamma}$ = shear rate in $s^{-1}$.

If the density of the material is known, then it is also possible to convert the calculated dynamic viscosity into the kinematic viscosity ($\nu$, Equation 2.3.23).

$$\nu = \frac{\eta}{\rho}$$

**Equation 2.3.23 –** Converting dynamic viscosity into kinematic viscosity, where $\nu$ = kinematic viscosity in $m^2\ s^{-1}$, $\eta$ = dynamic viscosity in Pa s and $\rho$ = density in kg $m^{-3}$.

### 2.3.6 – Scanning Electron Microscopy (SEM)

SEM is a method used to generate images of three-dimensional surfaces that are both high in magnification and resolution, capable of observing features on a nanometre scale.[9] These images can give useful information on the topography, morphology and composition of the surface, particularly when combined with closely related methods, such as energy-dispersive X-ray spectroscopy (EDX). The technique uses a focused beam of electrons, which is scanned over the surface of the sample in a raster pattern. The electrons of the beam interact with the atoms on the surface of the sample creating various signals, which can be measured. These signals include secondary electrons, back-scattered electrons and characteristic X-rays, among other photons of various energies. Most commonly, it is the secondary electrons that are used for imaging as these are confined to a very small volume close to the electron beam impact area, which allows images to be obtained at a resolution approximately the size of the focused electron beam.[9]

### 2.3.7 – Differential Scanning Calorimetry (DSC)

DSC is a thermal analysis technique that measures the amount of energy that is absorbed or released (i.e. heat flow) when a sample of known mass is heated or cooled. This is compared simultaneously against a reference that has a well-defined heat capacity over the desired temperature range. The temperature of the sample and the reference are maintained at the same temperature and heated or cooled at a constant rate (i.e. sweep rate) whilst simultaneous measuring the difference in heat flow between them. This method enables the detection of various phase transitions, such as the melting points and glass transition temperatures, as well as chemical reactions, such as curing and denaturation.

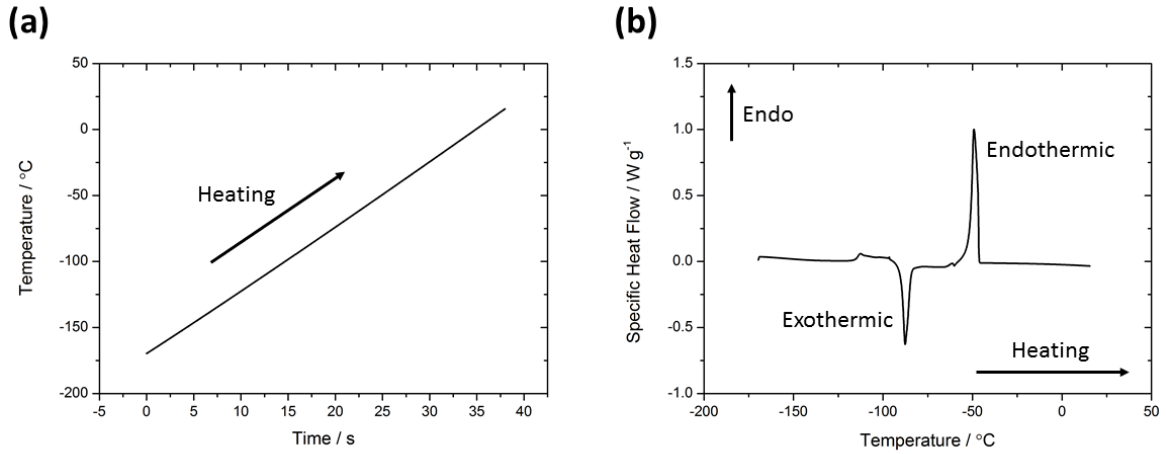


**Figure 2.3.12 –** (a) The temperature of the sample if ramped linearly with time, illustrated heating rate is 5 °C $min^{-1}$. (b) The measured specific heat flow of the sample as a function of temperature as the sample is heated.

### 2.3.8 – Titrimetry

Titration, also known as volumetric analysis, is a common and quantitative analytical technique that is used to determine the concentration of an analyte solution. A standard solution, also known as a titrant, is prepared by dissolving a reagent into solution giving a known concentration. The titrant is used to react with the analyte and once the end point has been reached (often indicated by a colour change), it is possible to calculate the analyte concentration. This is possible since the volumes of analyte and titrant used are both known, as is the titrant concentration (Equation 2.3.24).

$$c_{\text{analyte}} = \frac{c_{\text{titrant}} V_{\text{titrant}} M}{V_{\text{analyte}}}$$

**Equation 2.3.24 –** Determining the concentration of the analyte in solution, where $c_{analyte}$ = concentration of the analyte in mol $dm^{-3}$, $c_{titrant}$ = concentration of the titrant in mol $dm^{-3}$, $V_{titrant}$ = volume of the titrant in $dm^3$, $M$ = molar ratio of analyte and reactant in the balanced chemical equation ($moles_{analyte}/moles_{titrant}$) and $V_{analyte}$ = volume of the analyte in $dm^3$.

There are several types of titration, which vary depending on the chemistry involved; these include acid-base titrations, redox titrations, complexometric titrations and precipitation titrations. During this report, only redox titrations are discussed, which involve the oxidation and reduction between the titrant and analyte. Either a potentiometer

or a redox indicator are commonly used to determine the endpoint of a redox titration. Iodometry is a commonly used redox titration, which utilises the iodine/iodide redox reaction to analyse the concentration of oxidising agents in aqueous solutions. To perform iodometry and determine the unknown concentration of an analyte (e.g. $A^+$, in Equation 2.3.25), a known excess of iodide solution is added to a known volume of the analyte. The analyte reacts with some of the iodide to form iodine, which is soluble in the presence of iodide forming triiodide. The solution is then titrated against a standard solution of thiosulfate, which gives iodide and tetrathionate ions (Equation 2.3.25).

$$I^-(excess) + 2\,A^+ \rightarrow I^-(excess) + 2\,A + I_3^-$$

$$I_3^- + 2\,S_2O_3^{2-} \rightarrow 3\,I^- + S_4O_6^{2-}$$

**Equation 2.3.25 –** Iodometric redox titration, where an excess of iodide reacts with a known volume of the analyte to give the reduced analyte, iodine present as triiodide and the remainder of the iodide. The iodine (present as triiodide) is then reduced back to iodide using a known quantity and concentration of thiosulfate. $A^+$ and A represent oxidised and reduced forms of analyte in this equation.

Although the colour change from dark brown to colourless should be enough to indicate the end point, a starch indicator is used to clarify the end point, since iodine binds to the helical chain of beta-amylose in starch to give a strong blue colour. The disappearance of this blue colour indicates complete reduction of iodine to iodide and shows the endpoint has been reached. Knowing the concentration and volume of the thiosulfate solution that has been used, as well as the volume of the analyte, it is possible to calculate the concentration of the analyte.

### 2.3.9 – Ultraviolet-Visible Absorption Spectroscopy

Ultraviolet-visible (UV-vis) spectroscopy can refer to either absorption or reflection spectroscopy in the ultraviolet-visible spectral region (200 – 800 nm), which corresponds to the light in the visible region (390 – 740 nm) and the adjacent regions, ultraviolet region (200 – 390 nm) and very near infrared region (740 – 800 nm). Throughout this report, only the absorption spectroscopy will be discussed. A molecule absorbing light in the ultraviolet-visible region is associated with excitation of the outer electrons from their ground state to an excited state. In organic molecules, this is normally

restricted to specific functional groups known as chromophores, which contain valence electrons that can absorb energy within the region (200 – 800 nm) and transition from the ground state to an excited molecular orbital. These commonly involve exciting either π or non-bonding electrons to higher anti-bonding molecular orbitals. However in transition metal complexes, the electrons are usually excited from a low energy d-orbital to high energy d-orbital (Figure 2.3.13).

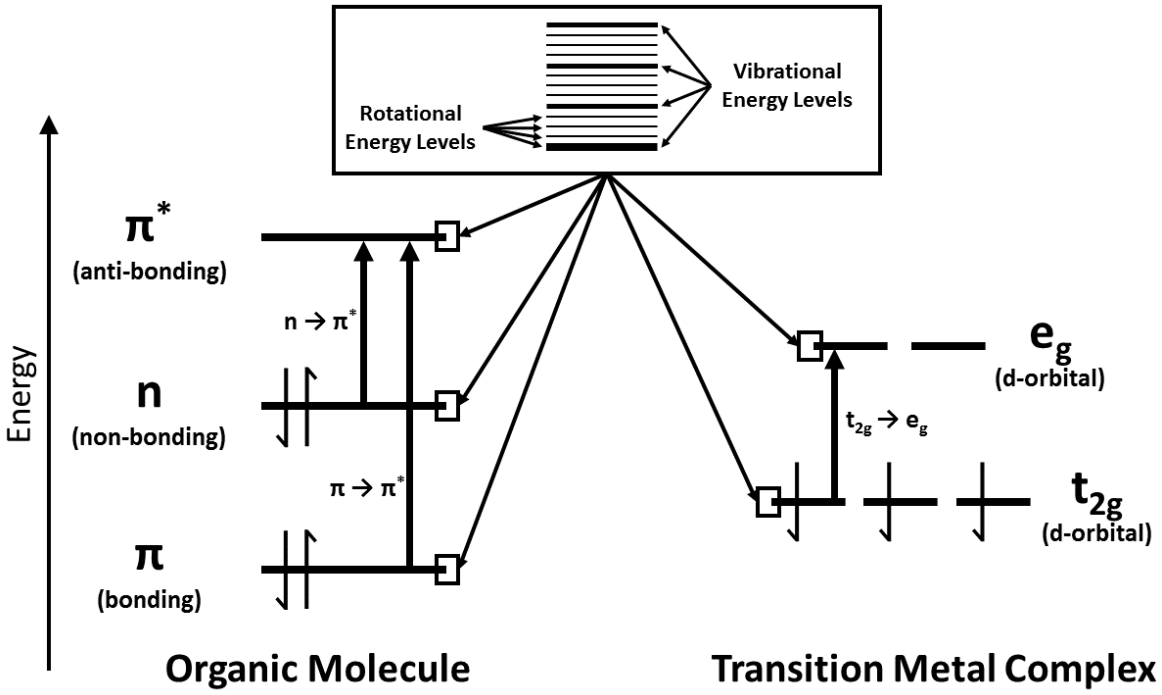


**Figure 2.3.13 –** The excitation of outer electrons from their ground states to their excited states caused by the absorption of light in the ultraviolet-visible region of the electromagnetic spectrum. Common electronic transitions observed using UV-vis spectroscopy illustrated for both an organic molecule and a transition metal complex. The associated vibrational and rotational energy levels are also shown.

Furthermore, both rotational and vibrational transitions occur simultaneously to electronic transitions, which explains why the absorption peaks appear as a continuous absorption band (Figure 2.3.14). The energy associated with these electronic transitions can be converted from wavelength into energy (Equation 2.3.26).

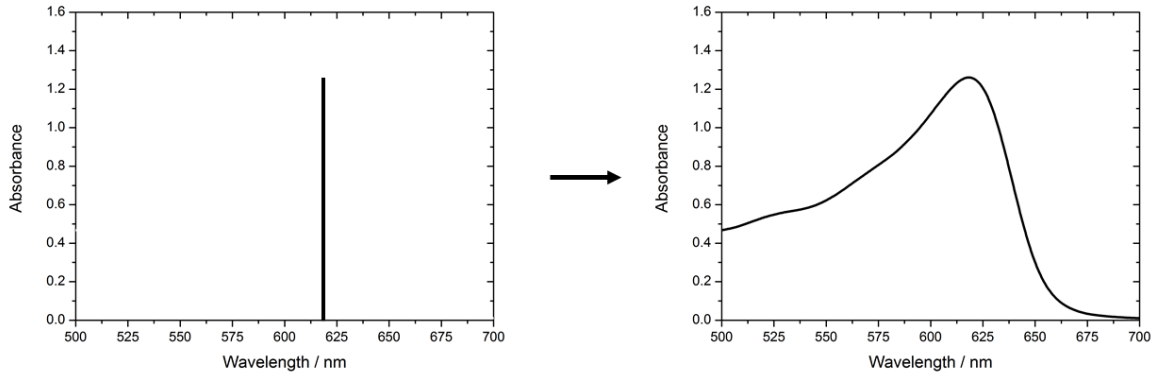


**Figure 2.3.14 –** The appearance of an absorption peak at 618 nm is experimentally broad due to the rotational and vibrational transitions that occur simultaneously to the electronic transitions.

$$E = h\nu = \frac{hc}{\lambda}$$

**Equation 2.3.26 –** Calculating the energy of a transition using wavelength, where $E$ = energy in J mol$^{-1}$, $h$ = Planck constant (6.626 x 10$^{-34}$ J s), $\nu$ = frequency in s$^{-1}$, $c$ = speed of light (3 x 10$^{8}$ m s$^{-1}$) and $\lambda$ = wavelength of absorption peak in m.

At a specific wavelength, the relationship between absorbance and concentration can be expressed using the Beer-Lambert law (Equation 2.3.27). This allows the molar extinction coefficient for that specific wavelength to be calculated.

$$A = \varepsilon c l$$

**Equation 2.3.27 –** The Beer-Lambert law, where $A$ = absorbance, $\varepsilon$ = molar extinction coefficient in dm$^3$ mol$^{-1}$ cm$^{-1}$, $c$ = concentration in mol dm$^{-3}$, $l$ = optical path length in cm.

UV-vis spectrometers are used to measure the absorbance of light in the ultraviolet-visible region by molecules at either a single wavelength or over a range wavelengths. The output light source is commonly produced by a combination of two lamps (halogen/tungsten and deuterium), which is focused onto a prism or diffraction grating used to split the light into its component wavelengths. This light is then passed through a small transparent container commonly known as a cuvette. The cuvette is usually made of quartz, which does not absorb in the ultraviolet-visible spectral region (200 – 800 nm). Firstly, a reference cuvette is prepared containing only the solvent in which the sample will be dissolved. For each wavelength, the intensity of light passing through the reference

cuvette is measured ($I_0$). Then, a sample cuvette is prepared containing the sample to be measured dissolved in the same solvent as measured in the reference. For each wavelength, the intensity of the light passing through the sample cuvette is measured ($I$). Using these two intensities, $I_0$ and $I$, it is possible to determine the absorbance (Equation 2.3.28). The calculated absorbance, which is unitless, is usually plotted against wavelength in nm (Figure 2.3.14).

$$A = \log_{10} \frac{I_0}{I}$$

**Equation 2.3.28 –** Calculating the absorbance from the measured intensities of the reference and sample cuvettes, where $A$ = absorbance, $I_0$ = measured intensity of the reference cuvette and $I$ = measured intensity of the sample cuvette.

## 2.4 – References

1. D. Pletcher, *A First Course in Electrode Processes*, Royal Society of Chemistry, 2009.

2. A. J. Bard and L. R. Faulkner, *Electrochemical Methods: Fundamentals and Applications*, Wiley, 2000.

3. W. Weppner and R. A. Huggins, *J. Electrochem. Soc.*, 1977, **124**, 1569-1578.

4. P. P. Prosini, M. Lisi, D. Zane and M. Pasquali, *Solid State Ionics*, 2002, **148**, 45-51.

5. Y. Zhu and C. Wang, *J. Phys. Chem. C*, 2010, **114**, 2830-2841.

6. M. R. Busche, P. Adelhelm, H. Sommer, H. Schneider, K. Leitner and J. Janek, *J. Power Sources*, 2014, **259**, 289-299.

7. C. J. Wen, B. A. Boukamp, R. A. Huggins and W. Weppner, *J. Electrochem. Soc.*, 1979, **126**, 2258-2266.

8. H. S. Carslaw and J. C. Jaeger, *Conduction of Heat in Solids*, Clarendon Press, Oxford, 1959.

9. J. Goldstein, *Scanning Electron Microscopy and X-ray Microanalysis: Third Edition*, Plenum, 2003.

# 3 – Lithium-Sulfur Cell Design and its Components

## 3.1 – Introduction

Before studying the electrochemistry associated with the Li-S battery components (e.g. sulfur electrode, lithium electrode, electrolyte etc.), it was important to select a suitable cell design, which would be used throughout the majority of the project. To determine which cell design to use, several different cell designs were tested and their cycling performance was analysed. Aspects that were considered important in choosing a suitable cell design were cycling performance, reproducibility and practicality.

The three cell designs considered were:

- A simple 'metal cell', which uses one external O-ring (Viton®) to seal the cell from the outer atmosphere and three screws to close the cell. The Li-S components are placed on top of a small current collector cap which sits on top of a spring (Figure 3.1.1a).
- A 'Nylon cell', which uses a combination of three internal O-rings (Viton®) to seal the cell from the outer atmosphere and three screws to close the cell. The Li-S components are placed inside the body of the cell, which is made from Nylon (Figure 3.1.1b).
- A 'Swagelok® cell', which uses no O-rings but rather ferrules (PFA) to seal the cell from the outer atmosphere and two ends that screw over the entire body of the cell to close. To prevent internal short-circuiting of the cell components, a sheet of FEP film was used to line the internal wall of the cell body. The Li-S components are placed inside the body of the cell, which is made from stainless steel (Figure 3.1.1c).

To test these cell designs, the three Li-S cells were assembled using the same Li-S battery components in each of the cells. Once a suitable cell design had been chosen, its reproducibility was analysed. Then in order to obtain a better understanding of the Li-S system, as well as improve cell performance, the Li-S cell components were modified. These modifications focussed primarily on protecting the lithium metal using indirect methods such as doping the electrolyte with lithium nitrate ($LiNO_3$).

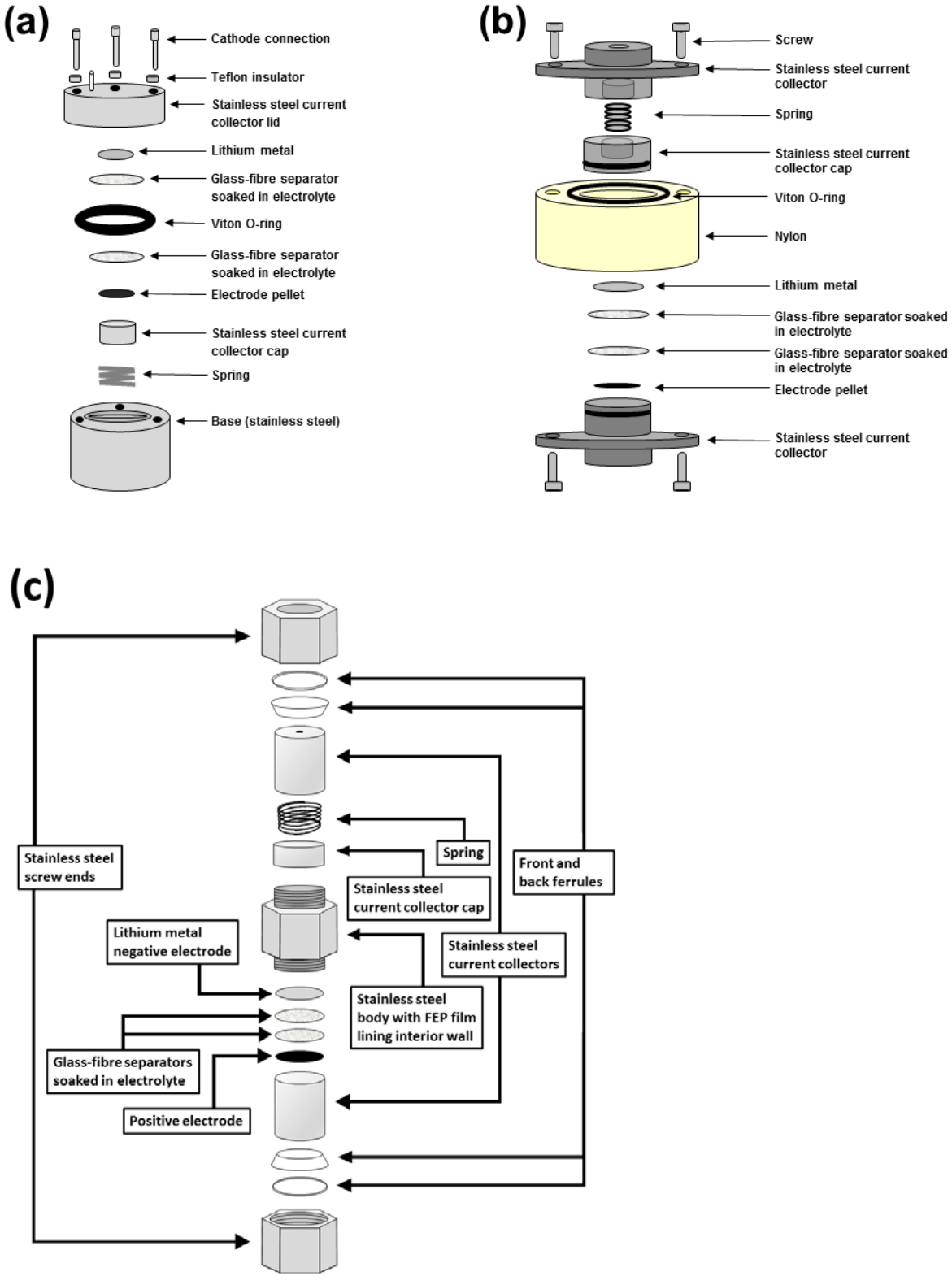


**Figure 3.1.1 –** Schematic diagram of Li-S cell designs: (a) metal cell, (b) Nylon cell and (c) Swagelok cell. The illustrations of the metal and Nylon cells were originally drawn by Saddam Al-Mahmoud.

## 3.2 – Experimental Details

### 3.2.1 – Preparation of Sulfur/Acetylene Black Composite Positive Electrodes

Sulfur (sublimed, 100 mesh, Sigma-Aldrich, 0.25 g) and acetylene black (0.75 g) were ground together and ball milled continuously for 30 min at 20 rps using a ball mill (Retsch MM 200, Germany) in a stainless steel vessel (10 mL) with a stainless steel ball (Ø = 10 mm). The ball milled composite (25 wt% sulfur, 0.18 g) and PTFE (Pellets, DuPont, 0.02 g) were ground together giving 90 wt% composite to 10 wt% binder. The mixture was rolled into a sheet (80-120 μm) using a roll press and the sheet was then cut into positive electrode pellets ($S_8$ loading = 22.5%, Ø = 11 mm, A = 1 $cm^2$) and dried under vacuum at 40°C for approximately 16 h.

### 3.2.2 – Pre-treating the Lithium Metal Negative Electrode

The lithium metal was pre-treated by gently pressing the lithium metal disk onto a current collector cap, which was then submerged in a $LiNO_3$ (0.2 M, 99.99%, Sigma-Aldrich, dried at 130°C under vacuum for 72 h) electrolyte solution for ~48 h. The standard electrolyte consisted of 1 M LiTFSI (99.95 %, Sigma-Aldrich, dried at 130 °C under vacuum for 72 h) in 1:1 mixture of TEGDME (≥ 99%, Sigma-Aldrich, dried at 90 °C under vacuum for 72 h) and DOL (99%, anhydrous, Sigma-Aldrich). After ~48 h, the pre-treated lithium metal and current collector caps were used in preparing the Swagelok cell (Section 3.3.3).

### 3.2.3 – Preparation of Cells (Metal, Nylon and Swagelok)

For full details on the cell construction of each cell, see Section 2.2. In this chapter, only Swagelok cells with an internal diameter of ½ inch were used. In an argon filled glove box, the cells were assembled using a sulfur/acetylene black composite positive electrode ($S_8$ loading = 22.5%, Ø = 11 mm, A = 1 $cm^2$) prepared in Section 3.2.1, two glass-fibre separators (GF/F, Whatman®, Ø = 12 mm, dried), 1 M LiTFSI in 1:1 mixture of TEGDME:DOL electrolyte (0.125 mL) and a lithium metal negative electrode (Ø = 10 mm). For the cells containing $LiNO_3$ (99.99%, Sigma-Aldrich, dried at 130°C under

vacuum for 72 h) as an electrolyte additive, 1 M LiTFSI + 0.2 M $LiNO_3$ in 1:1 mixture of TEGDME:DOL electrolyte (0.125 mL) was used.

### 3.2.4 – Galvanostatic Cycling

All electrochemical measurements were recorded using a multichannel potentiostat (VMP2 or MPG, Bio-Logic) using EC-Lab software (Bio-Logic). All cells were cycled between 1.5 V and 2.8 V unless the cell contained $LiNO_3$, which is known to be irreversibly reduced below 1.6 V, then the cells were cycled between 1.7 V and 2.8 V.[1] All cells were cycled at C/10 rate i.e. $i$ = 167.2 mA $g_S^{-1}$.

## 3.3 – Results and Discussion

### 3.3.1 – Comparison of Cell Designs

In order to test the performance of the three cell designs (metal cell, Nylon cell and Swagelok cell, Figure 3.1.1), each was assembled using conventional Li-S battery components and galvanostatically cycled at C/10 rate, i.e. $i$ = 167.2 mA $g_S^{-1}$ (Figure 3.3.1).

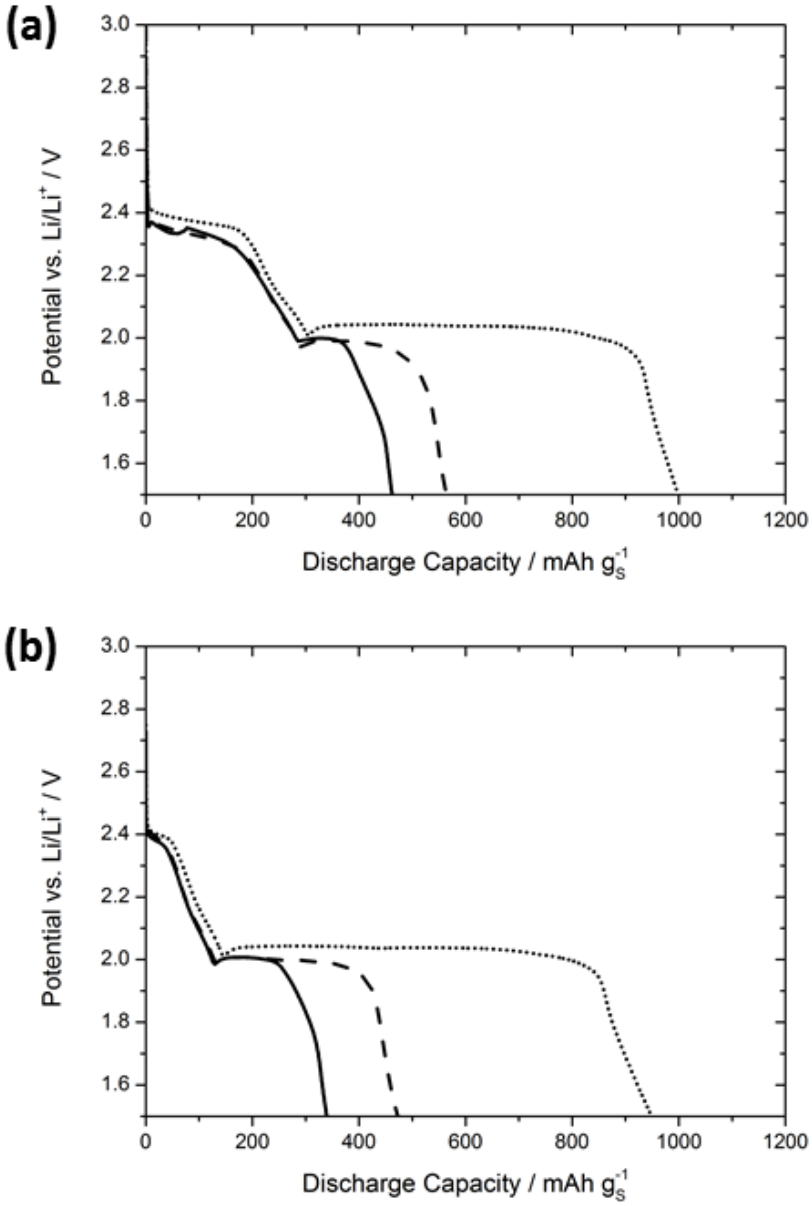


**Figure 3.3.1 –** Discharge profiles of three differently designed Li-S cells (— metal cell, --- Nylon cell, ···· Swagelok cell) during (a) the first discharge and (b) the second discharge cycled at C/10 rate (i.e. $i$ = 167.2 mA $g_S^{-1}$) using a sulfur/acetylene black/PTFE composite positive electrode ($S_8$ = 22.5%, areal capacity = 4.9 – 5.6 mA h $cm^{-2}$, ∅ = 11 mm, A = 1 $cm^2$), two glass-fibre separators, 1 M LiTFSI in TEGDME:DOL (1:1 v:v) electrolyte and a lithium metal negative electrode. Capacities are normalised to the mass of sulfur ($g_S$) in the positive electrode and all cells were cycled at 25 °C.

It is observed that using different cell designs has a notable effect on discharge capacity, as shown in Figure 3.3.1. The same components were used in each of the three cell designs, however it is observed that using the Swagelok cell affords the greatest discharge capacity, followed by the Nylon cell and then lastly the metal cell. The second discharge plateau (observed between 2.0 – 2.1 V) is the main contributor for larger discharge capacities of the Swagelok and Nylon cells, since the capacity associated with the first discharge plateau is similar in all cells. Using primarily metal components without the use of O-rings, Swagelok cells are likely to exclude air/moisture better than the Nylon and metal cells. As the name suggests, the cell body of the Nylon cell is made of Nylon, which is relatively permeable to water and the metal cell has only one O-ring to protect the contents of the cell from the atmosphere.[2] Moisture reacting with the lithium negative electrode would form lithium hydroxide and hydrogen gas; lithium hydroxide can corrode the cell components and hydrogen gas would create gas bubbles responsible for loss of active material. Furthermore, moisture reacting with lithium sulfide at the lithium negative electrode would prevent the SEI from forming, reducing the discharge capacity and enhancing polysulfide shuttling.

Another notable observation is that the discharge capacity associated with the first plateau decreases significantly from the first discharge (210 – 230 mA h $g^{-1}$, measured at 2.2 V) to the second discharge (70 – 90 mA h $g^{-1}$, measured at 2.2 V), irrespective of the design used. In fact, the capacity loss associated with the first plateau is measured between 138 mA h $g^{-1}$ and 139 mA h $g^{-1}$ for all cell designs. The first discharge plateau is commonly associated with the reduction of $S_8$ to polysulfides and therefore, it stands to reason that during the second discharge there is less sulfur available to undergo reduction.[3-7] This loss in $S_8$ could be caused by loss of active material that has shuttled to the negative electrode and reacted directly with the lithium, forming an SEI layer during the first discharge/charge cycle. Another cause could be passivation of the positive electrode carbon framework by $S_8$ during charge, preventing full oxidation of the polysulfides back to $S_8$.

After 20 cycles, it was observed that the Swagelok cell still offered by far the largest discharge capacity compared to the metal and Nylon cells (Figure 3.3.2). However, it should be noted that the metal cell showed the least capacity fading, followed by

Swagelok cell and the Nylon cell showed the largest capacity fade. Once again, the relatively high water permeability of Nylon is likely the cause of the cells rapid decline in discharge capacity on cycling.

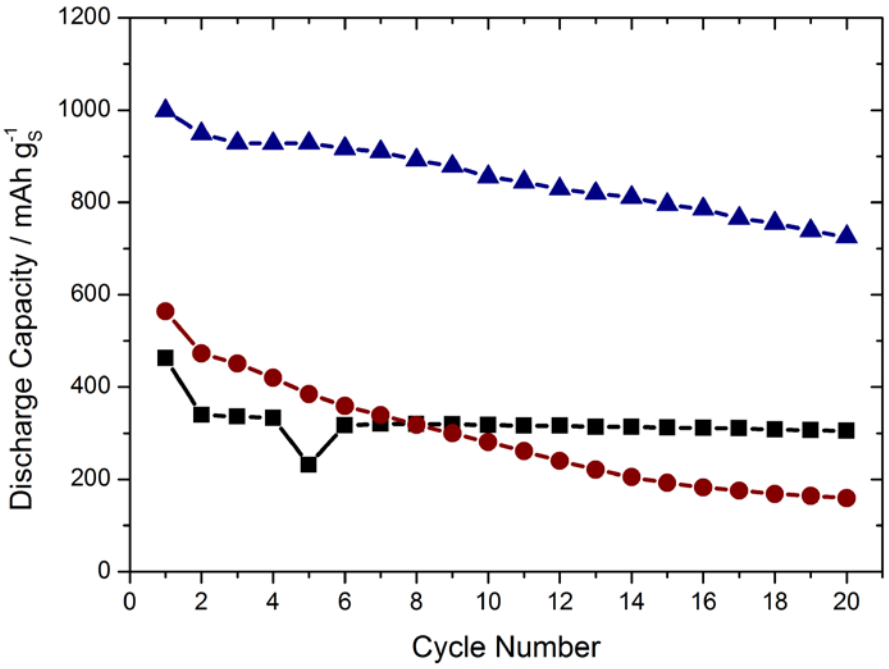


**Figure 3.3.2 –** Cycling stability of the three differently designed Li-S cells (■ metal cell, ● Nylon cell, ▲ Swagelok cell) cycled at C/10 rate (i.e. $i$ = 167.2 mA $g_S^{-1}$) using a sulfur/acetylene black/PTFE composite positive electrode ($S_8$ = 22.5%, areal capacity = 4.9 – 5.6 mA h cm$^{-2}$, ∅ = 11 mm, A = 1 cm$^2$), two glass-fibre separators, 1 M LiTFSI in TEGDME:DOL (1:1 v:v) electrolyte and a lithium metal negative electrode. Capacities are normalised to the mass of sulfur ($g_S$) in the positive electrode and all cells were cycled at 25 °C.

Based on the results obtained, it would appear that the Swagelok cell design is the most promising, with the largest discharge capacity and relatively small capacity fading on cycling. Furthermore, the Swagelok cell design uses a piece of FEP film to line the internal wall of the cell to prevent short-circuiting. This film is disposed of after each use which prevents the build-up of any unwanted contaminants. In addition to this, the Swagelok cell configuration is widely used in Li-S battery research, which would enable the results obtained in this project to be more accurately compared to those in the literature.[8-13] Therefore, it was decided that the Swagelok cell would be the cell design of choice, when using a stacked electrode configuration, for the remainder of the project.

### 3.3.2 – Reproducibility: The Effects of Cell Construction

In order to test the reproducibility of the Swagelok cell design, four Swagelok cells were prepared using the same Li-S battery components and cycled under the same conditions. On checking the open-circuit potential (OCP), it was clear that one of the four cells had short-circuited, however the other three cells possessed an OCP of over 3 V. These three cells were then cycled at C/10 rate. The discharge capacities, charge capacities and Coulombic efficiencies were compared (Equation 3.3.1 and Figures 3.3.3, 3.3.4 and 3.3.5).

$$Coulombic\ Efficiency = \frac{N^{th}\ Discharge\ Capacity}{N^{th}\ Charge\ Capacity}\ x\ 100\%$$

**Equation 3.3.1 –** Calculating the Coulombic efficiency, where cells were prepared in the fully charged state and the charge/discharge cycle is defined as first discharge → first charge → second discharge → second charge → third discharge → third charge and so forth.

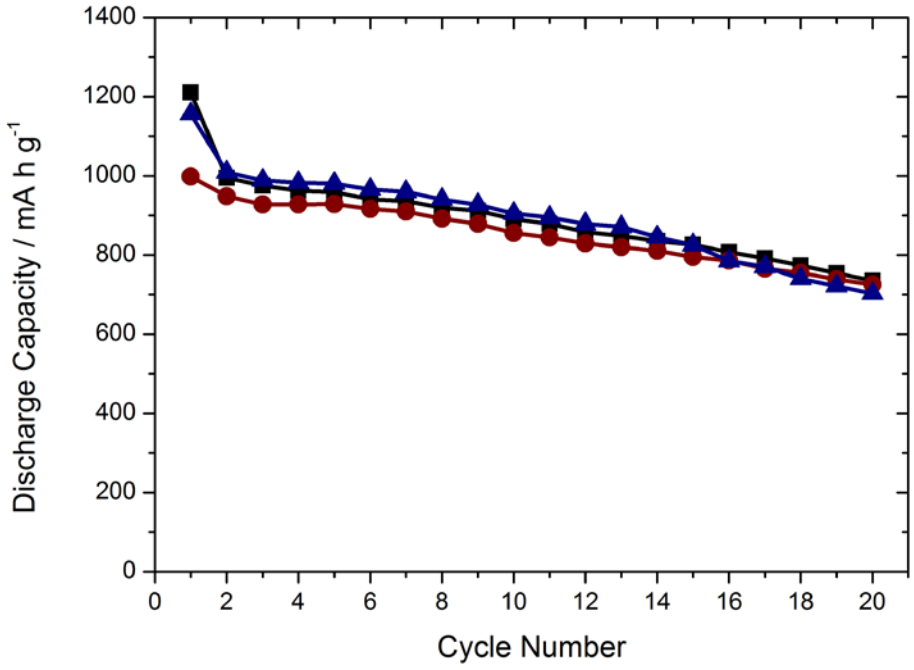


**Figure 3.3.3 –** Discharge capacities of the three metal Swagelok cells at cycled C/10 rate (i.e. $i$ = 167.2 mA $g_S^{-1}$) over 20 cycles using a sulfur/acetylene black/PTFE composite positive electrode ($S_8$ = 22.5%, areal capacity = 4.4 – 4.9 mA h $cm^{-2}$, ∅ = 11 mm, A = 1 $cm^2$), two glass-fibre separators, 1 M LiTFSI in TEGDME:DOL (1:1 v:v) electrolyte and a lithium metal negative electrode. Capacities are normalised to the mass of sulfur ($g_S$) in the positive electrode and all cells were cycled at 25 °C.

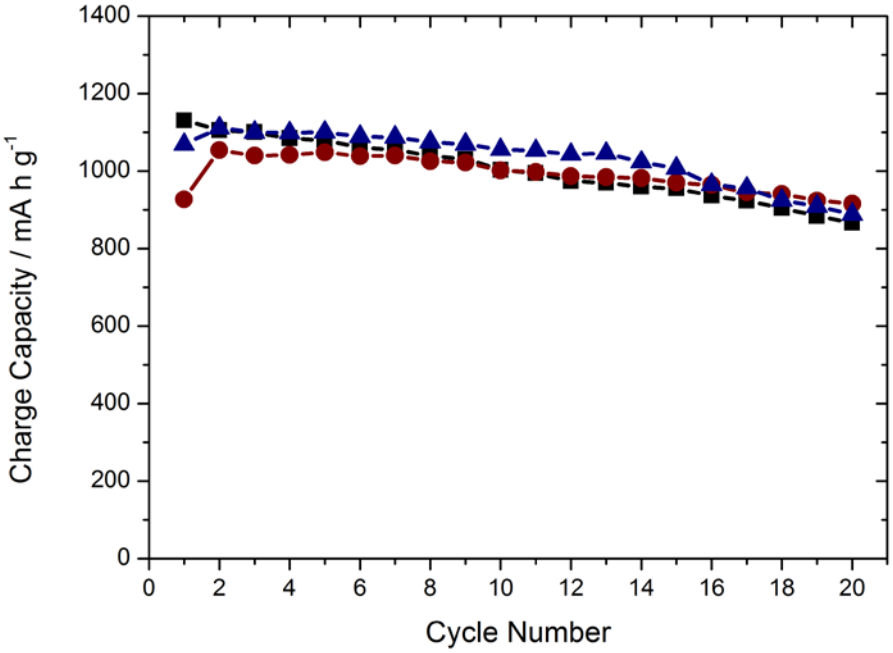


**Figure 3.3.4 –** Charge capacities of the three metal Swagelok cells at cycled C/10 rate (i.e. $i$ = 167.2 mA $g_S^{-1}$) over 20 cycles using a sulfur/acetylene black/PTFE composite positive electrode ($S_8$ = 22.5%, areal capacity = 4.4 – 4.9 mA h $cm^{-2}$, ∅ = 11 mm, A = 1 $cm^2$), two glass-fibre separators, 1 M LiTFSI in TEGDME:DOL (1:1 v:v) electrolyte and a lithium metal negative electrode. Capacities are normalised to the mass of sulfur ($g_S$) in the positive electrode and all cells were cycled at 25 °C.

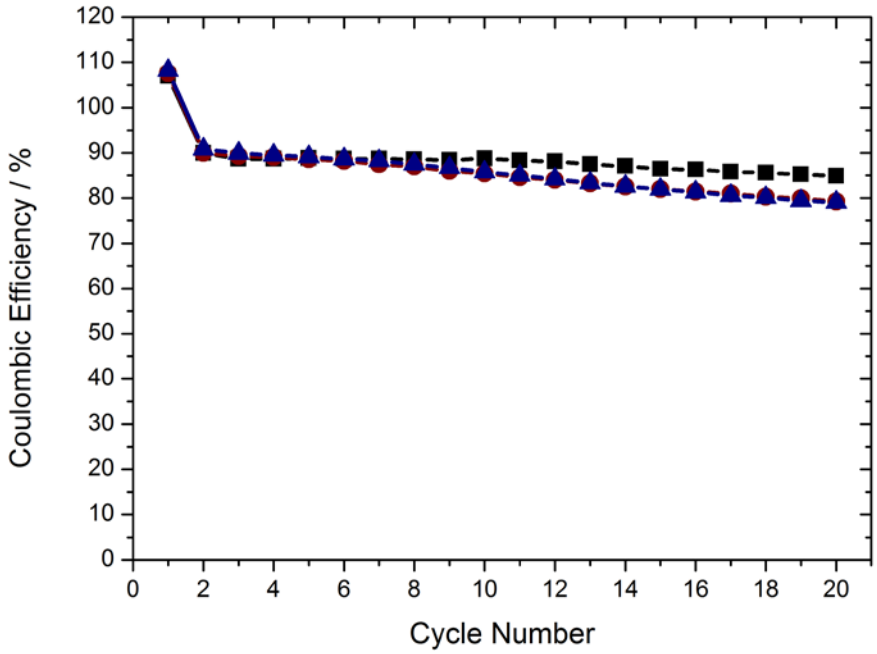


**Figure 3.3.5 –** Calculated Coulombic efficiencies of the three metal Swagelok cells at C/10 rate (i.e. $i$ = 167.2 mA $g_S^{-1}$) over 20 cycles using a sulfur/acetylene black/PTFE composite positive electrode ($S_8$ = 22.5%, areal capacity = 4.4 – 4.9 mA h $cm^{-2}$, ∅ = 11 mm, A = 1 $cm^2$), two glass-fibre separators, 1 M LiTFSI in TEGDME:DOL (1:1 v:v) electrolyte and a lithium metal negative electrode. Capacities are normalised to the mass of sulfur ($g_S$) in the positive electrode and all cells were cycled at 25 °C.

Over 20 cycles, it is observed that both the discharge and charge capacities, as well as the Coulombic efficiency are reproducible, giving good precision. Excluding the first cycle (discussed below), each data point per cycle in all categories is within 8% of one another, with the majority of data points within 5%. It appears that the first cycle discharge and charge capacities are far less reproducible, giving a larger random error of approximately 20%. This variation in the first discharge and charge capacities is observed despite taking the same amount of time to prepare each cell before cycling, under 10 minutes in each case. Therefore, it is unlikely that any significant self-discharge should have occurred, which is verified by the measured OCP of each cell (over 3 V). Through general observation during this entire project, it should be noted that the first discharge and charge capacities of Li-S cells are relatively irreproducible, giving different values each time although subsequent cycles appear far more reproducible, as is observed in this study.

This demonstrates that for the first 20 cycles (excluding the first cycle), the measured values of the discharge and charge capacities, as well as the Coulombic efficiencies are reproducible for the Swagelok cell design giving less than 8% random error. This error is likely a result of the slight differences in cell construction caused by human error (e.g. pressure applied on stack) and a build-up of small differences in the quality of each component used (e.g. electrode thickness, dryness, surface impurities etc.). However, it should be noted that these errors are only strictly applicable when cycling at C/10 and in future work, the cells should be cycled at different C-rates to determine if the magnitude of the error varies on changing the timescale of the galvanostatic cycling experiments.

### 3.3.3 – Effect of Lithium Nitrate as an Electrolyte Additive

In Section 3.3.1, it was determined that using the Swagelok cell design (Figure 3.1.1c) yielded the largest discharge capacities over 20 cycles and a reduced capacity fading on cycling. Despite this, it is observed that the charge capacity is much greater than the discharge capacity, leading to poor Coulombic efficiency (Figure 3.3.6 and Equation 3.3.1). Poor Coulombic efficiency can be attributed to extensive shuttling behaviour.[14] The effect of polysulfide shuttling on increasing charge capacities is discussed in greater detail in Section 4.3.1.

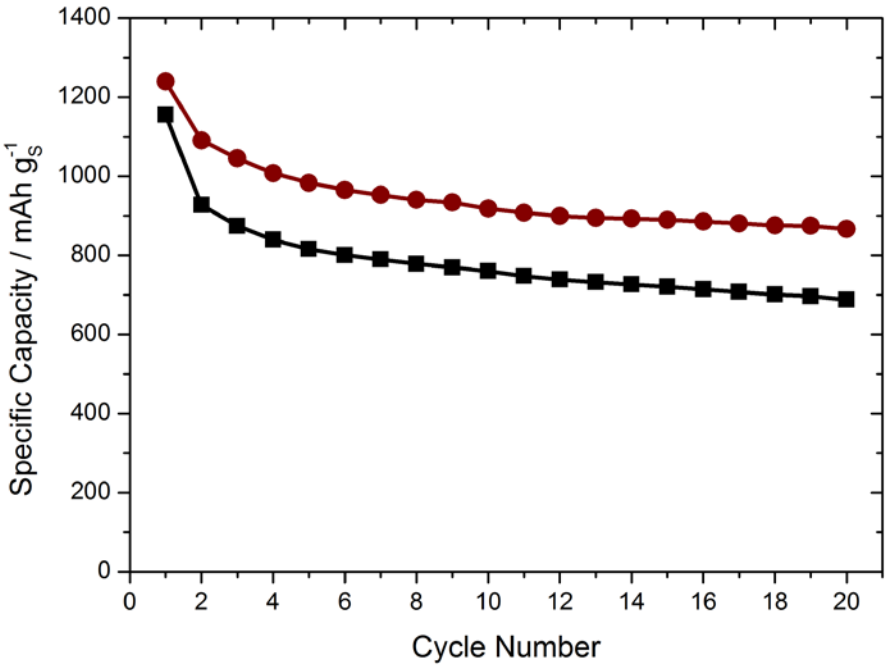


**Figure 3.3.6 –** Specific capacity of Swagelok cell (■ discharge, ● charge) at C/10 rate (i.e. $i$ = 167.2 mA $g_S^{-1}$) over 20 cycles using a sulfur/acetylene black/PTFE composite positive electrode ($S_8$ = 22.5%, areal capacity = 3.3 mA h cm$^{-2}$, ∅ = 11 mm, A = 1 cm$^2$), two glass-fibre separators, 1 M LiTFSI in TEGDME:DOL (1:1 v:v) electrolyte and a lithium metal negative electrode. Capacities are normalised to the mass of sulfur ($g_S$) in the positive electrode and the cell was cycled at 25 °C.

It has been widely reported that using $LiNO_3$ as an electrolyte additive allows a solid electrolyte interface (SEI) layer to form on the negative electrode, which effectively protects the lithium from the shuttling behaviour of the lithium polysulfides.[15-18] This reduced polysulfide shuttling behaviour should improve the Coulombic efficiency of the Li-S cell. To investigate, two Swagelok cells were prepared using the same conditions described above (Figure 3.3.6), except that $LiNO_3$ (0.2 M) was dissolved into the electrolyte of both cells and in one of the two cells, the lithium metal electrode was pre-treated with $LiNO_3$ doped electrolyte solution (Figure 3.3.7, see Section 3.2.2 for details on pre-treating the lithium).

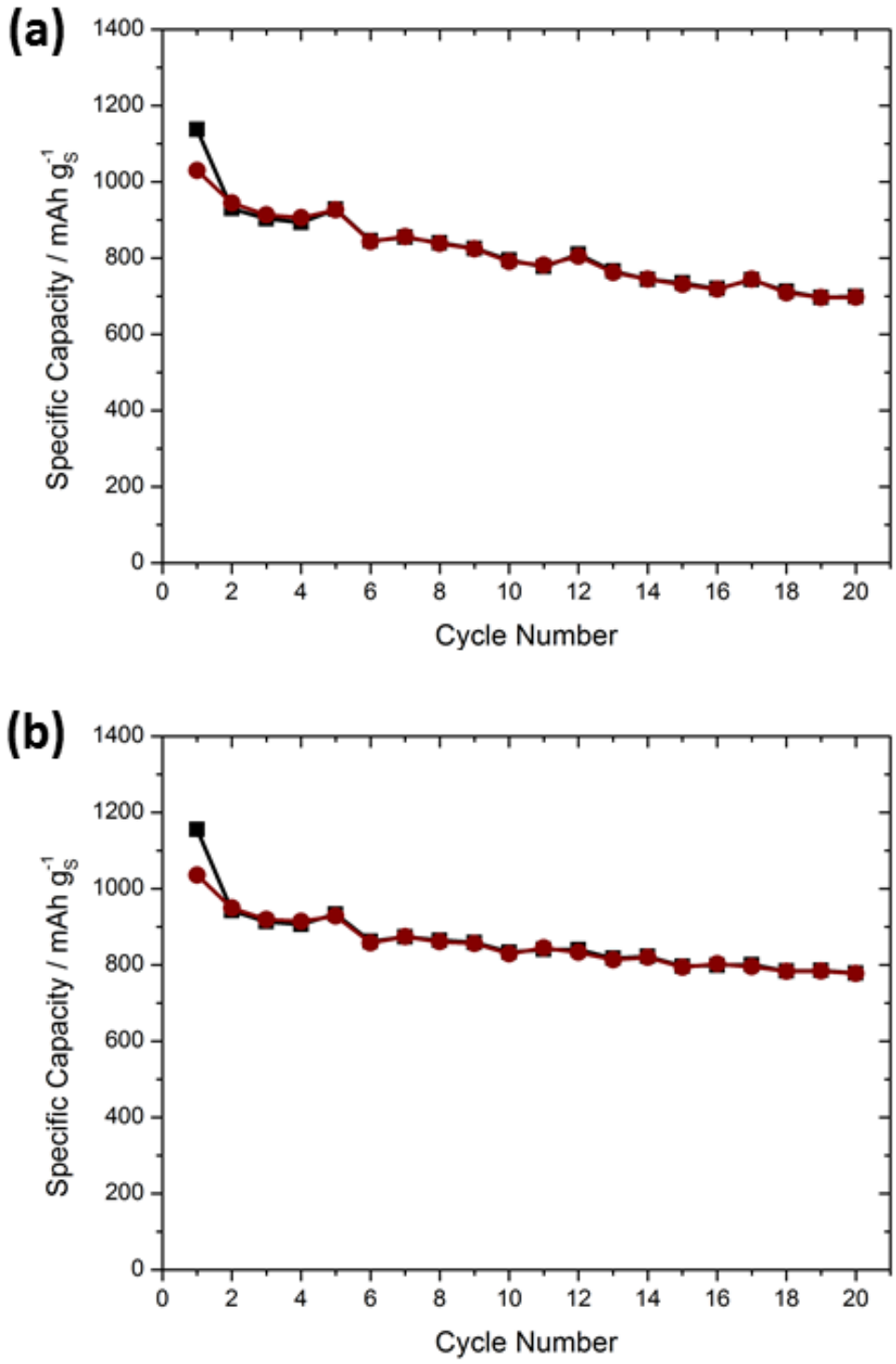


**Figure 3.3.7 –** Specific capacities of Swagelok cells (■ discharge, ● charge) at C/10 rate (i.e. $i$ = 167.2 mA $g_S^{-1}$) using (a) 1 M LiTFSI and 0.2 M $LiNO_3$ in TEGDME:DOL (1:1 v:v) electrolyte with untreated lithium metal and (b) 1 M LiTFSI and 0.2 M $LiNO_3$ in TEGDME:DOL (1:1 v:v) electrolyte with lithium metal that had been pre-treated with $LiNO_3$ on one side. Each contained a sulfur/acetylene black/PTFE composite positive electrode ($S_8$ = 22.5%, areal capacity = 2.9 – 3.1 mA h $cm^{-2}$, ∅ = 11 mm, A = 1 $cm^2$) and two glass-fibre separators. Capacities are normalised to the mass of sulfur ($g_S$) in the positive electrode and both cell were cycled at room temperature.

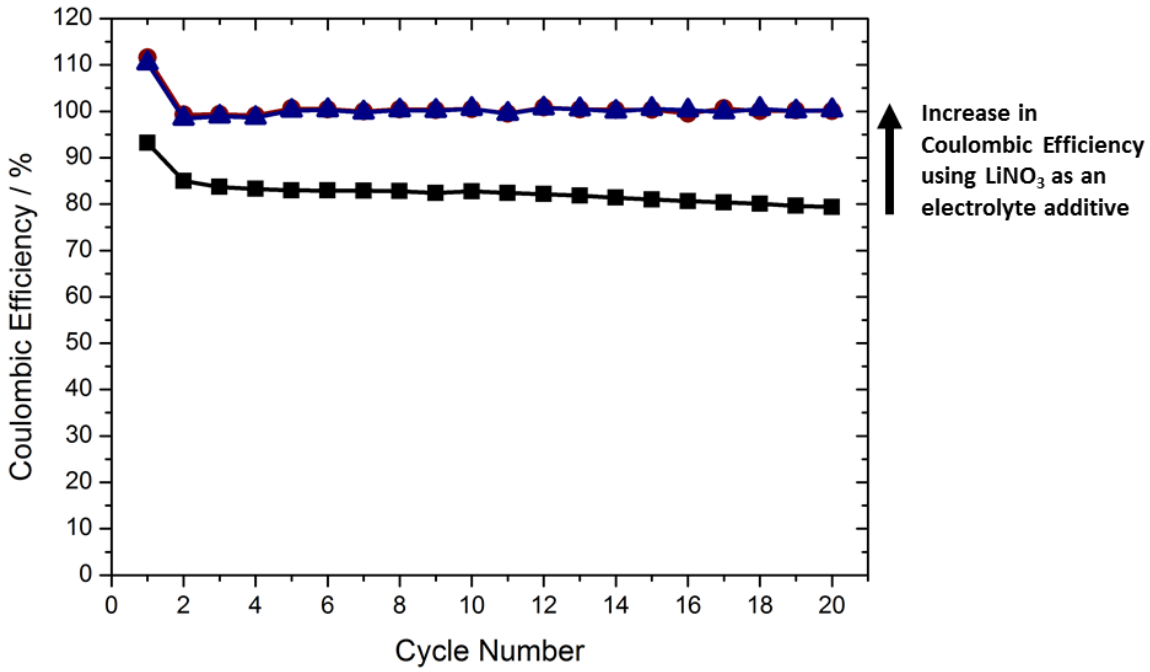


**Figure 3.3.8 –** Coulombic efficiency of the three Swagelok cells (■ No $LiNO_3$, ● $LiNO_3$ in electrolyte, ▲ $LiNO_3$ in electrolyte and pre-treated lithium metal) cycled at C/10 rate (i.e. $i$ = 167.2 mA $g_S^{-1}$) over 20 cycles using a sulfur/acetylene black/PTFE composite positive electrode ($S_8$ = 22.5%, areal capacity = 2.9 – 3.3 mA h $cm^{-2}$, ∅ = 11 mm, A = 1 $cm^2$), two glass-fibre separators, 1 M LiTFSI in TEGDME:DOL (1:1 v:v) electrolyte and a lithium metal negative electrode. One cell contained no $LiNO_3$ electrolyte additive, one contained $LiNO_3$ (0.2 M) as an electrolyte additive and the other cell contained the $LiNO_3$ (0.2 M) electrolyte additive and lithium metal pre-treated on one side with $LiNO_3$ solution. Capacities are normalised to the mass of sulfur ($g_S$) in the positive electrode. The cell with no $LiNO_3$ in the electrolyte was cycled at 25 °C, whereas the other two cells containing $LiNO_3$ in the electrolyte were cycled at room temperature.

It is observed that using $LiNO_3$ as an electrolyte additive greatly improves the Coulombic efficiency of the Li-S cells (Figure 3.3.8). After the first cycle, the cell with no $LiNO_3$ as an electrolyte additive possesses a Coulombic efficiency of 85% which slowly decreases reaching 79% by cycle 20. However, both cells that contain $LiNO_3$ as an electrolyte additive show stable Coulombic efficiencies with values close to 100% for every cycle after the first. The reason for this improved Coulombic efficiency appears to be primarily due to the reduction in charge capacity, which brings the values of the charge and discharge capacities much closer to one another (Figure 3.3.9). The fluctuations seen in the discharge and charge capacities of the cells containing $LiNO_3$ as an electrolyte additive (Figure 3.3.7) are likely due to temperature fluctuations in the laboratory as these experiments were not conducted with temperature control.

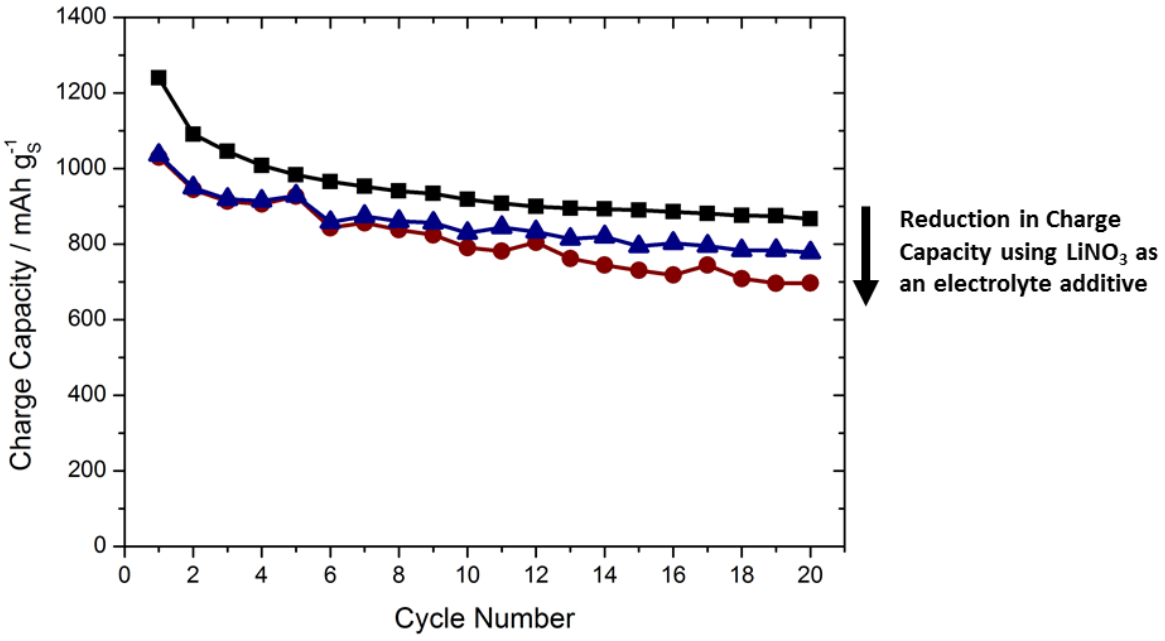


**Figure 3.3.9 –** Charge capacities of the three Swagelok cells (■ No $LiNO_3$, ● $LiNO_3$ in electrolyte, ▲ $LiNO_3$ in electrolyte and pre-treated lithium metal) cycled at C/10 rate (i.e. $i$ = 167.2 mA $g_S^{-1}$) over 20 cycles using a sulfur/acetylene black/PTFE composite positive electrode ($S_8$ = 22.5%, areal capacity = 2.9 – 3.3 mA h $cm^{-2}$, ∅ = 11 mm, A = 1 $cm^2$), two glass-fibre separators, 1 M LiTFSI in TEGDME:DOL (1:1 v:v) electrolyte and a lithium metal negative electrode. One cell contained no $LiNO_3$ electrolyte additive, one contained $LiNO_3$ (0.2 M) as an electrolyte additive and the other cell contained the $LiNO_3$ (0.2 M) electrolyte additive and lithium metal pre-treated on one side with $LiNO_3$ solution. Capacities are normalised to the mass of sulfur ($g_S$) in the positive electrode. The cell with no $LiNO_3$ in the electrolyte was cycled at 25 °C, whereas the other two cells containing $LiNO_3$ in the electrolyte were cycled at room temperature.

Furthermore, it is observed that the first cycle shows a much higher Coulombic efficiency than subsequent cycles, regardless of whether $LiNO_3$ is present in the electrolyte or not (Figure 3.3.8). As mentioned previously in Section 3.3.1, this could due to the irreversible loss of active material, during the formation of the SEI layer at the lithium metal negative electrode, which forms in all cases. The active sulfur is reduced at the positive electrode to a soluble polysulfide species (increasing discharge capacity), which then reacts at the lithium metal negative electrode in SEI formation and this lost active material is not re-oxidised on charge. This would artificially increase the discharge capacity of the first cycle, which causes the Coulombic efficiency to increase. Once again, another cause could be passivation of the positive electrode by $S_8$ during charge, which would prevent full oxidation of the polysulfides back to $S_8$. This would also lead to an artificially large discharge capacity on the first cycle, causing the Coulombic efficiency to

increase. In the case where no $LiNO_3$ is present as an electrolyte additive, the artificial increase in the first discharge capacity, moves its value closer to the value of the first charge capacity, giving a larger Coulombic efficiency. In the cases where $LiNO_3$ is present as an electrolyte additive, the artificial increase in first discharge capacity make the values larger than their respective charge capacities. This explains the apparent first cycle Coulombic efficiencies with values larger than 100%.

The improved Coulombic efficiency of the Li-S cells prepared using $LiNO_3$ as an electrolyte additive is very distinct as is the decrease in charge capacity (Figures 3.3.8 and 3.3.9). However, whether $LiNO_3$ actually improves discharge capacity or reduces capacity fading on cycling is unclear in this study (Figure 3.3.10).

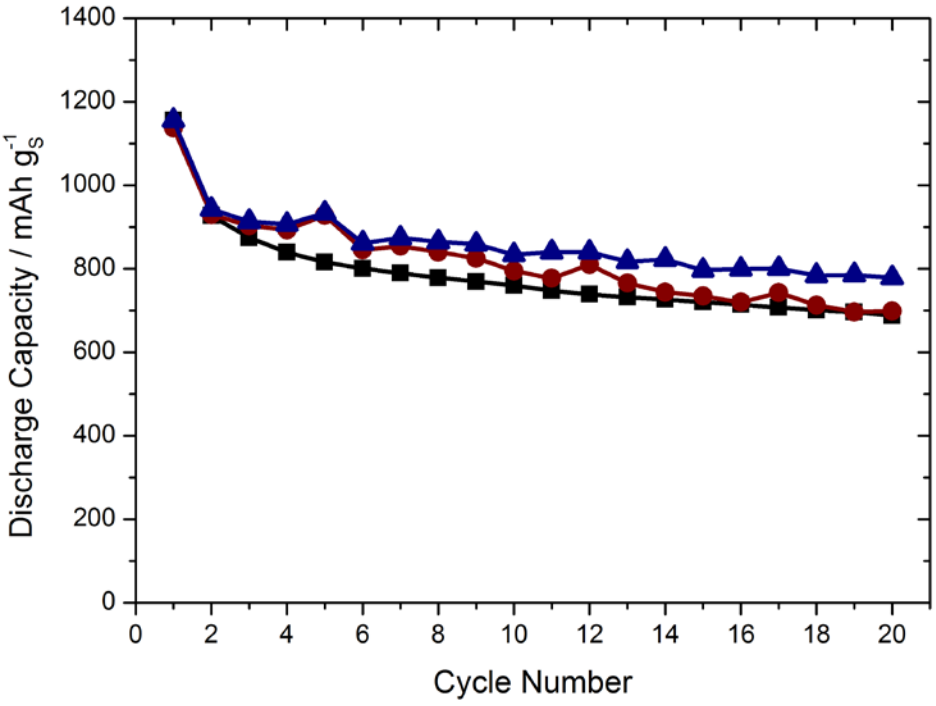


**Figure 3.3.10 –** Discharge capacities of the three Swagelok cells (■ No $LiNO_3$, ● $LiNO_3$ in electrolyte, ▲ $LiNO_3$ in electrolyte and pre-treated lithium metal) cycled at C/10 rate (i.e. $i$ = 167.2 mA $g_S^{-1}$) over 20 cycles using a sulfur/acetylene black/PTFE composite positive electrode ($S_8$ = 22.5%, areal capacity = 2.9 – 3.3 mA h cm$^{-2}$, ∅ = 11 mm, A = 1 cm$^2$), two glass-fibre separators, 1 M LiTFSI in TEGDME:DOL (1:1 v:v) electrolyte and a lithium metal negative electrode. One cell contained no $LiNO_3$ electrolyte additive, one contained $LiNO_3$ (0.2 M) as an electrolyte additive and the other cell contained the $LiNO_3$ (0.2 M) electrolyte additive and lithium metal pre-treated on one side with $LiNO_3$ solution. Capacities are normalised to the mass of sulfur ($g_S$) in the positive electrode. The cell with no $LiNO_3$ in the electrolyte was cycled at 25 °C, whereas the other two cells containing $LiNO_3$ in the electrolyte were cycled at room temperature.

On analysing the discharge capacities of the three cells (Figure 3.3.10), it can be seen that both of the cells treated with $LiNO_3$ give improved discharge capacities initially. However, the cell containing $LiNO_3$ (0.2 M) but untreated lithium metal shows quick capacity fading on cycling, yielding a similar discharge capacity to the cell not treated with $LiNO_3$ by cycle number 20. The cell containing $LiNO_3$ (0.2 M) and pre-treated lithium metal shows both improved discharge capacity and reduced capacity fading on cycling, however the effect observed is not conclusive and could be due to cell quality, rather than a direct effect of $LiNO_3$ itself (see Section 3.3.2 for reproducibility). Barchasz *et al.* reported a similar study, doping $LiNO_3$ (0.1 M) into 1 M LiTFSI in 1:1 TEGDME:DOL electrolyte and found that whilst the Coulombic efficiency improved significantly, the discharge capacity and capacity fading was unaffected.[19] This experiment would need to be repeated multiple times with full temperature control in order to determine whether this effect is due to the $LiNO_3$ electrolyte additive or quality of cell construction. However, due to time constraints and given the many studies in the literature reporting the effects of using $LiNO_3$ as an electrolyte additive for Li-S batteries, these results were considered satisfactory for the purpose of this study.

## 3.4 – Conclusions and Further Work

The Swagelok cell was determined to be the best of the three cell designs, yielding the largest discharge capacities over 20 cycles, as well as reduced capacity fading on cycling. Others advantages of the Swagelok cell design include its primary use of metal components, aiding in the exclusion of air/moisture without resorting to O-rings. Furthermore, an FEP film is used to line the internal cell wall, which is disposed of after each use to prevent any undesired contamination. In addition to the enhanced cycling performance of the Swagelok cell, it offers good reproducibility, which was tested by cycling four identical Swagelok cells over 20 cycles. Apart from one of the cells, which short-circuited, the other three cells gave reproducible discharge capacities, charge capacities and coulombic efficiencies. It was observed that except for the first discharge and charge capacities, which appear relatively random (up to 20% variation), the remaining discharge and charge capacities from cycle 2 to cycle 20 gave values that were within 8% of one another in all cases, with the majority of them being within 5%. Therefore, all preceding work has been completed using the Swagelok cell design, when using stacked cell geometry, unless specified otherwise.

Once a suitable cell design had been chosen, the effects of using $LiNO_3$ as an electrolyte additive were investigated. It was determined that using $LiNO_3$ greatly improves the Coulombic efficiency of the cell from 85 – 79% (without $LiNO_3$, cycle numbers 2 – 20) to a consistent 100% (with $LiNO_3$, cycle numbers 2 – 20). According to the literature, this is likely due to the formation of an SEI layer on the lithium metal negative electrode, reducing the effect of the shuttle mechanism.[15, 20-23] To a lesser extent, $LiNO_3$ may improve the overall discharge capacity and reduce capacity fading on cycling. Although, this experiment would need to be repeated multiple times with full temperature control in order to determine whether this effect is due to the $LiNO_3$ electrolyte additive or the quality of cell construction, i.e. reproducibility. However, due to time constraints, these results were considered satisfactory for the purpose of this study. In further work, four cells could be prepared, one with untreated lithium, one with lithium pre-treated with sulfur, one with lithium pre-treated with $LiNO_3$ and one with lithium pre-treated with both sulfur and $LiNO_3$. This would determine which combination would form the best SEI layer for lithium protection. Also, the effect of pre-treating the lithium on the charge capacities as well as the discharge capacities should be investigated further.

## 3.5 – References


1. S. S. Zhang, *Electrochim. Acta*, 2012, **70**, 344-348.

2. L. K. Massey, in *Permeability Properties of Plastics and Elastomers (Second Edition)*, William Andrew Publishing, Norwich, NY, 2003, DOI: https://doi.org/10.1016/B978-188420797-6.50002-4, pp. 1-56.

3. M. Wild, L. O'Neill, T. Zhang, R. Purkayastha, G. Minton, M. Marinescu and G. J. Offer, *Energ. Environ. Sci.*, 2015, **8**, 3477-3494.

4. D. Zheng, X. Zhang, J. Wang, D. Qu, X. Yang and D. Qu, *J. Power Sources*, 2016, **301**, 312-316.

5. H.-L. Wu, L. A. Huff and A. A. Gewirth, *ACS Appl. Mater. Inter.*, 2014, **7**, 1709-1719.

6. M. Cuisinier, P. E. Cabelguen, S. Evers, G. He, M. Kolbeck, A. Garsuch, T. Bolin, M. Balasubramanian and L. F. Nazar, *J. Phys. Chem. Lett.*, 2013, **4**, 3227-3232.

7. C. Barchasz, F. Molton, C. Duboc, J.-C. Leprêtre, S. Patoux and F. Alloin, *Anal. Chem.*, 2012, **84**, 3973-3980.

8. M. Safari, C. Y. Kwok and L. F. Nazar, *ACS Central Science*, 2016, **2**, 560-568.

9. L. A. Huff, J. L. Rapp, J. A. Baughman, P. L. Rinaldi and A. A. Gewirth, *Surf. Sci.*, 2015, **631**, 295-300.

10. M. U. M. Patel, I. Arčon, G. Aquilanti, L. Stievano, G. Mali and R. Dominko, *ChemPhysChem*, 2014, **15**, 894-904.

11. V. S. Kolosnitsyn, E. V. Kuzmina and S. E. Mochalov, *J. Power Sources*, 2014, **252**, 28-34.

12. N. A. Cañas, D. N. Fronczek, N. Wagner, A. Latz and K. A. Friedrich, *J. Phys. Chem. C*, 2014, **118**, 12106-12114.

13. X. Ji, K. T. Lee and L. F. Nazar, *Nat Mater*, 2009, **8**, 500-506.

14. A. Manthiram, Y. Fu, S.-H. Chung, C. Zu and Y.-S. Su, *Chem. Rev.*, 2014, **114**, 11751-11787.

15. S. Z. Xiong, K. Xie, Y. Diao and X. B. Hong, *J. Power Sources*, 2014, **246**, 840-845.

16. A. Rosenman, R. Elazari, G. Salitra, E. Markevich, D. Aurbach and A. Garsuch, *J. Electrochem. Soc.*, 2015, **162**, A470-A473.

17. D. Aurbach, E. Pollak, R. Elazari, G. Salitra, C. S. Kelley and J. Affinito, *J. Electrochem. Soc.*, 2009, **156**, A694-A702.

18. S. S. Zhang, *J. Power Sources*, 2016, **322**, 99-105.

19. C. Barchasz, J.-C. Leprêtre, F. Alloin and S. Patoux, *J. Power Sources*, 2012, **199**, 322-330.

20. I. Bauer, S. Thieme, J. Bruckner, H. Althues and S. Kaskel, *J. Power Sources*, 2014, **251**, 417-422.

21. J. Bruckner, S. Thieme, H. T. Grossmann, S. Dorfler, H. Althues and S. Kaskel, *J. Power Sources*, 2014, **268**, 82-87.

22. S. Walus, C. Barchasz, J. F. Colin, J. F. Martin, E. Elkaim, J. C. Lepretre and F. Alloin, *Chem. Commun.*, 2013, **49**, 7899-7901.

23. G. Y. Xu, B. Ding, J. Pan, P. Nie, L. F. Shen and X. G. Zhang, *J. Mater. Chem. A*, 2014, **2**, 12662-12676.

# 4 – Electrolyte Salt Concentration: Analysis of Properties and Performance

## 4.1 – Introduction

It is widely accepted that for most conventional Li-S battery systems, the mechanism of discharge and charge involves the formation of several soluble polysulfide species.[1-4] Due to the strong interactions between the polysulfide intermediates and the electrolyte, it has been demonstrated that polysulfide formation and speciation can be influenced by the properties of the chosen electrolyte system.[5-9] In particular, there have been several studies describing the importance of the electrolyte salt concentration.[10, 11] Suo *et al.* investigated a new class of electrolyte, known as 'Solvent-in-Salt' electrolyte, which was demonstrated to effectively reduce the solubility of the polysulfide intermediate species.[10] They state that taking into account the conductivity, viscosity and poor solubility of lithium salts, traditionally salt concentrations are typically lower that 1.2 M. However, they prepared electrolytes with 'ultrahigh' salt concentrations, which were found to exhibit enhanced cyclic and safety performance *via* an effective suppression of lithium dendrite growth, shape change in the metallic lithium negative electrode and inhibition of lithium polysulfide dissolution. Specifically, they tested LiTFSI in 1:1 DOL:DME (ether-based solvents) at concentrations up to 7 mol $L^{-1}_{solvent}$. They mixed these SIS electrolytes with $S_8$ and $Li_2S$, which under 'normal' conditions would lead to polysulfide formation. In particular, they added $S_8$ and $Li_2S$ in a ratio that would give $Li_2S_8$ and a nominal concentration [S] of 4 mol $L^{-1}_{electrolyte}$ if complete dissolution were to occur. They found on using the 7 mol $L^{-1}_{solvent}$ LiTFSI in 1:1 DOL:DME, that almost no polysulfide species had dissolved into the electrolyte, even after 18 days.[10] This study follows the work of Shin *et al.* who describe using 5 M LiTFSI electrolyte to inhibit polysulfide dissolution into the electrolyte.[11] They attributed this to the 'common-ion effect' and comment that increasing the salt concentration increases the viscosity, which in turn decreases the ionic conductivity.

Both of these studies demonstrate that the mechanism by which Li-S batteries discharge and charge, as well as the battery performance, is greatly affected by the salt concentration of the chosen electrolyte system. Therefore, it was deemed important to obtain a thorough understanding of the properties and cycling performance of our chosen electrolyte system and in particular, to determine the effect of altering the electrolyte salt

concentration. For simplicity, it was decided to investigate the electrolyte system of LiTFSI in DOL, where DOL is the only solvent used. Using one solvent should simplify analysis of the data as only interactions between the LiTFSI and DOL need be considered. It was decided to use DOL as the only solvent since it is the most popular co-solvent used in Li-S battery electrolytes as reported in the literature, which commonly dissolve LiTFSI in mixtures of the either DOL/DME or DOL/TEGDME.[12-17] In this chapter, some preliminary measurements are shown (Section 4.3.1), where several different concentrations of LiTFSI in DOL electrolyte (1, 3, 5 and 7 mol $L^{-1}_{solvent}$) were tested using galvanostatic cycling with the standard Swagelok cell setup. Following this, a more in depth study is presented. Several electrolyte solutions were prepared using different concentrations of LiTFSI in DOL (0.2 M, 0.5 M, 1 M, 1.5 M, 2 M, 2.5 M, and 3 M). The physico-chemical properties of these electrolytes that were investigated include density, viscosity, conductivity, thermal phase transitions and polysulfide solubility. Furthermore, the cycling performance of these electrolytes when applied to Li-S cells was investigated further and subsequent corrosion of the lithium negative electrodes after cycling was analysed using SEM.

### 4.1.1 – Conversion between molarity (M) and 'molality' (mol $L^{-1}_{solvent}$)

Suo *et al.*, among many other research groups studying battery electrolytes, measure the concentration of electrolyte using a form of 'molality' in moles of salt per litre of solvent added (mol $L^{-1}_{solvent}$).[10] This avoids the need to use volumetric flasks, required when using molarity in moles of salt per litre of prepared electrolyte (M or mol $L^{-1}_{electrolyte}$) and enables the use of vials and auto-pipettes. In this chapter, literature concentrations reported by Suo *et al.* and the preliminary results (Section 4.3.1) are reported in this form of 'molality' (mol $L^{-1}_{solvent}$). Results obtained whilst on placement at Oxis Energy Ltd. (Sections 4.3.2 – 4.3.8) are reported in molarity (M). To convert between the two methods of reporting electrolyte concentration, a table and graph have been included (Table 4.1.1 and Figure 4.1.1). These conversion tools can only strictly be used to convert between molarity and molality for the LiTFSI in DOL electrolyte system, but it is likely that this can also be used as a good approximation for many electrolyte systems where LiTFSI is the only electrolyte salt present and ether based solvents are used, such as for the commonly used LiTFSI in DOL:DME and LiTFSI in DOL:TEGDME electrolyte systems.

| Concentration in Molarity (M or mol $L^{-1}_{electrolyte}$) | Concentration in 'Molality' (mol $L^{-1}_{solvent}$) |
|---|---|
| 0.2 | 0.2 |
| 0.5 | 0.5 |
| 1.0 | 1.2 |
| 1.5 | 1.9 |
| 2.0 | 2.8 |
| 2.5 | 3.8 |
| 3.0 | 5.1 |
| 3.5 | 6.8 |
| 4.0 | 9.0 |

**Table 4.1.1 –** Converting the concentration of LiTFSI containing electrolyte from molarity (M or mol $L^{-1}_{electrolyte}$) into 'molality' (mol $L^{-1}_{solvent}$) assuming the density of dissolved LiTFSI is 2.07 g $mL^{-1}$ (determined in Section 4.3.2).

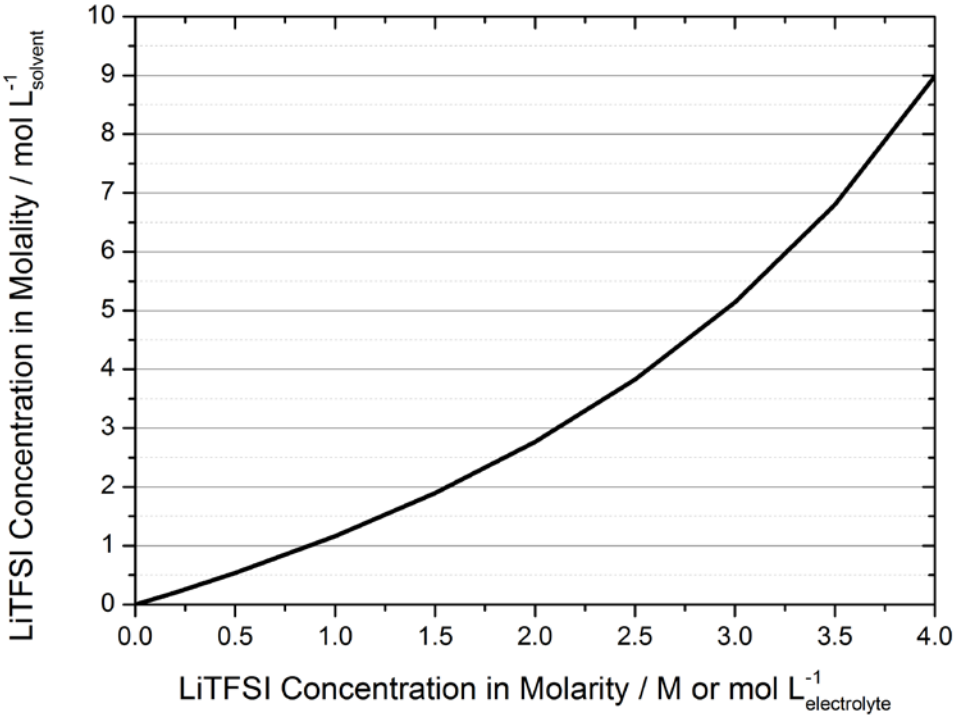


**Figure 4.1.1 –** Converting the concentration of LiTFSI containing electrolyte from molarity (M or mol $L^{-1}_{electrolyte}$) into 'molality' (mol $L^{-1}_{solvent}$) assuming the density of dissolved LiTFSI is 2.07 g $mL^{-1}$ (determined in Section 4.3.2).

## 4.2 – Experimental Details

### 4.2.1 – Preparation of Electrolytes

In Section 4.3.1, the electrolytes were prepared in an argon-filled glove box, using 'molality' (mol $L^{-1}_{solvent}$, discussed in Chapter 2.1.1). The 7 mol $L^{-1}_{solvent}$ LiTFSI in DOL electrolyte was found to be saturated in LiTFSI and so was filtered using a glass syringe and filter (PTFE syringe filters, 0.2 μm pore size, dried). In Sections 4.3.2 – 4.3.9, the electrolytes were prepared in a dry room, using molarity (M or mol $L^{-1}_{electrolyte}$). For example, 1 M LiTFSI in DOL was prepared as follows: For 20 mL, LiTFSI (5.7418 g) was weighed into a volumetric flask (20 mL) and DOL was then added until the bottom of the meniscus reached the graduation line. The solution was inverted to dissolve the LiTFSI and then DOL was added again until the bottom of the meniscus reached the graduation line.

### 4.2.2 – Preparation of Sulfur/Acetylene Black Composite Positive Electrodes

Sulfur (sublimed, 100 mesh, Sigma-Aldrich, 0.25 g) and acetylene black (0.75 g) were ground together and ball milled continuously for 30 min at 20 rps using a ball mill (Retsch MM 200, Germany) in a stainless steel vessel (10 mL) with a stainless steel ball (Ø = 10 mm). The ball milled composite (25 wt% sulfur, 0.18 g) and PTFE (Pellets, DuPont, 0.02 g) were ground together giving 90 wt% composite to 10 wt% binder. The mixture was rolled into a sheet (80-120 μm) using a roll press and the sheet was then cut into positive electrode pellets ($S_8$ loading = 22.5%, Ø = 11 mm, A = 1 $cm^2$) and dried under vacuum at 40°C for approximately 16 h.

### 4.2.3 – Preparation of Swagelok Cell

For full details on cell construction see Section 2.2.1. In this chapter, only Swagelok cells with an internal diameter of ½ inch were used. In an argon filled glove box, the remainder of the Swagelok cell was assembled using a sulfur/acetylene black/PTFE composite positive electrode ($S_8$ = 22.5%, areal capacity = 5.2 – 5.8 mA h $cm^{-2}$, ∅ = 11 mm, A = 1 $cm^2$), two glass-fibre separators (Ø = 12 mm), LiTFSI in DOL electrolyte (various concentrations, 0.125 mL) and a lithium metal negative electrode (Ø = 10 mm).

### 4.2.4 – Galvanostatic Cycling (Preliminary Experiments – Section 4.3.1)

All electrochemical measurements in Section 4.3.1 were recorded using a multichannel potentiostat (MPG, Bio-Logic) using EC-Lab software (Bio-Logic). All cells were cycled between potential limits of 1.5 V and 2.8 V at C/10 rate, i.e. $i$ = 167.2 mA $g_S^{-1}$.

### 4.2.5 – Measuring the Electrolyte Conductivity

In a dry room (dew point < -40 °C), the conductivity of each electrolyte was measured using a Jenway bench conductivity meter (model 4510) at 25 °C. The following settings were used: Cell K = 1.040, COEFF = 0.000, REF T = 25 °C.

### 4.2.6 – Measuring the Electrolyte Dynamic (Shear) Viscosity

The dynamic (shear) viscosity was measured using a rheometer (Discovery HR-2, TA instruments) at 25 °C. For pure DOL, the viscosity was measured over shear rates of 0 – 200 $s^{-1}$. For the LiTFSI in DOL electrolyte solutions, the viscosity was measured over shear rates of 8 – 50 $s^{-1}$.

### 4.2.7 – Preparation of Coin Cells

For full details on cell construction see Section 2.2.4. In an argon filled glove box, the coin cells were assembled using the following components in order: standard Oxis positive electrode (2.5 mA h $cm^{-2}$, Ø = 13.9 mm, single-sided), LiTFSI in DOL electrolyte (various concentrations, 10 μL), Toray T20 separator (polypropylene, Ø = 16.6 mm), one glass-fibre separator (GF/C, Ø = 16.6 mm), LiTFSI in DOL electrolyte (various concentrations, 40 μL), Toray T20 separator (polypropylene, Ø = 16.6 mm) and a lithium metal negative electrode (China energy, d = 100 μm, Ø = 16 mm), spacer (d = 1 mm) and spring. The cell was sealed using a crimper.

### 4.2.8 – Galvanostatic Cycling (Sections 4.3.8 – 4.3.9)

In Sections 4.3.2 – 4.3.9, all electrochemical measurements were recorded using a multichannel potentiostat (MACCOR 6). All cells (except 3 M LiTFSI in DOL) were cycled between 1.9 V and 2.6 V, whereas the 3 M LiTFSI in DOL coin was cycled between 1.5 V and 2.6 V. All cells were discharged at C/10 rate, i.e. $i$ = 167.2 mA $g_S^{-1}$ for the first cycle and cycled at C/5 rate, i.e. $i$ = 334.4 mA $g_S^{-1}$ for all subsequent cycles.

### 4.2.9 – Scanning Electron Microscopy (SEM)

In a dry room (dew point < -40 °C), a benchtop scanning electron microscope (NeoScope™ JCM-6000 from JEOL) was used to study the lithium metal negative electrode surfaces. The negative electrodes were obtained by disassembling the cycled coin cells inside of an argon-filled glovebox, rinsing with DOL (anhydrous) and allowing to dry before transferring inside of a sealed argon-filled bag to the dry room where the SEM was located. The cells were then stored in these argon-filled bags in the dry room until analysis using SEM.

### 4.2.10 – Preparation of Lithium Polysulfide Electrolyte Solutions

In an argon-filled glove box, $Li_2S$ and $S_8$ were added into vials containing electrolytes of LiTFSI in DOL (0.5 M, 1 M, 2 M or 3 M). Assuming full dissolution, the $Li_2S$ and $S_8$ were added in ratios to give $Li_2S_6$ and a nominal concentration [S] of 1 M. The solutions were heated to 60°C for 5 days and left to stand at room temperature for 2 days. The 0.5 M and 1 M LiTFSI in DOL polysulfide electrolyte solutions were not stirred whilst heating whereas the 2 M and 3 M solutions contained stir bars. The concentration of the prepared solutions is always noted in terms of atomic sulfur ($[S]_T^{mix.}$ / M), e.g. $Li_2S_6$ (0.167 M in DOL) gives an atomic sulfur concentration of 1 M, as $Li_2S_6$ contains 6 sulfur atoms (6 x 0.167 M = 1 M).

$$Li_2S + \frac{5}{8} S_8 \rightarrow Li_2S_6$$

**Equation 4.2.1 –** Reaction of $Li_2S$ and $S_8$ in the correct ratios to give $Li_2S_6$

### 4.2.11 – Differential Scanning Calorimetry (DSC)

In a dry room (dew point < -40 °C), DSC measurements were performed using a Pyris™ Diamond DSC from Perkin Elmer™ instruments and ~10 mg of LiTFSI in DOL electrolyte was sealed in an aluminum pan. The pan and the electrolyte were cooled to -170 °C using a Cryofill™ Liquid Nitrogen Cooling System and then heated to at least -30 °C at a heating rate of 5 °C $min^{-1}$ under nitrogen flow.

## 4.3 – Results and Discussion

### 4.3.1 – Cycling Performance (Preliminary Results)

Following on from the work of Suo *et al.* and Shin *et al.*, it was decided to prepare several different concentrations of LiTFSI in DOL electrolyte (1, 3, 5 and 7 mol $L^{-1}_{solvent}$) and test them using the standard Swagelok cell setup described in Chapter 3.[10, 11] It was decided to use LiTFSI in DOL only (i.e. without TEGDME) to ensure that only one solvent was present to solvate the LiTFSI salt, simplifying the analysis and discussion. DOL was chosen over TEGDME since it is more commonly used as a co-solvent in Li-S battery electrolytes, where DOL/DME or DOL/TEGDME are the most often cited solvent systems.[12-17] It should be noted that the electrolyte solutions prepared in this section were prepared using molality in mol $L^{-1}_{solvent}$. It should also be noted that the 7 mol $L^{-1}_{solvent}$ LiTFSI concentration was saturated and required filtration before use. The cells were galvanostatically cycled over 100 cycles (Figure 4.3.1, 4.3.2 and 4.3.3).

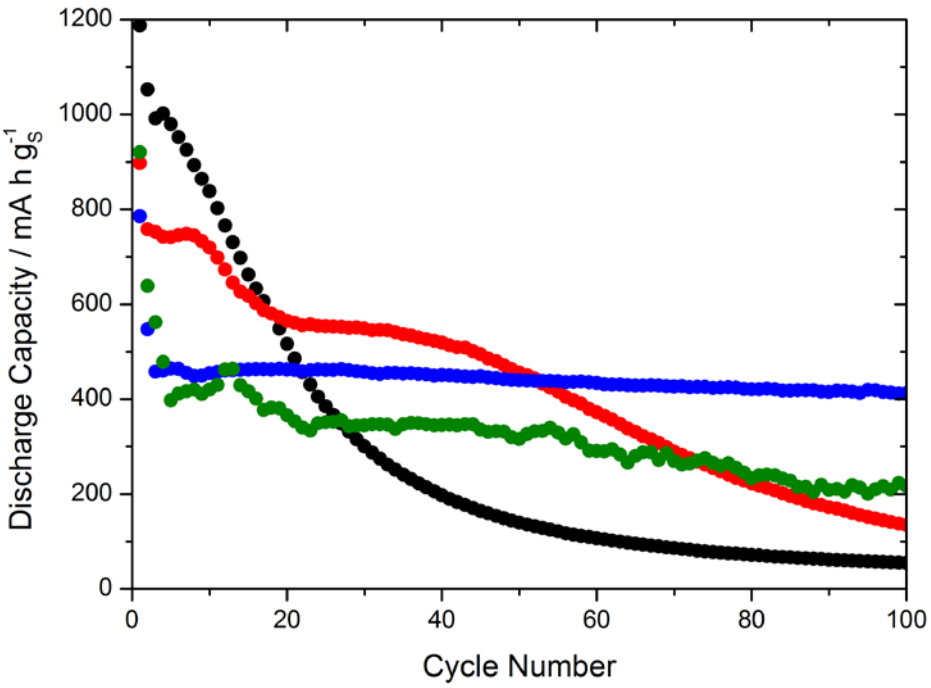


**Figure 4.3.1 –** Discharge capacities of Swagelok cells at C/10 rate (i.e. $i$ = 167.2 mA $g_S^{-1}$) using different concentrations of LiTFSI in DOL electrolyte (1 •••, 3 •••, 5 ••• and 7 (saturated) ••• mol $L^{-1}_{solvent}$), two glass-fibre separators, a sulfur/acetylene black/PTFE composite positive electrode ($S_8$ = 22.5%, areal capacity = 5.2 – 5.8 mA h $cm^{-2}$, ∅ = 11 mm, A = 1 $cm^2$) and a lithium metal negative electrode. The cells were cycled between potential limits of 2.8 and 1.5 V. Capacities are normalised to the mass of sulfur ($g_S$) in the positive electrode and all cells were cycled at 25 °C.

It is observed that increasing the LiTFSI concentration reduces the initial discharge capacity, e.g. comparing the 5$^{th}$ cycle discharge capacities: 980 mA h g$^{-1}$ (1 mol L$^{-1}_{solvent}$), 741 mA h g$^{-1}$ (3 mol L$^{-1}_{solvent}$), 465 mA h g$^{-1}$ (5 mol L$^{-1}_{solvent}$) and 398 mA h g$^{-1}$ (7 mol L$^{-1}_{solvent}$ / saturated). The 5$^{th}$ cycle is used for comparison as it is the first cycle where reversible capacity is observed for all concentrations, indicated by the stabilising values on cycling. The suppressed initial discharge capacity is likely an effect of the reduced polysulfide solubility and increased viscosity. Suo *et al.* observed that as the concentration of electrolyte salt was increased, the polysulfide dissolution was increasingly suppressed indicating that the solubility was being reduced.[10] Reducing the solubility of the polysulfides limits the concentration of active material present in the electrolyte at any one time. This hinders full utilisation of sulfur as it is unable to dissolve quickly enough to be reduced. Furthermore, Suo *et al.* also report that increasing the electrolyte salt concentration increases the viscosity. Therefore at high LiTFSI concentrations, it is likely that the dissolved sulfur and polysulfide species do not diffuse far into the solution but rather stay close to the surface of the positive electrode. As a result, the lithium sulfide end product forms a thin but even dispersed passivation layer over the surface of the sulfur electrode, blocking the use of any unreacted solid sulfur and quickly passivating the conductive carbon framework, preventing any further polysulfide reduction.

On the other hand, it is observed that increasing the LiTFSI concentration reduces capacity fading, e.g. on comparing the remaining capacity (as a percentage) on the 100$^{th}$ cycle to the initial capacity on the 5$^{th}$ cycle: 6% (1 mol L$^{-1}_{solvent}$), 18% (3 mol L$^{-1}_{solvent}$), 89% (5 mol L$^{-1}_{solvent}$) and 55% (7 mol L$^{-1}_{solvent}$ / saturated). It would appear that the capacity fading is reduced on increasing the electrolyte salt concentration up until 5 mol L$^{-1}_{solvent}$ LiTFSI concentration at which point capacity fading is minimised and 412 mA h g$^{-1}$ of discharge capacity is retained after 100 cycles. Higher than this concentration (e.g. 7 mol L$^{-1}_{solvent}$ / saturated) and the capacity fading is more severe. The reduced capacity fading using higher concentrations of LiTFSI can be explained by the effects of polysulfide solubility and electrolyte viscosity. On increasing the LiTFSI concentration, the polysulfide solubility is supressed and the viscosity is increased, which prevents mass diffusion of the polysulfide species to the lithium negative electrode, i.e. the polysulfides remain localised at the sulfur positive electrode. This suppresses the

polysulfide shuttle-mechanism and the loss of active sulfur through reaction with the lithium metal.

It is also observed that the three lower concentrations (1 mol $L^{-1}_{solvent}$, 3 mol $L^{-1}_{solvent}$ and 5 mol $L^{-1}_{solvent}$) give smooth profiles (consistent changes in discharge capacity cycle on cycle), whereas at the highest concentration (7 mol $L^{-1}_{solvent}$ / saturated), the profile is more erratic and scattered (random changes in discharge capacity cycle on cycle, less consistent). This could be caused by the fact that the 7 mol $L^{-1}_{solvent}$ LiTFSI concentration is actually saturated in LiTFSI, which makes it the most viscous, causing poor wetting of the sulfur electrode giving poor electrical contact. Furthermore, the polysulfides could be practically insoluble in this electrolyte solution as a result of the 'common ion effect', which would force the reduction of sulfur to occur *via* a 'solid-state' mechanism leading to large over potentials.

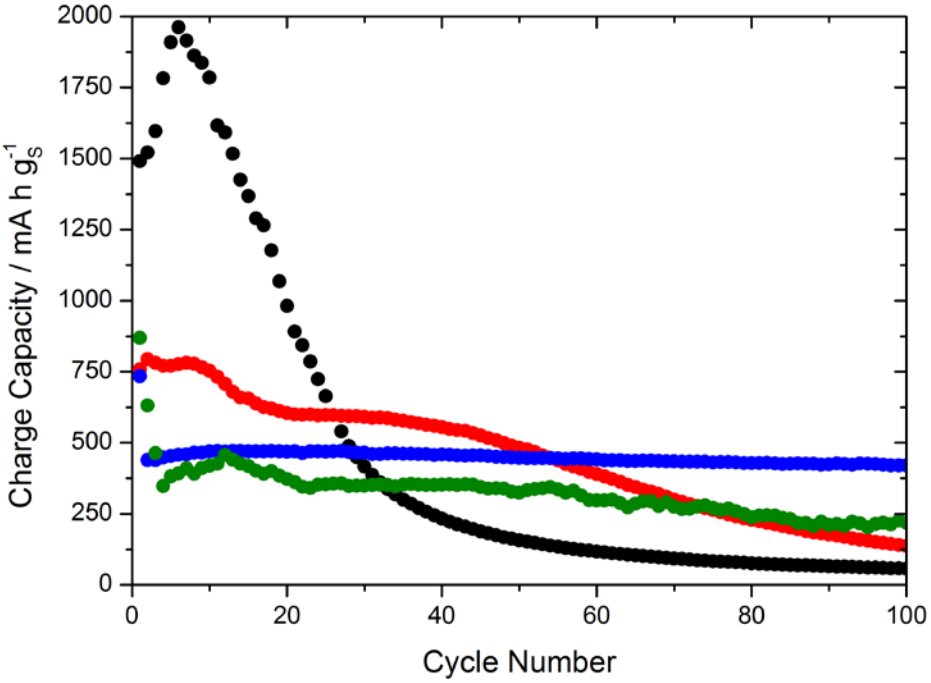


**Figure 4.3.2 –** Charge capacities of Swagelok cells at C/10 rate (i.e. $i$ = 167.2 mA $g_S^{-1}$) using different concentrations of LiTFSI in DOL electrolyte (1 •••, 3 •••, 5 ••• and 7 (saturated) ••• mol $L^{-1}_{solvent}$), two glass-fibre separators, a sulfur/acetylene black/PTFE composite positive electrode ($S_8$ = 22.5%, areal capacity = 5.2 – 5.8 mA h $cm^{-2}$, ∅ = 11 mm, A = 1 $cm^2$) and a lithium metal negative electrode. The cells were cycled between potential limits of 2.8 and 1.5 V. Capacities are normalised to the mass of sulfur ($g_S$) in the positive electrode and all cells were cycled at 25 °C.

It can be seen that on increasing the electrolyte salt concentration, the initial charge capacity is reduced (Figure 4.3.2) e.g. on comparing the 5$^{th}$ charge capacities: 1909 mA h g$^{-1}$ (1 mol L$^{-1}_{solvent}$), 771 mA h g$^{-1}$ (3 mol L$^{-1}_{solvent}$), 453 mA h g$^{-1}$ (5 mol L$^{-1}_{solvent}$) and 382 mA h g$^{-1}$ (7 mol L$^{-1}_{solvent}$ / saturated). The large charge capacities at low salt concentrations are likely a result of extensive polysulfide shuttling, caused by the high polysulfide solubility and low viscosity. However, this will become clearer once the Coulombic efficiency has been analysed. Similar to discharge, at lower concentrations the charge capacity fading is more severe than at higher concentrations (Figure 4.3.2) e.g. comparing the remaining charge capacity as a percentage from the 5$^{th}$ cycle to the 100$^{th}$ cycle: 3% (1 mol L$^{-1}_{solvent}$), 18% (3 mol L$^{-1}_{solvent}$), 93% (5 mol L$^{-1}_{solvent}$) and 57% (7 mol L$^{-1}_{solvent}$ / saturated). Once again, it is also observed that the three lower concentrations (1 mol L$^{-1}_{solvent}$, 3 mol L$^{-1}_{solvent}$ and 5 mol L$^{-1}_{solvent}$) give smooth profiles (consistent changes in charge capacity cycle on cycle), whereas at the highest concentration (7 mol L$^{-1}_{solvent}$ / saturated), the profile is more erratic and scattered (random changes in charge capacity cycle on cycle, less consistent).

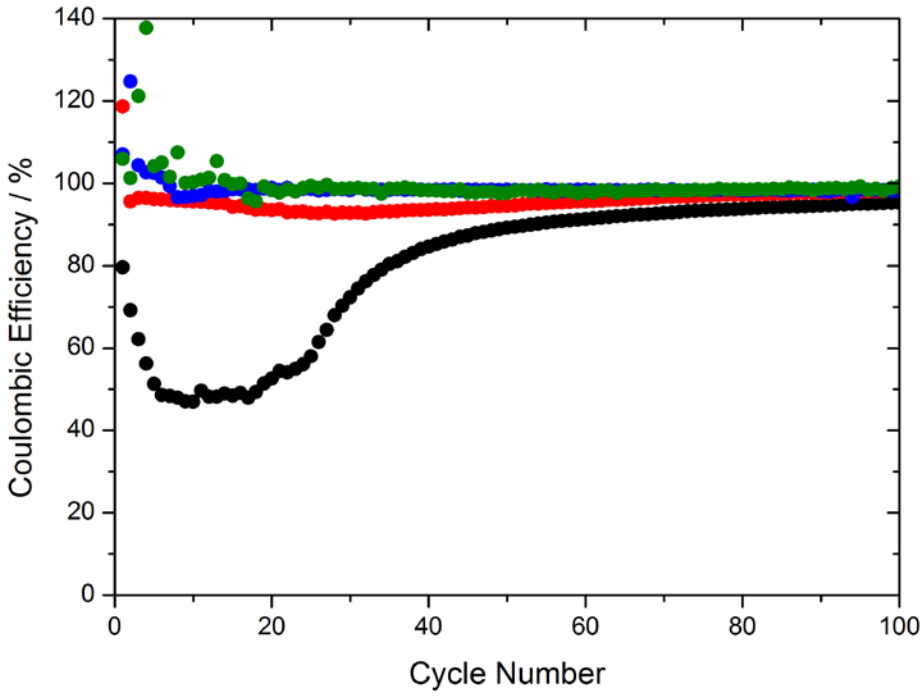


**Figure 4.3.3 –** Coulombic efficiencies of Swagelok cells at C/10 rate (i.e. $i$ = 167.2 mA $g_S^{-1}$) using different concentrations of LiTFSI in DOL electrolyte (1 •••, 3 •••, 5 ••• and 7 (saturated) ••• mol L$^{-1}_{solvent}$), two glass-fibre separators, a sulfur/acetylene black/PTFE composite positive electrode ($S_8$ = 22.5%, areal capacity = 5.2 – 5.8 mA h cm$^{-2}$, ∅ = 11 mm, A = 1 cm$^2$) and a lithium metal negative electrode. The cells were cycled between potential limits of 2.8 and 1.5 V. Capacities are normalised to the mass of sulfur ($g_S$) in the positive electrode and all cells were cycled at 25 °C.

It can be seen that on increasing the electrolyte salt concentration, the Coulombic efficiency is initially increased (Figure 4.3.3) e.g. on comparing the 10$^{th}$ cycles: 47% (1 mol $L^{-1}_{solvent}$), 96% (3 mol $L^{-1}_{solvent}$), 97% (5 mol $L^{-1}_{solvent}$) and 100% (7 mol $L^{-1}_{solvent}$ / saturated). However, it should be noted that after 100 cycles the Coulombic efficiencies of all concentrations are similar: 95% (1 mol $L^{-1}_{solvent}$), 98% (3 mol $L^{-1}_{solvent}$), 98% (5 mol $L^{-1}_{solvent}$) and 99% (7 mol $L^{-1}_{solvent}$ / saturated). This means that apart from the lowest concentration of 1 mol $L^{-1}_{solvent}$ LiTFSI, all the concentrations gave initial Coulombic efficiencies above 95%. This indicates that using concentrated LiTFSI (3 mol $L^{-1}_{solvent}$ and above) can aid in improving Coulombic efficiency. At low salt concentrations, the high polysulfide solubility and low viscosity leads to enhanced polysulfide shuttling. This leads to charge capacities that are much larger than the respective discharge capacities, giving poor Coulombic efficiency. During charging, the polysulfides are electrochemically oxidised at the positive electrode, increasing the concentration of high-order polysulfide species. Due to the high solubility of the polysulfides at low electrolyte salt concentrations, the polysulfide species can reach high concentrations and the low viscosity means the polysulfides can quickly diffuse away from the positive electrode towards the lithium negative electrode. At the lithium negative electrode, the polysulfides are chemically reduced to low-order polysulfides and as the concentration of these polysulfides increases, they begin to diffuse back to the positive electrode where they are either electrochemically re-oxidised at the electrode surface, or react directly with sulfur, which itself needs to be re-oxidised electrochemically. This can be thought of like an internal short-circuit, which ultimately degrades the battery over time.

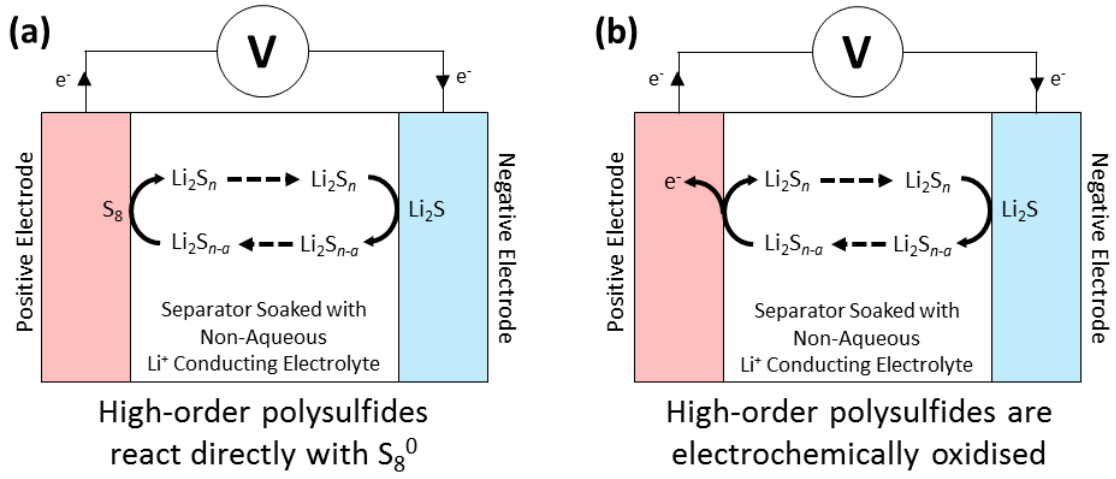


**Figure 4.3.4 –** During charge, the polysulfides are able to shuttle between the two electrodes. After the high-order polysulfides are chemically reduced at the negative electrode, the polysulfides diffuse back to the positive electrode, where they can (a) chemically react with sulfur or (b) be electrochemically re-oxidised.

The effect of polysulfide shuttling could be analysed further by cycling the cells using different C-rates and should be considered in future work. It is expected that cycling the cells at higher C-rates would reduce the effect of polysulfide shuttling since there would be less time for the polysulfides to diffuse from one electrode to the other, which would subsequently reduce charge capacity and improve the Coulombic efficiency. On the contrary, cycling the cells at lower C-rates would increase the effect of shuttling since there would be more time for the polysulfides to diffuse from one electrode to the other, which would subsequently increase charge capacity and reduce the Coulombic efficiency.

Furthermore, it should be noted that for some of the initial cycles (first 20 cycles, Figure 4.3.3) the Coulombic efficiency exceeds 100%, which indicates that the measured discharge capacity is larger than its respective charge capacity. A possible explanation includes the consumption of active material during discharge *via* the direct reaction of the polysulfides with the lithium metal negative electrode. Another possible reaction could be electrolyte degradation (reduction) at the positive electrode surface during discharge, which would artificially improve the discharge capacity above its corresponding charge capacity.

To investigate the effects of changing the electrolyte salt concentration further, more electrolyte solutions were prepared, varying the LiTFSI concentration in DOL. These solutions have then been analysed thoroughly, determining physico-chemical properties such as density, viscosity, conductivity, phase transition temperatures and polysulfide solubility. Furthermore, their cycling performance in coin cells has been tested and post-mortem analyses has been performed on the lithium negative electrode to give an insight into the cause of cell death.

### 4.3.2 – Density

Various concentrations of LiTFSI in DOL electrolyte were prepared (0.2 M, 0.5 M, 1 M, 1.5 M, 2 M, 2.5 M and 3 M). It should be noted that from this section onwards (Sections 4.3.2 – 4.3.9), true molarity (M or mol $L^{-1}_{electrolyte}$) is used and each solution was made using a volumetric flask. Through measuring the mass of each prepared LiTFSI in DOL electrolyte, it was possible to determine the density (Figure 4.3.5).

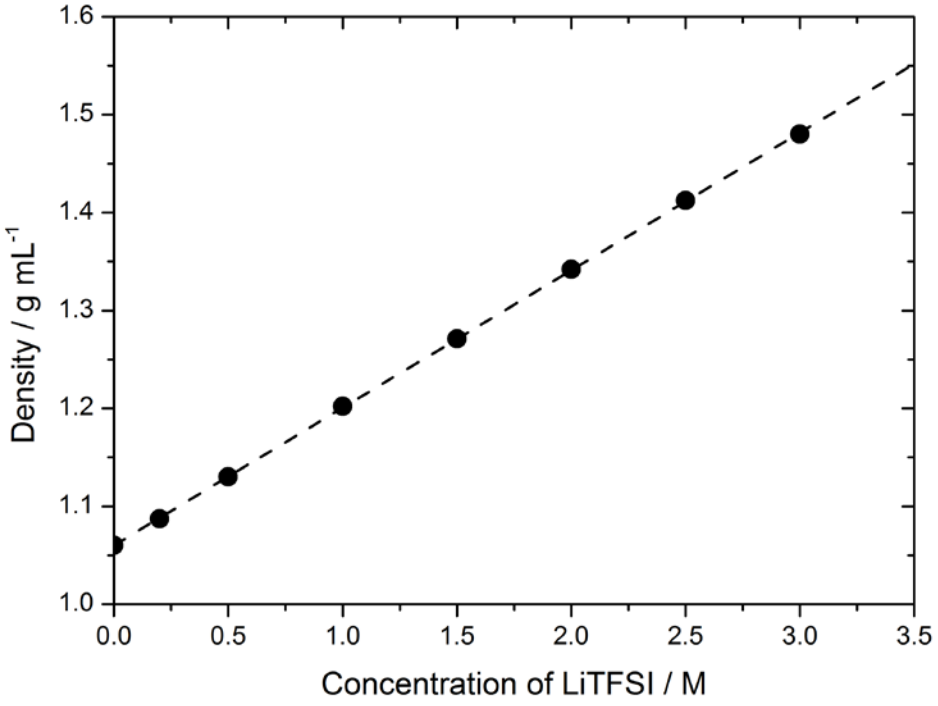


**Figure 4.3.5 –** Densities of LiTFSI in DOL, where the slope of the gradient is 0.14 g $mL^{-1}$ $M^{-1}$ and the $R^2$ value is 1.

Using the data presented in Figure 4.3.5 and Equation 4.3.1, it was possible to determine that the density of LiTFSI, when dissolved in DOL, is 2.07 g $mL^{-1}$. It should be noted that LiTFSI has a solid (powder) density of 1.334 g $mL^{-1}$, which indicates that the density of LiTFSI increases on dissolution in DOL by approximately 35%.

$$\text{mass}_{\text{electrolyte}} = \rho_{\text{electrolyte}}\, V_{\text{electrolyte}}$$

$$V_{\text{DOL}} = \frac{\text{mass}_{\text{DOL}}}{\rho_{\text{DOL}}} = \frac{\text{mass}_{\text{electrolyte}} - \text{mass}_{\text{LiTFSI}}}{\rho_{\text{DOL}}}$$

$$\rho_{\text{LITFSI}} = \frac{\text{mass}_{\text{LiTFSI}}}{V_{\text{LiTFSI}}} = \frac{\text{mass}_{\text{LiTFSI}}}{V_{\text{electrolyte}} - V_{\text{DOL}}}$$

**Equation 4.3.1 –** Determining the density of LiTFSI once dissolved in DOL using the measured density of the electrolyte solutions ($\rho_{\text{electrolyte}}$), where $\text{mass}_x$ = mass of component *x*, $\rho_x$ = density of component *x* and $V_x$ = volume of component *x*.

A saturated LiTFSI in DOL electrolyte solution was prepared by attempting to dissolve 4 M LiTFSI in DOL. To ensure that enough DOL was added, the correct mass of DOL (calculated using the slope in Figure 4.3.5) was added to the volumetric flask assuming that the LiTFSI would fully dissolved. The thick solution was then filtered and the density measured to be 1.47 g $mL^{-1}$, which is the same density as measured for the 3 M LiTFSI in DOL electrolyte. Since all of the LiTFSI dissolved in the prepared 3 M LiTFSI in DOL electrolyte, it is likely that the saturation concentration of LiTFSI in DOL is slightly over 3 M. The number of moles of DOL per mole of LiTFSI was calculated (Figure 4.3.6). It was determined that at a concentration of 3 M LiTFSI in DOL, which is close to the saturation concentration, there are approximately 3 molecules of DOL per molecule of LiTFSI.

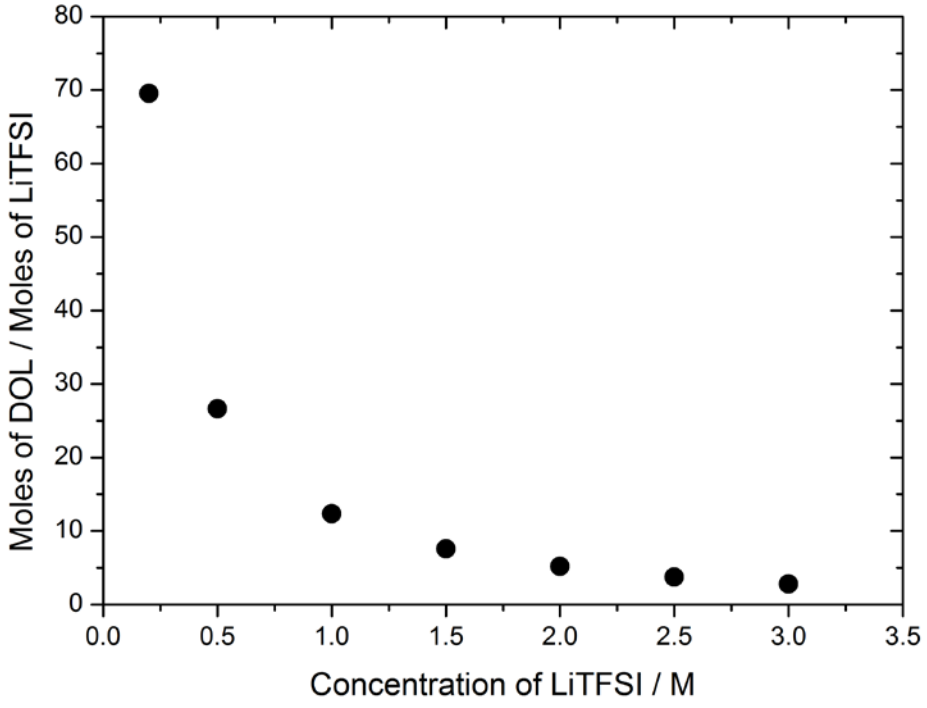


**Figure 4.3.6 –** Ratio of moles of DOL to moles of LiTFSI as a function of LiTFSI concentration

| LiTFSI concentration / M | Volume occupied by LiTFSI / % | Mass attributed to LiTFSI / % |
|---|---|---|
| 0.2 | 1 | 3 |
| 0.5 | 4 | 7 |
| 1.0 | 8 | 16 |
| 1.5 | 13 | 26 |
| 2.0 | 19 | 37 |
| 2.5 | 27 | **52** |
| 3.0 | 36 | **70** |

**Table 4.3.1 –** Determining which solutions prepared can be described as SIS electrolyte, using LiTFSI RMM = 287.09 g $mol^{-1}$, LiTFSI density = 2.07 g $mL^{-1}$ and DOL density = 1.06 g $mL^{-1}$. Only 2.5 M and 3.0 M can be described as SIS electrolytes as the LiTFSI accounts for over 50% of the mass.

In order to determine at which concentration the electrolyte becomes a SIS electrolyte will depend on the definition of SIS used. Suo *et al.* define a SIS electrolyte as one where either the salt accounts for over 50% of the electrolyte volume, the salt accounts for over 50% of the electrolyte mass, or both.[10] Using these definitions, only the 2.5 M and 3 M LiTFSI in DOL electrolyte solutions can be described as SIS electrolytes, since the LiTFSI accounts for over 50% of the mass in these electrolytes (Table 4.3.1). It should be noted that for none of the prepared electrolyte does the LiTFSI account for over 50% of the electrolyte volume and since 3 M LiTFSI in DOL is very close to saturation, it is assumed that this is not possible for the LiTFSI in DOL system.

### 4.3.3 – Dynamic (Shear) Viscosity

The dynamic (shear) viscosity ($\eta$) of DOL was measured using a rheometer over a large range of shear rates, in order to determine over which range the viscosity remained constant (Figure 4.3.7, see Section 2.3.5 on the theory of measuring viscosity using rheometry). It was observed that between shear rates of 10 – 200 $s^{-1}$, the viscosity of DOL remains constant (5.50 – 5.63 mPa s). Below shear rates of 10 $s^{-1}$, shear thinning was observed. The viscosity of each of the LiTFSI in DOL electrolyte solutions was then measured between shear rates of 8 – 50 $s^{-1}$ (Figure 4.3.8).

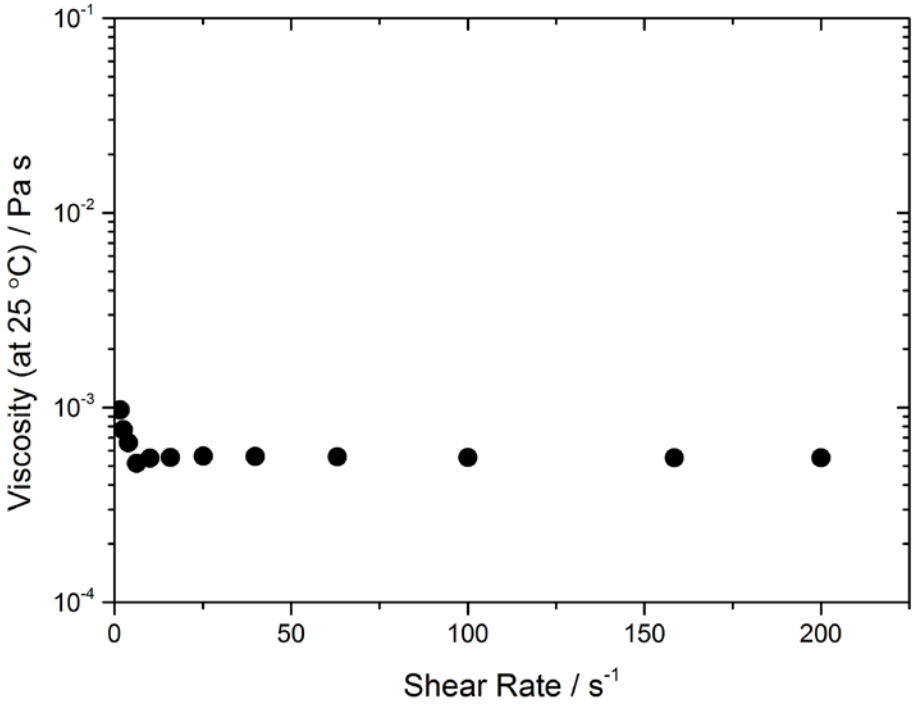


**Figure 4.3.7 –** Viscosity measurements of DOL recorded at 25 °C using a rheometer (Discovery HR-2, TA instruments) over a large range of shear rates (0 – 200 $s^{-1}$). Shear thinning is observed below 10 $s^{-1}$.

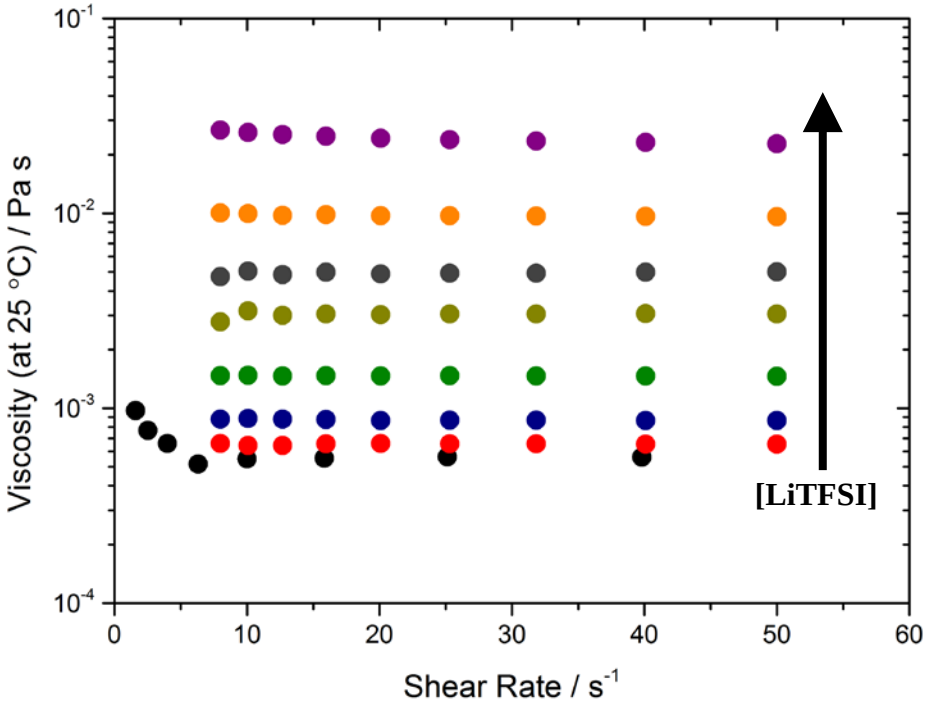


**Figure 4.3.8 –** Viscosity measurements of electrolytes possessing different LiTFSI in DOL concentrations (pure DOL – **black**, 0.2 M – **red**, 0.5 M – **blue**, 1.0 M – **green**, 1.5 M – **yellow**, 2.0 M – **grey**, 2.5 M – **orange**, 3 M – **purple**) recorded at 25 °C using a rheometer (Discovery HR-2, TA instruments) over a large range of shear rates (8 – 50 $s^{-1}$).

Similarly to that of DOL, it was observed that above shear rates of 10 $s^{-1}$, the viscosity of each electrolyte solution remained constant. The viscosity measurements recorded at shear rates of 40 $s^{-1}$ were plotted against LiTFSI concentration (Figures 4.3.9 and 4.3.10). It was observed that increasing the LiTFSI concentration caused the viscosity to increase exponentially. This result is consistent with data reported by Suo *et al.* for the LiTFSI in 1:1 DOL:DME electrolyte system, which also exhibits an exponential increase in viscosity with LiTFSI concentration.[10] Furthermore, the actual values of viscosity reported here for the LiTFSI in DOL system are very similar to those obtained by Suo *et al.* for the LiTFSI in DOL:DME system, e.g. the measured viscosity of 3 M LiTFSI in DOL was 23 mPa s (Figure 4.3.9) and the viscosity reported by Suo *et al.* for the ~3 M LiTFSI in 1:1 DOL:DME was ~21 mPa s. This indicates that the DME co-solvent does not heavily influence the viscosity of LiTFSI/DOL/DME mixtures.

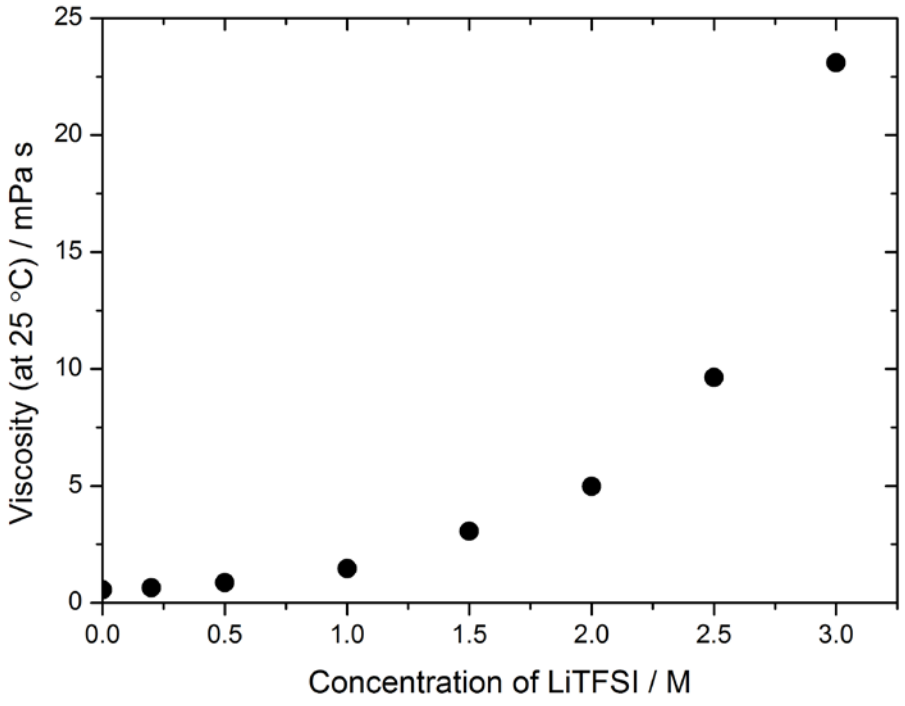


**Figure 4.3.9 –** Viscosity measurements of electrolytes possessing different LiTFSI in DOL concentrations recorded at 25 °C using a shear rate of 40 $s^{-1}$. Measurements were made using a rheometer (Discovery HR-2, TA instruments).

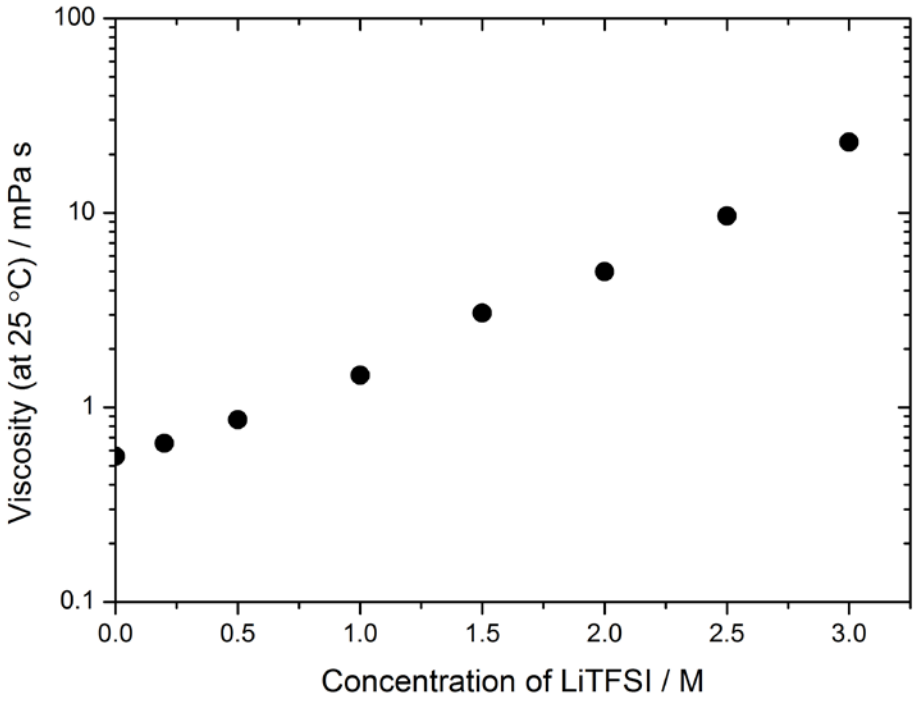


**Figure 4.3.10 –** Viscosity measurements plotted exponentially for electrolytes possessing different LiTFSI in DOL concentrations recorded at 25 °C using a shear rate of 40 $s^{-1}$. Measurements were made using a rheometer (Discovery HR-2, TA instruments).

### 4.3.4 – Conductivity

The conductivity of each of the LiTFSI in DOL electrolyte solutions was measured using a conductivity meter (Figure 4.3.11, see Section 2.3.4 on the theory of measuring conductivity). It is observed that the conductivity of the electrolyte solutions increases with increasing LiTFSI concentration initially until it peaks at 2 M (7.24 mS $cm^{-1}$). After this point, the conductivity then starts to decrease as the LiTFSI concentration increases. During this region (up to 2 M), the increased $Li^+$ ion concentration improves the electrolytic conductivity as there are more charge carriers whilst the change in viscosity is quite small (< 5 mPa $s^{-1}$) and hence the movement of the $Li^+$ ions is not greatly hindered. This is contradictory to that reported by Suo *et al.* during their SIS study using LiTFSI in 1:1 DOL:DME. They reported that the conductivity of the electrolyte decreased on increasing the LiTFSI concentration, despite measuring similar values of viscosity.[10] On increasing the LiTFSI concentration past 2 M, it is likely that the viscosity increases significantly enough (5 – 23 mPa $s^{-1}$) so that the effect of increased $Li^+$ ion concentration to improve the electrolytic conductivity is counteracted by the impeded movement of the $Li^+$ ions (see Section 4.3.3 for viscosity).

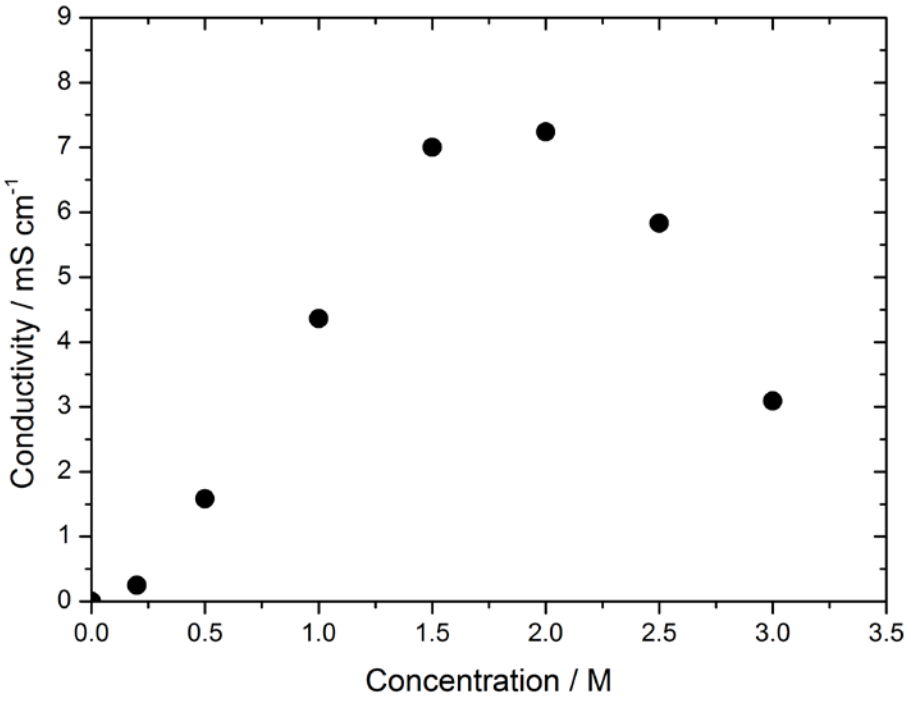


**Figure 4.3.11 –** Conductivity measurements of electrolytes with a range of LiTFSI concentrations in DOL using a Jenway bench conductivity meter (model 4510) at 25 °C. The following settings were used: Cell K = 1.040, COEFF = 0.000, REF T = 25 °C.

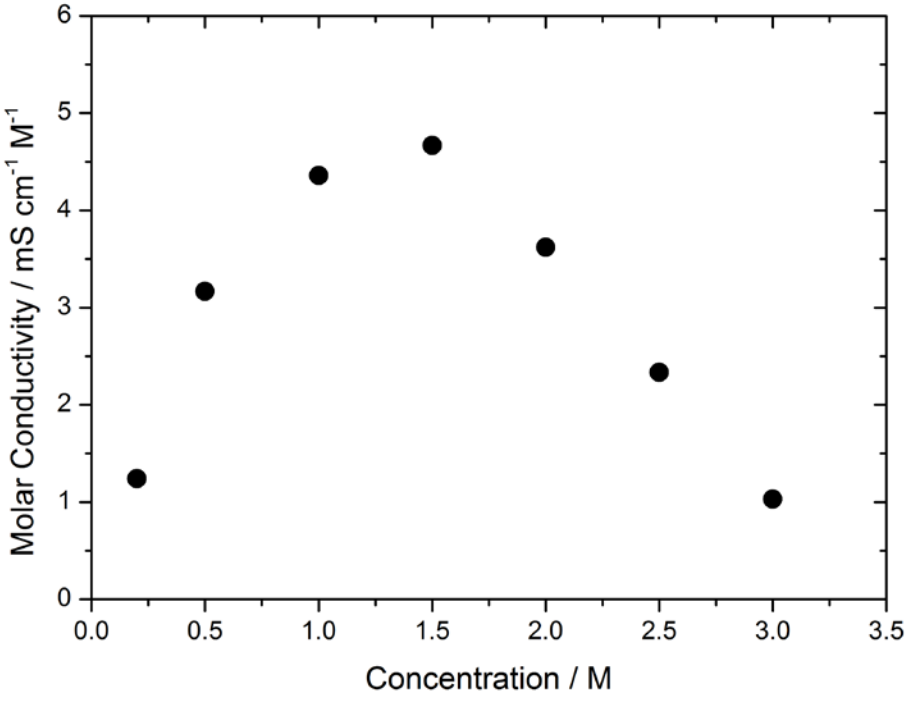


**Figure 4.3.12 –** Molar conductivity measurements of electrolytes with a range of LiTFSI concentrations in DOL. See Figure 4.3.11 for experimental details.

In order to analyse the effect of changing the LiTFSI concentration on conductivity further, the molar conductivity ($\Lambda$) was plotted against LiTFSI concentration (Figure 4.3.12). This enables the 'ionicity' of the ions produced on dissolution to be evaluated, where the 'degree of ionicity' can be defined as the availability of the ions to participate in the conduction processes.[18] It is observed that on increasing the LiTFSI concentration from 0.2 M to 1.5 M, the molar conductivity of the electrolyte increases, which indicates that the ions are becoming more available to participate in the conduction processes. This is not often the case, since molar conductivity commonly decreases with increasing electrolyte concentration due to the increase in viscosity, as observed by Suo *et al.*[10] In low salt concentrations, the $Li^+$ ions are coordinated with the DOL molecules and form large solvation shells, which hinder the mobility of the solvated $Li^+$ cations. It is possible that increasing the $Li^+$ ion concentration, reduces the size the $Li^+$ ion solvation shells, which improves the $Li^+$ ion mobility and enhances the ions conductivity. However, this is unlikely since the largest increase in conductivity is observed on increasing the LiTFSI concentration from 0.2 M (1.24 mS $cm^{-1}$ $M^{-1}$) to 0.5 M (3.17 mS $cm^{-1}$ $M^{-1}$) but the number of molecules DOL present per molecule of LiTFSI at 0.5 M still remains very high (DOL/LiTFSI > 26). Therefore, it is considered unlikely that the size of the $Li^+$ ion solvation shell will be significantly reduced in size given the large number of molecules of DOL that still remain. Another explanation could be a change in ion structure, where at low LiTFSI concentrations (e.g. 0.2 M), the formation of LiTFSI ion pairs is dominant but as the concentration increases, more charged triple ions form increasing the ions conductivity (Equation 4.3.2). This is known to occur in electrolytes where the solvent possesses a low dielectric constant ($\varepsilon < 10$) and DOL is known to possess a dielectric constant of 6.99.[19, 20] On increasing the LiTFSI concentration past 1.5 M, the molar conductivity of the electrolyte decreases linearly with LiTFSI concentration. As previously mentioned, this is likely an effect of the increased viscosity, impeding the movement of the dissolved ions.

$$3\ \mathrm{LiTFSI} \rightleftharpoons \mathrm{Li_2(TFSI)^+} + \mathrm{Li(TFSI)_2^-}$$

**Equation 4.3.2 –** The formation of charged triple ions from neutral ions pairs, which becomes more dominant as the LiTFSI concentration increases from 0.2 M to 3.0 M LiTFSI in DOL.

### 4.3.5 – Walden Plot: Analysis of Molar Conductivity and Fluidity

The Walden rule relates the equivalent (or molar) conductivity ($\Lambda$) of an ionically conducting liquid to its viscosity ($\eta$) and states that for an infinitely dilute electrolyte solution the product of molar conductivity and viscosity will be constant when measured at different temperatures (Equation 4.3.3).[21]

$$\Lambda \eta^{\gamma} = C$$

**Equation 4.3.3 –** The Walden rule, where $\Lambda$ = equivalent (or molar) conductivity, $\eta$ = viscosity, $\gamma$ = an exponent where $0 \leq \gamma \leq 1$ and C = the Walden product

For ideal electrolyte solutions, which contain large and weakly bound co-ordinating ions dissolved in solvents with non-specific ion-solvent interactions, such as dilute KCl in water, the exponent take the value of $\gamma = 1$.[18, 22, 23] However, for non-aqueous ionic systems containing ions that are mismatched in size, strongly co-ordinated and/or dissolved in solvents with specific ion-solvent interactions, the exponent takes a value of $0 \leq \gamma \leq 1$. In this study, exponent values of $0 \leq \gamma \leq 1$ would imply that the solutions are becoming more conductive at higher concentrations than expected and such deviations are often referred to as 'superionic' behaviour.[21]

The Walden rule is often used in its logarithmic form, where the molar conductivity is plotted against the fluidity, i.e. $\log_{10} \Lambda$ vs. $\log_{10} \eta^{-1}$ (Equation 4.3.4). This is known as a Walden plot and can be used to qualitatively evaluate the ionicity in ionic liquids, which describes the ions availability to participate in the conduction process.[18, 21] Usually, data representing an aqueous 0.01 M KCl solution is plotted as a useful calibration line, against which electrolytes (commonly ionic liquids) are compared. This calibration line represents the ideal behaviour, where the ions are completely dissociated and able to participate fully in the conductivity processes. For ionic liquids, the Walden plot is usually produced by plotting points of the measured molar conductivity and fluidity at different temperatures. However for this study, the temperature will be fixed at 25 °C and the data points plotted will represent the LiTFSI in DOL electrolyte system using different concentrations of LiTFSI (Figure 4.3.13).

$$\log_{10} \Lambda = \log_{10} C + \gamma \log_{10} \frac{1}{\eta}$$

**Equation 4.3.4 –** The Walden rule, where $\Lambda$ = equivalent (or molar) conductivity, $\eta$ = viscosity, $\gamma$ = an exponent where $0 \leq \gamma \leq 1$ and $C$ = the Walden constant.

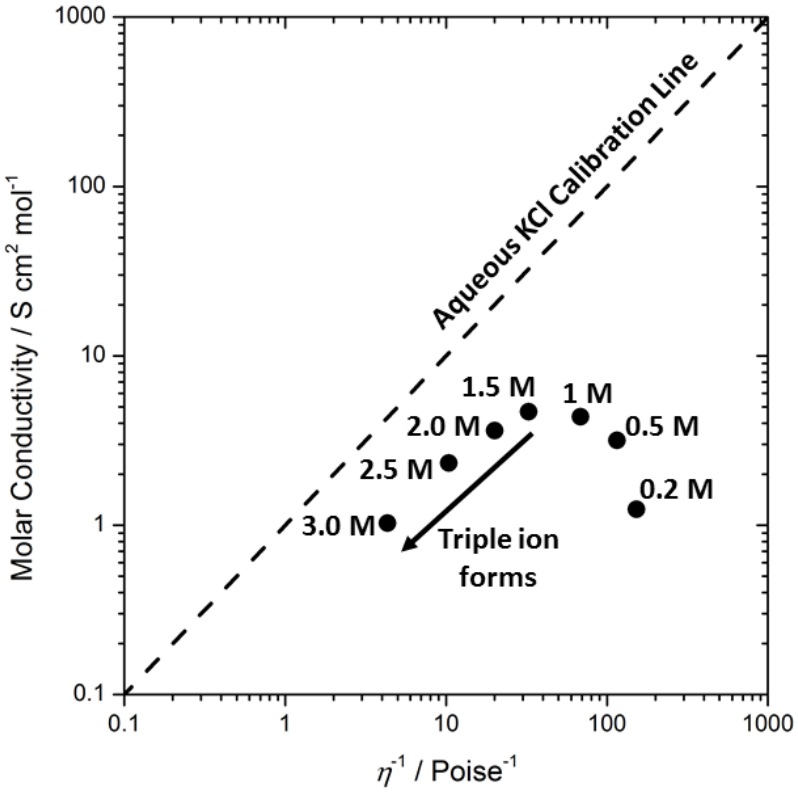


**Figure 4.3.13 –** Walden plot for all the different LiTFSI in DOL electrolyte concentrations, where the conductivity and viscosity for each concentration was measured at 25 °C. The dashed line indicates the ideal behaviour of dilute aqueous solutions ($\Lambda\eta^{\gamma} = C$, where exponent $\gamma = 1$) from which the Walden rule was originally formulated, usually 0.01 M KCl is used. Molar conductivity is plotted in units of S cm$^2$ mol$^{-1}$ (equivalent to mS cm$^{-1}$ M$^{-1}$ used in Section 4.3.4) and fluidity ($\eta^{-1}$) is plotted in Poise$^{-1}$ (10 Poise = Pa s).

Between LiTFSI concentrations of 0.2 M and 1.5 M, it is observed that the molar conductivity increases as the fluidity decreases, i.e. as the viscosity increases. This is counter-intuitive since increasing viscosity should reduce ion mobility, however it appears the $Li^+$ ions are becoming more mobile. Whilst molar conductivity and viscosity are not mutually exclusive, in general, it is observed that the ion mobility is decreased by viscosity. As discussed in Section 4.3.4, the increase in molar conductivity could be due to the size of the $Li^+$ solvation sphere decreasing, although it is more likely due a change in ion structure from neutral LiTFSI ion pairs to charged triple ions. The neutral ion pairs possess an overall charge of zero, whereas the charged triple ions possess an overall charge

of either + 1 or – 1 (Equation 4.3.2). Therefore, it is reasonable to suggest that the increased percentage of charged triple ions could improve the molar conductivity through increasing the effective charge of the ions, despite the increase in viscosity (reduced ion mobility). Between LiTFSI concentrations of 1.5 M and 3.0 M, a linear trend is observed between the molar conductivity and the fluidity, where the molar conductivity decreases as the fluidity decreases, i.e. as the viscosity increases. This linear behaviour indicates that the electrolytes within this LiTFSI concentration range are behaving like ionic liquids. Fitting an exponential trendline through these concentrations and applying the Walden rule gives an exponent value of $\gamma = 0.75$ (Equation 4.3.4, Figure 4.3.13). This exponent value falls within the range of $0 \leq \gamma \leq 1$, which indicates that highly concentrated LiTFSI in DOL electrolytes display 'superionic behaviour'. Again, this is likely caused by the preferential formation of the charged triple ions, rather than neutral ion pairs. Whilst it is possible to state that the neutral ions pairs will be composed of one $Li^+$ ion and one $TFSI^-$ ion, whereas the charged triple ions will be composed of either one $Li^+$ ion and two $TFSI^-$ ions or two $Li^+$ ions and one $TFSI^-$ ion (Equation 4.3.2), it would be difficult to propose further details of the ion structure without further work.

### 4.3.6 – Phase Transition Temperatures

In order to determine which phase transitions are present in the LiTFSI in DOL electrolytes, differential scanning calorimetry (DSC) was performed (Figures 4.3.14 and 4.3.15). DSC was performed on pure DOL, as well as electrolytes containing different concentrations of LiTFSI in DOL (0.5 M, 1 M, 1.5 M, 2 M, 2.5 M and 3 M). The 3 M LiTFSI in DOL electrolyte was measured twice in order to observe the glass transition temperature, although due to the quite different phase transitions observed in each measurement, both have been plotted (Figures 4.3.14 and 4.3.15) and compared (Figure 4.3.16). In order to observe the phase transitions more clearly, the traces were scaled according to their largest peaks (Figure 4.3.15).

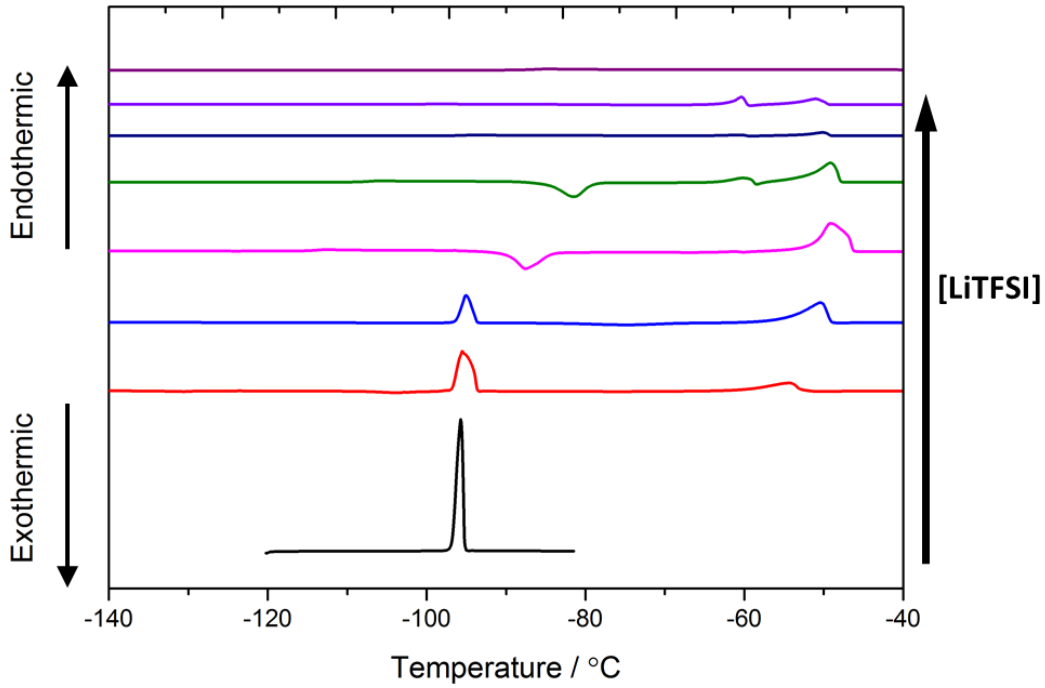


**Figure 4.3.14 –** Unscaled DSC measurements of DOL (**black**) and electrolytes possessing different concentrations of LiTFSI in DOL (0.5 M – **red**, 1 M – **blue**, 1.5 M – **pink**, 2 M – **green**, 2.5 M – **navy**, 3 M – **purple** and **maroon**). The measurements were recorded using approximately 10 mg of electrolyte and heated at 5 °C $min^{-1}$.

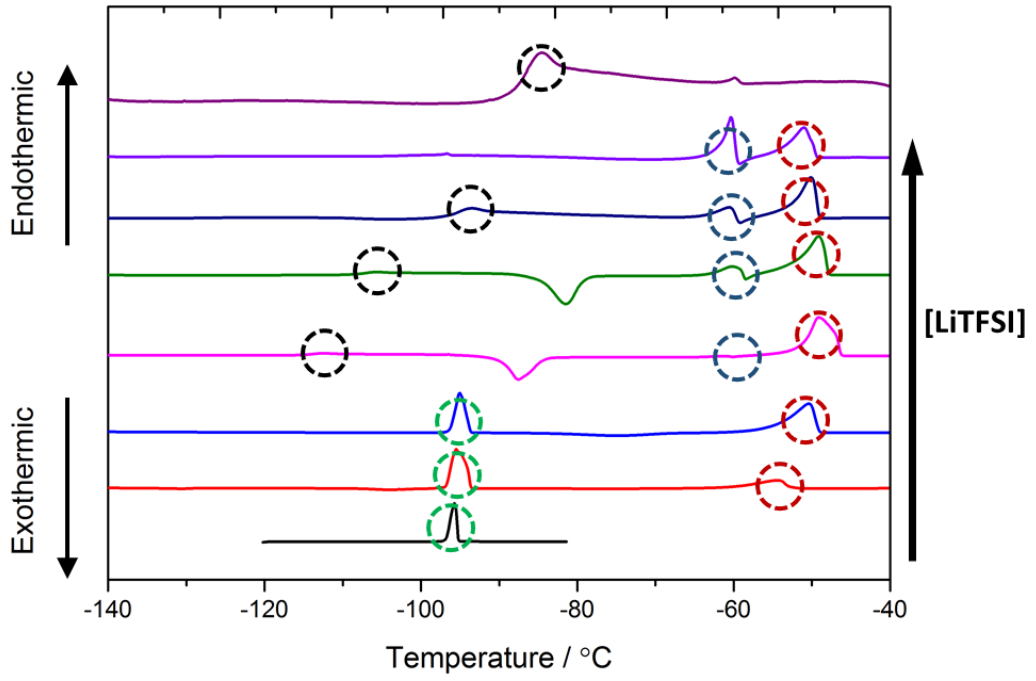


**Figure 4.3.15 –** Scaled DSC measurements of DOL (**black**) and electrolytes possessing different concentrations of LiTFSI in DOL (0.5 M – **red**, 1 M – **blue**, 1.5 M – **pink**, 2 M – **green**, 2.5 M – **navy**, 3 M – **purple** and **maroon**). The measurements were recorded using approximately 10 mg of electrolyte and heated at 5 °C $min^{-1}$.

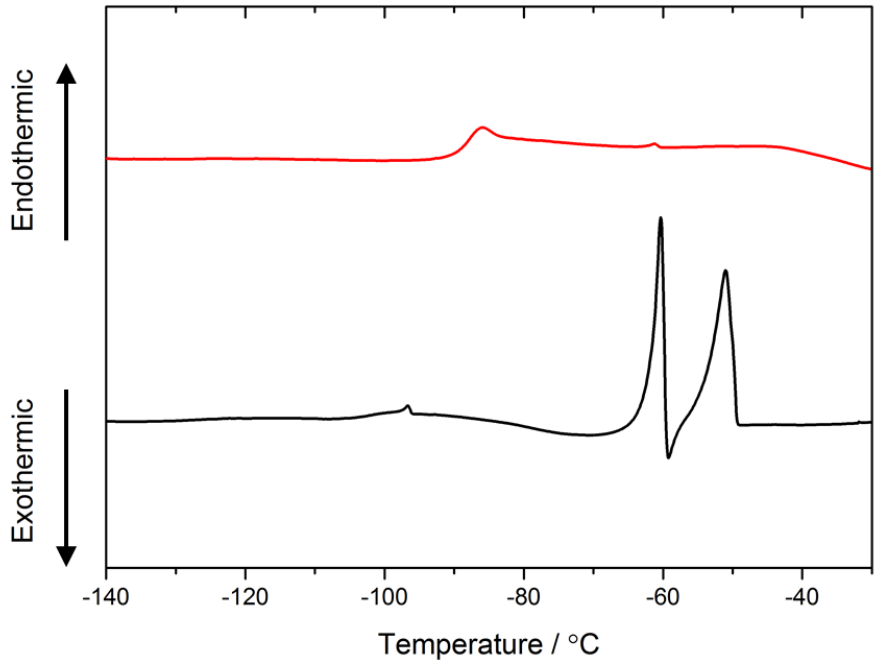


**Figure 4.3.16 –** Repeated DSC measurements of 3 M LiTFSI in DOL. The measurements were recorded using approximately 10 mg of electrolyte and heated at 5 °C $min^{-1}$. A glass transition peak is observed in the **red** trace and peaks associated with the crystallisation/melting of an LiTFSI solvate are observed in the **black** trace.

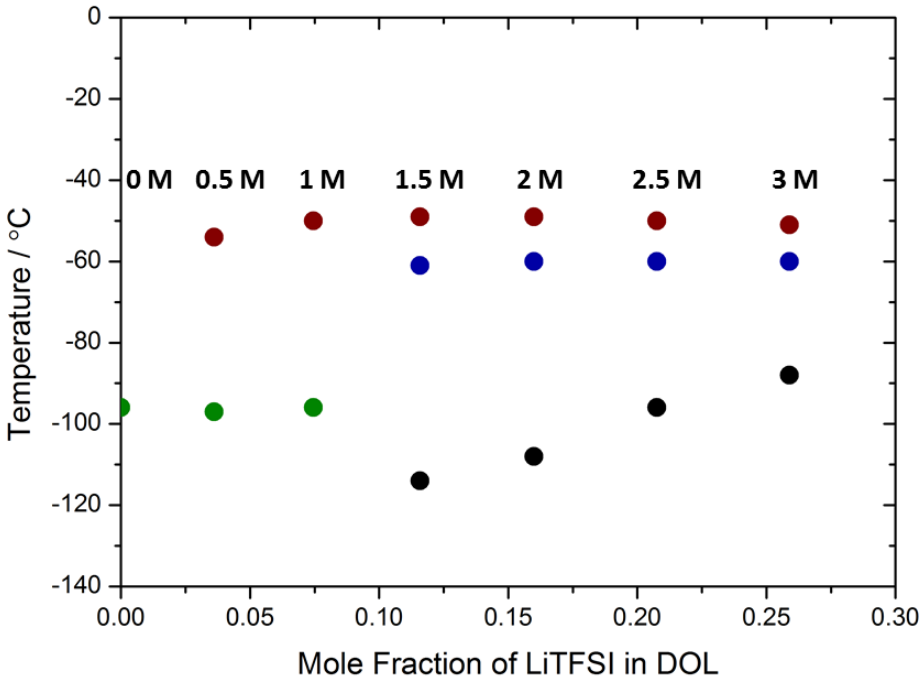


**Figure 4.3.17 –** Observed phase transitions in each of the electrolyte solutions plotted as a function of mole fraction of LiTFSI present and temperature at which the transition occurred. **Green** = DOL melting temperature, associated with uncoordinated molecules of DOL, **red** = LiTFSI solvate melting temperature, associated with neutral LiTFSI ion pairs, **blue** = LiTFSI solvate crystallisation/melting temperature, associated with charged triple ions and **black** = glass transition temperature.

It is observed that DOL has a melting point of -96 °C, which agrees with literature values (-97.22 °C, Figures 4.3.14, 4.3.15 and 4.3.17).[24] This peak remains present in the electrolytes with lower LiTFSI concentrations (0.5 M and 1 M, green circles) and is attributed to the melting of uncoordinated DOL. This indicates that up to a concentration 1 M LiTFSI in DOL, uncoordinated molecules of DOL remain present. On introducing LiTFSI into the DOL (0.5 M), an LiTFSI solvate melting peak is observed at -54 °C (red circles), which is present in all electrolytes containing LiTFSI, although its position varies slightly between -54 °C and -49 °C. This peak could be attributed to the neutral LiTFSI ion pairs, discussed in Sections 4.3.4 and 4.3.5. On increasing the concentration of LiTFSI, two other peaks are observed, another LiTFSI solvate crystallisation/melting peak (blue circles) and a glass transition peak (black circles). The LiTFSI solvate crystallisation/melting peaks (blue circles) occur consistently at -60 °C and these could be attributed to the charged triple ions, also discussed in Sections 4.3.4 and 4.3.5. It is observed that on increasing the LiTFSI concentration from 1.5 M to 3.0 M, the size of the triple ion peak (blue circles) increases with respect to the neutral ion pair peak (red circles). This indicates that the percentage of triple ions present compared to ion pairs is increasing, which agrees with the hypothesis presented to explain the increasing molar conductivity, discussed in Sections 4.3.4 and 4.3.5). However, without further study this hypothesis remains fairly speculative. The temperature at which the glass transition peak (black circles) occurs increases as the concentration of the LiTFSI increases, from -114 °C in 1.5 M LiTFSI in DOL to -88 °C in 3 M LiTFSI in DOL. This increase in the glass transition temperature with increasing LiTFSI concentration can be correlated with increasing viscosity. This is consistent with data reported by Suo *et al.* for the LiTFSI in 1:1 DOL:DME electrolyte system, which also exhibits a glass transition temperature at higher LiTFSI concentrations (3 mol $L^{-1}_{solvent}$ and above) that also increases with increasing LiTFSI concentration and viscosity.

### 4.3.7 – Polysulfide Solubility

In order to observe the effect of changing the LiTFSI concentration in DOL on the solubility of polysulfides, four polysulfide electrolyte solutions were prepared. For each electrolyte solution ([LiTFSI] = 0.5 M, 1 M, 2 M or 3 M), $Li_2S$ was added to the electrolyte followed by $S_8$ in a ratio that would give $Li_2S_6$ with a concentration 1 M [S], assuming full

dissolution. On addition of the $Li_2S$ to each electrolyte solution, it was observed that $Li_2S$ solid fell to the bottom of the vial, except for the 3 M LiTFSI in DOL electrolyte solution, in which the $Li_2S$ solid was initially suspended before falling to the bottom (Figure 4.3.18). This is likely due to the density of the 3 M LiTFSI in DOL electrolyte solution ($\rho_{3M}$ = 1.48 g $cm^{-3}$) becoming closer to the density of $Li_2S$ ($\rho_{Li2S}$ = 1.66 g $cm^{-3}$).

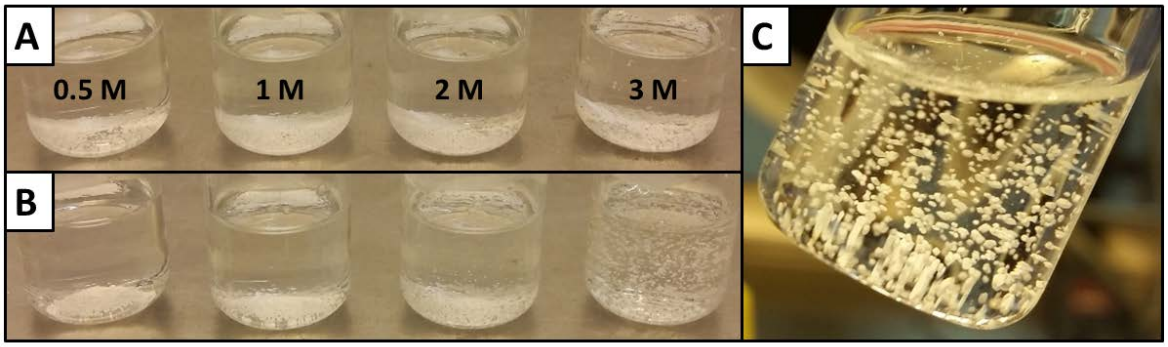


**Figure 4.3.18 –** Lithium sulfide (0.167 M) in electrolyte (LiTFSI in DOL) with the following concentrations of LiTFSI from left to right: 0.5 M, 1 M, 2 M and 3 M. The pictures show the settled lithium sulfide at the bottom of the vials (A), after agitating the vials it can be seen that the lithium sulfide returns to the bottom of the vials (B) except for in the 3 M LiTFSI in DOL electrolyte where it remains suspended (C).

On addition of the sulfur, polysulfides started to form (Figure 4.3.19a). The polysulfide electrolyte solutions were then heated to 60 °C for 5 days. After 1 day at 60 °C, it is observed that most of the solid sulfur and $Li_2S$ in the 0.5 M and 1 M LiTFSI in DOL polysulfide electrolyte solutions had dissolved, whereas solid was still present in both the 2 M and 3 M solutions (Figure 4.3.19b). However, after 5 days at 60 °C, it was observed that all of the solid sulfur and $Li_2S$ in the 0.5 M, 1 M and 2 M LiTFSI in DOL polysulfide electrolyte solutions had dissolved, whereas solid still remained in the 3 M solution (Figure 4.3.19c). It is expected that as the concentration of LiTFSI increases in the electrolyte, the solubility of the polysulfides should decrease due to the 'common-ion effect'. Therefore, the presence of solid remaining in the most concentrated electrolyte solution (3 M LiTFSI in DOL) is expected. However, since the concentration of polysulfides prepared is relatively low (only 1 M [S]), it would appear that the polysulfide solubility limits for these electrolytes ([LiTFSI] = 0.5 M, 1 M and 2 M) have not been reached and hence all of the solid has dissolved. It is observed that the polysulfides dissolved quicker in the 0.5 M and 1 M LiTFSI in DOL electrolytes than in the 2 M LiTFSI in DOL electrolyte, which is likely due to the increased viscosity of the 2 M solution. It should also be noted that after

dissolution of the polysulfide species, the 0.5 M LiTFSI in DOL polysulfide electrolyte solution became abnormally viscous, with a similar consistency to honey, whereas all of the other solutions ([LiTFSI] = 1 M, 2 M and 3 M) were all relatively fluid. This was particularly notable when the polysulfide electrolyte solutions were inverted after being left to sit for an extended period of time (Figure 4.3.20). This could be a co-ordination effect between the polysulfide species and LiTFSI molecules, which under these specific experimental conditions exhibits unusually high viscosity, although this experiment would need to be repeated to validate this.

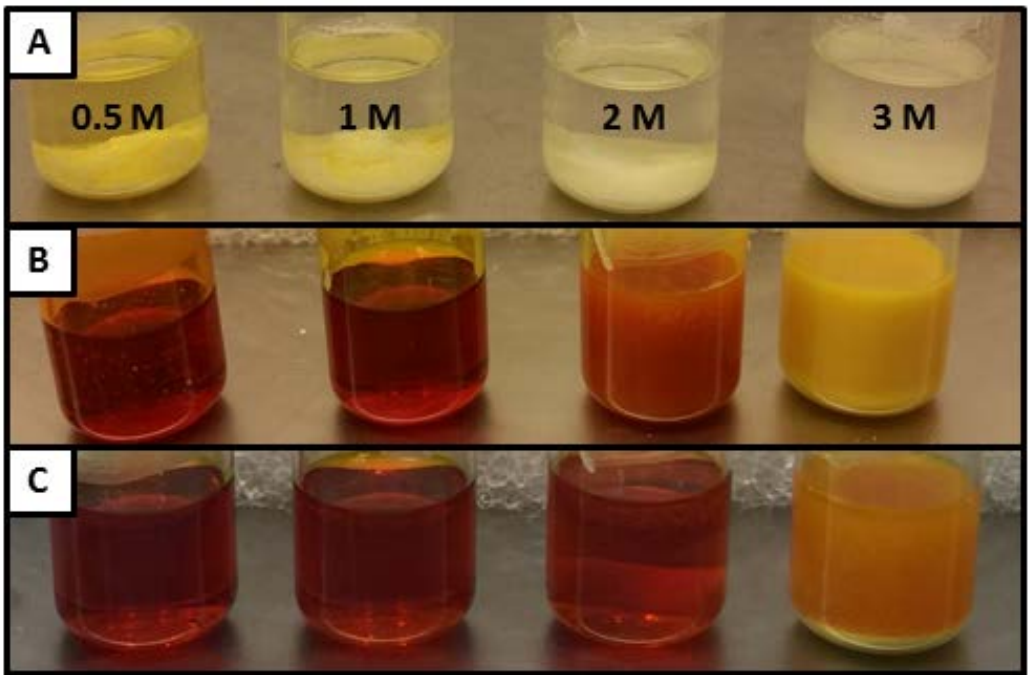


**Figure 4.3.19 –** $Li_2S_6$ (1 M [S]) in electrolyte (LiTFSI in DOL) with the following concentrations of LiTFSI from left to right: 0.5 M, 1 M, 2 M and 3 M, (A) directly after the addition of sulfur to the lithium sulfide, (B) after 1 day at 60 °C and (C) after 5 days at 60 °C and 2 days at room temperature. It should be noted that stir bars were not used for the 0.5 M and 1 M LiTFSI in DOL polysulfide electrolyte solutions, whereas stir bars were used for the 2 M and 3 M LiTFSI in DOL polysulfide electrolyte solutions in order to mix the solids.

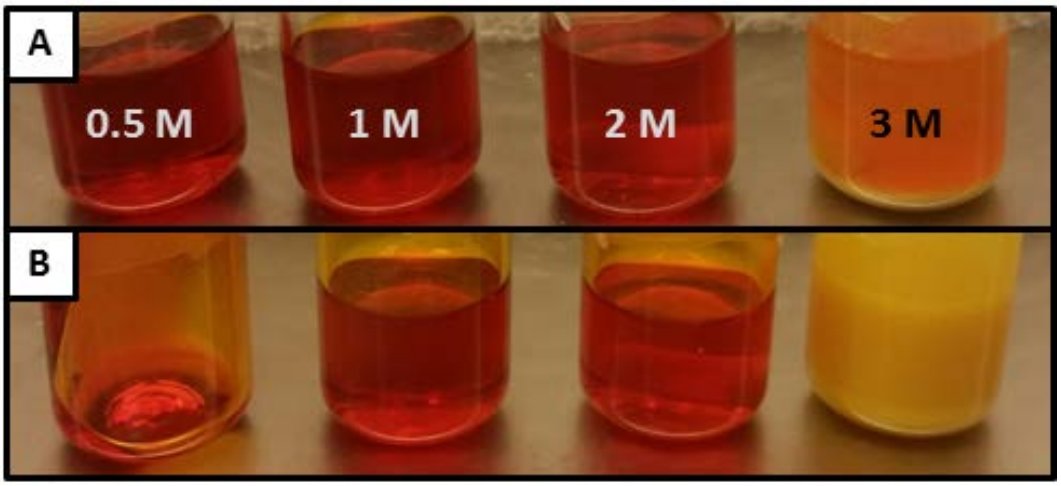


**Figure 4.3.20 –** $Li_2S_6$ (1 M [S]) in electrolyte (LiTFSI in DOL) with the following concentrations of LiTFSI from left to right: 0.5 M, 1 M, 2 M and 3 M, after 5 days at 60 °C and 2 days at room temperature (A) before inverting and (B) shortly after inverting.

### 4.3.8 – Galvanostatic Cycling

Coin cells were prepared, each using an electrolyte with a different concentration of the LiTFSI in DOL. The cells were then cycled at C/10 rate during the first cycle, followed by C/5 rate during subsequent cycles (Figure 4.3.21).

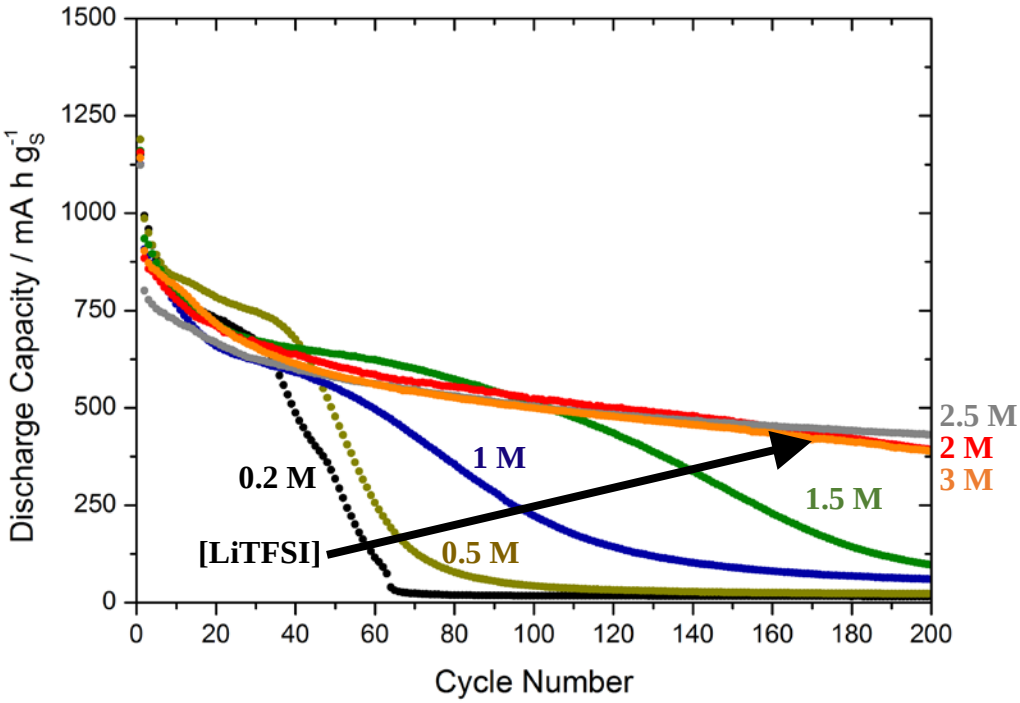


**Figure 4.3.21 –** Discharge capacities of eight coin cells, each containing different concentrations of LiTFSI in DOL electrolyte. First discharge at C/10 rate (i.e. $i$ = 167.2 mA $g_S^{-1}$) and thereafter cycled at C/5 rate (i.e. $i$ = 334.4 mA $g_S^{-1}$) using LiTFSI in DOL (••• 0.2 M, ••• 0.5 M, ••• 1 M, ••• 1.5 M, ••• 2 M, ••• 2.5 M and ••• 3 M) electrolyte, one glass-fibre separator, two PP separators, lithium metal negative electrode and Oxis positive electrode (2.5 mA h cm$^{-2}$, Ø = 13.9 mm). Cycling potential limits of 1.9 – 2.6 V were used, except for the 3 M LiTFSI in DOL cell (1.5 – 2.6 V). Capacities are normalised to the mass of sulfur ($g_S$) in the positive electrode.

It is clearly observed that on increasing the concentration of LiTFSI in DOL from 0.2 M to 2.0 M, the cells exhibit reduced capacity fading on cycling. This is consistent with the cycling data obtained using the Swagelok cell design (Section 4.3.1). As discussed previously, the reduced capacity fading at higher salt concentrations can be attributed to suppressed polysulfide shuttling caused by lower polysulfide solubility (Section 4.3.7) and higher electrolyte viscosity (Section 4.3.3). On increasing the LiTFSI in DOL concentration beyond 2 M does not show any improvement whilst cycling is limited to 200 cycles, all yielding similar discharge capacities over 385 mA h g$^{-1}$ after 200 cycles.

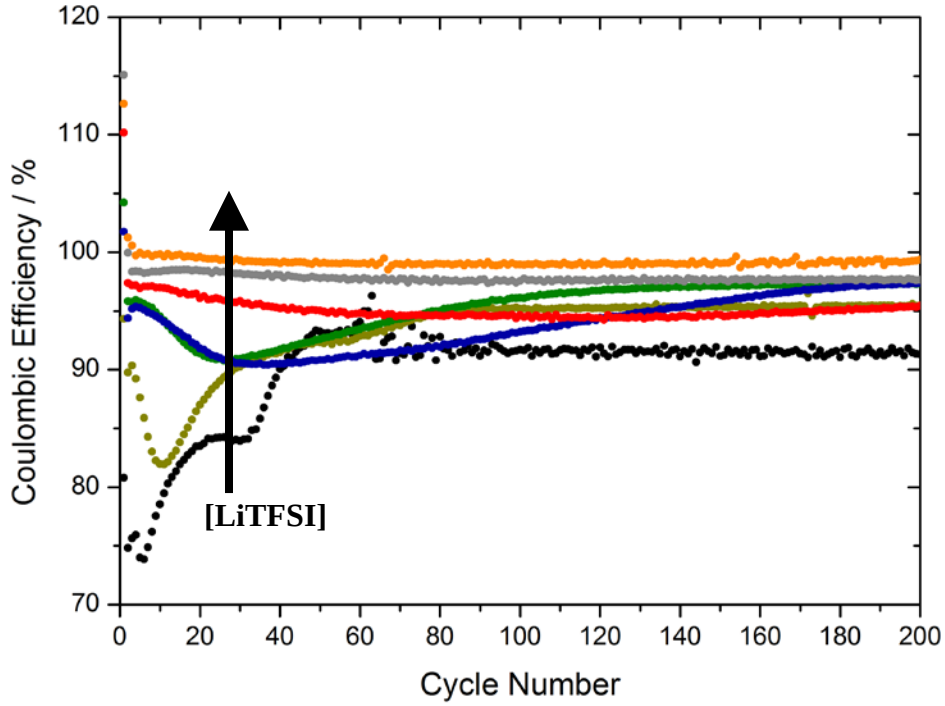


**Figure 4.3.22 –** Coulombic efficiency of eight coin cells, each containing different concentrations of LiTFSI in DOL electrolyte. First discharge at C/10 rate (i.e. $i$ = 167.2 mA $g_S^{-1}$) and thereafter cycled at C/5 rate (i.e. $i$ = 334.4 mA $g_S^{-1}$) using LiTFSI in DOL (••• 0.2 M, ••• 0.5 M, ••• 1 M, ••• 1.5 M, ••• 2 M, ••• 2.5 M and ••• 3 M) electrolyte, one glass-fibre separator, two PP separators, lithium metal negative electrode and Oxis positive electrode (2.5 mA h $cm^{-2}$, Ø = 13.9 mm). Cycling potential limits = 1.9 – 2.6 V, except for 3 M LiTFSI in DOL (1.5 – 2.6 V). Capacities are normalised to the mass of sulfur ($g_S$) in the positive electrode.

$$Coulombic\ Efficiency = \frac{N^{th}\ Discharge\ Capacity}{N^{th}\ Charge\ Capacity}\ x\ 100\%$$

**Equation 4.3.5 –** Coulombic efficiency where cells were prepared in the fully charged state and the charge/discharge cycle is defined as first discharge → first charge → second discharge → second charge → third discharge → third charge and so forth.

It is also observed that increasing the LiTFSI concentration improves the Coulombic efficiency (Figure 4.3.22 and Equation 4.3.5). Below 2 M, it is observed that the Coulombic efficiency initially decreases on cycling before starting to increase again after approximately 30 cycles. This initial decrease could be due to polysulfide shuttling and initial SEI formation on the lithium metal surface. For LiTFSI concentrations of 2 M and higher, the Coulombic efficiency remains fairly constant throughout cycling. The highest LiTFSI concentration, 3 M LiTFSI in DOL, displayed the best Coulombic efficiency of over 98% throughout.

Furthermore, it should be noted that the trends observed in these galvanostatic cycling results using coin cells (Section 4.3.8) are in agreement with the preliminary galvanostatic cycling data obtained previously using Swagelok cells (Section 4.3.1). In both sets of data, it has been shown that increasing the LiTFSI concentration reduces capacity fade on cycling (except at LiTFSI saturation) and increases the Coulombic efficiency. However, whilst the trends observed are consistent, the actual values obtained for discharge capacity, charge capacity and Coulombic efficiency differ. This can be attributed to several differences between the two experiments.

Firstly and most obviously, the two sets of cycling data were obtained using different test cell designs. As discussed in Chapter 3, using different test cell designs can have a significant effect on cycling performance even if the same internal cell components (i.e. electrodes, electrolyte and separator) are used. Secondly, different materials were used. In the preliminary experiments using Swagelok cells, a sulfur composite electrode pellet ($S_8$ = 22.5%, areal capacity = 5.2 – 5.8 mA h $cm^{-2}$, ∅ = 11 mm, A = 1 $cm^2$) was used as the positive electrode with two glass-fibre separators and an electrolyte loading of 23 μL $mA^{-1}$ $h^{-1}$. In these experiments using coin cells, Oxis electrodes (areal capacity = 2.5 mA h $cm^{-2}$, Ø = 13.9 mm, A = 1.5 $cm^2$) were used as the positive electrode with two polypropylene separators, one glass-fibre separator and an electrolyte loading of 33 μL $mA^{-1}$ $h^{-1}$. Lastly, different cycling conditions were used for each set of data. In the preliminary experiments using Swagelok cells, cycling was performed at C/10 rate (i.e. $i$ = 167.2 mA $g_S^{-1}$) for all cycles between potential limits of 2.8 and 1.5 V. In these experiments using coin cells, cycling was performed at C/10 (i.e. $i$ = 167.2 mA $g_S^{-1}$) for the first cycle only followed by C/5 rate (i.e. $i$ = 334.4 mA $g_S^{-1}$) for all subsequent cycles between potential limits of 2.6 and 1.9 V (except 3 M, between 2.6 and 1.5 V).

These differences between the two sets of galvanostatic cycling data (Sections 4.3.1 and 4.3.8) explain the variation observed for values of discharge capacity, charge capacity and Coulombic efficiency. However, despite these differences, the trends observed for both sets of data are consistent.

### 4.3.9 – Post-Mortem Analysis using Scanning Electron Microscopy (SEM)

After cycling the coin cells that each used an electrolyte containing a different LiTFSI concentration in DOL (Section 4.3.8), they were disassembled in an argon-filled glovebox and the lithium metal negative electrode was isolated. Then a scanning electron microscope was used to observe the surface of the cycled lithium metal negative electrodes (Figure 4.3.23). It was observed that on increasing the LiTFSI concentration in the electrolyte, the corrosion of the lithium metal negative electrode surface was reduced. At low LiTFSI concentrations (0.2 M and 0.5 M), the lithium surface appears rough and dendritic, however as the concentration of LiTFSI in the electrolyte increases, the lithium surface appears more smooth with fewer dendrites present.

It is expected that increasing the LiTFSI concentration will reduce the polysulfide solubility in the electrolyte. Lowering the concentration of polysulfides in the electrolyte coupled with increased viscosity will lead to diminished shuttling, reducing corrosion of the lithium metal by the polysulfide species. Moreover, the Chazalviel model reports that in non-aqueous liquid electrolyte, dendrites start to grow when the anion of the electrolyte salt is depleted close to the electrode surface, i.e. where plating occurs.[10, 25] Therefore, it is expected that for higher concentrations of the electrolyte salt, it is less likely that anion depletion will occur close to the electrode surface, making dendrite growth less favourable. Furthermore, Suo *et al.* have reported that due to the increased lithium-ion transference number (0.73) at high concentrations of LiTFSI, there is both a large amount of available lithium-ion flux as well as a raised lithium ion mass transfer rate between the electrolyte and lithium metal electrode, which enhances the uniformity of lithium deposition and dissolution in the charge/discharge processes.[10]

This theory nicely explains the observed effect that increasing the LiTFSI concentration of the electrolyte reduces the corrosion and dendrite formation on the lithium metal negative electrode surface. However, in order to properly test the effect of LiTFSI concentration on the degradation of the lithium metal negative electrode, the experiment should be modified so that the cells are all only partially discharged and charged over a specified number of cycles, which all cells will be capable of achieving. In this way, the amount of charge and discharge experienced by each cell will be the same.

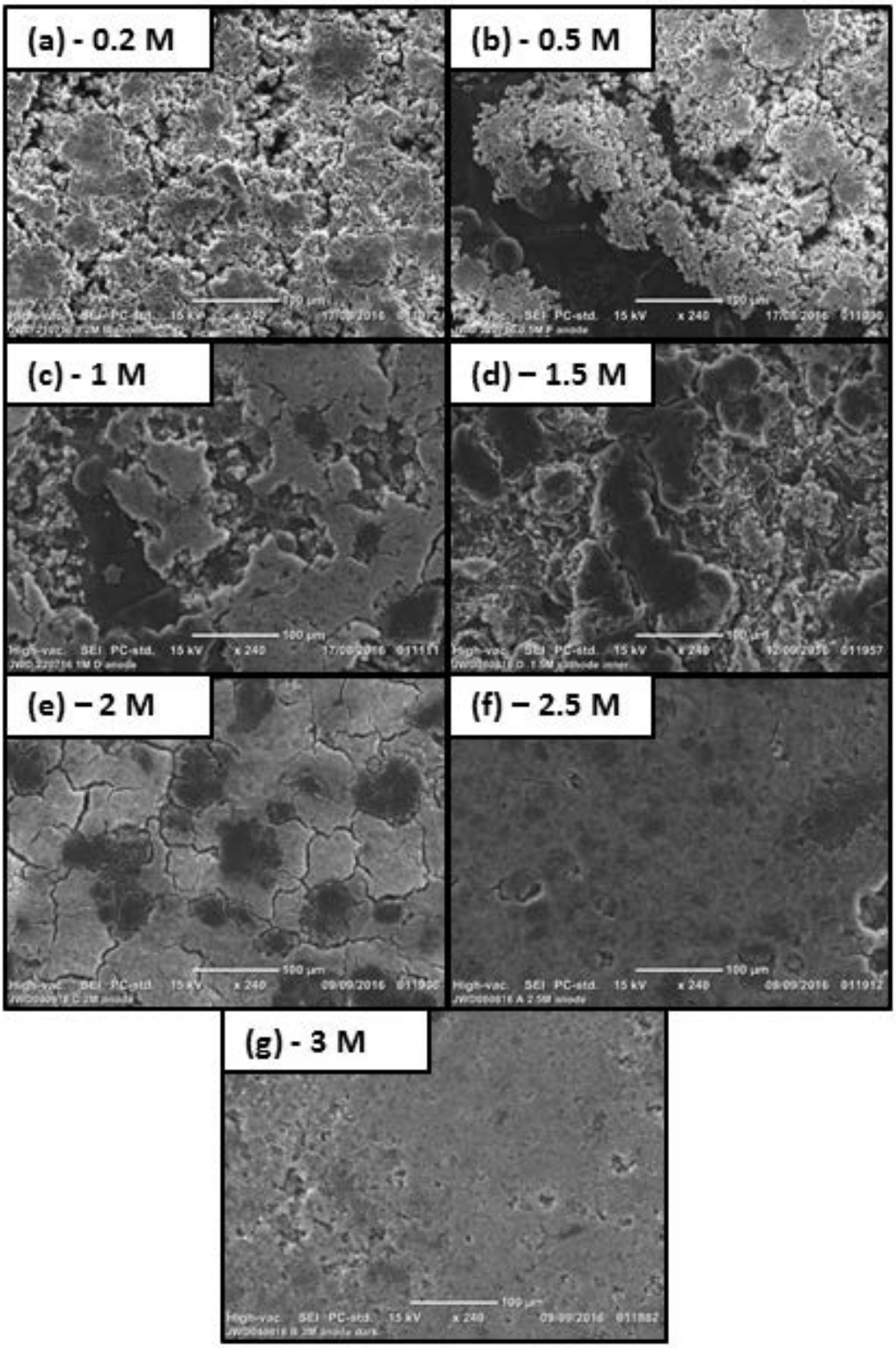


**Figure 4.3.23 –** Scanning electron microscopy (SEM) images of metallic lithium negative electrodes after cycling. The negative electrodes were obtained by disassembling the cycled coin cells inside of the glovebox, rinsing the electrodes with DOL (anhydrous) and allowing to dry before transferring inside a sealed argon-

filled bag to a dry room (dew point < -40 °C) where the SEM was located. Each of the SEM images has been taken using a magnification of x 240 and the scale bar on each image represents 100 μm. (**a**) 0.2 M LiTFSI in DOL electrolyte after 200 cycles, potential limits = 2.6 – 1.9 V, current = C/5 rate, total discharge capacity = 38,047 mA h $g^{-1}$, total charge capacity = 45,490 mA h $g^{-1}$. (**b**) 0.5 M LiTFSI in DOL electrolyte after 200 cycles, potential limits = 2.6 – 1.9 V, current = C/5 rate, total discharge capacity = 48,045 mA h $g^{-1}$, total charge capacity = 53,719 mA h $g^{-1}$. (**c**) 1 M LiTFSI in DOL electrolyte after 200 cycles, potential limits = 2.6 – 1.9 V, current = C/5 rate, total discharge capacity = 63,583 mA h $g^{-1}$, total charge capacity = 67,576 mA h $g^{-1}$. (**d**) 1.5 M LiTFSI in DOL electrolyte after 200 cycles, potential limits = 2.6 – 1.9 V, current = C/5 rate, total discharge capacity = 94,263 mA h $g^{-1}$, total charge capacity = 101,234 mA h $g^{-1}$. (**e**) 2 M LiTFSI in DOL electrolyte after 200 cycles, potential limits = 2.6 – 1.9 V, current = C/5 rate, total discharge capacity = 109,981 mA h $g^{-1}$, total charge capacity = 115,026 mA h $g^{-1}$. (**f**) 2.5 M LiTFSI in DOL electrolyte after 200 cycles, potential limits = 2.6 – 1.9 V, current = C/5 rate, total discharge capacity = 106,678 mA h $g^{-1}$, total charge capacity = 108,433 mA h $g^{-1}$. (**g**) 3 M LiTFSI in DOL electrolyte after 200 cycles, potential limits = 2.6 – 1.5 V, current = C/5 rate, total discharge capacity = 106,982 mA h $g^{-1}$, total charge capacity = 107,321 mA h $g^{-1}$.

## 4.4 – Conclusions and Further Work

During this chapter, LiTFSI in DOL electrolytes were prepared using a range of LiTFSI concentrations (0.2 M – 3.0 M) and the physicochemical properties of the electrolytes, as well as their cycling performances, were thoroughly analysed. It was determined that the saturation concentration of LiTFSI in DOL is slightly over 3 M and the solid (powder) density of LiTFSI (1.334 g $cm^{-3}$) increases to 2.07 g $cm^{-3}$ on dissolution in DOL (increase of 35%). Close to the saturation concentration of 3.0 M LiTFSI in DOL, it was calculated that there are approximately 3 molecules of DOL per molecules of LiTFSI. Additionally, it was determined that increasing the LiTFSI concentration from 0.2 M to 3.0 M causes the viscosity to increase exponentially. The conductivity of the electrolyte solutions increases with increasing LiTFSI concentration until 2 M (7.24 mS $cm^{-1}$), after which the conductivity starts to decrease as the LiTFSI concentration increases. The molar conductivity also increases with increasing the LiTFSI concentration until 1.5 M, despite the increase in viscosity. This is possibly due to enhanced $Li^+$ ion mobility caused by a reduced DOL solvation sphere surrounding the $Li^+$ ions as the LiTFSI concentration increases. However, a more likely explanation is a change in ion formation from neutral LiTFSI ion pairs to charged triple ions. After 1.5 M, the molar conductivity decreases linearly with LiTFSI concentration, likely caused by the increase in viscosity. Using the Walden plot, it was determined that highly concentrated LiTFSI in DOL electrolytes act like ionic liquids and possess 'superionic' behaviour, where the exponent $\gamma = 0.75$ ($\Lambda\eta^{\gamma} = C$).

Analysis of the phase transition temperatures using DSC showed that on increasing the concentration of LiTFSI in DOL, different LiTFSI phase transitions were present that could be associated the with different LiTFSI solvate structures. In every DSC trace containing LiTFSI, a peak was observed between -54 °C and -49 °C, which was attributed to the melting of an LiTFSI solvate, possibly in the form of neutral ion pairs. For electrolytes with LiTFSI concentrations of 1.5 M and higher, another peak was observed consistently at -60 °C, which was also attributed to the crystallisation/melting of an LiTFSI solvate, possibly in the form of charged triple ions. In addition to this, the size of the peak associated with charged triple ions increases with respect to the peak associated with neutral ion pairs, as LiTFSI concentration is increased. This indicates that the percentage of triple ions present compared to ion pairs is increasing, which agrees with the hypothesis

presented to explain the increasing molar conductivity. In pure DOL, a peak was observed at approximately -96 °C, which was attributed to the melting of DOL and this peak was also observed in the most dilute LiTFSI in DOL electrolytes (0.5 M and 1 M), indicating the presence of uncoordinated molecules of DOL. For electrolytes with LiTFSI concentrations of 1.5 M and higher, a peak attributed to a glass transition was observed. This peak increased with increasing LiTFSI concentration, from -114 °C in 1.5 M LiTFSI in DOL to -88 °C in 3 M LiTFSI in DOL, which agrees with the observations made by Suo *et al* and can be correlated with increasing viscosity.[10] On analysing the polysulfide solubility, it was determined that the polysulfides prepared in a ratio to give $Li_2S_6$ with a concentration of 1 M [S] fully dissolved in the LiTFSI in DOL electrolytes with LiTFSI concentrations of 2 M and lower. However, the polysulfides did not fully dissolve in the 3 M LiTFSI in DOL electrolyte, indicating lower polysulfide solubility. Unfortunately, the polysulfide concentration used was too small to evaluate their solubility any further.

Finally, it has been demonstrated that increasing the LiTFSI concentration in DOL improves the cycle life when used as an electrolyte in Li-S coin cells. Increasing the LiTFSI concentration from 0.2 M to 2 M enhances the cyclability from approximately 60 cycles, where cell death occurred, to at least 200 cycles. However, all electrolytes containing LiTFSI concentrations of 2 M and higher performed similarly when cycling was limited to 200 cycles, all achieving capacities over 385 mA h $g^{-1}$. The Coulombic efficiency was also improved on increasing the LiTFSI concentration, with the highest concentration (3 M LiTFSI in DOL) performing the best (over 98% throughout). On disassembling these cycled cells and performing SEM on the lithium metal negative electrodes, it was observed that increasing the LiTFSI concentration in the electrolyte resulted in smoother less degraded lithium surfaces.

In further work, electrolytes with much lower LiTFSI concentrations in DOL could be studied (e.g. 0.1 – 200 mM) as this would allow a better understanding of the ion structure within the electrolyte to be obtained. In addition to this, other electrolyte salts (e.g. LiFSI, $LiNO_3$, LiOTf or LiI) or solvents (DME, TEGDME) could be studied in order to try and find an optimised system for the Li-S battery. This project has been continued as the MESS project (Reference: EP/P019099/1), a collaboration between the University of Southampton and Oxis Energy Limited and is supported by Innovate UK and the EPSRC.

## 4.5 - References


1. M. Wild, L. O'Neill, T. Zhang, R. Purkayastha, G. Minton, M. Marinescu and G. J. Offer, *Energ. Environ. Sci.*, 2015, **8**, 3477-3494.

2. X. L. Ji and L. F. Nazar, *J. Mater. Chem.*, 2010, **20**, 9821-9826.

3. A. Manthiram, Y. Fu and Y.-S. Su, *Acc. Chem. Res.*, 2012, **46**, 1125-1134.

4. Y. Yang, G. Zheng and Y. Cui, *Chem. Soc. Rev.*, 2013, **42**, 3018-3032.

5. H.-L. Wu, L. A. Huff and A. A. Gewirth, *ACS Appl. Mater. Inter.*, 2014, **7**, 1709-1719.

6. M. Cuisinier, P. E. Cabelguen, B. D. Adams, A. Garsuch, M. Balasubramanian and L. F. Nazar, *Energ. Environ. Sci.*, 2014, **7**, 2697-2705.

7. S. S. Zhang, *Electrochim. Acta*, 2013, **97**, 226-230.

8. K. Ueno, J. W. Park, A. Yamazaki, T. Mandai, N. Tachikawa, K. Dokko and M. Watanabe, *J. Phys. Chem. C*, 2013, **117**, 20509-20516.

9. Q. Zou and Y.-C. Lu, *J. Phys. Chem. Lett.*, 2016, **7**, 1518-1525.

10. L. Suo, Y.-S. Hu, H. Li, M. Armand and L. Chen, *Nat. Commun.*, 2013, **4**, 1481.

11. E. S. Shin, K. Kim, S. H. Oh and W. I. Cho, *Chem. Commun.*, 2013, **49**, 2004-2006.

12. A. Manthiram, Y. Fu, S.-H. Chung, C. Zu and Y.-S. Su, *Chem. Rev.*, 2014, **114**, 11751-11787.

13. S. S. Zhang, *J. Power Sources*, 2013, **231**, 153-162.

14. Y.-X. Yin, S. Xin, Y.-G. Guo and L.-J. Wan, *Angew. Chem. Int. Ed.*, 2013, **52**, 13186-13200.

15. W. Li, H. Yao, K. Yan, G. Zheng, Z. Liang, Y. M. Chiang and Y. Cui, *Nat. Commun.*, 2015, **6**, 7436.

16. C. Barchasz, J.-C. Leprêtre, F. Alloin and S. Patoux, *J. Power Sources*, 2012, **199**, 322-330.

17. S. M. Al-Mahmoud, J. W. Dibden, J. R. Owen, G. Denuault and N. Garcia-Araez, *J. Power Sources*, 2016, **306**, 323-328.

18. D. R. MacFarlane, M. Forsyth, E. I. Izgorodina, A. P. Abbott, G. Annat and K. Fraser, *PCCP*, 2009, **11**, 4962-4967.

19. A. Venkateswaran, J. R. Easterfield and D. W. Davidson, *Can. J. Chem.*, 1967, **45**, 884-886.

20. M. N. Roy, T. Ray, M. Chandra Roy and B. Datta, *RSC Advances*, 2014, **4**, 62244-62254.

21. C. Austen Angell, Y. Ansari and Z. Zhao, *Faraday Discuss.*, 2012, **154**, 9-27.

22. C. Schreiner, S. Zugmann, R. Hartl and H. J. Gores, *Journal of Chemical & Engineering Data*, 2010, **55**, 1784-1788.

23. M. Yoshizawa, W. Xu and C. A. Angell, *J. Am. Chem. Soc.*, 2003, **125**, 15411-15419.

24. D. R. Lide, *CRC Handbook of Chemistry and Physics, 85th Edition*, Taylor & Francis, 2004.

25. J. N. Chazalviel, *Physical Review A*, 1990, **42**, 7355-7367.

# 5 – An Experimental Ternary Phase Diagram for the Li-S Battery

## 5.1 – Introduction

The Li-S battery discharge process begins with the dissolution of solid $S_8$ and ends with the precipitation of solid $Li_2S$. Likewise, the charge process beings with the dissolution of the solid $Li_2S$ and ends with the precipitation of solid $S_8$. In between the beginning and end of both processes several polysulfide species are formed, the identity of which are widely debated. It is known that whilst the solubility of $S_8$ and $Li_2S$ in most conventional Li-S battery electrolytes is relatively low, the solubility of the intermediate polysulfides is relatively high.[1-3] There are a wide range of studies presented in the literature, which focus on understanding the Li-S battery mechanism of discharge and charge and whilst these studies have improved our general knowledge of the Li-S battery discharge and charge processes, there is no universally accepted mechanism. This is in part due to inconsistency in the electrolyte systems and cell setups employed during these investigations, which will themselves affect the mechanistic pathway. In addition to this, analysing the lithium polysulfide species is notoriously difficult, since they are moisture sensitive, unstable as solids and able to com-/disproportionate, making them impossible to isolate as individual species.[4] Furthermore, these com-/disproportionation reactions cause the composition of the polysulfides to change on dilution.[5] Therefore, most spectroscopic techniques that are employed to directly identify the polysulfide species present will be unreliable. This is due to the lack of individual polysulfide references, which could be used to accurately assign peaks. Also most spectroscopic techniques require dilution of the sample, which will inherently change the composition of the polysulfides in solution. Finally, there are very few spectroscopic techniques, capable of detecting the polysulfide intermediates, as well as solid $S_8$ and solid $Li_2S$.

A ternary phase diagram representing the Li-S battery system would provide a key insight into the thermodynamic properties underpinning the discharge and charge processes. It would provide information on the precipitation and dissolution of solid $S_8$ and solid $Li_2S$, whilst also giving information on the polysulfide species dissolved in the electrolyte. Such information would include the concentration of the polysulfide species dissolved in the electrolyte and the average oxidation state of the polysulfides, which can be loosely compared to average polysulfide chain length. Currently, only one ternary phase

diagram has been reported in the literature to explain the Li-S battery discharge mechanism (see Chapter 1.5.3 for full details).[6] Whilst this proposed phase diagram offers a novel insight into the thermodynamics of the Li-S battery system and has been used effectively to explain experimental observations during discharge, it has been drawn qualitatively without the use of experimental data. An experimentally determined ternary phase diagram of the $S_8$-$Li_2S$-electrolyte system, using quantitative measurements would be a practical tool capable of predicting characteristics of the Li-S battery mechanisms of discharge and charge (see Chapter 1.5.4 for full details). Such characteristics include:

- Polysulfide concentration within the electrolyte
- Polysulfide speciation in terms of average oxidation state ($S^{m-}$)
- Dissolution and precipitation of solid $S_8$ and solid $Li_2S$
- Appearance of the discharge and charge equilibrium potential profiles

As mentioned previously, the ternary phase diagram is a purely thermodynamic treatment based on the equilibrium between the three components (solid $S_8$, solid $Li_2S$ and electrolyte) and as a result, there will be limitations. The kinetically controlled processes that occur within the Li-S battery discharge and charge processes will not be considered. Therefore, mechanistic features such as the observed differences between the discharge and charge processes, supersaturation, trapped active material and polysulfide shuttling are not predictable using this approach.[4] However, this model will give a useful insight into the underpinning thermodynamic properties of the Li-S battery system, which will provide an essential starting point to study the kinetics.

As discussed in Chapter 1.5, in a ternary phase diagram the three variables must sum to a constant and hence only two variables must be known to describe the ternary composition.[7] This means that two dimensions must be determined in order to construct complete $S_8$-$Li_2S$-electrolyte ternary phase diagram. In this report, two novel techniques have been developed to quantitatively determine:

1. The concentration of the total dissolved sulfur containing species, presented as dissolved atomic sulfur $[S]_T^{sol.}$
2. The average oxidation state of the dissolved sulfur containing species, presented as $S^{m-}$.

The concentration of the total dissolved sulfur containing species represents a good approximation for the total polysulfide concentration, due to the low solubilities of $S_8$ and $Li_2S$. Furthermore, knowing the total sulfur content of the electrolyte allows the quantity of the electrolyte present (variable 1) to be determined. Then, knowing that $Li_2S$ (i.e. $S^{2-}$) is solely responsible for the reduction of sulfur and determines the oxidation state ($S^{m-}$), the quantity of $Li_2S$ (variable 2) can be determined. When combined with the $[S]_T^{sol.}$, this enables the quantity of $S_8$ (variable 3) to be determined. The calculation will be described in greater detail throughout this chapter.

In order to simulate the conditions of the Li-S battery, lithium polysulfide electrolyte solutions were prepared using the standard procedure of adding solid $S_8$ and solid $Li_2S$ to an electrolyte, then stirring and heating to react. Once equilibrated, these polysulfide electrolyte solutions were analysed to determine the variables described above. As a starting point, the methods suggested by Rauh *et al.*, as well as Schwarzenbach and Fischer were consulted.[3, 8] It is important to note that any polysulfide electrolyte solution can be represented on the ternary phase diagram, since each of the solutions can be described as a mixture of the three components $S_8$, $Li_2S$ and electrolyte (Equation 5.1.1). This includes mixtures that contain both polysulfide electrolyte solution and solid precipitate (solid $S_8$ and/or solid $Li_2S$). In addition to this, any state of charge of the Li-S battery can be characterised by a given amount of the three components $S_8$, $Li_2S$ and electrolyte, which can also be represented on the ternary phase diagram.

$$Li_2S_{n\,(solv.)} \rightleftharpoons \frac{(n-1)}{8} S_{8\,(s)} + Li_2S_{\,(s)} + \text{electrolyte (e.g. LiTFSI in DOL)}$$

**Equation 5.1.1 –** An illustration that any polysulfide electrolyte solution can be presented as a mixture of the three components sulfur ($S_8$), lithium sulfide ($Li_2S$) and electrolyte (e.g. LiTFSI in DOL).

## 5.2 – Experimental Details

### 5.2.1 – Iodometric Titration

Iodine (0.032 g, 1.25 x $10^{-4}$ moles, 0.025 M) was dissolved in TEGDME (5 mL) and titrated against sodium thiosulfate solution (0.025 M). As the end point was almost reached, determined by the faintening of the yellow colour, a few drops of starch indicator solution were added. After the solution first appeared to go colourless, the volume of sodium thiosulfate solution added was recorded.

### 5.2.2 – Preparation of Lithium Polysulfide Electrolyte Solutions

In an argon-filled glove box, lithium sulfide (99.98%, Sigma-Aldrich) and sulfur (100 mesh, sublimed, Sigma-Aldrich, dried at 50 °C under vacuum over 72 h) were added into a vial in ratios to give the desired $Li_2S_n$ composition (Equation 5.2.1), followed by adding electrolyte (1 M LiTFSI in DOL). The solutions were then allowed to stir at 60°C for at least 96 h and then at room temperature for at least 48 h. The solutions were filtered using PTFE syringe filters (0.2 μm, dried) to remove any excess precipitate before analysis. The concentration of the prepared solutions is always noted in terms of atomic sulfur ($[S]_T^{mix.}$ / M) e.g. $Li_2S_8$ (1.25 M) gives an atomic sulfur concentration of 10 M, as $Li_2S_8$ contains 8 sulfur atoms (8 x 1.25 M = 10 M).

$$Li_2S + \frac{(n-1)}{8} S_8 \rightarrow Li_2S_n$$

**Equation 5.2.1 –** Preparation of $Li_2S_n$ where the average chain length *n* can be varied

### 5.2.3 – Gravimetric Analysis

In an argon filled glove box, known quantities of the lithium polysulfide electrolyte solutions (filtered) were placed into round bottom flasks (RBFs). These were sealed using rubber septa and taken outside of the glove box and into the fume cupboard. The rubber septa were used to ensure that the contents of the RBFs were kept under an inert argon atmosphere to prevent the loss of the polysulfides as hydrogen sulfide. Ammonium hydroxide (28-30%, Sigma-Aldrich) was then added to each RBF slowly using a needle

and syringe, followed by hydrogen peroxide (30% (w/w) in $H_2O$, Sigma-Aldrich) whilst stirring. Once the reactions had ceased, the reaction mixtures were heated to 40 °C for 1 h to remove any excess ammonia and hydrogen peroxide. The solutions were then diluted using water (deionised) before adding hydrochloric acid (HCl, 37%, Sigma-Aldrich) dropwise until the solution was slightly acidified (pH < 7). Excess barium nitrate (99.999 %, Sigma-Aldrich) was added and the solution stirred for 1 h. The mixtures were each poured into pre-weighed glass crucibles (porosity grade 4, 30 mL) and filtered under vacuum. Each barium sulfate retentate was then washed with water (deionised) and the glass crucibles were placed in the vacuum oven (80 °C) for ~24 h. Each of the glass crucibles was then removed, allowed to cool and weighed.

### 5.2.4 – UV-Vis Spectroscopic Redox Titration Measurements

UV-vis absorption measurements were made using an Ocean Optics DH-2000-BAL UV-vis NIR light source, which was switched on for at least 30 minutes before use in order to allow the spectrometer to reach operating temperature indicated by the stabilisation of the light output. Quartz cuvettes were used (path length = 1 cm), which had been modified to accommodate a screw cap lid. This allowed the cuvettes to be filled in an argon-filled glove box, sealed, transferred out of the glove box and measured on the UV-vis spectrometer, without contamination by moisture/oxygen. Ferrocenium tetrafluoroborate ($FcBF_4$, 95%, Sigma-Aldrich, dried) was dissolved in 1,3-dioxolane (DOL, anhydrous, Sigma-Aldrich) for at least 1 h to give a known concentration. The ferrocenium solutions were then filtered to remove small particles that raised the UV-vis baseline using a syringe filter (PTFE, 0.2 μm pore size). A UV-vis spectrum was obtained of the $FcBF_4$ in DOL stock solution. Then, aliquots (different volumes) of the polysulfide electrolyte solution under analysis were added to a known volume of the ferrocenium solution. The solutions were then shaken and a UV-vis spectrum was obtained for each.

### 5.2.5 – X-Ray Diffraction (XRD)

XRD was performed on a Bruker D2 PHASER using a 0.6 mm beam selection slit and a beam knife 1 mm above the sample. The setting used were: start $2\theta = 10°$, end $2\theta = 80°$, increment = 0.04°, dwell time = 1 s and files were saved as RAW V4 .txt.

## 5.3 – Results and Discussion

### 5.3.1 – Gravimetric Analysis: Determining the Concentration of Polysulfides

The methods undertaken by Rauh *et al.* to study the formation of lithium polysulfides in aprotic media were initially investigated.[3] They successfully studied the formation of lithium polysulfides ($Li_2S_n$) in several different aprotic organic solvents by reaction of $S_8$ with $Li_2S$ (Equation 5.3.1).

$$Li_2S + \frac{(n-1)}{8} S_8 \rightarrow Li_2S_n$$

**Equation 5.3.1 –** Preparation of $Li_2S_n$ where the average chain length *n* can be varied

To analyse the lithium polysulfide species, they used chemical analysis methods suggested by Schwarzenbach and Fischer.[3, 8] The concentration of the total dissolved sulfur $[S]_T^{sol.}$ was determined by oxidising the polysulfide species to sulfate ($SO_4^{2-}$) and then precipitating as barium sulfate ($BaSO_4$). They reportedly used a known quantity of $Li_2S_n$ solution and added ammonium hydroxide ($NH_4OH$) followed by hydrogen peroxide ($H_2O_2$). The basic $NH_4OH$ solution prevents the formation of hydrogen sulfide ($H_2S$) and the $H_2O_2$ oxidises the polysulfides ($S_n^{2-}$) to $SO_4^{2-}$. The solution was then heated to remove the excess $NH_3$ and $H_2O_2$, before making the solution up to 50 mL in a volumetric flask with water and a few drops of hydrochloric acid (HCl). Then a known quantity of the $SO_4^{2-}$ solution was diluted with methanol, the pH was adjusted to between 2.5 and 4 and finally, the solution was titrated against barium perchlorate ($Ba(ClO_4)_2$) in the presence of a thorin indicator. Thorin indicator is yellow but turns pink in the presence of barium ions ($Ba^{2+}$).[9] As the $Ba(ClO_4)_2$ is added, the $Ba^{2+}$ immediately reacts with the $SO_4^{2-}$ to form $BaSO_4$, which is practically insoluble in water (~ 2.5 μg $mL^{-1}$) and precipitates.[10] Therefore, the thorin indicator remains yellow, as no dissolved $Ba^{2+}$ remains in the presence of dissolved $SO_4^{2-}$. Once all of the $SO_4^{2-}$ is exhausted and all of the $BaSO_4$ has precipitated, any further addition of $Ba(ClO_4)_2$ results in dissolved $Ba^{2+}$ and the Thorin indicator turn pink, signalling the end point. This process has been summarised in Equation 5.3.2.

$$S_n^{2-}{}_{(aq)} \xrightarrow{[O]} n\ SO_4^{2-}{}_{(aq)} \xrightarrow{a\ Ba(ClO_4)_2} n\ BaSO_{4(s)} + (a-n)\ Ba^{2+}{}_{(aq)} + 2a\ ClO_4^-{}_{(aq)}$$

**Equation 5.3.2 –** Summarised procedure reported by Rauh *et al.* to determine the total sulfur content of the polysulfide electrolyte solutions. Thorin indicator is yellow but turns pink in the presence of $Ba^{2+}$ ions.

However, due to the high toxicity of thorin (an arsenic compound), a safer approach was desired. Due to the high molecular mass of $BaSO_4$ (233.38 g $mol^{-1}$) gravimetric analysis appeared to be a logical approach. This would enable the majority of steps in the aforementioned procedure to be utilised, except after removal of the $NH_3$ and $H_2O_2$ through heating, an excess of barium nitrate ($Ba(NO_3)_2$) could be added to the solution resulting in the precipitation of $BaSO_4$ (Equation 5.3.3, Figure 5.3.1).

$$S_n^{2-}{}_{(aq)} \xrightarrow{[O]} n\ SO_4^{2-}{}_{(aq)} \xrightarrow{a\ Ba(NO_3)_2} n\ BaSO_{4(s)} + (a-n)\ Ba^{2+}{}_{(aq)} + 2a\ NO_3^-{}_{(aq)}$$

**Equation 5.3.3 –** Proposed procedure of gravimetric analysis using $Ba(NO_3)_2$ to precipitate $SO_4^{2-}$ as $BaSO_4$, which can then be collected in a pre-weighed glass sintered crucible using filtration and weighed.

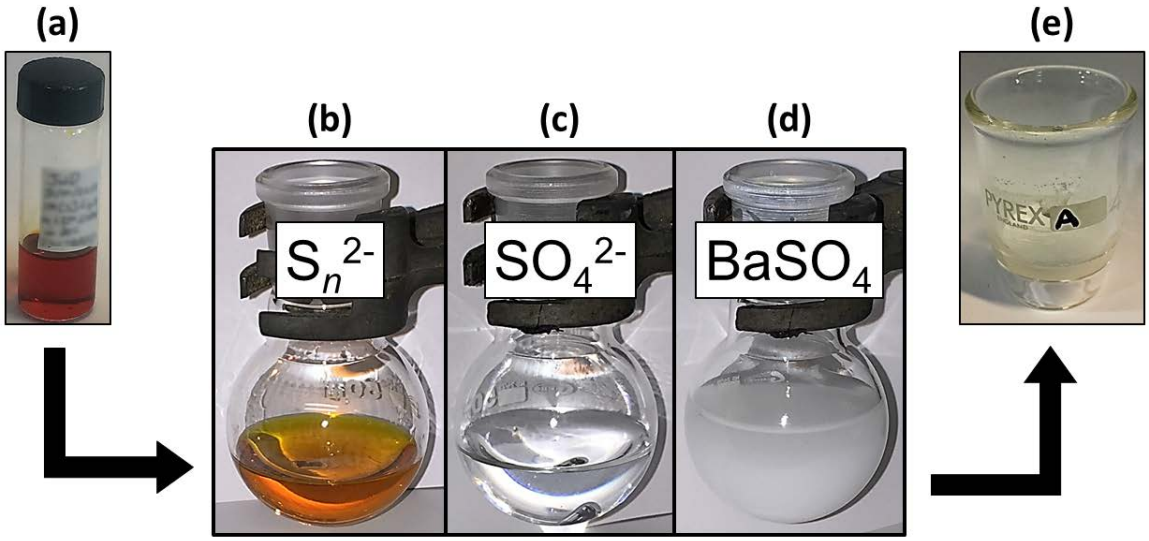


**Figure 5.3.1 –** The gravimetric analysis procedure, beginning with the filtered lithium polysulfide electrolyte solution (a), from which a known quantity is placed into a round bottom flask and $NH_4OH$ is added (b). It is observed that on addition of $NH_4OH$, the polysulfides dissolve into the $NH_4OH$ solution without reacting to form $H_2S$. Then $H_2O_2$ is added to oxidise the $S_n^{2-}$ into $SO_4^{2-}$, which is observed by a colour change from orange to colourless (c). After heating at 40 °C for 1 h, diluting with deionised water and acidifying using HCl, an excess of $Ba(NO_3)_2$ was added to precipitate $SO_4^{2-}$ as $BaSO_4$ (d). The $BaSO_4$ is observed as a white powder, which can then be collected in a pre-weighed glass sintered crucible using filtration and weighed to determine the mass of $BaSO_4$ (e).

The $BaSO_4$ could then be filtered using a pre-weighed glass sintered crucible (porosity grade 4, recommended for $BaSO_4$ collection), washed, dried and the crucible re-weighed in order to determine the mass of $BaSO_4$ obtained. Using this mass would enable the concentration of the total dissolved sulfur in the electrolyte $[S]_T^{sol.}$ to be calculated (Equation 5.3.4).

$$[S]_T^{sol.} = \frac{\text{mass}_{BaSO_4}}{\text{RMM}_{BaSO_4}\, V_{S_n^{2-}}}$$

**Equation 5.3.4 –** Calculating the total dissolved sulfur in the electrolyte $[S]_T^{sol.}$ using the mass of $BaSO_4$ determined from the gravimetric analysis ($\text{mass}_{BaSO_4}$), where $\text{RMM}_{BaSO_4}$ = 233.38 g mol$^{-1}$ and $V_{S_n^{2-}}$ = initial volume of polysulfide electrolyte solution analysed.

To validate this method a polysulfide electrolyte solution was prepared, where complete dissolution of the solid ($S_8$ and $Li_2S$) had occurred. For a polysulfide electrolyte solution where both solids completely dissolve, both the concentration of the total dissolved sulfur $[S]_T^{sol.}$ is known, as is the average oxidation state ($S^{m-}$, Equation 5.3.5). Therefore, by performing the developed gravimetric analysis method on the polysulfide electrolyte solution, it should be possible to obtain a value for the concentration of the total dissolved sulfur containing species $[S]_T^{sol.}$, which matches the known value.

$$Li_2S + \frac{(n-1)}{8} S_8 \rightarrow Li_2S_n \qquad [S]_T^{sol.} = n\ S \qquad S^{m-} = S^{(2/n)-}$$

**Equation 5.3.5 –** Preparation of $Li_2S_n$ where the average chain length $n$ can be varied

The polysulfide electrolyte solution prepared was 1 M $[S]_T^{mix.}$ $Li_2S_6$ dissolved in 1 M LiTFSI in DOL. As discussed above, due to complete dissolution of the solids ($S_8$ and $Li_2S$), the concentration of the total dissolved sulfur $[S]_T^{sol.}$ is known ($[S]_T^{sol.}$ = 1 M) as is the average oxidation state ($S^{m-} = S^{0.33-}$). The gravimetric analysis method was performed on this solution three times to obtain an understanding of the reproducibility of the procedure, as well as the accuracy (Table 5.3.1).

| Sample | $BaSO_4$ / g | $[S]_T^{sol.}$ / M |
|---|---|---|
| A | 0.240 | 1.03 |
| B | 0.239 | 1.02 |
| C | 0.243 | 1.04 |

**Table 5.3.1 –** Gravimetric analysis results on analysing three samples of 1 M $[S]_T^{mix.}$ $Li_2S_6$ dissolved in 1 M LiTFSI in DOL electrolyte. The volume of each polysulfide electrolyte solution analysed ($V_{S_n^{2-}}$) was 1 mL.

As it can be seen from Table 5.3.1, the concentration of the total dissolved sulfur $[S]_T^{sol.}$ was calculated to be 1.03 ± 0.02 M (error determined using descriptive statistics, 95% confidence level). This is close to the expected value of 1.00 M with a small range of error giving good precision, although the values obtained are all slightly too high indicating a small amount of inaccuracy (~ 3%). This extra mass could be due to an insoluble impurity. Using powder x-ray diffraction (XRD) the product obtained was confirmed to be $BaSO_4$ and no impurity peaks were identified.[11]

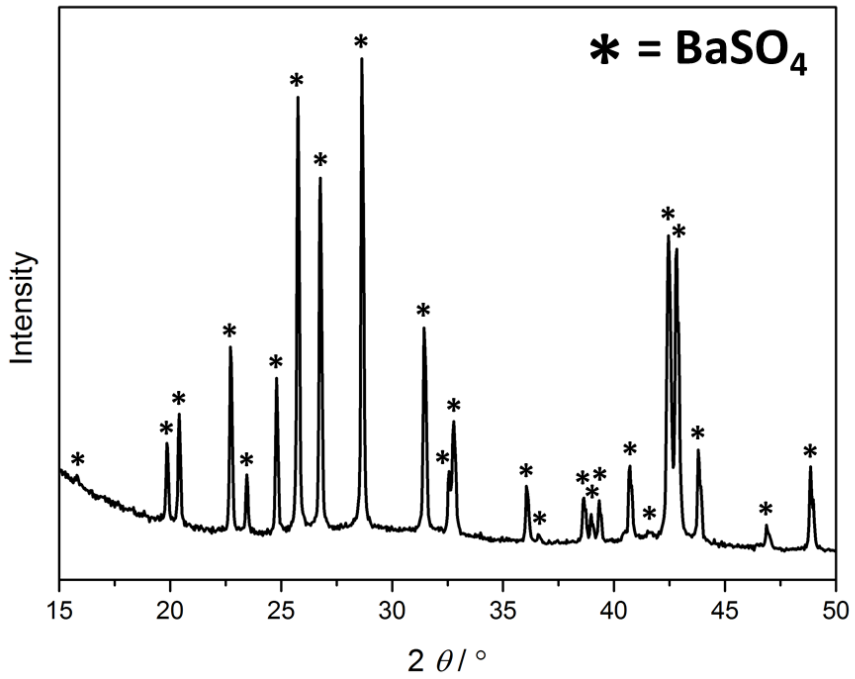


**Figure 5.3.2 –** Powder XRD of product (white powder) obtained from gravimetric analysis procedure, which was confirmed to be $BaSO_4$.[11]

Whilst this confirms that solid $BaSO_4$ was produced, any non-crystalline impurities would not be identified. Other spectroscopic techniques, such as IR or Raman, could be used to identify any possible impurities and should be considered in future analysis. Another possible cause of inaccuracy could be a systematic error associated with the auto-pipette used to extract the initial volume of polysulfide electrolyte solution analysed. If the volume extracted is consistently ~ 3% too much, then this would explain the error observed. To eliminate this error, the density of the prepared polysulfide electrolyte solution could be measured using a small volumetric flask (e.g. 1 mL) and then the initial volume of polysulfide electrolyte solution used could be weighed and the exact volume calculated. However, despite the small inaccuracy measured, a method was successfully developed capable of analysing polysulfide containing electrolyte solutions to quantitatively determine the concentration of the total dissolved sulfur $[S]_T^{sol.}$ with a small associated error ($\leq 5\%$). Further optimisation using the approaches discussed should enable the associated error to be minimised even further.

### 5.3.2 – UV-Vis Spectroscopic Redox Titration

In order to determine the average oxidation state of the dissolved sulfur ($S^{m-}$), the concentration of 'dissolved sulfide' $[S^{2-}]$ must be determined. The term 'dissolved sulfide' is used as all of the negative charge associated with the polysulfide is effectively provided by the initial quantity of solid $Li_2S$ added. Then using this and the concentration of total dissolved sulfur (determined in Section 5.3.1), it is possible to calculate the average oxidation state of the dissolved sulfur ($S^{m-}$), which can be loosely correlated to an average polysulfide chain length (Equation 5.3.6).

$$\text{(a)} \qquad m\,(S^{m-}) = \frac{2\,[S^{2-}]}{[S]_T^{sol.}}$$

$$\text{(b)} \qquad n\,(Li_2S_n) = \frac{2}{m\,(S^{m-})}$$

**Equation 5.3.6 –** (a) Calculating the average oxidation state of the dissolved sulfur ($S^{m-}$) from the concentration of dissolved sulfide $[S^{2-}]$ and the concentration of total dissolved sulfur $[S]_T^{sol.}$. (b) Calculating the 'average polysulfide chain length' ($Li_2S_n$) from the average oxidation state of the dissolved sulfur ($S^{m-}$).

Once again the methods undertaken by Rauh *et al.* to study the formation of lithium polysulfides in aprotic media were initially investigated.[3] To determine the concentration of 'dissolved sulfide' [$S^{2-}$], they used standard iodometric titration. This involved adding a known excess of iodine ($I_2$) to a known volume of the polysulfide solution, shaking and titrating the remaining unreacted $I_2$ against sodium thiosulfate ($Na_2S_2O_3$) using starch as an indicator (Equation 5.3.7).

(a) $$x\ S_n^{2-} + y\ I_2\ (\text{excess}) \rightarrow 2x\ I^- + \frac{(xn)}{8}\ S_8 + (y\text{-}x)\ I_2$$

(b) $$(y\text{-}x)\ I_2 + 2(y\text{-}x)\ Na_2S_2O_3 \rightarrow 2(y\text{-}x)\ NaI + (y\text{-}x)\ Na_2S_4O_6$$

**Equation 5.3.7 –** (a) Overall reaction of a known excess of $I_2$ with a known volume of polysulfides, giving sulfur ($S_8$), iodide ($I^-$) and an unknown amount of unreacted $I_2$ remaining. (b) The unreacted $I_2$ is then titrated against $Na_2S_2O_3$ until the $I_2$ is exhausted, given by a colour change from brown to colourless. At this end point, the moles of $Na_2S_2O_3$ added is noted.

Determining the volume of $Na_2S_2O_3$ required to completely react with the remaining $I_2$ (and knowing the concentration of the $Na_2S_2O_3$ solution) allows the number of moles of $Na_2S_2O_3$ used to be calculated. Using this and the initial number of moles of $I_2$ added in excess, enables the number of moles of 'dissolved sulfide' [$S^{2-}$] present in the initial volume of polysulfide electrolyte solution to be determined, which enables the concentration of 'dissolved sulfide' [$S^{2-}$] to be calculated (Equation 5.3.8).

$$[S^{2-}] = \frac{\left(\text{Moles of } I_2 - \frac{\text{Moles of } Na_2S_2O_3}{2}\right)}{V_{S_n^{2-}}} = \frac{\left(y - \frac{2(y-x)}{2}\right)}{V_{S_n^{2-}}} = \frac{x}{V_{S_n^{2-}}}$$

**Equation 5.3.8 –** Calculating the concentration of 'dissolved sulfide' [$S^{2-}$] from the moles of $Na_2S_2O_3$ calculated from the iodometric titration.

However, on testing the iodometric titration using solutions of $I_2$ dissolved in various non-aqueous solvents, it was determined that this method produced inaccurate and depending on the solvent irreproducible results (see Appendix A1 for more information). Whilst, $I_2$ is a suitable oxidising agent for the polysulfides due to its high redox potential ($I_3^-/I^-$ = ~3.58 V vs. $Li/Li^+$) and reversible electron transfer kinetics, it appears that its

reduced form, iodide ($I^-$) is unstable in ethereal solvents due to their ability to chelate $Li^+$.[12, 13] Therefore, a new approach was required to determine [$S^{2-}$]. On review of several suitable redox couples, it was decided that the ferrocene/ferrocenium ($Fc/Fc^+$) redox pair would be suitable to use in a redox titration. $Fc/Fc^+$ possesses a suitably high redox potential (~ 3.2 V vs. $Li/Li^+$) and reversible electron transfer kinetics, which means that $Fc^+$ is able to quantitatively oxidise the polysulfide species ($S_8^0/S_n^{2-}$ = ~ 2.4 V vs. $Li/Li^+$) in the prepared polysulfide electrolyte solutions to give Fc and $S_8$ (Equation 5.3.9 and Figure 5.3.3). Additionally, the progress of the reaction can be monitored using UV-vis spectroscopy, as $Fc^+$ possesses an absorption peak at 620 nm, which does not overlap with any absorption peaks of the products, Fc or $S_8$ (Figure 5.3.4).

$$2\ Fc^+\ (\textbf{blue}) + S_n^{2-} \rightarrow 2\ Fc\ (\textbf{yellow}) + \frac{n}{8} S_8$$

**Equation 5.3.9 –** Complete reaction of ferrocenium ($Fc^+$ or $[Fe(C_5H_5)_2]^+$) with polysulfide species ($S_n^{2-}$) to form ferrocene (Fc or $[Fe(C_5H_5)_2]$) and sulfur ($S_8$)

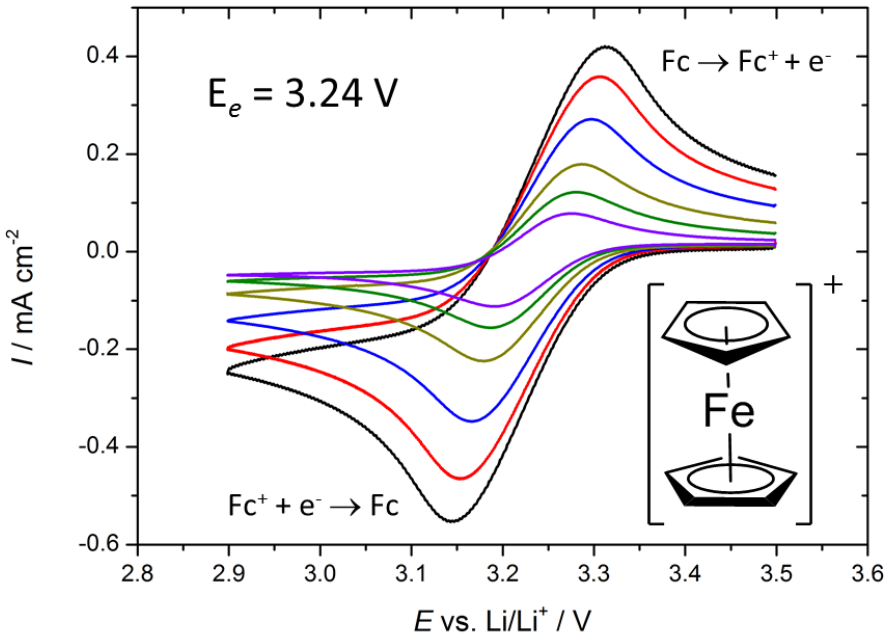


**Figure 5.3.3 –** Cyclic voltammetry measurements of $Fc^+$, illustrating the position of the redox potential. Scan rates of **— 200** mV $s^{-1}$, **— 100** mV $s^{-1}$, **— 50** mV $s^{-1}$, **— 20** mV $s^{-1}$, **— 10** mV $s^{-1}$ and **— 5** mV $s^{-1}$ were used. The two-compartment U-cell consisted of a glassy carbon working electrode (Ø = 3 mm), 3 mM $FcBF_4$ dissolved in 1 M LiTFSI in DOL electrolyte in the working electrode compartment, 1 M LiTFSI in DOL electrolyte in the counter/reference electrode compartment and a lithium metal counter/reference electrode. First cycles at specified scan rates are shown. Between changing the scan rates, the potential of the working electrode was held at 3.5 V for at least 2 minutes.

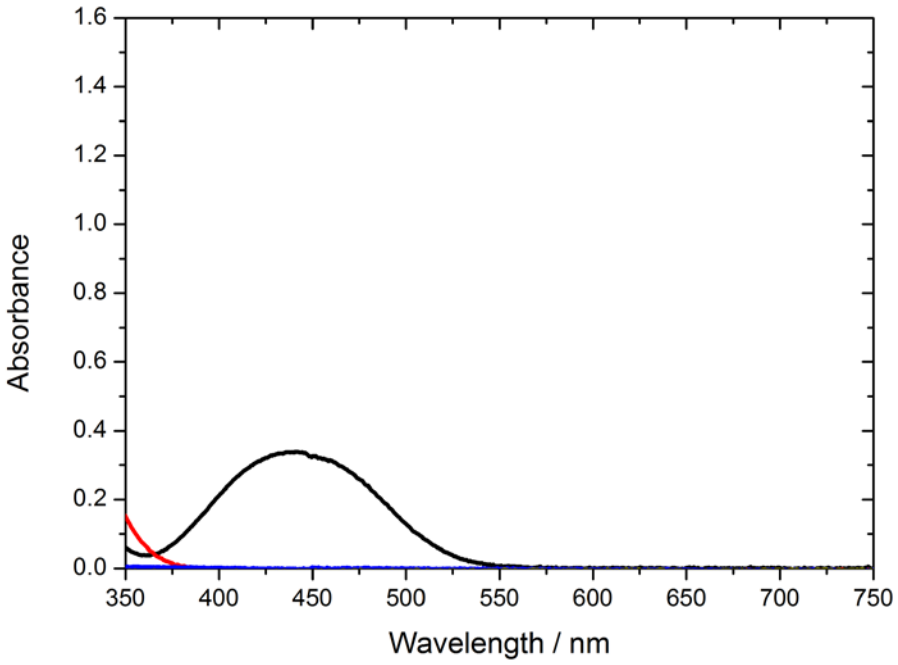


**Figure 5.3.4 –** (a) UV-vis absorption spectra of **— Fc (3 mM)**, **— $S_8$ (1 mM)**, **— LiTFSI (10 mM)** and **— $LiBF_4$ (5 mM)**, each dissolved in DOL. Fc and $S_8$ are reaction products, LiTFSI is present in the polysulfide electrolyte solutions and $LiBF_4$ is produced if $FcBF_4$ is used as a source of $Fc^+$, as is the case in this study. Absorption at 620 nm is not observed.

Given a suitably dilute solution of $Fc^+$, the absorbance peak at 620 nm can be monitored whilst adding small aliquots of prepared lithium polysulfide electrolyte solutions. Initially the peak at 620 nm will be large as only $Fc^+$ is present but as aliquots of $Li_2S_n$ are added, reacting to form Fc and $S_8$, the peak will decrease as the concentration of $Fc^+$ decreases until no more $Fc^+$ is present and the peak disappears completely. Similarly to gravimetric analysis (Section 5.3.1), to validate this method a polysulfide electrolyte solution was prepared, where complete dissolution of the solid ($S_8$ and $Li_2S$) had occurred as this would ensure that both the concentration of the total dissolved sulfur $[S]_T^{sol.}$ and the average oxidation state ($S^{m-}$) were known. For comparability to gravimetric analysis, the polysulfide electrolyte solution (1 M $[S]_T^{mix.}$ $Li_2S_6$ dissolved in 1 M LiTFSI in DOL) was analysed (Figure 5.3.5).

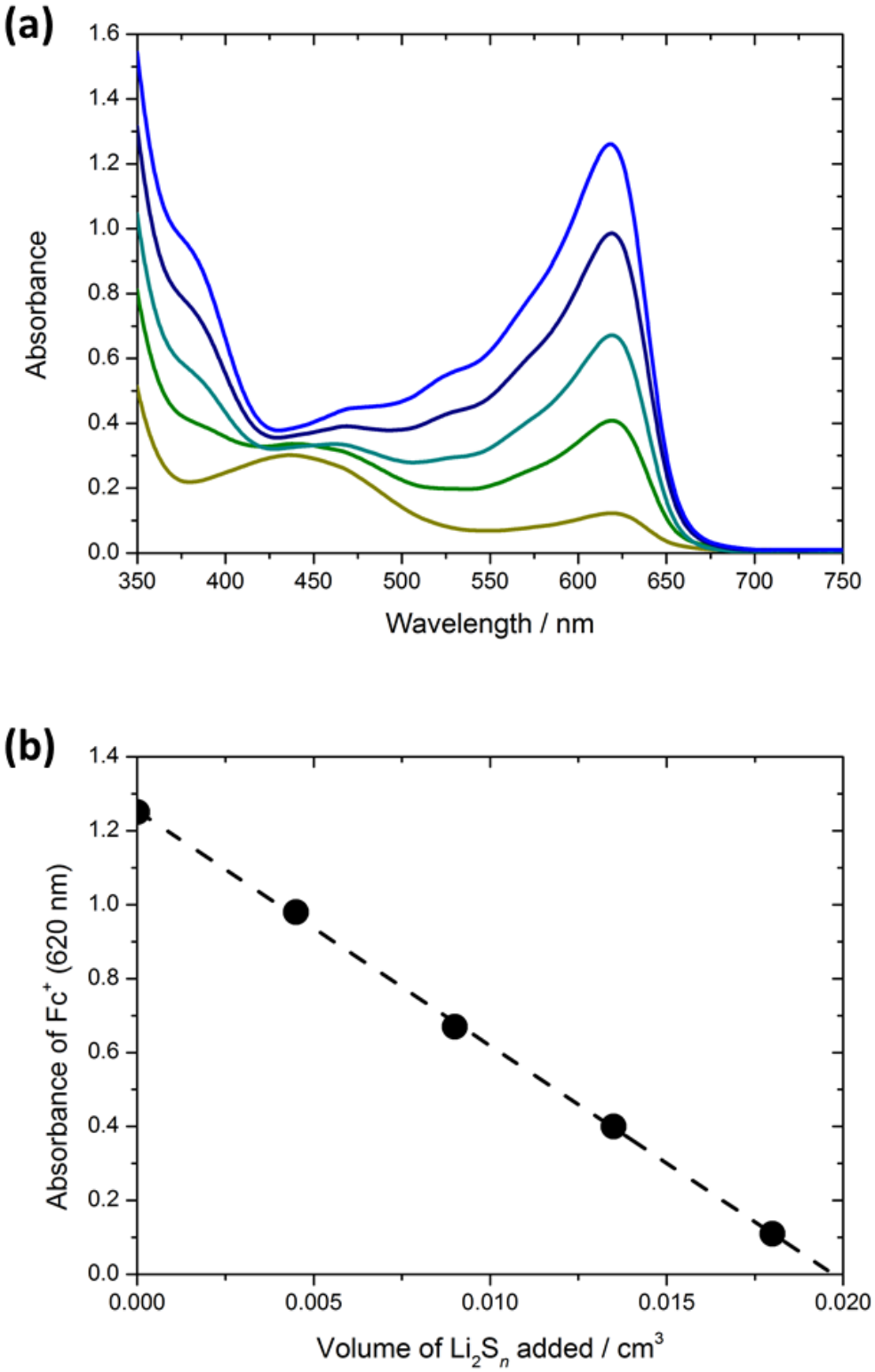


**Figure 5.3.5 –** (a) UV-vis absorption spectra of 3.1 mM $FcBF_4$ dissolved in DOL, where either 0 µL, 4.5 µL, 9.0 µL, 13.5 µL or 18.0 µL of the 1 M $[S]_T^{mix.}$ $Li_2S_6$ dissolved in 1 M LiTFSI in DOL were added. In each case, the polysulfide electrolyte solution was added to 2 mL of the $Fc^+$ solution. The data has been smoothed for appearance although the raw data is always used for calculations. (b) Absorbance values of each solution measured at 620 nm against the volume of polysulfide electrolyte solution added. Using a linear fit, the slope is calculated to be -63.56 $cm^{-3}$ and when absorbance = 0, the volume of $Li_2S_n$ = 0.0197 $cm^3$.

Using a linear fit, it was determined in order to reduce the absorbance at 620 nm to a value of zero, 19.7 μL (or 0.0197 $cm^3$) of the polysulfide electrolyte solution would be needed ($V_{S_n^{2-}}$). Using this, it is possible to calculate the concentration of 'dissolved sulfide' present [$S^{2-}$] (Equation 5.3.10).

$$[S^{2-}] = \frac{[Fc^+]\, V_{Fc^+}}{2\, V_{S_n^{2-}}} = \frac{0.0031\ \text{M} \,.\, 2\ \text{cm}^3}{2\,.\,0.0197\ \text{cm}^{-3}} = \mathbf{0.152\ M}$$

$$m\,(S^{m-}) = \frac{2\,[S^{2-}]}{[S]_T^{\text{sol.}}} = \frac{2\,.\ 0.152\ \text{M}}{1\ \text{M}} = \mathbf{0.30}\ (\mathbf{S^{0.30-}})$$

$$n\,(Li_2S_n) = \frac{2}{m\,(S^{m-})} = \frac{2}{0.30} = \mathbf{6.6}\ (\mathbf{Li_2S_{6.6}})$$

**Equation 5.3.10 –** Calculating the concentration of 'dissolved sulfide' [$S^{2-}$], where [$Fc^+$] = $Fc^+$ concentration of stock solution in M, $V_{Fc^+}$ = volume of $FcBF_4$ solution used to react with each volume of $Li_2S_n$ solution in $cm^3$ and $V_{S_n^{2-}}$ = volume of polysulfide electrolyte solution required to completely react with $Fc^+$. The average oxidation state of the dissolved sulfur ($S^{m-}$) is then calculated, as is the 'average polysulfide chain length' $Li_2S_n$.

From the calculation in Equation 5.3.10, it has been determined that the concentration of 'dissolved sulfide' [$S^{2-}$] present is 0.152 M. This value is approximately 6% less than the concentration expected, where [$S^{2-}$] should equal 0.167 M. In this procedure, the largest source of error is associated with calculating the $Fc^+$ concentration of the stock solution. Due to the small quantities of $FcBF_4$ weighed out and its relatively low purity (95%), the initial concentration of $Fc^+$ is subject to variation. To correct for this, the slope is used to evaluate the 'dissolved sulfide' concentration [$S^{2-}$] instead (Equation 5.3.11). The slope measures the change in $Fc^+$ concentration on adding increasingly larger volumes of the polysulfide electrolyte solution. This change in concentration can be calculated if the molar extinction coefficient of $Fc^+$ ($\varepsilon_{Fc^+}^{620\ \text{nm}}$) is known (see Appendix A2 for determination of $\varepsilon_{Fc^+}^{620\ \text{nm}}$). Using the slope to calculate the 'dissolved sulfide' concentration, offers the advantage of not requiring the $Fc^+$ concentration of the initial solution to be known. This method removes any random error in the $Fc^+$ concentration on preparing the $Fc^+$ stock solutions, improving the precision of the results.

$$[S^{2-}] = \frac{-\text{slope } V_{Fc^+}}{2\ l\ \varepsilon_{Fc^+}^{620\text{ nm}}} = \frac{-(-63.56 \pm 2.31)\text{ cm}^{-3}\ .\ 2\text{ cm}^3}{2\ .\ 1\text{ cm}\ .\ 390\text{ M}^{-1}\text{ cm}^{-1}} = (\mathbf{0.163 \pm 0.006})\ \mathbf{M}$$

$$m\ (S^{m-}) = \frac{2\ [S^{2-}]}{[S]_T^{sol.}} = \frac{2\ .\ (0.163 \pm 0.006)\text{ M}}{1\text{ M}} = \mathbf{0.33 \pm 0.01}\ (\mathbf{S^{0.33-}})$$

$$n\ (Li_2S_n) = \frac{2}{m\ (S^{m-})} = \frac{2}{0.33 \pm 0.01} = \mathbf{6.1 \pm 0.2}\ (\mathbf{Li_2S_{6.1}})$$

**Equation 5.3.11 –** Calculating the concentration of 'dissolved sulfide' [$S^{2-}$], where $V_{Fc^+}$ = volume of $FcBF_4$ solution used to react with each volume of $Li_2S_n$ solution in $cm^3$, $l$ = the UV-vis cuvette path length in cm and $\varepsilon_{Fc^+}^{620\text{ nm}}$ = the molar extinction coefficient of $FcBF_4$ at 620 nm in $M^{-1}\ cm^{-1}$. The average oxidation state of the dissolved sulfur ($S^{m-}$) is then calculated, as is the 'average polysulfide chain length' $Li_2S_n$.

From the calculation in Equation 5.3.11, it has been determined (using the slope in Figure 5.3.5b) that the concentration of 'dissolved sulfide' [$S^{2-}$] present is 0.163 M. This value is approximately 2% less than the concentration expected, where [$S^{2-}$] should equal 0.167 M. This remaining error is likely associated with the auto-pipette, which can be corrected for by weighing the quantity of $FcBF_4$ in DOL used for each measurement. However, despite the small error associated with the method (< 5%), a technique was successfully developed capable of analysing polysulfide containing electrolyte solutions to quantitatively determine the concentration of 'dissolved sulfide' [$S^{2-}$] present. This can be used to calculate the average oxidation state of the dissolved sulfur ($S^{m-}$) and an average polysulfide chain length ($Li_2S_n$). Further optimisation using the approaches, such as the reverse redox titration discussed (Section 5.3.4), should enable the associated error to be minimised even further.

### 5.3.3 – Concentrated Polysulfide Electrolyte Solutions

*Note: The experimental data presented in this section (Section 5.3.3) was obtained by John W. Smith, a fourth year undergraduate student (MChem), whom I mentored throughout his Master's project under the supervision of Professor John R. Owen and Dr Nuria Garcia-Araez (2015 – 2016). However, processing and analysis of the raw data has been performed by myself.*

On preparing polysulfide electrolyte solutions, there are four theoretical outcomes depending on which of the two solids ($S_8$ and $Li_2S$) completely dissolve. In the first scenario, both solids ($S_8$ and $Li_2S$) completely dissolve into the electrolyte (Equation 5.3.12a). These can be thought of as 'dilute' solutions and the polysulfide electrolyte solution used to validate the gravimetric analysis and UV-vis spectroscopic redox titration techniques (1 M $[S]_T^{mix.}$ $Li_2S_6$ dissolved in 1 M LiTFSI in DOL, Sections 5.3.1 and 5.3.2) falls into this category. For these 'dilute' solutions, the composition of the polysulfides in terms of concentration of the total dissolved sulfur $[S]_T^{sol.}$ and average oxidation state of the dissolved sulfur ($S^{m-}$), is known. Another property of 'dilute' solutions is that they only contain one phase, meaning that they have two degrees of freedom (see Gibbs' phase rule, Equation 5.3.13). This means that the addition of either solid will change the composition of the polysulfides.

For dilute solutions:

(a) $\frac{n-1}{8}S_8 + Li_2S \rightarrow Li_2S_{\boldsymbol{n}}$ (complete dissolution)

For 'saturated' solutions:

(b) $\frac{n-1}{8}S_8 + Li_2S \rightarrow Li_2S_{\boldsymbol{n-a}} + \frac{\boldsymbol{a}}{\boldsymbol{8}}\boldsymbol{S_8}$ ($\boldsymbol{S_8}$ precipitate present)

(c) $\frac{n-1}{8}S_8 + Li_2S \rightarrow Li_2S_{\frac{\boldsymbol{n}}{\boldsymbol{(1-b)}}} + \boldsymbol{b\ Li_2S}$ ($\boldsymbol{Li_2S}$ precipitate present)

(d) $\frac{n-1}{8}S_8 + Li_2S \rightarrow Li_2S_{\frac{\boldsymbol{n-a}}{\boldsymbol{(1-b)}}} + \frac{\boldsymbol{a}}{\boldsymbol{8}}\boldsymbol{S_8} + \boldsymbol{b\ Li_2S}$ ($\boldsymbol{S_8}$ and $\boldsymbol{Li_2S}$ precipitates present)

**Equation 5.3.12 –** Preparation of polysulfide electrolyte solutions, through direct reaction $S_8$ and $Li_2S$ in electrolyte, where (a) both solids fully react to give a one-phase polysulfide electrolyte solution, (b) solid $S_8$ remains in solution as precipitate giving two phases, where the polysulfide electrolyte solution is saturated with respect to $S_8$, (c) solid $Li_2S$ remains in solution as precipitate giving two phases, where the polysulfide electrolyte solution is saturated with respect to $Li_2S$ and (d) both solid $S_8$ and solid $Li_2S$ remain in solution as precipitates giving three phases, where the polysulfide electrolyte solution is completely saturated with respect to both $S_8$ and $Li_2S$.

$$\text{Freedom} = \text{Components} - \text{Phases}$$

**Equation 5.3.13 –** Gibbs' Phase Rule for determining the degrees of freedom at fixed temperature and pressure.

For the remaining three scenarios, the prepared polysulfide electrolyte solutions can be thought of as 'saturated', at least with respect to either solid $S_8$ or solid $Li_2S$. The solutions where only one solid (either $S_8$ or $Li_2S$) remains after equilibration can be said to be saturated with respect to that remaining solid (Equation 5.3.12b and 5.3.12c). However, it should be noted that whilst these solutions are saturated with respect to that one solid, they are not fully saturated with respect to polysulfides as adding more of the other (non-saturated) solid components will change the composition of the polysulfides present. This ability to affect the polysulfide concentration is supported by Gibbs' phase rule, where there is one degree of freedom due to there being two phases present. In the final scenario, where both solids ($S_8$ and $Li_2S$) remain after equilibration, the polysulfide electrolyte solutions can be said to be fully saturated (Equation 5.3.12d). Only in this scenario is the solution fully saturated with respect to polysulfides, as well as both solids, and adding more of either solid will not affect the composition of the polysulfides present. This is supported by Gibbs' phase rule, where there are zero degrees of freedom due to there being three phases present. Another important aspect applicable to all three of the 'saturated' solutions is that the polysulfide composition cannot be determined by simply knowing the quantities of $S_8$ and $Li_2S$ initially added, illustrated in Equation 5.3.12. Therefore, techniques are required that are capable of determining the polysulfide composition, such as the developed gravimetric analysis and UV-vis spectroscopic redox titration.

Determining the polysulfide composition of a completely saturated polysulfide electrolyte solution, i.e. where both solid $S_8$ and solid $Li_2S$ remain after equilibration, is particularly important as this defines the absolute limit of polysulfide 'solubility' in that particular electrolyte system. This would be a particularly interesting parameter for comparing various different electrolyte systems. Additionally, to maximise energy density in Li-S batteries the sulfur to electrolyte ratio should be as high as possible, which corresponds to an electrolyte system that is completely saturated in polysulfides. Furthermore, knowing the polysulfide composition of a completely saturated polysulfide electrolyte solution allows the congruent point on a ternary phase diagram to be placed. Therefore, it was decided to prepare polysulfide electrolyte solutions using the electrolyte system 1 M LiTFSI in DOL, where the solution should be completely saturated with respect to both solid $S_8$ and solid $Li_2S$. Four polysulfide electrolyte solutions were prepared, where assuming full dissolution, the average polysulfide composition would

have been '$Li_2S_8$ ($S^{0.25-}$)' and '$Li_2S_6$ ($S^{0.33-}$)' and the concentration of total dissolved sulfur $[S]_T^{sol.}$ would have been '10 M' and '20 M' (Table 5.3.2).

| Prepared average polysulfide composition | Prepared conc. of dissolved sulfur $[S]_T^{mix.}$ / M | Gravimetric analysis determination of $[S]_T^{sol.}$ / M | UV-vis spectroscopic redox titration determination of $S^{m-}$ |
|---|---|---|---|
| $Li_2S_8$ ($S^{0.25-}$) | 10 | 4.1 | $S^{0.40-}$ ($Li_2S_{5.0}$) |
| $Li_2S_8$ ($S^{0.25-}$) | 20 | 5.3 | $S^{0.41-}$ ($Li_2S_{4.9}$) |
| $Li_2S_6$ ($S^{0.33-}$) | 10 | 5.9 | $S^{0.41-}$ ($Li_2S_{4.8}$) |
| $Li_2S_6$ ($S^{0.33-}$) | 20 | 6.3 | $S^{0.48-}$ ($Li_2S_{4.2}$) |

**Table 5.3.2 –** Analysis of 'saturated' polysulfide electrolyte solutions using the gravimetric analysis technique to determine the concentration of total dissolved sulfur $[S]_T^{sol.}$ and the UV-vis spectroscopic redox titration to determine the average oxidation state of the dissolved sulfur ($S^{m-}$), which can be 'loosely' correlated to average polysulfide chain length ($Li_2S_n$). See Appendix A3 for full details.

Using the developed gravimetric analysis, it was observed that a maximum concentration of dissolved sulfur $[S]_T^{sol.}$ of approximately 6 M was achieved in both of the polysulfide electrolyte solutions prepared as $Li_2S_6$. In these solutions, doubling the amount of starting material does not lead to a significant change in the polysulfide composition, corroborating that the congruent point has been reached. In addition to this, the polysulfide electrolyte solution prepared as 20 M $[S]_T^{sol.}$ $Li_2S_8$ also gives a similar polysulfide composition, which indicates that this solution also corresponds to the congruent point. However, it was observed that the polysulfide electrolyte solution prepared as 10 M $[S]_T^{sol.}$ $Li_2S_8$ appears to possess a notably lower concentration of total dissolved sulfur indicating that the solution was not saturated with respect to both solids. Using the determined polysulfide composition of the congruent solution, it has been determined that this polysulfide electrolyte solution (10 M $[S]_T^{sol.}$ $Li_2S_8$) does not possess enough $Li_2S$ to be fully saturated (see Table 5.3.3 for calculation). Additionally, using the developed UV-vis spectroscopic redox titration technique, it was possible to determine that the average oxidation state of the dissolved sulfur ($S^{m-}$) for the completely saturated solutions is between $S^{0.41-}$ and $S^{0.48-}$, which loosely corresponds to an average polysulfide chain lengths ($Li_2S_n$) of $Li_2S_{4.9}$ and $Li_2S_{4.2}$. Therefore, these results indicate that the polysulfide composition of the congruent point is ~ 6 M $[S]_T^{sol.}$, with an average oxidation state of the

dissolved sulfur ($S^{m-}$) of $S^{0.45-}$ corresponding to an average polysulfide chain length ($Li_2S_n$) of $Li_2S_{4.5}$. It should be noted that this congruent point will only be applicable for the 1 M LiTFSI in DOL electrolyte system.

Using this congruent point, it is possible to calculate the minimum amount of solid $S_8$ and solid $Li_2S$ required to prepare a fully saturated polysulfide electrolyte solution (Table 5.3.3). This can be used to determine which of the prepared polysulfide electrolyte solutions (Table 5.3.2) should be fully saturated.

| Prepared average polysulfide composition | Prepared concentration of dissolved sulfur $[S]_T^{sol.}$ / M | Solid $Li_2S$ required for 10 mL / g | Solid $S_8$ required for 10 mL / g |
|---|---|---|---|
| $Li_2S_{4.5}$ | 6 | 0.613 | 1.496 |
| $Li_2S_8$ | 10 | 0.574 | 2.805 |
| $Li_2S_8$ | 20 | 1.149 | 5.611 |
| $Li_2S_6$ | 10 | 0.768 | 2.672 |
| $Li_2S_6$ | 20 | 1.532 | 5.343 |

**Table 5.3.3 –** Determining the minimum amount of solid $S_8$ and solid $Li_2S$ to prepare 10 mL of the congruent polysulfide electrolyte solutions (6 M $[S]_T^{sol.}$ $Li_2S_{4.5}$) and comparing against the amount of solid used to prepare the four polysulfide electrolyte solutions analysed. The boxes shaded in **red** indicate that insufficient solid is used to reach the full saturation and boxes shaded in **green** indicate that sufficient solid is used.

It is calculated that only the polysulfide electrolyte solution prepared as 10 M $[S]_T^{sol.}$ $Li_2S_8$ solution will not be fully saturated as insufficient solid $Li_2S$ was used in its preparation. This indicates that this polysulfide electrolyte solution is only saturated with respect to $S_8$ and only exhibits two phases (polysulfides dissolved in electrolyte and solid $S_8$). This would account for the notably lower concentration of total dissolved sulfur determined using gravimetric analysis (Table 5.3.2). The values determined in Table 5.3.2 for the four polysulfide electrolyte solutions were then used to plot the first experimental ternary phase diagram for a Li-S battery system (Figure 5.3.6). For full details on the construction of this phase diagram, see Appendix A4.

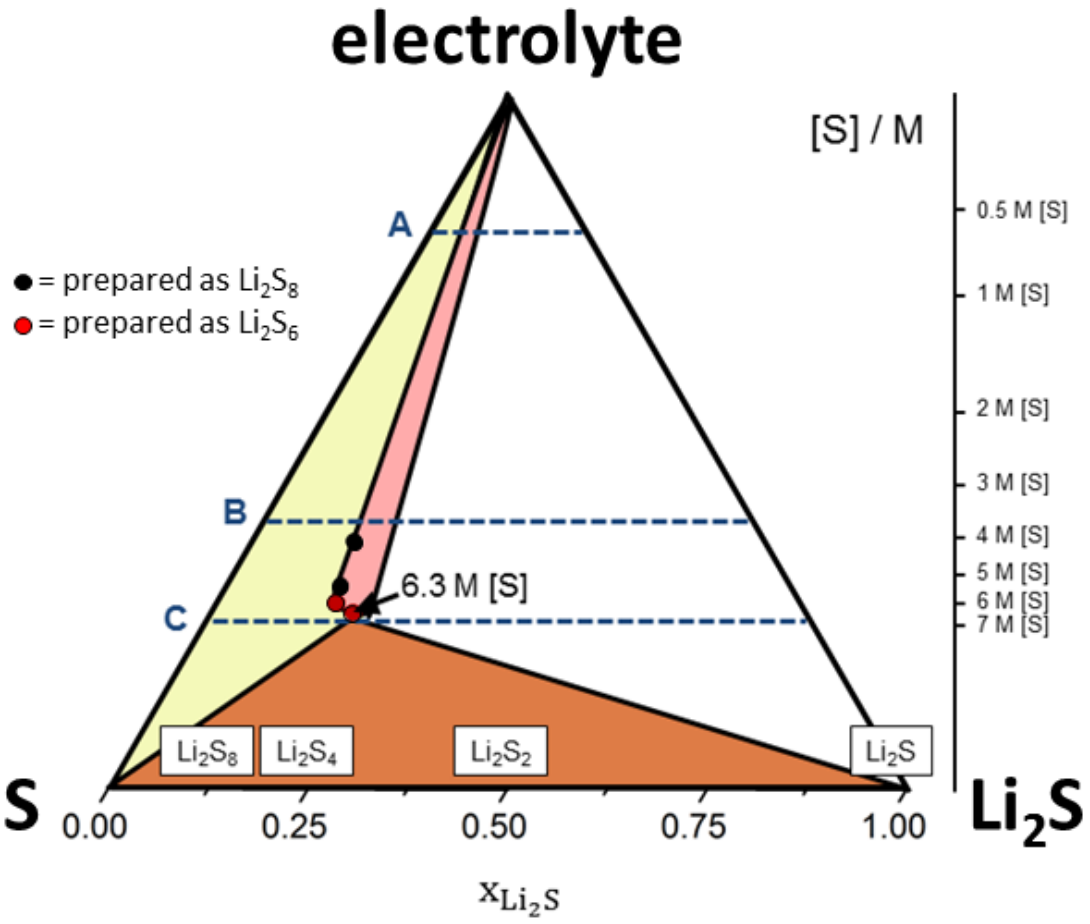


**Figure 5.3.6 –** Experimental ternary phase diagram for a system comprising of $S_8$, $Li_2S$ and the electrolyte 1 M LiTFSI in DOL. This phase diagram has been drawn using the results in Table 5.3.2. The pink area represents the one-phase region (no solids, just polysulfides dissolved in electrolyte), the yellow area represents a two-phase region (solid $S_8$ and polysulfides dissolved in electrolyte), the white area represents another two-phase region (solid $Li_2S$ and polysulfides dissolved in electrolyte) and the orange area represents the three-phase region (both solid $S_8$ and solid $Li_2S$, as well as polysulfides dissolved in electrolyte). Three potential discharge trajectories (A, B and C) of cells containing different sulfur to electrolyte ratios have been drawn.

On the ternary phase diagram, the polysulfide electrolyte solution prepared as 20 M $[S]_T^{sol.}$ $Li_2S_6$ has been drawn as the congruent point, although it can be seen that the three fully saturated solutions (20 M $[S]_T^{sol.}$ $Li_2S_8$, 10 M $[S]_T^{sol.}$ $Li_2S_6$ and 20 M $[S]_T^{sol.}$ $Li_2S_6$) start to converge. Furthermore, the phase diagram illustrates that the polysulfide electrolyte solution prepared as 10 M $[S]_T^{sol.}$ $Li_2S_8$ is notably further from the congruent point as it is not fully saturated. Below the congruent point, the three-phase region is observed (coloured orange) where solid $S_8$ and solid $Li_2S$ coexist in equilibrium with the congruent solution. The straight lines indicating the boundaries between the three-phase region and the two two-phase regions are straight due to the constant polysulfide composition. The

lines indicating the boundaries between the one-phase region and two two-phase regions have been drawn tentatively, taking into account the low solubility of $S_8$ and $Li_2S$ in the electrolyte. In further work, the exact position of these boundaries could be investigated in order to complete the phase diagram for this solvent system (1 M LiTFSI in DOL). Additionally, the congruent point could be determined in other commonly used Li-S battery electrolyte systems.

The phase diagram can also be used to rationalise the effect of changing the sulfur to electrolyte ratio on the Li-S battery equilibrium discharge profile. For simplicity, only one polysulfide species with an oxidation state of ($S^{m-}$) will be considered, although the same argument could be expanded considering a variety of polysulfide species. Considering the potential discharge trajectory labelled A on the phase diagram (Figure 5.3.6), discharge begins on the binary $S_8$-electrolyte axis where solid $S_8$ and electrolyte are present, i.e. two-phase region. Then as discharge proceeds, the $S_8$ dissolves into the electrolyte and is reduced to polysulfides until no more solid $S_8$ is present, i.e. the discharge trajectory enters the one-phase region where everything dissolves. Then as the discharge profile proceeds, solid $Li_2S$ precipitates, i.e. the discharge trajectory enters the two-phase region and discharge continues until the binary $Li_2S$-electrolyte axis is reached. These two main process (solid $S_8$ conversion to polysulfides and polysulfide conversion to solid $Li_2S$) can be described by the Nernst equation, leading to the formation of two discharge plateaux, labelled A (Equation 5.3.14, Figure 5.3.7). However, it should be noted that these two 'plateaux' can be more accurately described as quasi-plateaux since the potential will vary as the polysulfide concentration varies, as given by the Nernst equations:

$$\text{(a)} \qquad E = E_1^0 + \frac{RT}{mF} ln \frac{a_{S^0}}{a_{S^{m-}}}$$

$$\text{(b)} \qquad E = E_2^0 + \frac{RT}{(2-m)F} ln \frac{a_{S^{m-}}}{a_{S^{2-}}}$$

**Equation 5.3.14 –** Nernst equation for the redox reaction between (a) solid sulfur ($S^0$) and dissolved polysulfide species ($S^{m-}$) and (b) between dissolved polysulfide species ($S^{m-}$) and solid lithium sulfide ($S^{2-}$), where $a_{S^0}$, $a_{S^{m-}}$ and $a_{S^{2-}}$ are the activities of $S^0$, $S^{m-}$ and $S^{2-}$ species, respectively. $E_1^0$ and $E_2^0$ are the standard potentials of the $S^{m-}/S^0$ and $S^{2-}/S^{m-}$ redox couples, respectively.

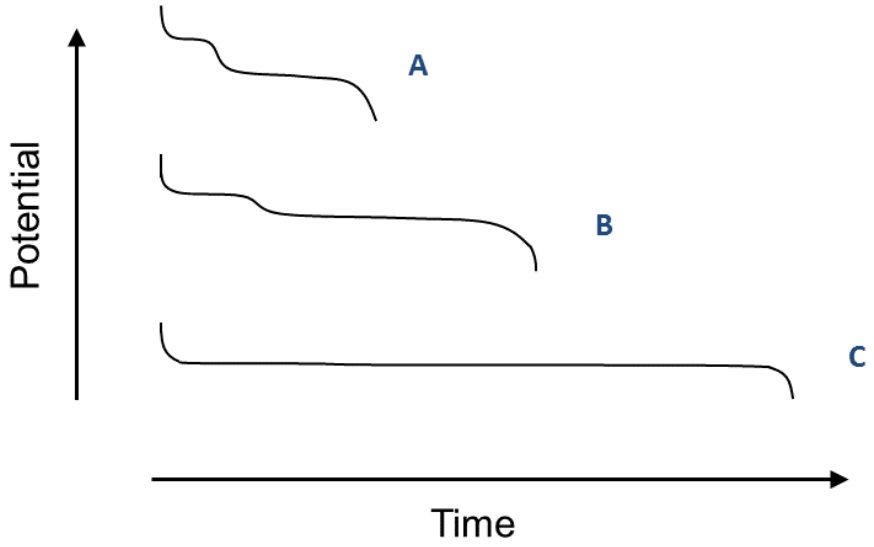


**Figure 5.3.7 –** Theoretical equilibrium discharge profiles illustrating the change in potentials of the discharge plateaux, as well as the capacity using different ratios of $S_8$ to electrolyte. Discharge profile A would be typical of coin cell data from the literature where the ratio of $S_8$ to electrolyte is small, i.e. excess electrolyte is used. Discharge profiles B and C could be observed in commercial pouch cells using less electrolyte.

The Nernst equations (Equation 5.3.14) have been written considering the activities of solid $Li_2S$ and solid $S_8$, which will be equal to one as long as those solids are present. Similar equations can be written considering the activity or concentration of dissolved $Li_2S$ and dissolved $S_8$, which again, will be constant provided that the corresponding solid is present. Using both the phase diagram and Nernst equations (Figure 5.3.6 and Equation 5.3.14), it is predicted that a larger $S_8$ to electrolyte ratio will result in the elongation of both plateaux, due to the presence of more active material, and the potential difference between the two plateaux will also decrease (Figures 5.3.6 and 5.3.7, discharge profile B). The second observation can be rationalised by the fact that a larger $S_8$ to electrolyte ratio will lead to a higher polysulfide concentration in the electrolyte. This causes the first plateau to appear at a lower potential and the second plateau to appear at a higher potential, since the equilibrium potentials of the plateaux are affected by the polysulfide activity ($a_{S^{m-}}$), which will be higher if the electrolyte volume is lower, because more concentrated solutions of polysulfides will be formed. When the $S_8$ to electrolyte ratio is increased even further, the electrolyte will become fully saturated in polysulfides during discharge, i.e. the congruent solution will be achieved (Figures 5.3.6 and 5.3.7, discharge profile C). Using the phase diagram, it is predicted that this will lead to only one discharge plateau, although it should be noted that this 'plateau' can once again be thought of as a quasi-plateau, since

the concentration of polysulfides will vary as the discharge proceeds within the two-phase regions.

Increasing the $S_8$ to electrolyte ratio even further (Figure 5.3.6, below potential discharge trajectory C), the equilibrium discharge profile will continue to give one discharge plateau, although as the three-phase region is traversed, a true plateau will be observed with a constant potential, predicted by the Nernst equation (Equation 5.3.15).

$$E_3^0 = \frac{mE_1^0 + (2-m)E_2^0}{2}$$

**Equation 5.3.15 –** Nernst equation combined for the two redox reactions between solid $S_8$, dissolved polysulfide species and solid $Li_2S$.

The observation of one-equilibrium discharge profile has been observed in the literature by Cuisinier *et al.* using a new class of Li-S battery electrolytes, known as 'non-solvents' (Figure 5.3.8).[14] This observation illustrates experimentally the effect of reaching polysulfide saturation during discharge predicted by discharge trajectory C in Figure 5.3.6. In this electrolyte, polysulfide dissolution and mobility are extremely low, which quickly leads to full saturation of the polysulfide species in the electrolyte close to the positive electrode surface. However, obtaining full saturation of polysulfide in the 1 M LiTFSI in DOL electrolyte system is much more challenging due to the much higher polysulfide solubility (~ 6 M $[S]_T^{sol.}$), which would take a long time equilibrate. Additionally, the high mobility of species in 1 M LiTFSI in DOL would lead to extensive polysulfide shuttling, which complicates the measurements.

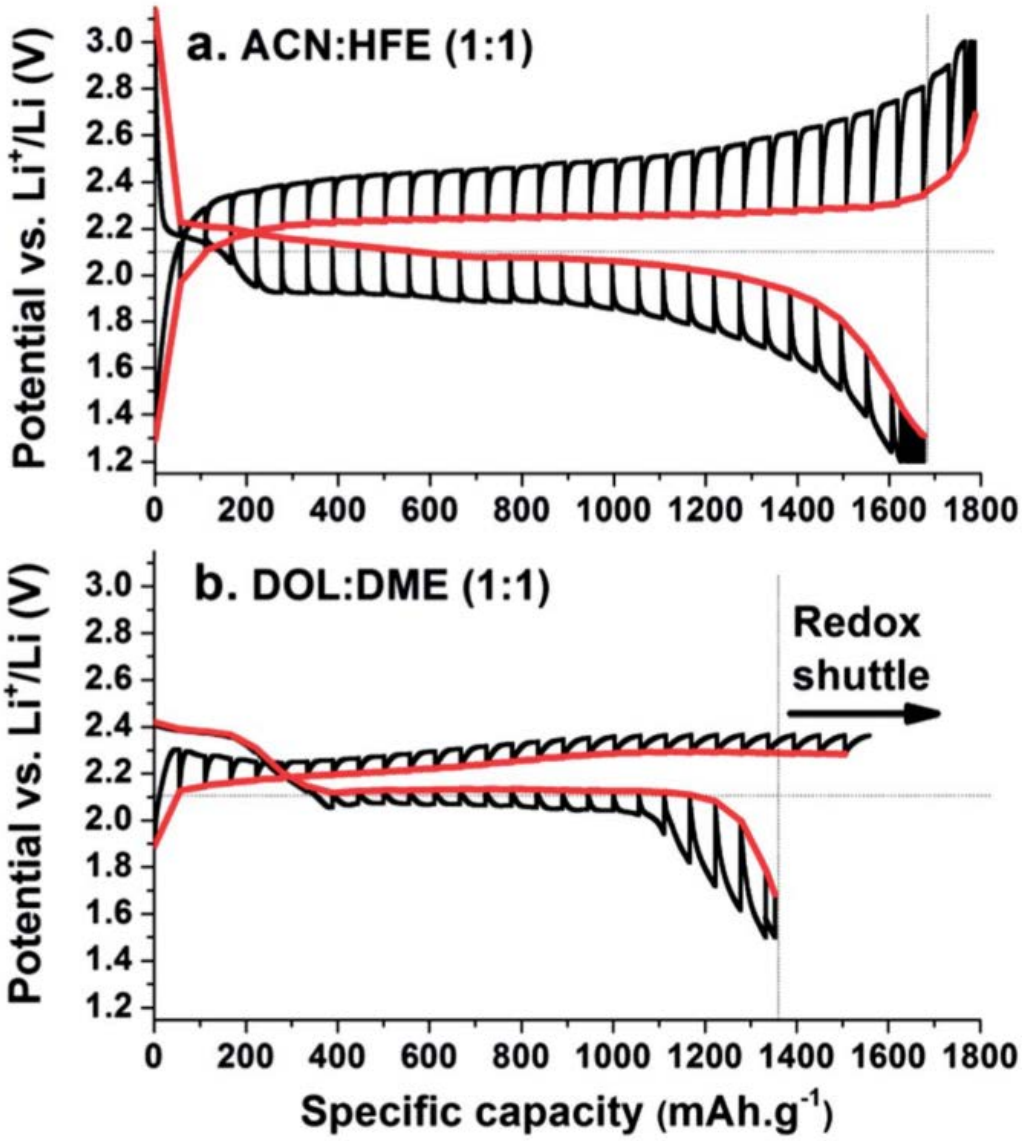


**Figure 5.3.8 –** Galvanostatic Intermittent Titration Technique (GITT) experiments in (a) LiTFSI dissolved in acetonitrile and hydrofluoroether (v/v = 1:1) and (b) LiTFSI dissolved in DOL:DME (v/v = 1:1) without $LiNO_3$ as electrolyte additive.[14] Reproduced from Ref.[14] with permission from the Royal Society of Chemistry.

### 5.3.4 – Reverse Redox Titration: Improving Precision

The concentrated polysulfide electrolyte solutions are viscous and only very small volumes are required to perform the titrations (a few microliters). In order to improve the associated errors with extracting such small volumes of a viscous solution, a reverse titration could be performed. Instead of adding different volumes of polysulfide electrolyte

solution to a fixed volume of $FcBF_4$ in DOL, different volumes of $FcBF_4$ in DOL can be added to a fixed volume of polysulfide electrolyte solution. The volume of polysulfide electrolyte solution can be initially much larger and can even exceed the volume required for complete reaction with the $FcBF_4$ in DOL (Equation 5.3.13).

$$2a\ Fc^{+}\ (\textbf{blue}) + b\ S_n^{2-} \rightarrow 2a\ Fc\ (\textbf{yellow}) + \frac{a\ n}{8} S_8 + (b - a)\ S_n^{2-}$$

**Equation 5.3.13 –** Complete reaction of ferrocenium ($Fc^+$ or $[Fe(C_5H_5)_2]^+$) with an excess of polysulfide species ($S_n^{2-}$) to form ferrocene (Fc or $[Fe(C_5H_5)_2]$), sulfur ($S_8$) and remaining polysulfide species ($S_n^{2-}$).

Once this solution has been prepared, fixed volumes can be taken and diluted using the $FcBF_4$ in DOL. Knowing the initial volume of polysulfide electrolyte solution and initial volume of $FcBF_4$ in DOL solution used allows an effective polysulfide electrolyte volume per $FcBF_4$ in DOL volume to be calculated, which can then be re-calculated once more $FcBF_4$ in DOL is added. This enables the same plot in Section 5.3.2 to be produced (Figure 5.3.5) and then using the slope method, the concentration of 'dissolved sulfide' $[S^{2-}]$ can be calculated. This method was tested using a freshly prepared polysulfide electrolyte solution of 20 M $[S]_T^{sol.}$ $Li_2S_6$, which was the same solution that gave the highest sulfur concentration in Section 5.3.3 (Figure 5.3.9). It should be noted that whilst it is not necessary to know the concentration of the $FcBF_4$ solution used, the same batch of $FcBF_4$ solution with a fixed constant concentration must be used throughout the titration.

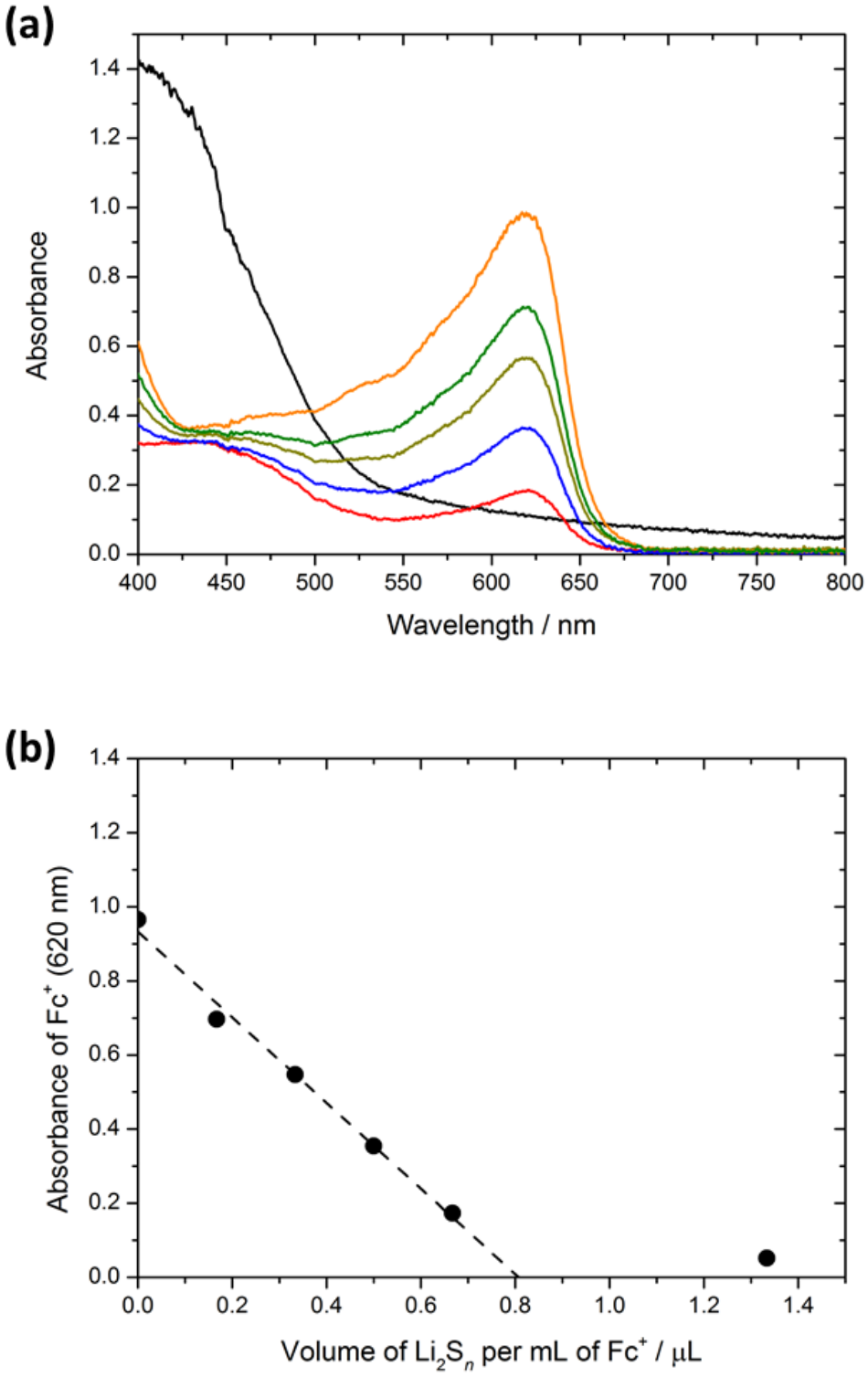


**Figure 5.3.9 –** (a) UV-vis absorption spectra of reverse titration solutions, prepared from an initial solution where 8 µL of the 20 M $[S]_T^{mix.}$ $Li_2S_6$ in 1 M LiTFSI in DOL was added to 6 mL of 3 mM $FcBF_4$ dissolved in DOL (1.33 µL per mL of $Fc^+$). Then aliquots of this solution were used to make subsequent solutions giving the following effective volumes of $Li_2S_n$ per mL of the $Fc^+$ solution, 0.67 µL per mL of $Fc^+$, 0.50 µL per mL of $Fc^+$, 0.33 µL per mL of $Fc^+$ and 0.17 µL per mL of $Fc^+$. Also the UV-vis absorbance spectrum of the pure $FcBF_4$ in DOL stock solution was measured. (b) Absorbance values of each solution measured at 620 nm. Using a linear fit, the slope is calculated to be -1.156 $\mu L^{-1}$.

| Solution used for preparation | Volume of polysulfide present per mL of $FcBF_4$ solution / μL $cm^{-3}$ | Volume taken / mL | Volume of 3 mM $FcBF_4$ in DOL added / mL | New volume of polysulfide present per mL of $FcBF_4$ solution / μL $cm^{-3}$ | New solution label |
|---|---|---|---|---|---|
| 20 M $[S]_T^{sol.}$ $Li_2S_6$ | Pure polysulfide electrolyte solution | 0.008 | 6.0 | **1.33** | A |
| A | 1.33 | 3.0 | 3.0 | **0.67** | B |
| B | 0.67 | 3.0 | 1.0 | **0.50** | C |
| A | 1.33 | 0.5 | 1.5 | **0.33** | D |
| C | 0.50 | 1.0 | 2.0 | **0.17** | E |

**Table 5.3.4 –** Preparation of reverse titration solutions by initially adding 8 μL of the 20 M $[S]_T^{mix.}$ $Li_2S_6$ in 1 M LiTFSI in DOL was added to 6 mL of 3 mM $FcBF_4$ dissolved in DOL (1.33 μL per mL of $Fc^+$). Then aliquots of this solution were used to make subsequent solutions giving the following effective volumes $Li_2S_n$ per mL of the $Fc^+$ solution, 0.67 μL per mL of $Fc^+$, 0.50 μL per mL of $Fc^+$, 0.33 μL per mL of $Fc^+$ and 0.17 μL per mL of $Fc^+$.

The method for preparing each of these solutions is given for clarity (Table 5.3.4). It is observed in Figure 5.3.9, that the reverse titration method can also be used to obtain a linear fit and slope from which the concentration of 'dissolved sulfide' $[S^{2-}]$ can be calculated (Equation 5.3.14). Since different quantities of the $FcBF_4$ were effectively added to a fixed volume of the polysulfide electrolyte solution, the data has been plotted in the form of volume of polysulfide electrolyte in μL per mL of $FcBF_4$ in DOL so that the solutions can easily be compared. It is observed in the UV-vis spectrum of the initially prepared solution (solution A, 1.33 μL per mL of $Fc^+$) that no peak at 620 nm is present, which indicates that the $Fc^+$ has full reacted and dissolved polysulfide will still be present. Therefore, the absorbance at 620 nm for this solution cannot be used to calculate the slope for determining the 'dissolved sulfide' $[S^{2-}]$. However, on diluting this solution by a factor of 2 (solution B, 0.67 μL per mL of $Fc^+$) a peak at 620 nm is observed, which indicates that $Fc^+$ is present and all of the dissolved polysulfide has reacted. Therefore, the absorbance at 620 nm for this solution (and any solution prepared as ≤ 0.67 μL per mL of $Fc^+$) can be used to calculate the slope for determining the 'dissolved sulfide' $[S^{2-}]$.

$$[S^{2-}] = \frac{-\text{slope } V_{Fc^+}}{2\ l\ \varepsilon_{Fc^+}^{620\text{ nm}}} = \frac{-(-1.156 \text{ x } 10^3)\text{ cm}^{-3}\ .\ 1\text{ cm}^3}{2\ .\ 1\text{ cm}\ .\ 390\text{ M}^{-1}\text{ cm}^{-1}} = \mathbf{1.48\ M}$$

$$m\ (S^{m-}) = \frac{2\ [S^{2-}]}{[S]_T^{sol.}} = \frac{2\ .\ 1.48\text{ M}}{6.3\text{ M}} = \mathbf{0.47}\ (\mathbf{S^{0.47-}})$$

$$n\ (Li_2S_n) = \frac{2}{m\ (S^{m-})} = \frac{2}{0.47} = \mathbf{4.3}\ (\mathbf{Li_2S_{4.3}})$$

**Equation 5.3.14 –** Calculating the concentration of 'dissolved sulfide' $[S^{2-}]$, where $V_{Fc^+}$ = volume of $FcBF_4$ solution used (in this case effectively 1 mL) in $cm^3$, $l$ = the UV-vis cuvette path length in cm and $\varepsilon_{Fc^+}^{620\text{ nm}}$ = the molar extinction coefficient of $FcBF_4$ at 620 nm in $M^{-1}\ cm^{-1}$. The average oxidation state of the dissolved sulfur ($S^{m-}$) is then calculated, as is the 'average polysulfide chain length' $Li_2S_n$.

The value obtained for the concentration of 'dissolved sulfide' $[S^{2-}]$ was 1.48 M, which gives an average oxidation state of the dissolved sulfur ($S^{m-}$) of $S^{0.47-}$ corresponding to an average polysulfide chain length ($Li_2S_n$) of $Li_2S_{4.3}$. This is very similar to that obtained for the 20 M $[S]_T^{sol.}$ $Li_2S_6$ polysulfide electrolyte solution prepared in Section 4.3.3, which gave an average oxidation state of the dissolved sulfur ($S^{m-}$) of $S^{0.48-}$ corresponding to an average polysulfide chain length ($Li_2S_n$) of $Li_2S_{4.2}$. This indicates that using the reverse titration method offers consistent results to that of the standard titration method, although a much larger initial volume of polysulfide electrolyte solution can be used to prepare the initial solution and all other solutions can be prepared from that by diluting aliquots with $FcBF_4$ in DOL electrolyte solution. This minimises the error associated with using small volumes of the viscous concentrated polysulfide electrolyte solutions. To improve upon this method further, the density of the prepared polysulfide electrolyte solution could be measured using a small (e.g. 1 mL) volumetric flask and then the initial volume of polysulfide electrolyte solution used could be weighed and the exact volume calculated. This could further enhance the precision of the technique.

In this chapter, two methods have been developed to quantitatively determine the concentration of total dissolved sulfur $[S]_T^{sol.}$ and the concentration of 'dissolved sulfide' $[S^{2-}]$, which can be used with the total dissolved sulfur to give the average oxidation state of the dissolved sulfur ($S^{m-}$). Whilst these methods need to be further optimised in order to

minimise error, they offer a simple and reliable method to quantitatively analyse polysulfide electrolyte solutions that enable the polysulfide solubility limits of electrolytes to be determined, as well as identification and quantification of any remaining precipitate. Additionally, these techniques have enabled the construction of the first experimental ternary phase diagram for a Li-S battery system, which has allowed us to make predictions regarding the equilibrium discharge and charge profiles.

## 5.4 – Conclusions and Further Work

During this chapter, two simple and reliable methods have been successfully designed that quantitatively analyse the polysulfide composition in prepared polysulfide electrolyte solutions. In particular, a gravimetric analysis technique has been developed to measure the concentration of total dissolved sulfur $[S]_T^{sol.}$ and a UV-vis spectroscopic redox titration has been developed to measure the average oxidation state of the dissolved sulfur ($S^{m-}$).

The gravimetric analysis method utilises the low solubility of $BaSO_4$ and it was precisely able to determine the concentration of total dissolved sulfur $[S]_T^{sol.}$ in a prepared 1 M $[S]_T^{sol.}$ $Li_2S_6$ polysulfide electrolyte to be 1.03 ± 0.02 M $[S]_T^{sol.}$. This method avoids the use of thorin indicator, which is a highly toxic arsenic compound. To identify the small source of inaccuracy, spectroscopic techniques such as IR or Raman, could be used to identify any possible non-crystalline impurities that could be present and should be considered in future analysis. Furthermore, to avoid any error associated with the auto-pipette, the density of the prepared polysulfide electrolyte solutions could be measured using a small volumetric flask (e.g. 1 mL) and then the volumes of polysulfide electrolyte solutions could be weighed in order to calculate exact volume.

The UV-vis spectroscopic redox titration utilises the high redox potential of ferrocene/ferrocenium ($Fc/Fc^+$, ~ 3.2 V vs. $Li/Li^+$) to quantitatively oxidise the polysulfides to sulfur. On adding aliquots of a prepared polysulfide electrolyte solution to a solution of $Fc^+$, the change in $Fc^+$ concentration can be used to determine the 'dissolved sulfide' concentration [$S^{2-}$]. The change in $Fc^+$ concentration is determined by measuring the change in a characteristic $Fc^+$ absorption peak at 620 nm in the UV-vis absorption spectrum. Using this method, the concentration of 'dissolved sulfide' present [$S^{2-}$] in a prepared 1 M $[S]_T^{sol.}$ $Li_2S_6$ polysulfide electrolyte was measured to be 0.163 ± 0.006 M, which gave an average oxidation state of the dissolved sulfur ($S^{0.33-}$) and an average polysulfide chain length of $Li_2S_{6.1}$. To optimise the technique further and minimise error, the quantity of $FcBF_4$ in DOL used for each measurement should be weighed and the volume used calculated using the density of DOL. This should minimise the error associated with using the auto-pipette.

Once these methods had been successfully developed, concentrated polysulfide electrolyte solutions were analysed (*experimental data in Section 5.3.3 was obtained by John W. Smith*) in order to determine the polysulfide composition when the electrolyte (1 M LiTFSI in DOL) was fully saturated with polysulfides, i.e. the congruent solution. The solutions analysed were prepared as 10 M $[S]_T^{sol.}$ $Li_2S_8$, 20 M $[S]_T^{sol.}$ $Li_2S_8$, 10 M $[S]_T^{sol.}$ $Li_2S_6$ and 20 M $[S]_T^{sol.}$ $Li_2S_6$ in an attempt to achieve saturation. Using the developed methods, it was possible to determine that the congruent solution possessed a concentration of total dissolved sulfur $[S]_T^{sol.}$ of ~ 6 M and an average oxidation state of the dissolved sulfur ($S^{m-}$) of $S^{0.45-}$ corresponding to an average polysulfide chain length ($Li_2S_n$) of $Li_2S_{4.5}$. Using this data, it was possible to construct an experimental ternary phase diagram of the $S_8$-$Li_2S$-electrolyte system, which was used to rationalise the effect of changing the sulfur to electrolyte ratio on the Li-S battery equilibrium discharge profile. This was also able to explain the one equilibrium discharge plateau observed by Cuisinier *et al.* using non-solvents, which possess very low polysulfide solubility.[14]

Concentrated polysulfide electrolyte solutions are viscous and only small volumes are required to fully react with the $FcBF_4$ in DOL solution. In order to improve the associated errors with extracting such small volumes of a viscous solution, a reverse titration could be performed. This was successfully demonstrated using a freshly prepared 20 M $[S]_T^{sol.}$ $Li_2S_6$ polysulfide electrolyte solution for which similar values of the average oxidation state of the dissolved sulfur ($S^{0.47-}$, previously $S^{0.48-}$) and the average polysulfide chain length ($Li_2S_{4.3}$, previously $Li_2S_{4.2}$) were measured as when performing the standard titration. The advantage of using the reverse titration method is that the volume of polysulfide electrolyte solution initially used can be much larger and even exceed the volume required for complete reaction with the $FcBF_4$ in DOL. The initially prepared solution of polysulfide electrolyte and $FcBF_4$ in DOL can then be 'diluted' with more $FcBF_4$ in DOL. This reduces the errors associated with extracting such small volumes of viscous solutions.

## 5.5 – References


1. N. A. Cañas, D. N. Fronczek, N. Wagner, A. Latz and K. A. Friedrich, *J. Phys. Chem. C*, 2014, **118**, 12106-12114.

2. S. Thieme, J. Bruckner, A. Meier, I. Bauer, K. Gruber, J. Kaspar, A. Helmer, H. Althues, M. Schmuck and S. Kaskel, *J. Mater. Chem. A*, 2015, **3**, 3808-3820.

3. R. D. Rauh, F. S. Shuker, J. M. Marston and S. B. Brummer, *J. Inorg. Nucl. Chem.*, 1977, **39**, 1761-1766.

4. M. Wild, L. O'Neill, T. Zhang, R. Purkayastha, G. Minton, M. Marinescu and G. J. Offer, *Energ. Environ. Sci.*, 2015, **8**, 3477-3494.

5. D. Zheng, X. R. Zhang, C. Li, M. E. McKinnon, R. G. Sadok, D. Y. Qu, X. Q. Yu, H. S. Lee, X. Q. Yang and D. Y. Qu, *J. Electrochem. Soc.*, 2015, **162**, A203-A206.

6. K. A. See, M. Leskes, J. M. Griffin, S. Britto, P. D. Matthews, A. Emly, A. Van der Ven, D. S. Wright, A. J. Morris, C. P. Grey and R. Seshadri, *J. Am. Chem. Soc.*, 2014, **136**, 16368-16377.

7. F. C. Campbell, *Phase Diagrams: Understanding the Basics*, ASM International, 2012.

8. G. Schwarzenbach and A. Fischer, *Helv. Chim. Acta*, 1960, **43**, 1365-1390.

9. D. L. Reger, S. R. Goode and D. W. Ball, *Chemistry: Principles and Practice*, Cengage Learning, 2009.

10. D. R. Lide, *CRC Handbook of Chemistry and Physics, 85th Edition*, Taylor & Francis, 2004.

11. M. Miyake, I. Minato, H. Morikawa and S. Iwai, *Am. Mineral.*, 1978, **63**, 506-510.

12. Y. Zhao, M. Hong, N. Bonnet Mercier, G. Yu, H. C. Choi and H. R. Byon, *Nano Lett.*, 2014, **14**, 1085-1092.

13. W. A. Henderson, N. R. Brooks and V. G. Young, *Chem. Mater.*, 2003, **15**, 4685-4690.

14. M. Cuisinier, P. E. Cabelguen, B. D. Adams, A. Garsuch, M. Balasubramanian and L. F. Nazar, *Energ. Environ. Sci.*, 2014, **7**, 2697-2705.

# 6 – Quantitative GITT Analysis using a Model Redox System

## 6.1 – Introduction

Galvanostatic intermittent titration technique (GITT) is an electrochemical technique, which utilises both steady-state and transient potential measurements to obtain useful information on the kinetic and thermodynamic properties of an electrochemical system (see Chapter 2.3.3 for full details and derivation). This includes the measurement of steady-state (or resting) potentials, which can be used to determine the potential of the system at equilibrium, whilst also removing the effect of IR drop; the transient (or under current) potentials, which with the steady-state potential allows the overpotential to be calculated, giving information on the electrode kinetics; the internal cell resistance, which gives information on the change in electrolyte conductivity or electrode passivation during cycling and diffusion coefficients, which give valuable information on mass transport. The technique, which was first introduced by Weppner and Huggins in 1977, involves a series of current pulses, each followed by a relaxation period where no current passes through the cell.[1] Whilst the technqiue has been widely used to probe electrode materials for Li-ion batteries, including both positive and negative electrode materials, its use in analysing Li-S batteries has been limited.[2-5]

However, there are a few studies in the literature that have used GITT to investigate the Li-S battery. Kim *et al.* used GITT to investigate the activation process of micropore-confined sulfur within hierarchical porous carbon.[6] In particular, they used GITT to determine the internal resistance of the Li-S battery during discharge and charge, relating the change in resistance to physical processes occurring within the cell, such as $Li_2S$ formation and dissolution. They performed current pulses of 5 minutes duration at C/10 rate (167.5 mA $g_S^{-1}$) to measure the 'closed-circuit voltage' followed by 10 minute relaxations to measure the 'quasi-open-circuit voltage'. Walus *et al.* used GITT to give insights into the electrochemical mechanism of the Li-ion/$Li_2S$ system using non-woven carbon paper as a current collector, focussing particularly on the first charge, which is known to be problematic due to the insulating nature of $Li_2S$ (conductivity = $10^{-13}$ S $cm^{-1}$).[7, 8] They used GITT to observe and compare the 'under current potential' and 'equilibrium potential', which can be used to measure the 'polarisation' or overpotential. They performed current pulses of 20 minutes at a current equivalent to C/20 rate followed

by relaxation periods of 30 minutes. They mention that the short relaxation time was selected in order to limit the shuttle/self-discharge mechanism but despite the short time, it was still long enough to reach a stable and reproducible potential. Cuisinier *et al.* used GITT to measure 'quasi OCV' of the Li-S battery discharge profiles comparing the use of non-solvents (LiTFSI dissolved in ACN/HFE) to a more traditional electrolyte system (LiTFSI in DOL/DME).[9] They determined that the non-solvent electrolyte system produced one equilibrium plateau on discharge unlike the two equilibrium discharge plateaux observed in more traditional Li-S battery electrolyte systems. They performed current pulses of 20 minutes duration at C/10 rate followed by relaxation for 60 minutes. Busche *et al.* used GITT to study the kinetics during the cycling of Li-S batteries, to evaluate the relaxation behaviour between different states of discharge/charge and to measure the resting potential.[10] They acknowledge that performing a quantitative analysis on the GITT data of a Li-S battery to determine diffusion coefficients would be complex and that the large number of processes occurring, along with the lack of knowledge regarding the polysulfide speciation and their equilibria makes analysis difficult. However, they state that it is still possible to obtain qualitative information on the cell kinetics. They perform current pulses of 30 minutes duration at C/10 rate followed by a relaxation period of 20 hours. Park *et al.* used GITT to study room temperature ionic liquids, comparing the resting potential and transient potentials to determine the 'overvoltage', which they relate to the rate of the electrode kinetics and use to indicate $Li_2S$ formation.[11] They performed current pulses of 10 minutes duration at C/12 rate (139 mA $g^{-1}_S$) followed by relaxation, which instead of being limited by time, continued until the voltage change became less than 15 mV $h^{-1}$. Similar to GITT, Lacey *et al.* used an intermittent current interrupt method to determine the internal resistance of Li-S batteries.[12, 13] They interrupted the applied current during the galvanostatic cycling of Li-S batteries to map the internal resistance and they illustrated that cell failure was associated with rapidly increasing resistance. These studies have nicely demonstrated that GITT can be employed in Li-S battery analysis and used to determine mechanistic characteristics, such as solid precipitation and the slow kinetics of $Li_2S$. However, they all use GITT qualitatively and there has not yet been any quantitative analysis using GITT to determine the diffusion coefficients of the active sulfur species in Li-S batteries. This is despite such analysis being common practice when using GITT to investigate Li-ion battery materials.

The Li-S battery is a complex system, possessing several unknown redox processes, a variety of unknown intermediate polysulfide species all with unknown equilibria. Furthermore, the active species are present at high concentrations (assuming high sulfur to electrolyte ratio) and precipitate forms at the end of discharge (solid $Li_2S$) and charge (solid $S_8$), which causes further complications. However, GITT has the potential to obtain important quantitative information regarding the mass transport of species within the Li-S battery during cycling. GITT does not require the concentration of the species or the number of electrons involved in the redox process to be known, which gives it a distinct advantage over more traditional methods of measuring properties of mass transport.

However, in order to determine the suitability of using GITT to quantitatively analyse the diffusion coefficients of the sulfur species present in the electrolyte, the GITT method has to be verified using a solution-based model redox system. Unlike the Li-S cell, the model redox system will possess a reversible one-electron redox process for which the diffusion coefficient has already been quantitatively determined for comparison. In addition to this, the model redox system will be present in low concentrations ($\leq 5$ mM) so that the extent of 'discharge' and 'charge' will not affect the mobility of the redox ions and all redox species will be soluble in the electrolyte, preventing the complications associated with solid formation/dissolution.

## 6.2 – Experimental Details

### 6.2.1 – Synthesis of Ethyl Viologen Ditriflate ($EtV(OTf)_2$)

Ethyl viologen diiodide ($EtVI_2$, 1.00115 g, 2.14 mmol, 99%, Sigma-Aldrich) and silver triflate (Ag(OTf), 1.0972 g, 4.27 mmol, ≥ 99%, Sigma-Aldrich) were dissolved in deionised water (~ 50 mL). On addition of the Ag(OTf) to the $EtVI_2$ dissolved in water, a yellowish precipitate crashed out of solution, assumed to be the insoluble silver iodide (AgI). The mixture was then filtered to remove the unwanted AgI solid from the filtrate containing the desired $EtV(OTf)_2$ product. The water was then removed from the filtrate by evaporation leaving a white powder, assumed to be $EtV(OTf)_2$. The white powder was then re-dissolved in the minimum amount of hot ethanol and re-filtered to remove any impurities. The ethanol was then removed from the filtrate by evaporation leaving a white crystalline powder. This was collected in a vial and dried under vacuum (< 0.2 mbar) at 120 °C for ~ 40 hours before taking into an argon-filled glovebox (oxygen and water content < 5 ppm) where it was stored until use.

$$EtVI_{2\,(aq.)} + 2\ Ag(OTf)_{(aq.)} \rightarrow EtV(OTf)_{2\,(aq.)} + 2\ AgI_{(s)}$$

**Equation 6.2.1 –** Synthesis of $EtV(OTf)_2$ using ion exchange between $EtVI_2$ and Ag(OTf)

### 6.2.2 – Cyclic Voltammetry

For cyclic voltammetry measurements, a U-cell configuration was used (for details on construction see Section 2.2.5). All cyclic voltammetry measurements were made using a multichannel potentiostat (VMP2, Bio-Logic) using EC-Lab software (Bio-Logic). For $FcBF_4$ (3 mM in 1 M LiTFSI in DOL), scan rates of 200, 100, 50, 20, 10 and 5 mV $s^{-1}$ were measured for 3 cycles each and the potential was held at 3.5 V for 2 minutes between changing scan rates to ensure that any Fc had been re-oxidised back into $Fc^+$, giving a starting current close to 0 mA. Two potential ranges were used: 3.5 – 2.9 V and 3.8 – 2.6 V. For $EtVI_2$ (5 mM in 1 M LiTFSI in DOL), scan rates of 200, 100, 50, 20, 10, 5 and 2 mV $s^{-1}$ were measured for 3 cycles each and the potential was held at 2.7 V for 2 minutes before changing scan rates to ensure that any $EtV^+$ had been re-oxidised back into $EtV^{2+}$, giving a starting current close to 0 mA. Three potential ranges were used: 2.7 – 2.2 V (all scan rates), 2.7 – 1.5 V (100 mV $s^{-1}$ only) and 3.8 – 1.5 V (100 mV $s^{-1}$ only). For

$EtV(OTf)_2$ (5 mM in 1 M LiTFSI in DOL), scan rates of 200, 100, 50, 20, 10, 5 and 2 mV $s^{-1}$ were measured for 3 cycles each and the potential was held at 2.7 V for 2 minutes before changing scan rates to ensure that any $EtV^+$ had been re-oxidised back into $EtV^{2+}$, giving a starting current close to 0 mA. Two potential ranges were used: 2.7 – 2.2 V (all scan rates) and 3.8 – 1.5 V (100 mV $s^{-1}$ only).

### 6.2.3 – Galvanostatic Pulse Technique (Sand Equation)

All galvanostatic (constant current pulse) measurements were made using a multichannel potentiostat (VMP2, Bio-Logic) using EC-Lab software (Bio-Logic). For the glass U-cell, a glassy carbon disc working electrode (Ø = 0.3 cm) was used to analyse $EtV(OTf)_2$ (5 mM in 1 M LiTFSI in DOL) using current densities of 0.14, 0.18, 0.21, 0.28, 0.35, 0.42, 0.50, 0.57, 0.71 and 0.85 mA $cm^{-2}$. Between measurements, the potential was held at 2.7 V for 2 minutes between changing current densities. For the Swagelok cell with an LICGC separator, a carbon coated aluminium foil working electrode (Ø = 1.5 cm, Figure 6.2.1) was used to analyse $EtV(OTf)_2$ (5 mM in 1 M LiTFSI in DOL) using current densities of 0.14, 0.17, 0.20 and 0.23 mA $cm^{-2}$. Between measurements the cell was charged to 2.8 V using a low current of 0.006 mA $cm^{-2}$ and allowed to rest for 20 minutes before changing current densities.

### 6.2.4 – Gavanostatic Intermittent Titration Technique (GITT)

Using a Bio-Logic VMP2, GITT was performed on the prepared Swagelok cell with an LICGC separator using a carbon coated aluminium foil working electrode (Ø = 1.5 cm, Figure 6.2.1). The OCP was measured for 60 minutes, followed by 5 seconds of discharge ($i$ / $I$ = 0.2 mA / 0.11 mA $cm^{-2}$) and then 60 minutes of rest. The pulse/rest procedure was repeated until it was determined that the $EtV^{2+}$ had been completely reduced to $EtV^+$, indicated by the rest potential reaching 2.3 V. During the current pulse, data points were recorded every 1 mV or 0.1 s, whereas during rest, data points were record every 1 mV or 600 s.

### 6.2.5 – Preparation of a Metal Swagelok Cell (Ø = 1 inch) with Ohara Glass

For full details on the cell construction, see Section 2.2.1. In this chapter, only Swagelok cells with an internal diameter of 1 inch were used in order to accommodate the LICGC separator and a current collector cap with an embedded O-ring (Size = BS019, FFKM 260B, Polymax Limited) was used (Figure 6.2.1). In an argon filled glove box, the rest of the metal Swagelok cell was assembled using the following components in order: a lithium metal negative electrode (Ø = 25 mm), a glass-fibre separator (GF/F, Whatman®, Ø = 25 mm, dried), 1 M LiTFSI in DOL electrolyte (0.25 mL), a piece of LICGC separator (Ø = 1 inch, Ohara Corporation), two glass-fibre separators (GF/F, Whatman®, Ø = 18 mm, dried), 5 mM $EtV(OTf)_2$ in 1 M LiTFSI in DOL electrolyte (0.25 mL) and a disc of carbon coated aluminium foil (d = 16 μm, Ø = 15 mm).

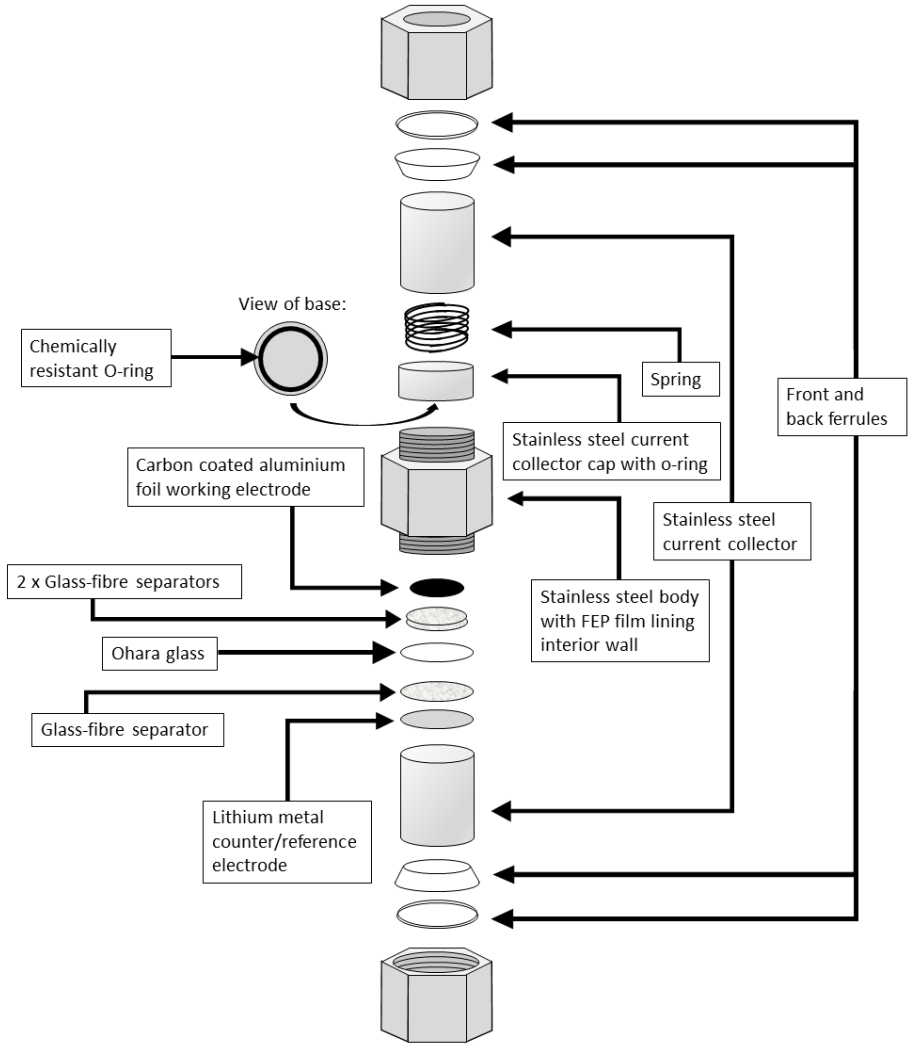


**Figure 6.2.1 -** Schematic of the Swagelok® cell with LICGC (Ohara) and current collector cap with embedded O-ring, which was always constructed from the bottom up

## 6.3 – Results and Discussion

In order to analyse GITT and evaluate its ability to quantitatively determine parameters such as the diffusion coefficient (*D*), an appropriate model redox system was required for analysis. The desired redox system needed to possess a one-electron redox process that is electrochemically reversible, both the oxidised and reduced forms should be soluble in the chosen Li-S battery electrolyte system (1 M LiTFSI in DOL) and it should also be stable, both chemically and electrochemically. Three potential candidates were investigated: ferrocenium tetrafluoroborate ($FcBF_4$, $Fc/Fc^+$), ethyl viologen diiodide ($EtVI_2$) and ethyl viologen ditriflate ($EtV(OTf)_2$). Using cyclic voltammetry, the electrochemical redox processes associated with each candidate were characterised, including the electrochemically reversibility. Additionally, the diffusion coefficients of each redox system were determined. Once a suitable model redox system had been chosen, it was analysed using galvanostatic pulse techniques and the experimental transition times were determined. Since GITT is derived from the Sand equation and shares much of the same theory, the diffusion coefficients calculated using the Sand equation from the measured transition times need to be comparable to the diffusion coefficients determined using cyclic voltammetry. In this way, the diffusion coefficients determined using GITT should be comparable to those determined using cyclic voltammetry. Once this had been demonstrated, the model redox system was used to quantitatively investigate GITT using a specially designed Swagelok cell design.

### 6.3.1 – Model Redox Systems: Ferrocenium Tetrafluoroborate ($FcBF_4$)

Ferrocenium tetrafluoroborate ($FcBF_4$) was investigated for use as a model redox system (Figure 6.3.1). Using cyclic voltammetry, it was observed that $FcBF_4$ possesses one electrochemical redox process when scanned between potential limits of 3.8 V and 2.6 V (Figure 6.3.2).

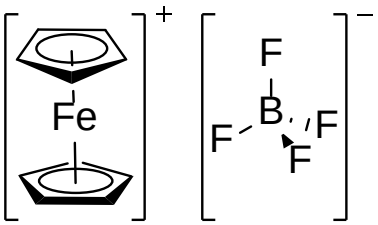


**Figure 6.3.1 –** Structure of ferrocenium tetrafluoroborate ($FcBF_4$)

This electrochemical redox process is attributed to the one-electron redox reaction $Fc/Fc^+$ and the formal potential ($E_e^{0'}$) is measured at +3.24 V vs. $Li/Li^+$. To assess the electrochemical reversibility of the redox process ($Fc/Fc^+$) and determine the diffusion coefficient of $Fc^+$, cyclic voltammetry was performed at various different scan rates between potential limits of 3.5 and 2.9 V (Figure 6.3.3). Between changing scan rates, the potential was held at 3.5 V for at least 2 minutes to ensure that any Fc had been re-oxidised back into $Fc^+$, giving a starting current close to 0 mA. The peak currents and potentials ($I_{pc}$, $I_{pa}$, $E_{pc}$, $E_{pa}$) were then recorded at the different scan rates (Table 6.3.1, for the method of calculating peak currents/potentials see Chapter 2.3.1).

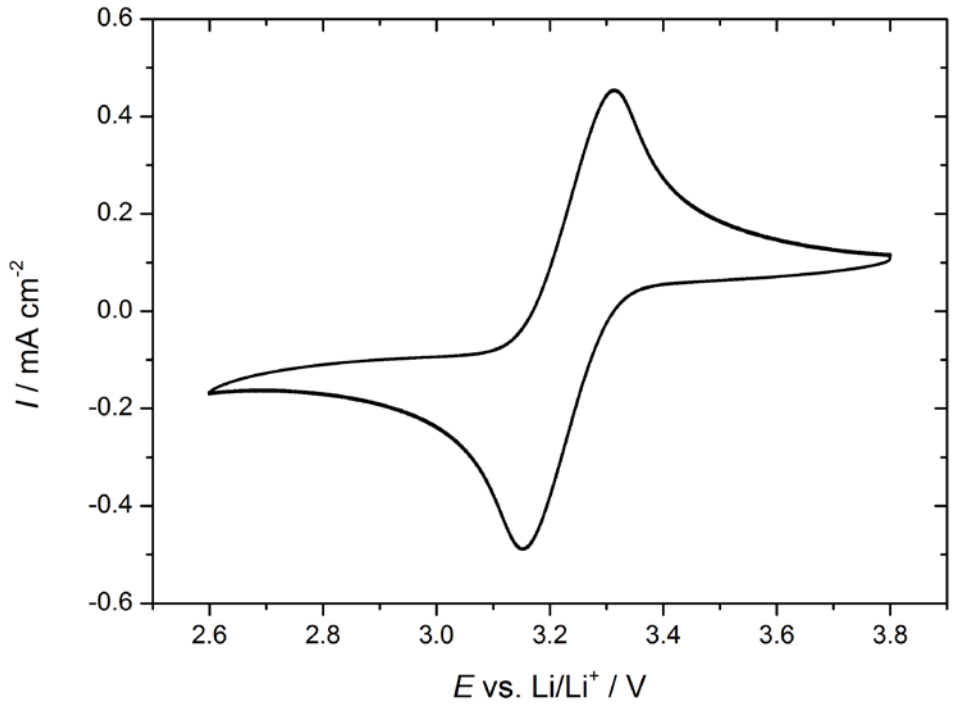


**Figure 6.3.2 –** Cyclic voltammetry measurement at a scan rate 100 mV $s^{-1}$ between the potential limits of 3.8 V and 2.6 V. The two-compartment U-cell consisted of a glassy carbon working electrode (Ø = 3 mm), 3 mM $FcBF_4$ dissolved in 1 M LiTFSI in DOL electrolyte in the working electrode compartment and 1 M LiTFSI in DOL electrolyte in the counter/reference electrode compartments and a lithium metal counter/reference electrode. The second cycle is shown.

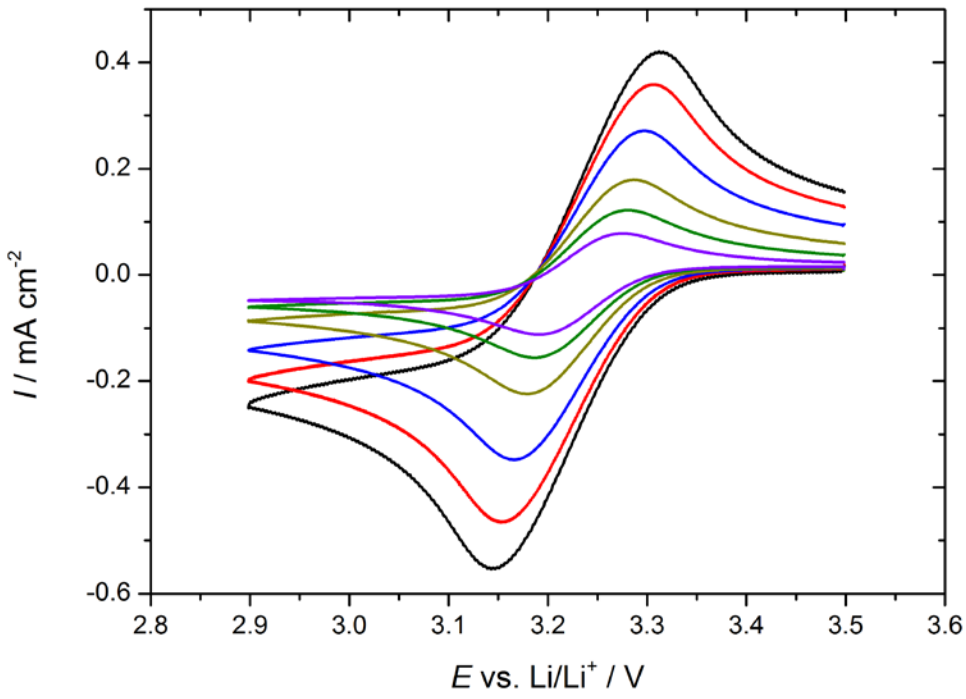


**Figure 6.3.3 –** Cyclic voltammetry measurements at scan rates of **— 200** mV $s^{-1}$, **— 100** mV $s^{-1}$, **— 50** mV $s^{-1}$, **— 20** mV $s^{-1}$, **— 10** mV $s^{-1}$ and **— 5** mV $s^{-1}$. The two-compartment U-cell consisted of a glassy carbon working electrode (Ø = 3 mm), 3 mM $FcBF_4$ dissolved in 1 M LiTFSI in DOL electrolyte in the working electrode compartment and 1 M LiTFSI in DOL electrolyte in the counter/reference electrode compartments and a lithium metal counter/reference electrode. First cycles at specified scan rates are shown. Between changing the scan rates, the potential of the working electrode was held at 3.5 V for at least 2 minutes.

| Scan rate / mV $s^{-1}$ | $E_{pc}$ / V | $I_{pc}$ / mA $cm^{-2}$ | $E_{pa}$ / V | $I_{pa}$ / mA $cm^{-2}$ | $\Delta E$ / mV |
|---|---|---|---|---|---|
| 200 | 3.14 | -0.56 | 3.32 | 0.53 | 172.9 |
| 100 | 3.15 | -0.48 | 3.31 | 0.46 | 155.0 |
| 50 | 3.17 | -0.36 | 3.30 | 0.35 | 131.6 |
| 20 | 3.18 | -0.24 | 3.29 | 0.23 | 106.9 |
| 10 | 3.19 | -0.17 | 3.28 | 0.16 | 94.4 |
| 5 | 3.19 | -0.13 | 3.28 | 0.11 | 83.9 |

**Table 6.3.1 –** Peak currents ($I_{pc}$ and $I_{pa}$), peak potentials ($E_{pc}$ and $E_{pa}$) and peak-to-peak separation ($\Delta E$) at scan rates 200, 100, 50, 20, 10 and 5 mV $s^{-1}$. See Figure 6.3.3 for experimental details.

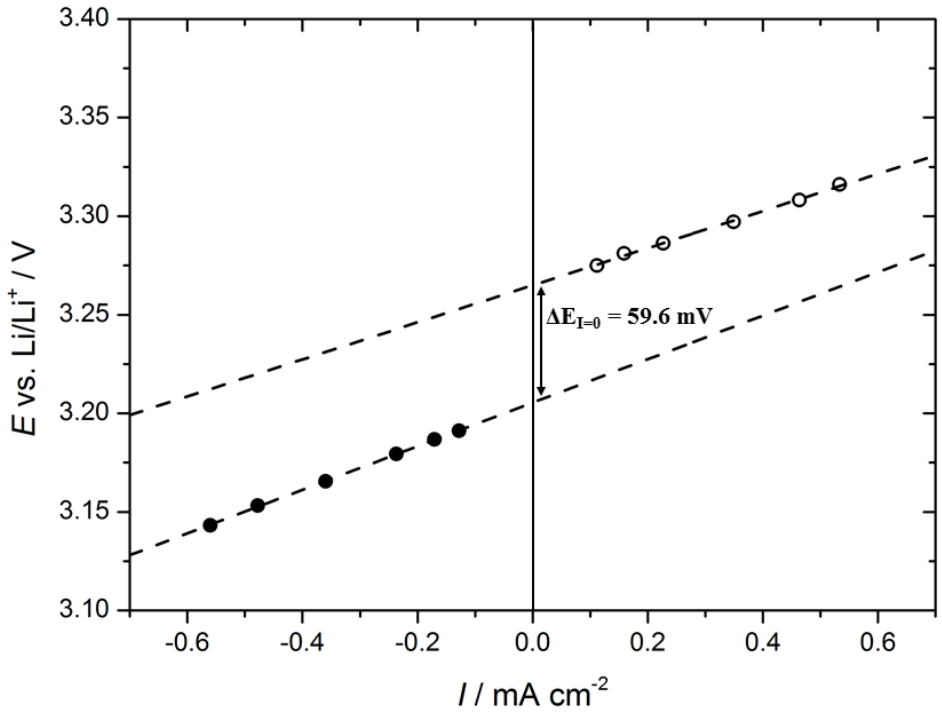


**Figure 6.3.4 –** Peak potentials ($E_{pc}$ and $E_{pa}$) plotted against the peak currents ($I_{pc}$ and $I_{pa}$) at different scan rates (200, 100, 50, 20, 10 and 5 mV $s^{-1}$). Linear trendlines have been used to determine the peak-to-peak separation at zero current ($\Delta E_{I=0}$). Reduction intercept = 3.2054 V and oxidation intercept = 3.2650 V.

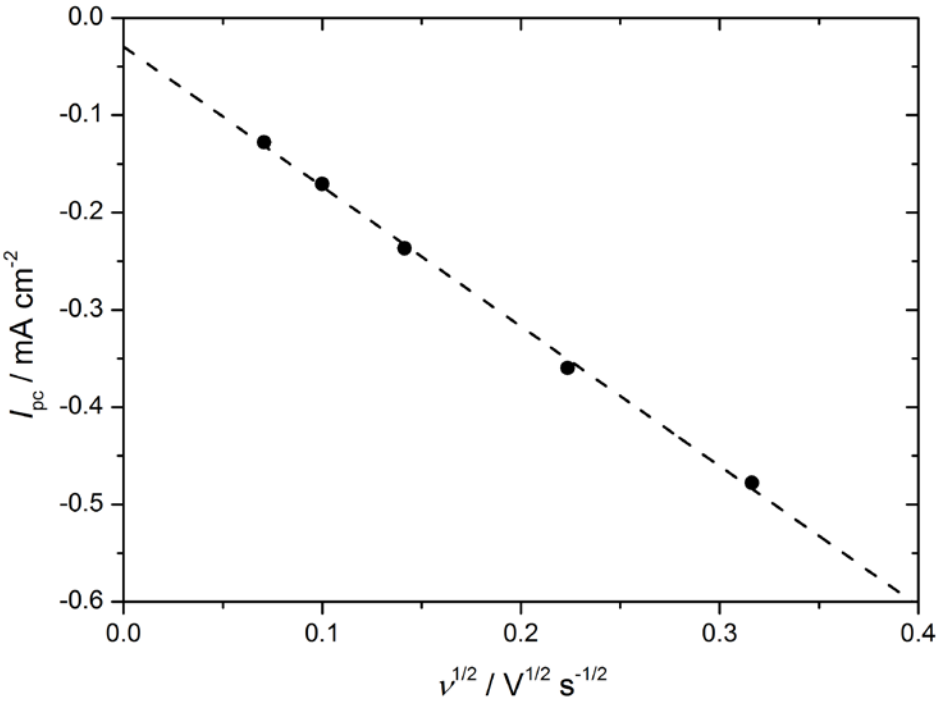


**Figure 6.3.5 –** Peak currents ($I_{pc}$) plotted against the square root of scan rate ($\nu^{1/2}$) at different scan rates (100, 50, 20, 10 and 5 mV $s^{-1}$). A linear trendline has been plotted and the slope (-1.44 mA $cm^{-2}$ $V^{-1/2}$ $s^{1/2}$) used in the Randles-Sevcik equation to determine $D_{Fc+}$.

The peak potentials ($E_{pc}$ and $E_{pa}$) were then plotted against the peak currents ($I_{pc}$ and $I_{pa}$) in order to assess the theoretical peak-to-peak separation at zero current ($\Delta E_{I=0}$) and assess the electrochemical reversibility of the $Fc/Fc^+$ redox pair (Figure 6.3.4). This enables the effect of resistance to be effectively removed. Using this plot, $\Delta E_{I=0}$ was determined to be 59.6 mV, which agrees with the theoretical peak-to-peak separation for reversible one-electron redox reactions (59/*n* mV) and so it can be assumed that the $Fc/Fc^+$ redox pair is electrochemically reversible. To determine the diffusion coefficient of $Fc^+$ ($D_{Fc+}$), the peak reduction current ($I_{pc}$) was plotted against the square root of the scan rate ($v^{1/2}$, Figure 6.3.5). Then using the measured slope (-1.44 x $10^{-3}$ A $cm^{-2}$ $V^{-1/2}$ $s^{1/2}$) and the Randles-Sevcik equation (Equation 6.3.1), $D_{Fc+}$ was determined to be 3.4 x $10^{-6}$ $cm^2$ $s^{-1}$.

$$i_p = (2.69 \times 10^5) n^{3/2} A c^* D^{1/2} v^{1/2}$$

**Equation 6.3.1 –** Randles-Sevcik equation, where $i_p$ is the peak current in A, *n* is the number of electrons involved in the electrode reaction, *A* is the electrode area in $cm^2$, $c^*$ is the solution species concentration in the bulk solution in mol $cm^{-3}$, *D* is the diffusion coefficient in $cm^2$ $s^{-1}$ and *v* is the scan rate in V $s^{-1}$.

Whilst the $Fc/Fc^+$ redox pair offers a reversible one-electron redox process, its formal potential ($E_e^{0'}$ = +3.24 V vs. $Li/Li^+$) is much higher than the formal potential for $S_8/S_n^{2-}$ ($E_e^{0'}$ = ~2.4 V vs. $Li/Li^+$). At these higher potentials, it was observed that DOL has the potential to polymerise slowly overtime. Whilst this does not occur in the timescales used for cyclic voltammetry experiments, GITT measurements usually take several days or even weeks to perform due to the long relaxation periods required for the system to equilibrate. In order to avoid any complications associated with DOL polymerisation, a model redox system with a formal potential closer to that of the Li-S battery nominal potential was desired.

### 6.3.2 – Model Redox Systems: Ethyl Viologen Diiodide ($EtVI_2$)

Ethyl viologen diiodide ($EtVI_2$) was investigated as an alternative reversible redox couple (Figure 6.3.6). Using cyclic voltammetry, it was observed that $EtVI_2$ possesses two electrochemical redox processes when scanned between potential limits of 2.7 V and 1.5 V (Figure 6.3.7).

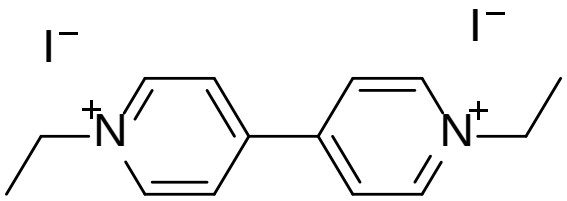


**Figure 6.3.6 –** Structure of ethyl viologen diiodide ($EtVI_2$)

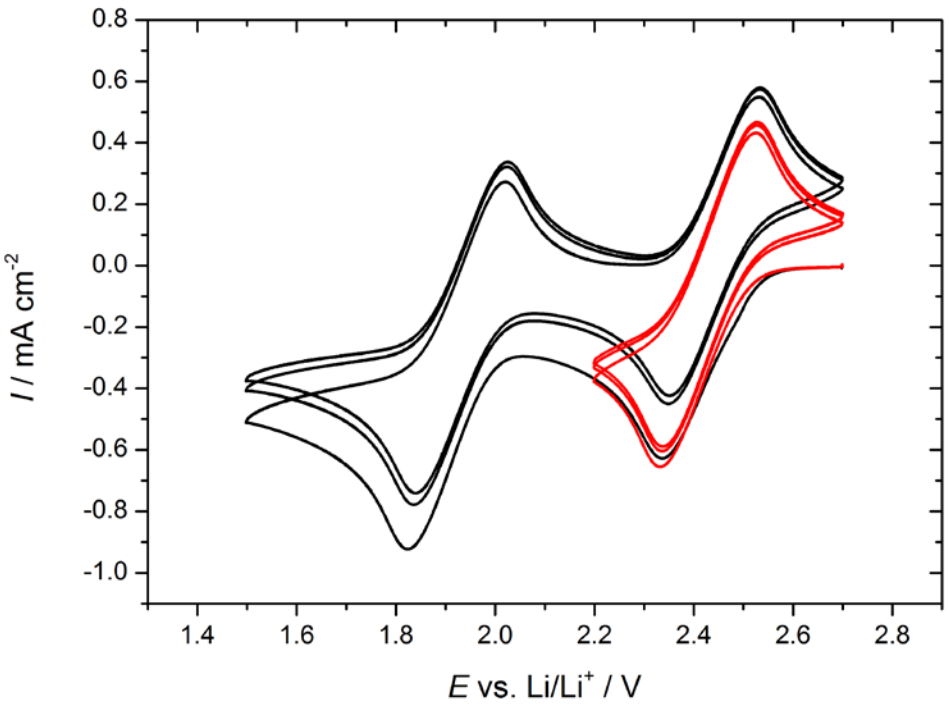


**Figure 6.3.7 –** Cyclic voltammetry measurements at scan rates of 100 mV $s^{-1}$ between the potential limits of **— 2.7 V and 1.5 V** and **— 2.7 and 2.2 V**. The two-compartment U-cell consisted of a glassy carbon working electrode (Ø = 3 mm), 5 mM $EtVI_2$ dissolved in 1 M LiTFSI in DOL electrolyte in the working electrode compartment and 1 M LiTFSI in DOL electrolyte in the counter/reference electrode compartments and a lithium metal counter/reference electrode. First three cycles at specified scan rate are shown. Before each CV, the potential of the working electrode was held at 2.7 V for at least 2 minutes.

On scanning from 2.7 V to 1.5 V, the first reduction peak observed at approximately 2.34 V represents the one-electron reduction of $EtV^{2+}$ to $EtV^{+}$. The second reduction peak observed at approximately 1.82 V represents the one-electron reduction of $EtV^{+}$ to $EtV^{0}$. On the return scan from 1.5 V back to 2.7 V, two oxidation peaks are observed. The first oxidation peaks observed at 2.02 V represents the one-electron oxidation of $EtV^{0}$ to $EtV^{+}$ and the second oxidation peak at 2.53 V represents the one-electron oxidation of $EtV^{+}$ to $EtV^{2+}$. Both of the observed redox processes appear electrochemically reversible, although further analysis would be required to confirm this. In order to analyse the redox processes of $EtVI_2$ further, the upper potential limit was extended from 2.7 V to 3.8 V (Figure 6.3.8).

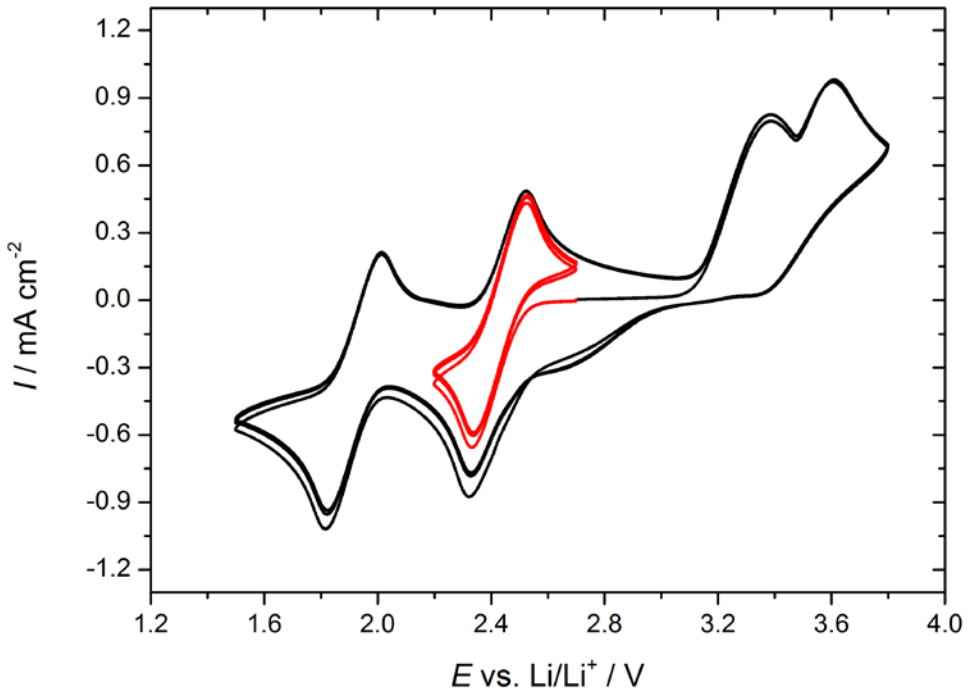


**Figure 6.3.8 –** Cyclic voltammetry measurements at scan rates of 100 mV $s^{-1}$ between the potential limits of **— 3.8 V and 1.5 V** and **— 2.7 and 2.2 V**. The two-compartment U-cell consisted of a glassy carbon working electrode (Ø = 3 mm), 5 mM $EtVI_2$ dissolved in 1 M LiTFSI in DOL electrolyte in the working electrode compartment and 1 M LiTFSI in DOL electrolyte in the counter/reference electrode compartments and a lithium metal counter/reference electrode. First three cycles at specified scan rate are shown. Before each CV, the potential of the working electrode was held at 2.7 V for at least 2 minutes.

On scanning from 2.7 V to 3.8 V, a further two oxidation peaks are observed, one at 3.4 V and the other at 3.6 V. These peaks can be attributed to the oxidation of the iodide to iodine *via* the formation of triodide (Equation 6.3.2), with similar iodide oxidation peaks reported elsewhere.[14, 15] On scanning from 3.8 V to 1.5 V, a further two reduction peaks can be observed, one at 3.4 V and 2.6 V. These peaks can be attributed to the reduction of iodine to iodide *via* the formation of the intermediate triiodide.

$$3I^- \rightarrow I_3^- + 2e^- \qquad (1)$$

$$I_3^- \rightarrow \frac{3}{2}I_2 + e^- \qquad (2)$$

$$---------- \qquad (3)$$

$$3I^- \rightarrow \frac{3}{2}I_2 + 3e^-$$

**Equation 6.3.2 –** Mechanism of iodide oxidation to iodine through the intermediate triiodide.[14] (1) Oxidation of iodide to intermediate triiodide, (2) oxidation of triiodide to iodine and (3) overall oxidation of iodide to iodine *via* triiodide.

To assess the electrochemical reversibility of the redox pair $EtV^+/EtV^{2+}$ and determine the diffusion coefficient of $EtV^{2+}$, cyclic voltammetry was performed at various different scan rates between potential limits of 2.7 V and 2.2 V (Figure 6.3.9). The redox pair $EtV^+/EtV^{2+}$ was chosen for analysis over $EtV/EtV^+$ since $EtVI_2$ was used to prepare the electrolyte solutions, enabling the initial (and bulk) concentration of $EtV^{2+}$ to be easily calculated. Between changing scan rates, the potential was held at 2.7 V for at least 2 minutes to ensure that any $EtV^+$ had been re-oxidised back into $EtV^{2+}$, giving a starting current close to 0 mA. The peak currents and potentials ($I_{pc}$, $I_{pa}$, $E_{pc}$, $E_{pa}$) were then recorded at the different scan rates (Table 6.3.2).

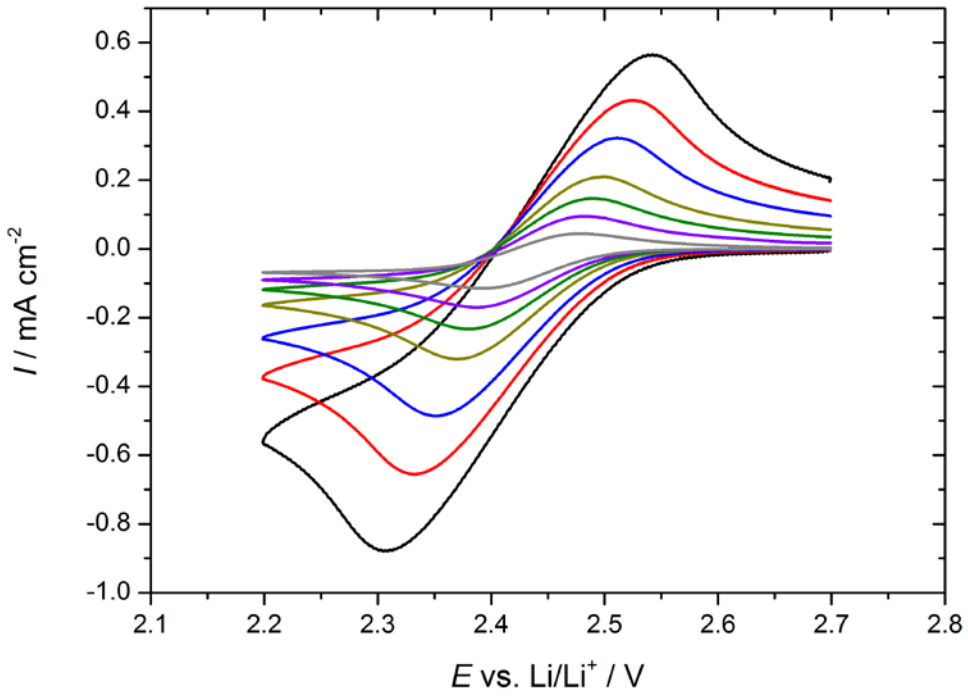


**Figure 6.3.9 –** Cyclic voltammetry measurements at scan rates of **— 200** mV $s^{-1}$, **— 100** mV $s^{-1}$, **— 50** mV $s^{-1}$, **— 20** mV $s^{-1}$, **— 10** mV $s^{-1}$, **— 5** mV $s^{-1}$ and **— 2** mV $s^{-1}$ between the potential limits of 2.7 V and 2.2 V. The two-compartment U-cell consisted of a glassy carbon working electrode (Ø = 3 mm), 5 mM $EtVI_2$ dissolved in 1 M LiTFSI in DOL electrolyte in the working electrode compartment and 1 M LiTFSI in DOL electrolyte in the counter/reference electrode compartments and a lithium metal counter/reference electrode. First cycles at specified scan rates are shown. Between changing the scan rates, the potential of the working electrode was held at 2.7 V for at least 2 minutes.

| Scan rate / mV $s^{-1}$ | $E_{pc}$ / V | $I_{pc}$ / mA $cm,^{-2}$ | $E_{pa}$ / V | $I_{pa}$ / mA $cm,^{-2}$ | $\Delta E$ / mV |
|---|---|---|---|---|---|
| 200 | 2.31 | -0.87 | 2.55 | 0.61 | 239.0 |
| 100 | 2.33 | -0.65 | 2.53 | 0.52 | 195.3 |
| 50 | 2.35 | -0.48 | 2.51 | 0.41 | 160.9 |
| 20 | 2.37 | -0.32 | 2.50 | 0.28 | 129.1 |
| 10 | 2.38 | -0.23 | 2.49 | 0.20 | 110.0 |
| 5 | 2.39 | -0.17 | 2.48 | 0.15 | 96.4 |
| 2 | 2.39 | -0.11 | 2.48 | 0.10 | 84.9 |

**Table 6.3.2 –** Peak currents ($I_{pc}$ and $I_{pa}$), peak potentials ($E_{pc}$ and $E_{pa}$) and peak-to-peak separation (ΔE) at scan rates 200, 100, 50, 20, 10, 5 and 2 mV $s^{-1}$. See Figure 6.3.9 for experimental details.

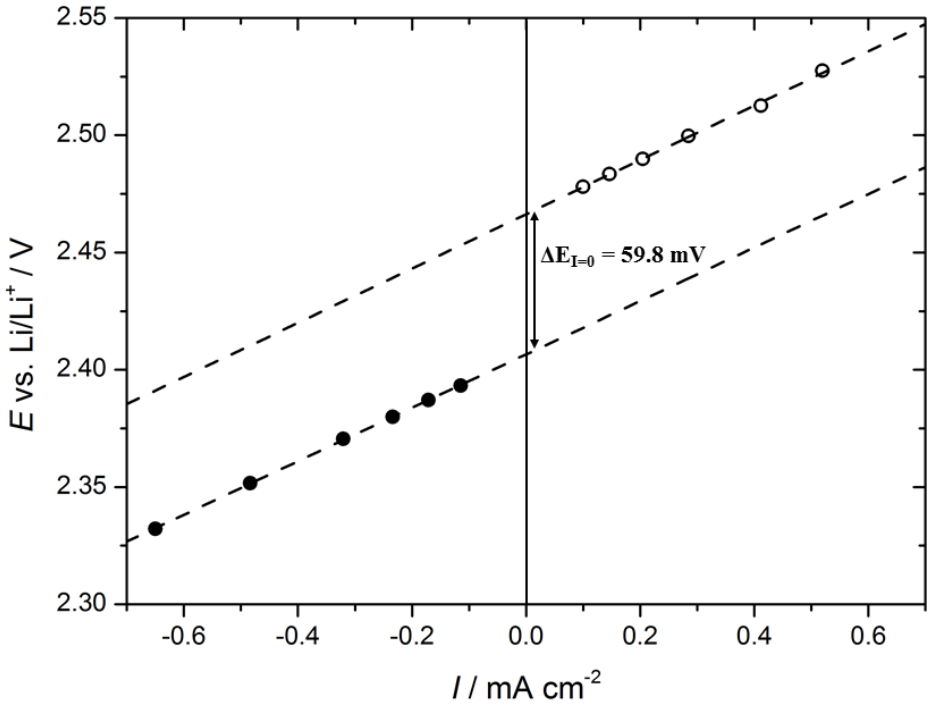


**Figure 6.3.10 –** Peak potentials ($E_{pc}$ and $E_{pa}$) plotted against the peak currents ($I_{pc}$ and $I_{pa}$) at different scan rates (100, 50, 20, 10, 5 and 2 mV $s^{-1}$). Linear trendlines have been used to determine the peak-to-peak separation at zero current ($\Delta E_{I=0}$). Reduction intercept = 2.4065 V and oxidation intercept = 2.4663 V.

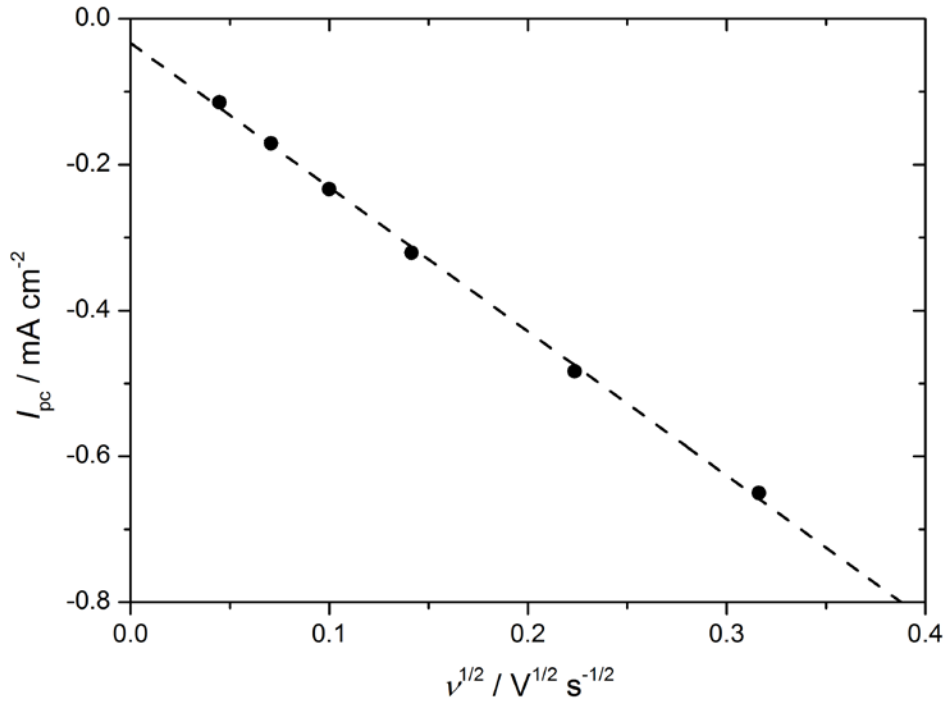


**Figure 6.3.11 –** Peak currents ($I_{pc}$) plotted against the square root of scan rate ($\nu^{1/2}$) at different scan rates (100, 50, 20, 10, 5 and 2 mV $s^{-1}$). A linear trendline has been plotted and the slope (-1.98 mA $cm^{-2}$ $V^{-1/2}$ $s^{1/2}$) used in the Randles-Sevcik equation to determine $D_{EtV2+}$.

The peak potentials ($E_{pc}$ and $E_{pa}$) were then plotted against the peak currents ($I_{pc}$ and $I_{pa}$) in order to assess the theoretical peak-to-peak separation at zero current ($\Delta E_{I=0}$) and assess the electrochemical reversibility of the $EtV^{+}/EtV^{2+}$ redox pair (Figure 6.3.10). This enables the effect of resistance to be effectively removed. Using this plot, $\Delta E_{I=0}$ was determined to be 59.8 mV, which is agrees with the theoretical peak-to-peak separation for reversible reactions (59/*n* mV) and so it can be assumed that the $EtV^{2+}/EtV^{+}$ redox pair is electrochemically reversible. To determine the diffusion coefficient of $EtV^{2+}$ ($D_{EtV2+}$), the peak reduction current ($I_{pc}$) was plotted against the square root of the scan rate ($v^{1/2}$, Figure 6.3.11). Then using the measured slope (-1.98 x $10^{-3}$ A $cm^{-2}$ $V^{-1/2}$ $s^{1/2}$), $D_{EtV2+}$ was determined to be 2.2 x $10^{-6}$ $cm^2$ $s^{-1}$. The $EtV^{+}/EtV^{2+}$ redox pair offers a reversible one-electron redox process and a suitable formal potential ($E_e^{0'}$ = +2.44 V vs. $Li/Li^{+}$), which is much lower than the formal potential determined for the $Fc/Fc^{+}$ redox pair ($E_e^{0'}$ = +3.24 V vs. $Li/Li^{+}$). Performing electrochemical measurements at these lower potentials should avoid any complication associated with DOL polymerisation. However, in order to avoid any complications associated with the $I^{-}/I_2$ redox pair, it was decided to synthesise and characterise $EtV(OTf)_2$, which should provide a suitable alternative for use as a model redox system.

### 6.3.3 – Model Redox Systems: Ethyl Viologen Ditriflate ($EtV(OTf)_2$)

Ethyl viologen ditriflate ($EtV(OTf)_2$) was synthesised *via* an ion exchange reaction, through direct combination of $EtVI_2$ and Ag(OTf) in solution (Equation 6.3.3).

$$EtVI_{2\ (aq.)} + 2\ Ag(OTf)_{\ (aq.)} \rightarrow EtV(OTf)_{2\ (aq.)} + 2\ AgI_{\ (s)}$$

**Equation 6.3.3 –** Synthesis of $EtV(OTf)_2$ using ion exchange between $EtVI_2$ and Ag(OTf)

Due to the low solubility of silver iodide (AgI), it crashes out of solution on formation, enabling the $EtV(OTf)_2$ dissolved in solution to be easily separated by filtration. The filtrate containing $EtV(OTf)_2$ was allowed to evaporate and the remaining solid was re-dissolved in the minimum amount of hot ethanol, which was filtered and re-crystallised for purification (see Section 6.2.1 for more details). Once the $EtV(OTf)_2$ product had been dried, cyclic voltammetry was performed between potential limits of 3.8 V and 1.5 V (Figure 6.3.12).

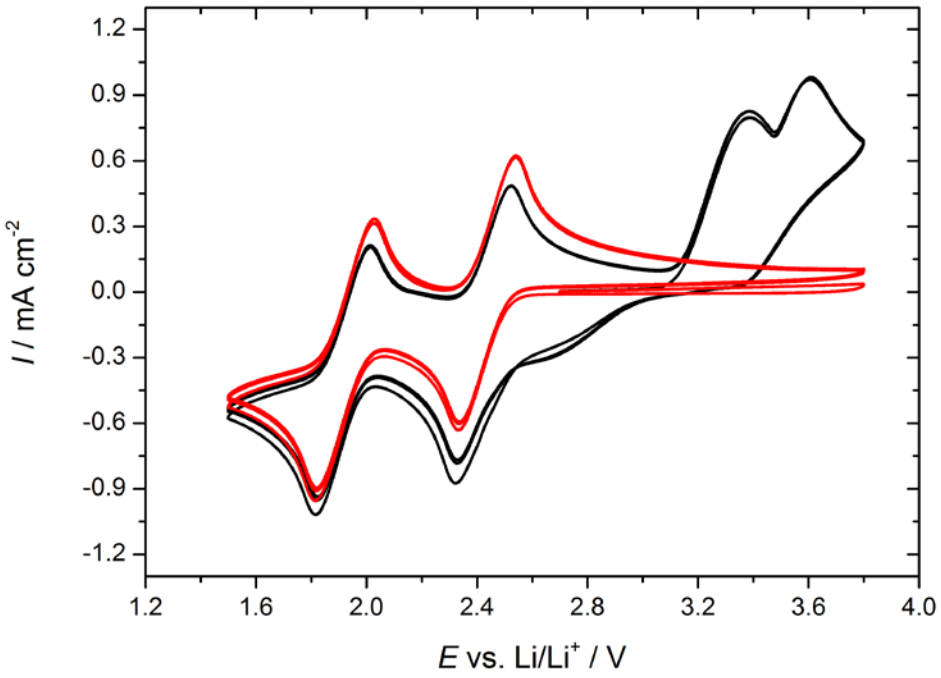


**Figure 6.3.12 –** Cyclic voltammetry measurements using of **— EtVI$_2$** and **— EtV(OTf)$_2$** at scan rates of 100 mV s$^{-1}$ between the potential limits of 3.8 V and 1.5 V. The two-compartment U-cell consisted of a glassy carbon working electrode (Ø = 3 mm), either 5 mM EtVI$_2$ or 5 mM EtV(OTf)$_2$ dissolved in 1 M LiTFSI in DOL electrolyte in the working electrode compartment and 1 M LiTFSI in DOL electrolyte in the counter/reference electrode compartments and a lithium metal counter/reference electrode. First three cycles at specified scan rate are shown. Before each CV, the potential of the working electrode was held at 2.7 V for at least 2 minutes.

On scanning from 2.7 V to 3.8 V, it is observed that the two oxidation peaks observed for EtVI$_2$ (labelled in black) are not present for EtV(OTf)$_2$ (labelled in red). As discussed in Section 6.3.2, these peaks can be attributed to the $I^-/I_2$ redox pair and their absence in the cyclic voltammogram of EtV(OTf)$_2$ indicates that the synthesised product does not contain any iodide. In order to further confirm the purity of the synthesised EtV(OTf)$_2$, cyclic voltammetry was performed between potential limits of 2.7 V and 2.2 V and the cyclic voltammogram compared with that obtained for EtVI$_2$ (Figure 6.3.13).

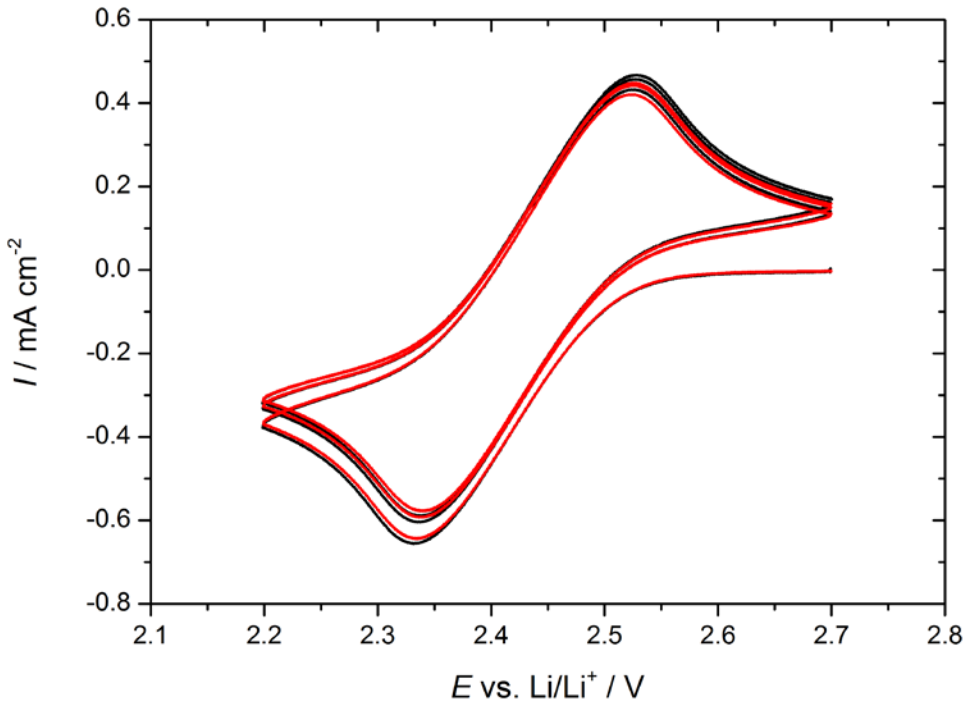


**Figure 6.3.13 –** Cyclic voltammetry measurements using of **— $EtVI_2$** and **— $EtV(OTf)_2$** at scan rates of 100 mV $s^{-1}$ between the potential limits of 2.7 V and 2.2 V. The two-compartment U-cell consisted of a glassy carbon working electrode (Ø = 3 mm), either 5 mM $EtVI_2$ or 5 mM $EtV(OTf)_2$ dissolved in 1 M LiTFSI in DOL electrolyte in the working electrode compartment and 1 M LiTFSI in DOL electrolyte in the counter/reference electrode compartments and a lithium metal counter/reference electrode. First three cycles at specified scan rate are shown. Before each CV, the potential of the working electrode was held at 2.7 V for at least 2 minutes.

It is observed that the synthesised 5 mM $EtV(OTf)_2$ dissolved in 1 M LiTFSI in DOL gives almost the exact same response as the equivalent $EtVI_2$ electrolyte solution. Since the $EtVI_2$ used is purchased from the supplier (Sigma-Aldrich) at 99% purity, the matching cyclic voltammetry indicates that the purity of the synthesised $EtV(OTf)_2$ is also high. This assumes that the diffusion coefficient of $EtV^{2+}$ in both solutions is similar, a reasonable assumption given the low concentration used (5 mM). To verify the purity further, spectroscopic techniques such as IR, NMR or mass spectrometry could be performed. On performing a similar analysis of $EtV(OTf)_2$ as discussed in Sections 6.3.1 and 6.3.2, the electrochemical reversibility of $EtV^{+}/EtV^{2+}$ was confirmed ($\Delta E_{I=0}$ = 62.6 mV) and the diffusion coefficient ($D_{EtV2+}$) was determined to be 2.1 x $10^{-6}$ $cm^2$ $s^{-1}$, which is very similar to the diffusion coefficient obtained using $EtVI_2$ ($D_{EtV2+}$ = 2.2 x $10^{-6}$ $cm^2$ $s^{-1}$). Furthermore, the $EtV^{+}/EtV^{2+}$ formal potential determined using $EtV(OTf)_2$ ($E_e^{0'}$ = +2.43 V vs. $Li/Li^{+}$) is also very similar to that obtained for $EtVI_2$

($E_e^{0'}$ = +2.44 V vs. Li/Li$^+$). Therefore, it was decided that EtV(OTf)$_2$ would be used to prepare the model redox system of EtV$^+$/EtV$^{2+}$. For the full details of this analysis see Appendix B1. However it should be noted that, since the value of $D_{EtV2+}$ determined using cyclic voltammetry was not performed with IR correction or temperature control, there is likely to be some error associated with the actual value of $D_{EtV2+}$. If time allowed, further experimentation could be performed to accurately determine $D_{EtV2+}$. Methods for reducing the effects of resistance include using IR corrected cyclic voltammetry or cyclic voltammetry using microelectrodes. Furthermore, an oil bath could be used to accurately control the temperature. However, the value of $D_{EtV2+}$ obtained (2 x 10$^{-6}$ cm$^2$ s$^{-1}$) is satisfactory for the purpose of this study.

### 6.3.4 – Galvanostatic Pulses, Transition Times and Transition to Swagelok Cell

Using cyclic voltammetry, it was possible to select a suitable model redox system (EtV$^+$/EtV$^{2+}$, prepared using 5mM EtV(OTf)$_2$ dissolved in 1 M LiTFSI in DOL electrolyte) for which the diffusion coefficient was determined using cyclic voltammetry and the Randles-Sevcik equation ($D_{EtV2+}$ = 2 x 10$^{-6}$ cm$^2$ s$^{-1}$). However, before using this model redox system to analyse GITT, it was decided that chronopotentiometry (i.e. constant current or galvanostatic pulse analysis) would be performed in order to determine if the diffusion coefficient could be calculated from the experimental transition times. The chronopotentiometry would be performed firstly using the same U-cell setup used in Section 6.3.3 to determine whether the same value of $D_{EtV2+}$ could be obtained. Then the same experiment would be performed using a Swagelok cell configuration to determine if chronopotentiometry could be applied in a Swagelok cell to quantitatively determine $D_{EtV2+}$. This is an important experiment as it requires utilisation of the Sand equation to determine $D_{EtV2+}$ using experimental transition times determined using a constant current pulse technique; the Sand equation is used to derive the equations used in GITT, which itself is a technique employing constant current pulses. If the Sand equation can be used to calculate reasonable values of $D_{EtV2+}$ using chronopotentiometry inside a Swagelok cell, then it should be possible to calculate reasonable values of $D_{EtV2+}$ using the same cell setup and performing GITT.

It should be noted that there are multiple methods of calculating the experimental transition time from the transient potential response produced by constant current pulse techniques. The first method is simply to define two potential limits ($E_1$ and $E_2$) and the transition time is the time taken for the potential to change from $E_1$ to $E_2$. In the example given below, the two potential limits $E_1$ and $E_2$ are defined as 3.5 V and 2.9 V respectively and the transitions time is labelled as $\tau_A$ (Figure 6.3.14). A second method is described by Reinmuth, whereby three linear fits are used, one on the initial descent (3.5 – 3.3 V), one on the plateau (approximately 3.2 V) and one on the second descent (3.1 – 2.9 V).[16] These linear fits are then used to determine the transition time labelled as $\tau_B$. A final method is to simply take the region where the plateau is considered linear to give the transition time labelled $\tau_C$.

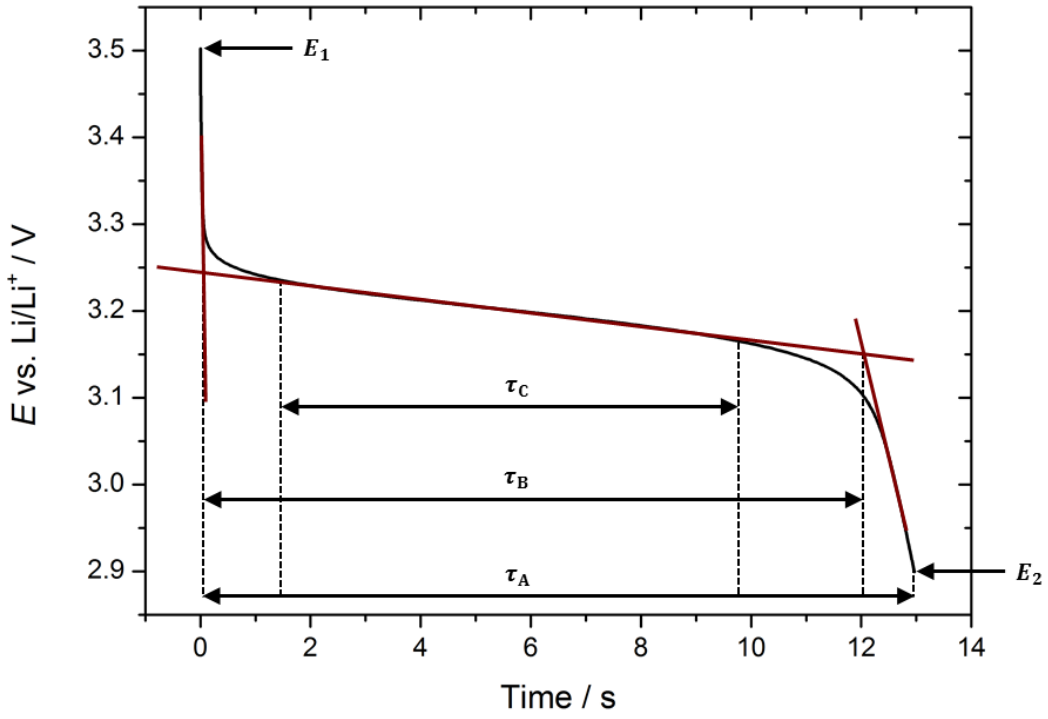


**Figure 6.3.14 –** Schematic depicting the various methods to determine the transition time (τ).

To compare the three methods of determining the experimental transition time discussed in Figure 6.3.14, galvanostatic cycling was performed on a solution of 5 mM $EtV(OTf)_2$ dissolved in 1 M LiTFSI in DOL electrolyte using a two-compartment glass U-cell (Figure 6.3.15, Table 6.3.3). In Section 6.3.3, the diffusion coefficient of $EtV(OTf)_2$ dissolved in 1 M LiTFSI in DOL ($D_{EtV2+}$ = 2 x $10^{-6}$ $cm^2$ $s^{-1}$) was determined using cyclic

voltammetry. Using this value of $D_{EtV2+}$ and the Sand Equation (Equation 6.3.4), the theoretical transition times ($\tau$) for a solution of 5 mM $EtV(OTf)_2$ dissolved in 1 M LiTFSI in DOL electrolyte were determined and compared to the experimentally determined values.

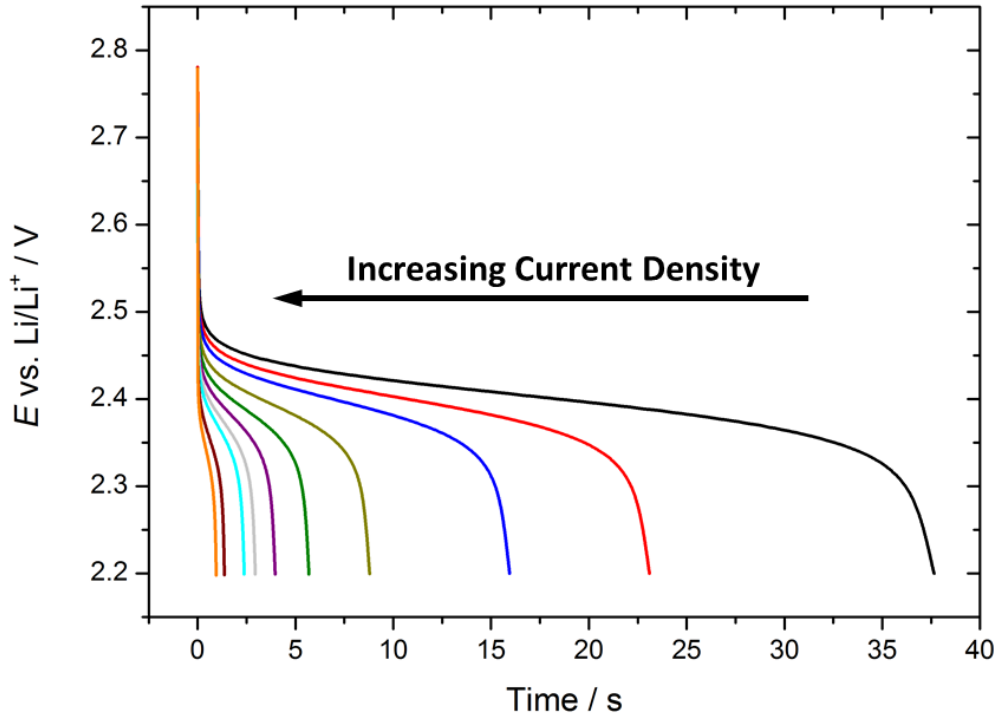


**Figure 6.3.15 –** Constant current pulses at currents of **— 0.14** mA cm$^{-2}$, **— 0.18** mA cm$^{-2}$, **— 0.21** mA cm$^{-2}$, **— 0.28** mA cm$^{-2}$, **— 0.35** mA cm$^{-2}$, **— 0.42** mA cm$^{-2}$, **— 0.50** mA cm$^{-2}$, **— 0.57** mA cm$^{-2}$, **— 0.71** mA cm$^{-2}$ and **— 0.85** mA cm$^{-2}$ between the potential limits of 2.2 V and 2.7 V. The two-compartment U-cell consisted of a glassy carbon working electrode (Ø = 3 mm), 5 mM $EtV(OTf)_2$ dissolved in 1 M LiTFSI in DOL electrolyte in the working electrode compartment and 1 M LiTFSI in DOL electrolyte in the counter/reference electrode compartments and a lithium metal counter/reference electrode. First cycles at specified currents are shown. Before applying each constant current pulse, the potential of the working electrode was held at 2.7 V for 5 minutes and then allowed to rest for 5 minutes.

$$\tau = \frac{c^* n^2 F^2 D \pi}{4 I^2}$$

**Equation 6.3.4 –** The Sand equation re-arranged, where $\tau$ = transition time in s, $c^*$ = bulk concentration of the reactant species in mol cm$^{-3}$, $n$ = number of electrons involved in redox process, $F$ = Faraday constant (96485 C mol$^{-1}$), $D$ = diffusion coefficient of the reactant species in cm$^2$ s$^{-1}$ and $I$ = current density in A cm$^{-2}$.

| Current Density / mA $cm^{-2}$ | Theoretical Transition Time / s | $\tau_A$ / s | $\tau_B$ / s | $\tau_C$ / s |
|---|---|---|---|---|
| 0.14 | 18.5 | 37.6 | 36.0 | 21.0 |
| 0.18 | 11.9 | 23.1 | 22.0 | 13.0 |
| 0.21 | 8.2 | 15.9 | 15.2 | 8.8 |
| 0.28 | 4.6 | 8.8 | 8.3 | 4.8 |
| 0.35 | 3.0 | 5.7 | 5.4 | 3.2 |
| 0.42 | 2.1 | 4.0 | 3.7 | 2.1 |
| 0.50 | 1.5 | 2.9 | 2.8 | 1.6 |
| 0.57 | 1.2 | 2.4 | 2.2 | 1.2 |
| 0.71 | 0.7 | 1.4 | 1.3 | 0.8 |
| 0.85 | 0.5 | 0.9 | 0.9 | 0.6 |

**Table 6.3.3 –** Theoretical and experimental transition times when constant current pulses were applied. For comparison, experimental transition times ($\tau_A$, $\tau_B$, $\tau_C$) for each pulse have been calculated using each of the three methods described in Figure 6.3.14. Theoretical transition times were calculated using the Sand equation with the variables as follows: $D$ = 2 x $10^{-6}$ $cm^2$ $s^{-1}$, $n$ = 1, $F$ = 96485 C $mol^{-1}$, $A$ = 0.071 $cm^2$ and $c^*$ = 5.03 x $10^{-6}$ mol $cm^{-3}$. See Figure 6.3.15 for details of experimental pulse measurements and cell components.

It is observed that the experimental transition times determined using the $\tau_A$ and $\tau_B$ methods were significantly larger than the theoretical transition times calculated using $D_{EtV2+}$ = 2 x $10^{-6}$ $cm^2$ $s^{-1}$ and the Sand equation. This was the case for all current densities used and could be due to convection within the cell. However, when the experimental transition times were determined using the $\tau_C$ method, there is good agreement with the theoretical transition times. This can be observed more clearly by plotting $\tau$ vs. $I^{-2}$, which also enables the diffusion coefficient to be calculated from the slope (Figure 6.3.16).

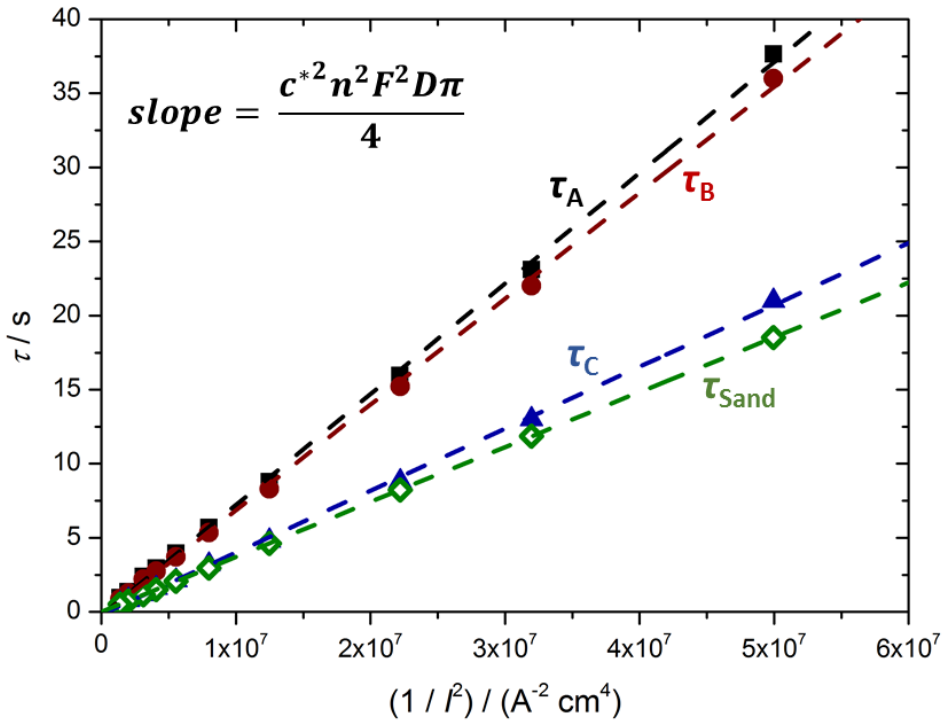


**Figure 6.3.16 –** Experimental transition times (■ = $\tau_A$, ● = $\tau_B$, ▲ = $\tau_C$) obtained using U-cell and theoretical transition times (◊ = $\tau_{Sand}$) against the reciprocal of the current density squared ($1/I^2$), which can be used to evaluate diffusion coefficient of $EtV^{2+}$. Using the slopes ($\tau_A$ = 7.5 x $10^{-7}$ $A^2$ s $cm^{-4}$, $\tau_B$ = 7.2 x $10^{-7}$ $A^2$ s $cm^{-4}$, $\tau_C$ = 4.2 x $10^{-7}$ $A^2$ s $cm^{-4}$ and $\tau_{Sand}$ = 3.7 x $10^{-7}$ $A^2$ s $cm^{-4}$) it was possible to calculate $D_{EtV2+}$ ($\tau_A$ = 4.0 x $10^{-6}$ $cm^2$ $s^{-1}$, $\tau_B$ = 3.9 x $10^{-6}$ $cm^2$ $s^{-1}$, $\tau_C$ = 2.3 x $10^{-6}$ $cm^2$ $s^{-1}$ and $\tau_{Sand}$ = 2 x $10^{-6}$ $cm^2$ $s^{-1}$)

Using the slopes from the linear fits (Figure 6.3.16), the diffusion coefficients of $EtV^{2+}$ were calculated for the experimentally determined transition times ($\tau_A$, $\tau_B$ and $\tau_C$). Using the $\tau_A$ and $\tau_B$ methods, the diffusion coefficients were determined to be 4.0 x $10^{-6}$ $cm^2$ $s^{-1}$ and 3.9 x $10^{-6}$ $cm^2$ $s^{-1}$ respectively. These values of $D_{EtV2+}$ are higher than the value determined using cyclic voltammetry ($D_{EtV2+}$ = 2 x $10^{-6}$ $cm^2$ $s^{-1}$), which could be due to convention within the cell. Using the $\tau_C$ method, $D_{EtV2+}$ was determined to be 2.3 x $10^{-6}$ $cm^2$ $s^{-1}$, which is in much better agreement with the value determined using cyclic voltammetry.

In preparation for GITT analysis, a Swagelok cell was modified to accommodate a piece of lithium-ion conducting glass-ceramic (LICGC, Ohara Corporation, see Section 6.2.5 for full details). This LICGC, composed of $Li_2O$-$Al_2O_3$-$SiO_2$-$P_2O_5$-$TiO_2$-$GeO_2$, acts as a separator between the carbon-coated aluminium foil working electrode and lithium metal negative electrode. It possesses high lithium ion conductivity (1 x $10^{-4}$ S $cm^{-1}$ at

room temperature) but prevents the diffusion of the redox species under investigation ($EtV^{2+}$ and $EtV^{+}$). This ensures that the redox species dissolved in the electrolyte can be isolated at the working electrode and prevent any reaction at the counter/reference lithium electrode. Utilising this Swagelok cell setup, the galvanostatic cycling experiments performed previously using a solution of 5 mM $EtV(OTf)_2$ dissolved in 1 M LiTFSI in DOL electrolyte in a U-cell (Figure 6.3.15, Table 6.3.3) were repeated in order to experimentally determine the transitions times ($\tau$) and compare them to those calculated using the Sand equation (Figure 6.3.17 and Equation 6.3.4).

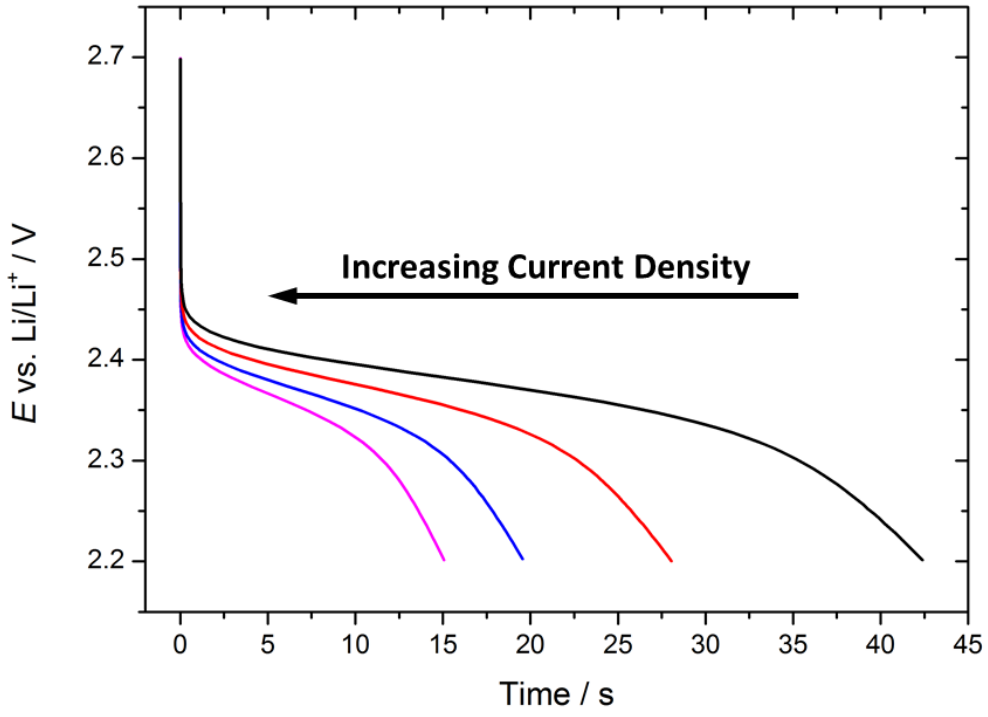


**Figure 6.3.17 –** Constant current pulses at currents of **— 0.14** mA $cm^{-2}$, **— 0.17** mA $cm^{-2}$, **— 0.20** mA $cm^{-2}$ and **— 0.23** mA $cm^{-2}$ between the potential limits of 2.7 V and 2.2 V. The Swagelok cell (see Figure 6.2.1 in Section 6.2.5) consisted of a carbon coated aluminium foil working electrode (Ø = 15 mm), 2 x glass-fibre separators (GF/F, Ø = 18 mm), 5 mM $EtV(OTf)_2$ dissolved in 1 M LiTFSI in DOL electrolyte (250 µL), LICGC (Ohara Corporation, Ø = 25.4 mm), glass-fibre separator (GF/F, Ø = 25 mm), 1 M LiTFSI in DOL electrolyte (250 µL) and a lithium metal (Ø = 25 mm) counter/reference electrode. First cycles at specified currents are shown. Before applying each constant current pulse, a small positive current was applied (0.006 mA $cm^{-2}$) until reaching 2.8 V, then the cell was allowed to rest for 20 mins before charging at the specified current and beginning the first negative constant current pulse.

| Current Density / mA $cm^{-2}$ | Theoretical Transition Time / s | $\tau_A$ / s | $\tau_B$ / s | $\tau_C$ / s |
|---|---|---|---|---|
| 0.14 | 19.5 | 42.4 | 34.8 | 20.0 |
| 0.17 | 13.5 | 28.1 | 22.7 | 14.0 |
| 0.20 | 9.9 | 19.6 | 15.5 | 9.6 |
| 0.23 | 7.6 | 15.1 | 11.8 | 7.2 |

**Table 6.3.4 –** Calculated and theoretical transition times when constant current pulses were applied. Theoretical transition time was calculated using the Sand equation with the variables as follows: $D$ = 2 x $10^{-6}$ $cm^2$ $s^{-1}$, $n$ = 1, $F$ = 96485 C $mol^{-1}$, $A$ = 1.767 $cm^2$ and $c^*$ = 5.16 x $10^{-6}$ mol $cm^{-3}$. See Figure 6.3.17 for details of experimental pulse measurements and cell components.

Similar to the results obtained using the U-cell, it is observed that the experimental transition times determined using the $\tau_A$ and $\tau_B$ methods were significantly larger than the theoretical transition times calculated using $D_{EtV2+}$ = 2 x $10^{-6}$ $cm^2$ $s^{-1}$ and the Sand equation. However, it is observed that the difference between the values obtained for $\tau_A$ and $\tau_B$ is greater in the Swagelok cell than in the U-cell. This can be attributed to the effect of capacitance since the method for calculating $\tau_A$ does not account for capacitance, unlike the method for calculating $\tau_B$. Since the Swagelok cell employs a large porous carbon coated aluminium foil electrode (Ø = 1.5 cm) and the U-cell employs a small planar (i.e. non-porous) glassy carbon electrode (Ø = 0.3 cm), it is likely that the capacitive effect for the Swagelok cell will be much greater than for the U-cell. Hence, it is likely that the difference between values obtained for $\tau_A$ and $\tau_B$ will be larger in the Swagelok cell than the U-cell, which is the case. Once again, the experimental transition times determined using the $\tau_C$ method were consistent with the theoretical transition times. To observe these results more clearly, the experimentally determined transition times using each of the three methods ($\tau_A$, $\tau_B$, and $\tau_C$) and the theoretically determined transition times ($\tau_{Sand}$) using the value of $D_{EtV2+}$ determined using cyclic voltammetry and the Sand Equation were plotted as $\tau$ vs. $I^{-2}$ (Figure 6.3.18). As in Figure 6.3.16, this enabled the diffusion coefficients to be calculated from the slopes using the Sand equation (Equation 6.3.4). The calculated diffusion coefficients were then compared to those calculated for the U-cell (Table 6.3.5).

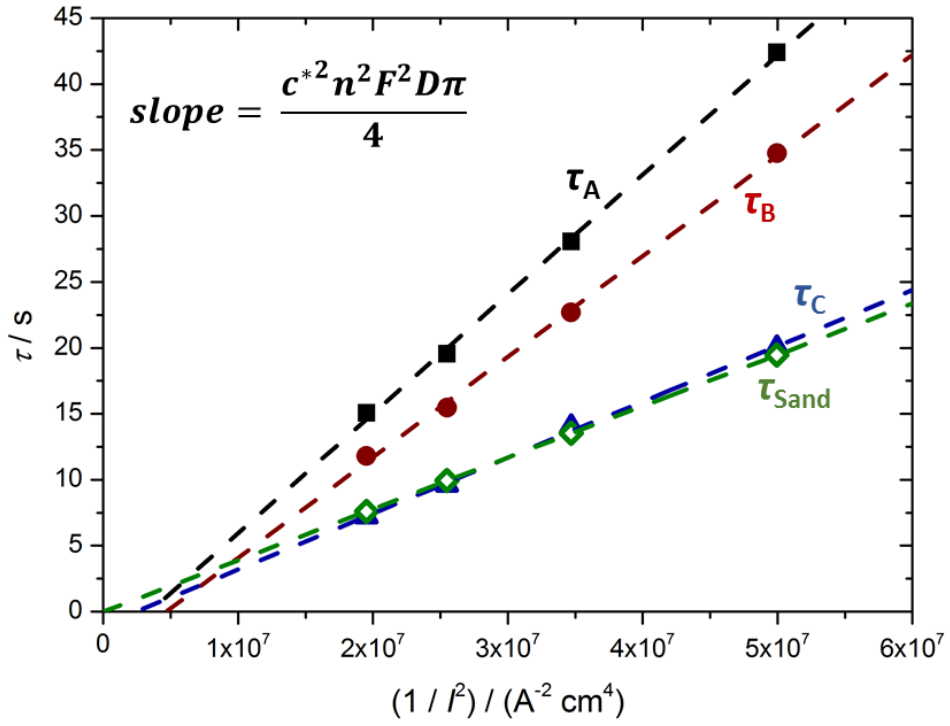


**Figure 6.3.18 –** Experimental transition times (■ = $\tau_A$, ● = $\tau_B$, ▲ = $\tau_C$) obtained using Swagelok cell and theoretical transition times (◊ = $\tau_{Sand}$) against the reciprocal of the current density squared ($1/I^2$), which can be used to evaluate diffusion coefficient of $EtV^{2+}$. Using the slopes ($\tau_A$ = 9.1 x $10^{-7}$ $A^2$ s $cm^{-4}$, $\tau_B$ = 7.6 x $10^{-7}$ $A^2$ s $cm^{-4}$, $\tau_C$ = 4.2 x $10^{-7}$ $A^2$ s $cm^{-4}$ and $\tau_{Sand}$ = 3.9 x $10^{-7}$ $A^2$ s $cm^{-4}$) it was possible to calculate $D_{EtV2+}$ ($\tau_A$ = 4.7 x $10^{-6}$ $cm^2$ $s^{-1}$, $\tau_B$ = 3.9 x $10^{-6}$ $cm^2$ $s^{-1}$, $\tau_C$ = 2.2 x $10^{-6}$ $cm^2$ $s^{-1}$ and $\tau_{Sand}$ = 2 x $10^{-6}$ $cm^2$ $s^{-1}$)

| Method of determining $\tau$ | $D_{EtV2+}$ calculated using U-cell / $cm^2$ $s^{-1}$ | $D_{EtV2+}$ calculated using Swagelok cell / $cm^2$ $s^{-1}$ |
|---|---|---|
| $\tau_A$ | 4.0 x $10^{-6}$ | 4.7 x $10^{-6}$ |
| $\tau_B$ | 3.9 x $10^{-6}$ | 3.9 x $10^{-6}$ |
| $\tau_C$ | 2.3 x $10^{-6}$ | 2.2 x $10^{-6}$ |
| $\tau_{Sand}$ | 2 x $10^{-6}$ | 2 x $10^{-6}$ |

**Table 6.3.5 –** Diffusion coefficients of $EtV^{2+}$ ($D_{EtV2+}$) calculated using the slopes from the linear fits in Figure 6.3.16 for the U-cell measurements and Figure 6.3.18 for the Swagelok cell measurements. For values of the measured slopes, see Figures 6.3.16 and 6.3.18.

Using the slopes from the linear fits (Figure 6.3.18), the diffusion coefficients of $EtV^{2+}$ ($D_{EtV2+}$) were calculated for the experimentally determined transition times ($\tau_A$, $\tau_B$ and $\tau_C$). These values of $D_{EtV2+}$ calculated using the Swagelok cell and the values calculated using the U-cell are summarised in Table 6.3.5. Similarly to the values of $D_{EtV2+}$ determined using the U-cell (Figure 6.3.16), the value of $D_{EtV2+}$ calculated using the $\tau_A$ and $\tau_B$ methods in the Swagelok cell ($4.7 \times 10^{-6}$ $cm^2$ $s^{-1}$ and $3.9 \times 10^{-6}$ $cm^2$ $s^{-1}$ respectively) were both much higher than the value determined using cyclic voltammetry ($D_{EtV2+}$ = $2 \times 10^{-6}$ $cm^2$ $s^{-1}$), which could be in part due to convection. Furthermore, the value of $D_{EtV2+}$ calculated using the $\tau_C$ method in the Swagelok cell ($2.2 \times 10^{-6}$ $cm^2$ $s^{-1}$) was consistent with the value obtained using cyclic voltammetry. On comparing the values of $D_{EtV2+}$ obtained using the U-cell and Swagelok cells, it is observed that the values $D_{EtV2+}$ obtained using the $\tau_A$ method varied (U-cell = $4.0 \times 10^{-6}$ $cm^2$ $s^{-1}$ and Swagelok = $4.7 \times 10^{-6}$ $cm^2$ $s^{-1}$) whereas the values obtained using the $\tau_B$ method were similar (both $3.9 \times 10^{-6}$ $cm^2$ $s^{-1}$). The difference observed using $\tau_A$ method can be attributed to the increased capacitive effect from using a large porous carbon coated aluminium foil electrode used in the Swagelok cell rather than the planar glassy carbon electrode used in the U-cell. Unlike the $\tau_A$ method, the $\tau_B$ method accounts for capacitive effects and hence the values of $D_{EtV2+}$ obtained using both the U-cell and Swagelok cell are similar. Furthermore, using the $\tau_C$ method for both the U-cell and Swagelok cell gave similar values of $D_{EtV2+}$ (U-cell = $2.3 \times 10^{-6}$ $cm^2$ $s^{-1}$ and Swagelok = $2.2 \times 10^{-6}$ $cm^2$ $s^{-1}$).

However, since the values of $D_{EtV2+}$ determined using cyclic voltammetry were not performed with IR correction or temperature control and the values obtained using the Sand equation varied between $2 \times 10^{-6}$ $cm^2$ $s^{-1}$ and $4 \times 10^{-6}$ $cm^2$ (using the $\tau_B$ and $\tau_C$ methods), it is not possible to precisely determine the actual value of $D_{EtV2+}$. It is likely that $D_{EtV2+}$ possesses a value in the range of $2 \times 10^{-6}$ $cm^2$ $s^{-1}$ and $4 \times 10^{-6}$ $cm^2$ $s^{-1}$, although to precisely determine the value of $D_{EtV2+}$, further experimentation is required. For this, IR corrected cyclic voltammetry could be performed or microelectrodes could be used. However, the determined range is satisfactory for the purpose of this study and does not affect the discussion regarding the GITT analysis presented in Section 6.3.5.

It has been determined that constant current pulse techniques can be performed using both a U-cell and Swagelok cell design to determine values of $D_{EtV2+}$ (between

2 x $10^{-6}$ $cm^2$ $s^{-1}$ and 4 x $10^{-6}$ $cm^2$ $s^{-1}$) similar to that determined using cyclic voltammetry (2 x $10^{-6}$ $cm^2$ $s^{-1}$). Calculating $D_{EtV2+}$ using transition times requires utilisation of the Sand equation (Equation 6.3.4), which is also used to derive the equations used in GITT (Equation 6.3.5). If the Sand equation can be used to calculate reasonable values of $D_{EtV2+}$ using constant current pulse techniques inside a Swagelok cell, then it should be possible to calculate reasonable values of $D_{EtV2+}$ using the same cell setup and performing GITT.

$$D = \frac{4L^2}{\pi\tau}\left(\frac{\Delta E_s}{\Delta E_t}\right)^2 \qquad \left(t \ll \frac{L^2}{D}\right)$$

**Equation 6.3.5 –** Simplified equation for determining the diffusion coefficient ($D$), where $L$ is the distance between where the electrochemical redox process occurs and the impermeable phase boundary (in this case, the distance between the electrode surface and the LICGC separator), $\tau$ is the duration of the current pulse, $\Delta E_s$ is the change in steady-state potential over a single current pulse and $\Delta E_t$ is the total change in potential during the current pulse, excluding *IR* drop.

### 6.3.5 – Galvanostatic Intermittent Titration Technique (GITT)

In Section 6.3.4, it was shown that constant current pulse techniques can be used in combination with the Sand equation (Equation 6.3.6a) to determine the diffusion coefficient of $EtV^{2+}$. Furthermore, it was demonstrated that the diffusion coefficient can be determined using either a U-cell or Swagelok cell design. However, it is only possible to determine the diffusion coefficient using this method if both the concentration of the bulk species and the number of electrons transferred in the redox process are known (Equation 6.3.6a). This would not be the case inside a Li-S battery where several polysulfide species exist, at various different concentrations and a wide variety of redox processes are occurring, involving an unknown number of electrons.

$$\text{(a)} \qquad D = \frac{4I^2\tau}{n^2F^2c^{*2}\pi}$$

$$\text{(b)} \qquad D = \frac{4\mathrm{L}^2}{\pi\tau}\left(\frac{\Delta \mathrm{E_s}}{\Delta \mathrm{E_t}}\right)^2$$

**Equation 6.3.6 –** (a) A rearranged form of the Sand equation illustrating that to determine the diffusion coefficient ($D$) requires knowledge of the number of electrons transferred ($n$) and bulk concentration ($c^*$), whereas (b) using the GITT equation to determine the diffusion coefficient requires neither $n$ nor $c^*$.

GITT requires neither the concentration of the species nor the number of electrons transferred to be known (Equation 6.3.6b), which would make it a very powerful tool to analyse the multi-electron redox processes that occur in the Li-S battery. Therefore, it is important that the GITT technique is evaluated for the analysis of species dissolved in solution, unlike the 'mixed-conducting compound' trilithium antimonide ($Li_3Sb$) for which it was originally developed.[1] To minimise complications in obtaining quantitative data, the model redox system used ($EtV(OTf)_2$ dissolved in 1 M LiTFSI in DOL, described in Sections 6.3.3 and 6.3.4) possesses a reversible one-electron redox process, which occurs at an appropriate potential (~ 2.4 V vs. $Li/Li^+$), which avoids the possibility of DOL polymerisation that can occur at higher potentials. Furthermore, both the reactant ($EtV^{2+}$) and product ($EtV^+$) are both soluble to avoid effects caused by precipitation and a low concentration of active material ($[EtV^{2+}]$ = 5 mM) is used with a high concentration of background electrolyte ([LiTFSI] = 1 M), to minimise the effect that the reduction process has on the properties of the electrolyte itself.

Using the selected model system of 5 mM $EtV(OTf)_2$ dissolved in 1 M LiTFSI in DOL electrolyte and a Swagelok cell configuration with an LICGC separator (same setup used in Section 6.3.4), GITT was performed (Figure 6.3.19). During the current pulses, a current of -0.2 mA was applied for a duration of 5 s, followed by a relaxation period of 60 minutes. Assuming $D_{EtV2+} = 2 \times 10^{-6}$ cm$^2$ s$^{-1}$, the time required for a molecules to travel from the electrode surface ($x = 0$), to the LICGC separator ($x = 0.07$ cm) would be approximately 40 minutes (where $t = L^2 / D_{EtV2+}$). Therefore, using a 60 minute relaxation period should be long enough for the species to equilibrate, allowing a stable steady-state potential to be measured. To fully reduce the $EtV^{2+}$ to $EtV^+$, it was calculated that 124 mC of charge is required and since during each current pulse 1 mC of charge is passed, it should take 124 pulses for the full reduction of $EtV^{2+}$, i.e. 100% reduction of $EtV^{2+}$.

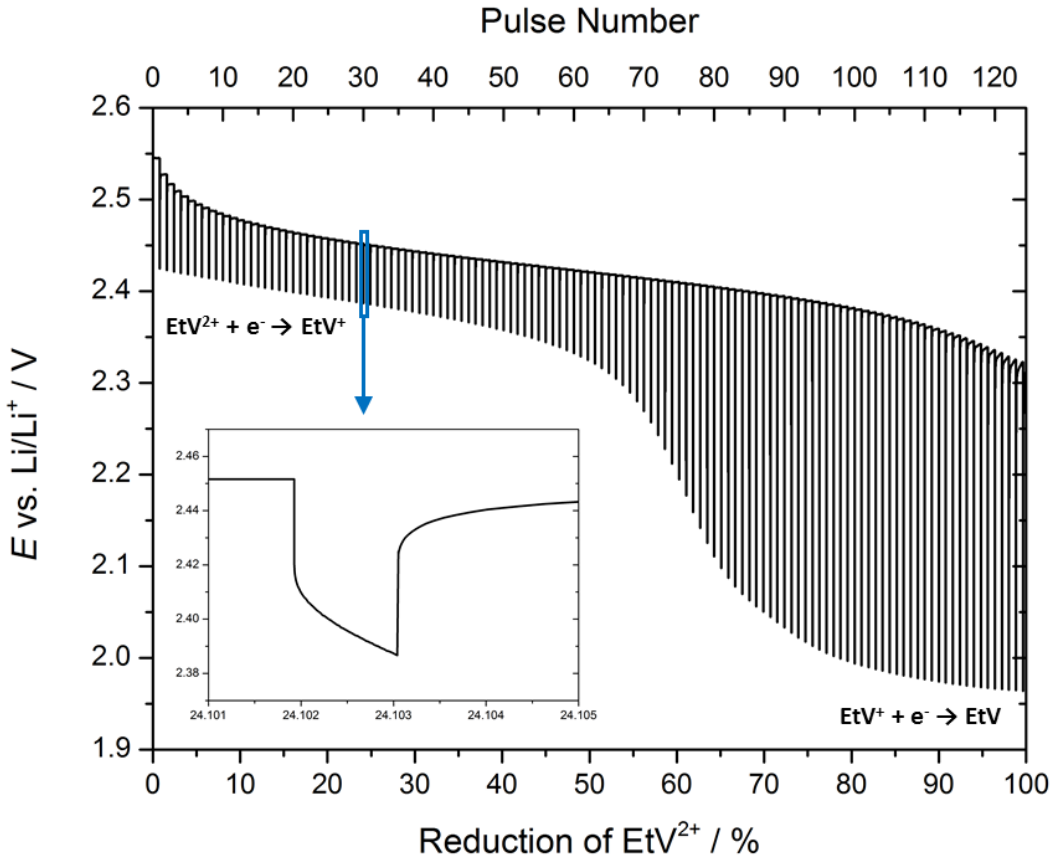


**Figure 6.3.19 –** GITT discharge profile of a Swagelok cell consisting of a carbon coated aluminium foil working electrode (Ø = 15 mm), 2 x glass-fibre separators (GF/F, Ø = 18 mm), 5 mM EtV(OTf)$_2$ dissolved in 1 M LiTFSI in DOL electrolyte (250 µL), LICGC (Ohara Corporation, Ø = 25.4 mm), glass-fibre separator (GF/F, Ø = 25 mm), 1 M LiTFSI in DOL electrolyte (250 µL) and a lithium metal (Ø = 25 mm) counter/reference electrode. The cell was allowed to rest at OCP for 60 min, followed by 5 s discharge at -0.11 mA cm$^{-2}$, followed by a rest period of 60 min and so on.

Furthermore, it was calculated that the steady-state concentration (i.e. the uniform concentration after the relaxation period) of $EtV^{2+}$ should decrease by approximately 0.04 mM after each pulse and the concentration of $EtV^{+}$ should increase by the same amount. Through knowing the change in the equilibrium concentrations of $EtV^{2+}$ and $EtV^{+}$ after each current pulse, it is possible to use the Nernst equation (Equation 6.3.7) to calculate the equilibrium (or steady-state) potential, which can be compared with the steady-state potential obtained experimentally (Figure 6.3.20). A formal potential ($E_e^{0'}$) of 2.42 V vs. Li/Li$^+$ was used, which is similar to the formal potential determined for the $EtV^{+}/EtV^{2+}$ redox pair using cyclic voltammetry ($E_e^{0'}$ = 2.43 V vs. Li/Li$^+$). The intial concentration of $EtV^{2+}$ was calculated to be 5.16 mM.

$$E_{\mathrm{e}} = E_{\mathrm{e}}^{0\prime} + \frac{RT}{F} \ln \frac{[\mathrm{EtV}^{2+}]}{[\mathrm{EtV}^{+}]}$$

**Equation 6.3.7 –** The Nernst equation, where $E_e^{0'}$ was determined to be 2.42 V and the initial bulk concentration of $EtV^{2+}$ was calculated to be 5.16 mM.

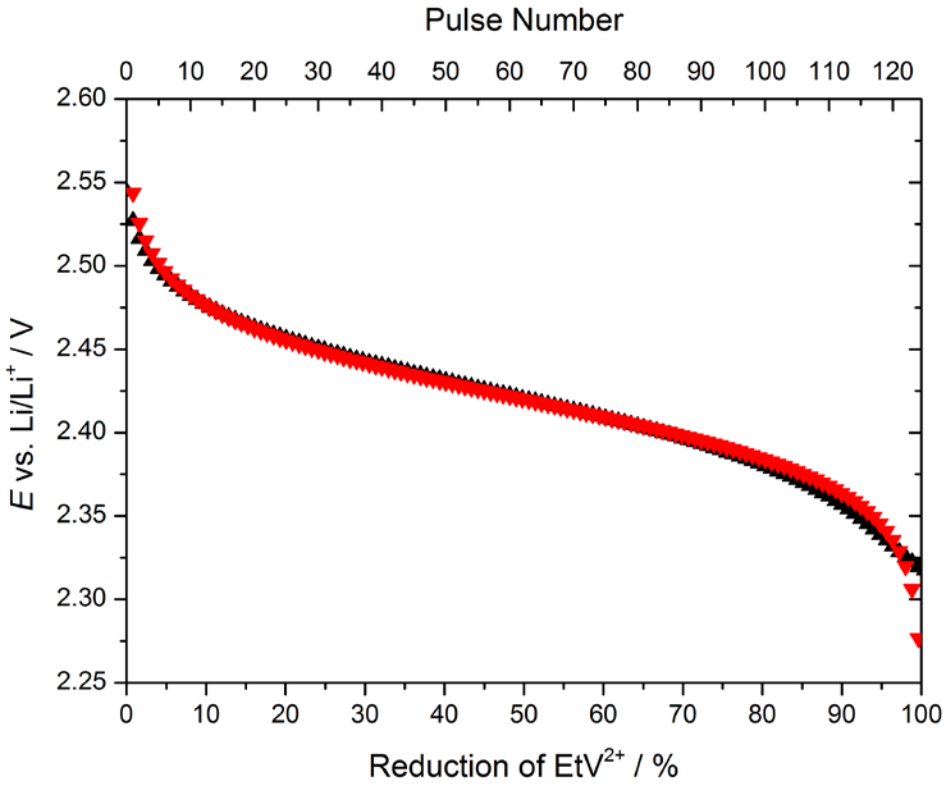


**Figure 6.3.20 –** Values of steady-state potential measured from GITT data ▲ and calculated using the Nernst equation ▼. To calculate the values of steady-state potential using the Nernst equation, $E_e^{0'}$ was determined to be 2.42 V, the initial bulk concentration of $EtV^{2+}$ was 5.16 mM, the initial number of moles of $EtV^{2+}$ was 1.29 x $10^{-6}$ moles, which equates to 0.124 A s of charge. During each current pulse 0.001 A s are passed (200 µA for 5 s). Therefore, after 124 pulses the $EtV^{2+}$ should be fully reduced. See Appendix B2 for further details.

In Figure 6.3.20, it is observed that the measured values of steady-state potential obtained from the GITT measurement are in good agreement with the model values calculated from the Nernst equation, which indicates that the values of steady-steady state potential measured from GITT are reliable. The measured values deviate from the model values by a small amount before 5% and after 75% reduction of $EtV^{2+}$. Before 5% reduction, the steady-state potentials measured from the GITT data are slightly suppressed when compared to the model values, which is likely due to the presence of a small amount

of $EtV^{+}$ before the first current pulse was performed. After 75% reduction, the steady-state potentials measured from GITT data are lower than the model values, which is likely due to presence of $EtV^{0}$, formed during the second redox process (i.e. reduction of $EtV^{+}$ to $EtV^{0}$, the cause of the second plateau at 1.97 V in Figure 6.3.19) that could also be affecting the measured steady-state potential. This can be further explained by analysing the values of transient potential (potential under current) obtained from the GITT measurement. In Figure 6.3.19, it is observed that the transient potential starts to decrease from approximately 2.3 V to below 2.0 V at around 60% reduction, whereas the steady-state potential (potential at rest) only begins to decrease after 90% reduction. This can be explained by considering the change in the concentration of $EtV^{2+}$ at the electrode surface (i.e. $x = 0$) during the current pulse. Using the Sand equation (Equation 6.3.8), it was calculated that the concentration of $EtV^{2+}$ at the electrode surface changes by approximately 2 mM during a current pulse.

$$c_{\mathrm{O}}(0,t) = c_{\mathrm{O}}^{*} + \frac{2I\sqrt{t}}{nFA\sqrt{D\pi}}$$

**Equation 6.3.8 –** The Sand equation, where $c_O(x,t)$ is the concentration of the oxidised species at the electrode/electrolyte interface ($x = 0$) at time = t and $c_O^*$ is the bulk concentration of the oxidised species.

Therefore, it is expected that once the steady-state concentration reaches 2 mM (i.e. 60% reduction of $EtV^{2+}$) the concentration of $EtV^{2+}$ at the electrode surface will reach 0 mM during the current pulse, which would cause the potential to drop until either the current pulse ends (at $t = 5$ s) or a second redox process occurs (i.e. reduction of $EtV^{+}$ to $EtV^{0}$). To illustrate this, the concentration profiles of $EtV^{2+}$ at the end of the 1st and 74th pulse were calculated (Equation 6.3.9, Figure 6.3.21).

$$c_{\mathrm{O}}(x,t) = c_{\mathrm{O}}^{*} - \frac{i}{nFAD_{\mathrm{O}}}\left\{2\sqrt{\frac{D_{\mathrm{O}}t}{\pi}}\exp\left(-\frac{x^2}{4D_{\mathrm{O}}t}\right) - x\,\mathrm{erfc}\left[\frac{x}{2\sqrt{D_{\mathrm{O}}t}}\right]\right\}$$

**Equation 6.3.9 –** An extended version of the Sand equation used to plot the concentration profile of the oxidised species (e.g. $EtV^{2+}$) over distance from the electrode surface ($x$) at a given time (e.g. $t = 5$ s).

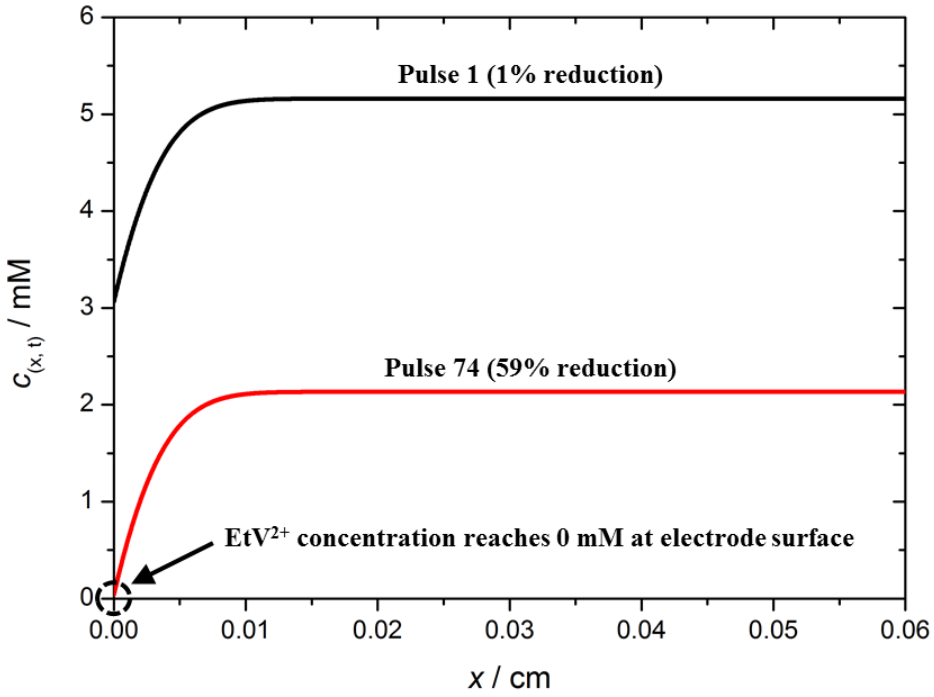


**Figure 6.3.21 –** Calculated concentration profiles for $EtV^{2+}$ — at the end of the pulse 1 (1% reduction) and — at the end of the pulse 74 (59% reduction). The concentration profiles were calculated using the Sand equation (Equation 6.3.9), where the initial bulk concentration of $EtV^{2+}$ was either 5.16 mM for pulse 1 (1% reduction) or 2.13 mM for pulse 74 (59%), time of pulse = 5 s, current = 200 μA, electrode area = 1.767 $cm^2$ and $D_{EtV2+}$ = 2 x $10^{-6}$ $cm^2$ $s^{-1}$. $c_{(x, t)}$ is the concentration of $EtV^{2+}$ and $x$ is the distance from the electrode surface.

In Figure 6.3.21, it is observed that at 59% reduction of $EtV^{2+}$ (current pulse 74), the concentration of the $EtV^{2+}$ at the electrode surface reaches 0 mM by the end of the current pulse ($t$ = 5 s). This means that during every current pulse after 59% reduction of $EtV^{2+}$, the concentration of the $EtV^{2+}$ at the electrode surface will reach 0 mM during the current pulse. This will cause the measured transient potential to drop until either the current pulse ends ($t$ = 5 s) or it reaches the second redox process ($EtV^+$ to $EtV^0$ at 1.97 V). However on rest, $EtV^{2+}$ diffuses back to the surface from the bulk electrolyte, which causes the potential to increase towards the formal potential of $EtV^+/EtV^{2+}$ at around 2.4 V. In Figure 6.3.19, it should be noted that at 75%, the measured transient potential begins to reach the second plateau at 1.97 V. This means that some of the charge associated with each pulse will be used for the reduction of $EtV^+$ to $EtV^0$ and the calculated equilibrium concentrations of $EtV^{2+}$ and $EtV^+$ after this point will become less accurate. This explains the deviations observed in Figure 6.3.20 after 75% reduction of $EtV^{2+}$, on comparing the model values of steady-state potential with the experimental values measured using GITT.

This effect of exhausting the concentration of $EtV^{2+}$ close to the electrode surface during the current pulse can be further highlighted by analysing the individual pulses throughout the GITT measurement (Figure 6.3.22).

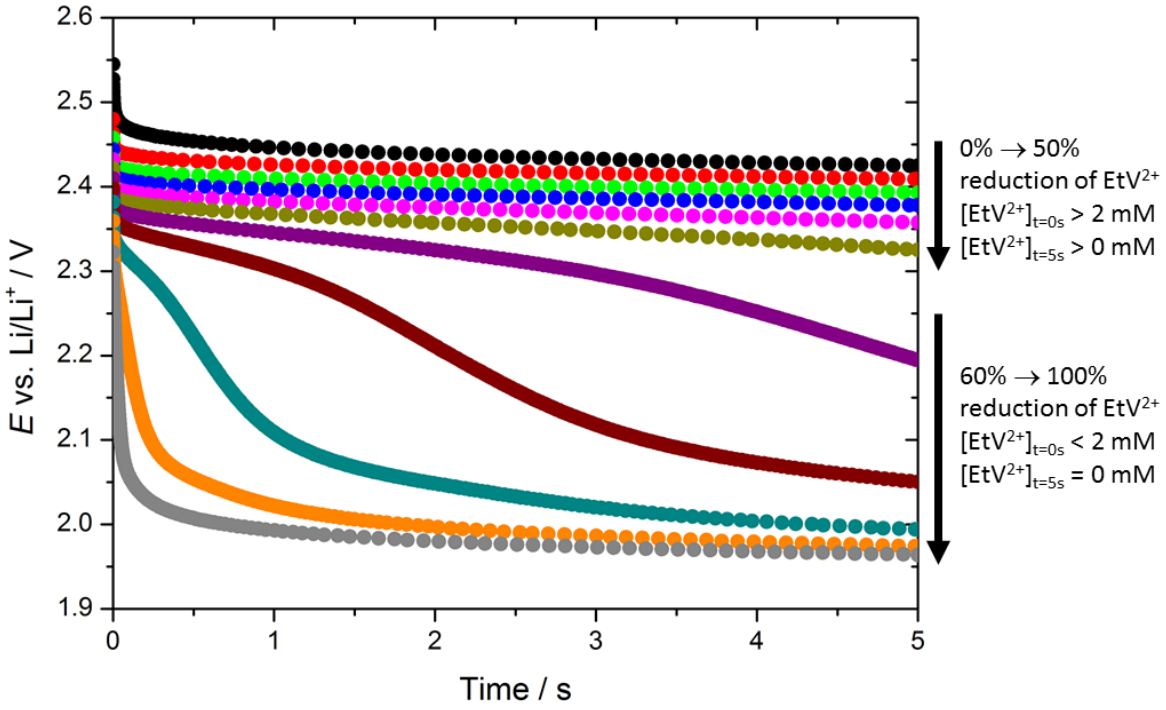


**Figure 6.3.22 –** Discharge profiles of $EtV^{2+}$ for 11 pulses (1% reduction ●●●, 10% reduction ●●●, 20% reduction ●●●, 30% reduction ●●●, 40% reduction ●●●, 50% reduction ●●●, 60% reduction ●●●, 70% reduction ●●●, 80% reduction ●●●, 90% reduction ●●● and 100% reduction ●●●).

In Figure 6.3.22, it is observed that from 0% to 50% reduction of $EtV^{2+}$, the potential remains above 2.3 V over the entire current pulse since the concentration of $EtV^{2+}$ close to the electrode surface is over 2 mM before the current pulse begins and remains above 0 mM at the end of the current pulse. From 60% to 100% reduction of $EtV^{2+}$, the potential during the current pulse begins to drop below 2.3 V at shorter and shorter times during the current pulse. This is a result of the concentration of $EtV^{2+}$ close to the electrode surface being less than 2 mM before the current pulse begins and reaching 0 mM during the current pulse. Since it has been demonstrated that the concentration of $EtV^{2+}$ close to the electrode surface reaches 0 mM from 60% reduction of $EtV^{2+}$ onwards, it was decided that analysis of the GITT data would be restricted to pulses occurring before 60% reduction of $EtV^{2+}$ (i.e. pulses 1 – 74).

If the derived equation to determine the diffusion coefficient from GITT (Equation 6.3.10) is applicable to both solid-state and solution based redox systems, it should be possible to use this GITT data to determine the diffusion coefficient for $EtV^{2+}$, previously determined using cyclic voltammetry and galvanostatic cycling to between 2 x $10^{-6}$ $cm^2$ $s^{-1}$ and 4 x $10^{-6}$ $cm^2$ $s^{-1}$. Using the GITT data, the diffusion coefficient of $EtV^{2+}$ was calculated for each pulse (Figure 6.3.23).

$$D = \frac{4L^2}{\pi\tau}\left(\frac{\Delta E_s}{\Delta E_t}\right)^2 \qquad \left(t \ll \frac{L^2}{D}\right)$$

**Equation 6.3.10 –** Simplified equation for determining the diffusion coefficient ($D$), where $L$ is the distance between where the electrochemical redox process occurs and the impermeable phase boundary (in this case, the distance between the electrode surface and the LICGC separator), $\tau$ is the duration of the current pulse, $\Delta E_s$ is the change in steady-state potential over a single current pulse and $\Delta E_t$ is the total change in potential during the current pulse, excluding *IR* drop.

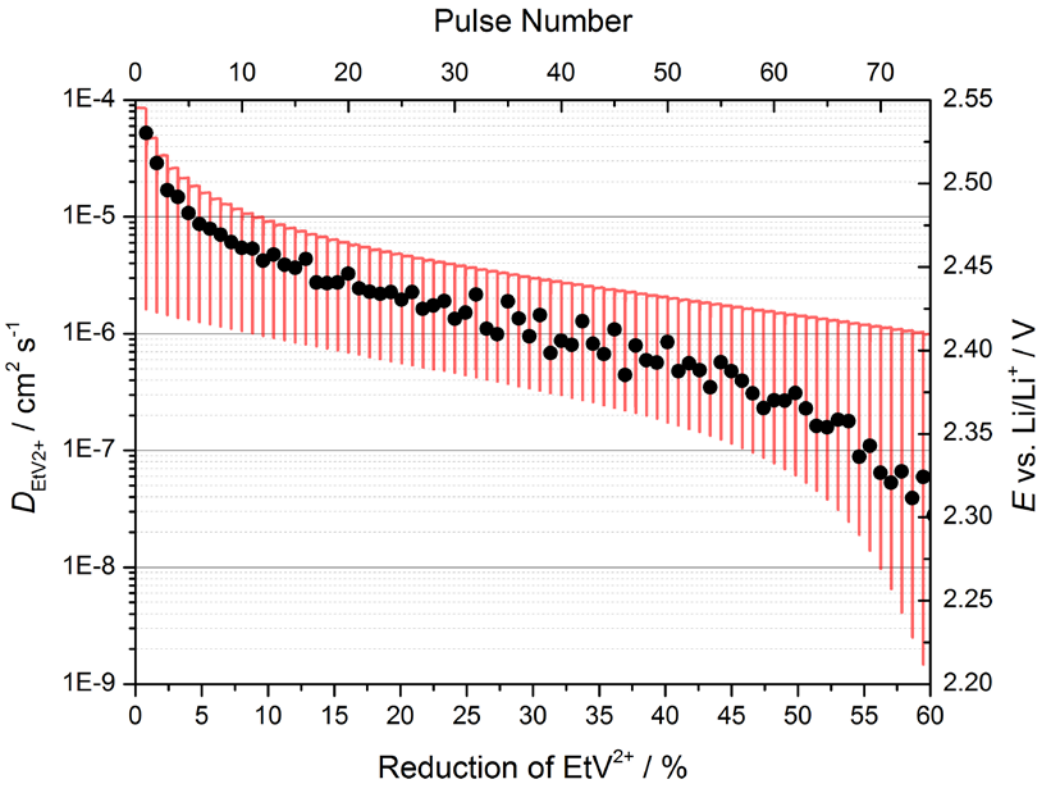


**Figure 6.3.23 –** The diffusion coefficient of $EtV^{2+}$ ($D_{EtV2+}$) ●●● measured using Equation 6.3.10 and the GITT data —. An IR correction ($R$ = 168 Ω) is used for all pulses. See Appendices B3 and B4 for full details on calculating resistance and values of $D_{EtV2+}$ using Equation 6.3.10.

In Figure 6.3.23, it is observed that measured diffusion coefficient of $EtV^{2+}$ varies continually throughout the GITT measurement and the values obtained range over 3 orders of magnitude, between 5 x $10^{-5}$ $cm^2$ $s^{-1}$ and 4 x $10^{-8}$ $cm^2$ $s^{-1}$. This huge fluctuation in the measured diffusion coefficient is clearly not reasonable and likely to be a consequence of the analysed solution-based redox system not fitting the mathematics developed for the GITT equation (Equation 6.3.10). An important assumption when using the GITT equation is that the equation can only be applied if the entire transient response of the pulse is a linear function of the square root of time (Figure 6.3.24, see Chapter 2.3.3 for derivation).

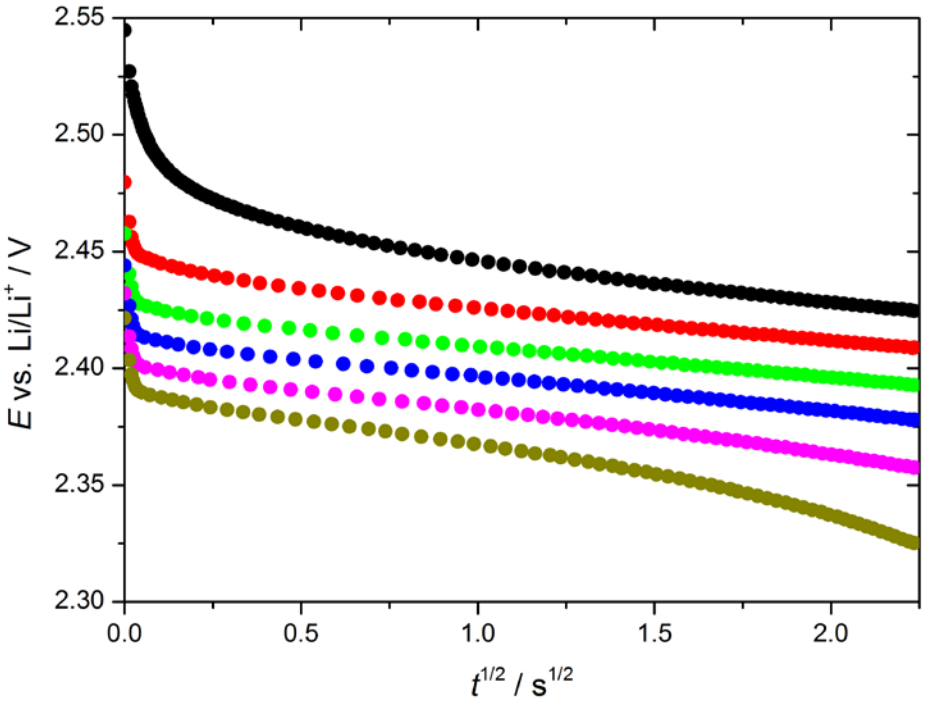


**Figure 6.3.24 –** Transient potential responses of $EtV^{2+}$ against the square root of time for 6 pulses (1% reduction ●●●, 10% reduction ●●●, 20% reduction ●●●, 30% reduction ●●●, 40% reduction ●●●, 50% reduction ●●●). Only the pulses between 10% and 40 % $EtV^{2+}$ reduction give linear transient responses.

In Figure 6.3.24, it is observed that initially (below 0.25 $s^{1/2}$) there is a small deviation from the linear trend in all cases. This is likely due to internal cell resistance, as well as capacitive effects of the porous carbon coated aluminium foil. However, the diffusion coefficients presented in Figure 6.3.23 using the GITT equation (Equation 6.3.10) have been calculated using an IR correction, which removes the majority of this effect (see Appendix B3 for further details). Therefore, ignoring the initial deviation from linearity (below 0.25 $s^{1/2}$), it is observed that only pulses between 10% and 40% reduction display a linear transient potential response when plotted as a function of the square root of

time. It is important that only these pulses are considered when calculating diffusion coefficients using the GITT equation (Equation 6.3.10). For comparison, there is another equation which allows only the slope of the partial linear response to be considered (Equation 6.3.11).

$$D = \frac{4L^2 \, {\Delta E_s}^2}{\tau^2 \, slope^2 \, \pi}$$

**Equation 6.3.11 –** Determining the diffusion coefficient of $EtV^{2+}$ ($D_{EtV2+}$) from the slope of the linear portion of the transient response plotted against the square root of time.

This equation can only be applied to the pulses which display a linear response when plotting the transient potential against the square root of time for significant portions of the pulse. If data points that are measured after 0.5 $s^{1/2}$ are only taken into account (in order to remove any deviations at short times), then only pulses between 10% and 40% reduction are considered linear (Figure 6.3.25). Using the slopes measured from these transient potential responses, the diffusion coefficients were calculated and compared to those previously determined (Figure 6.3.26).

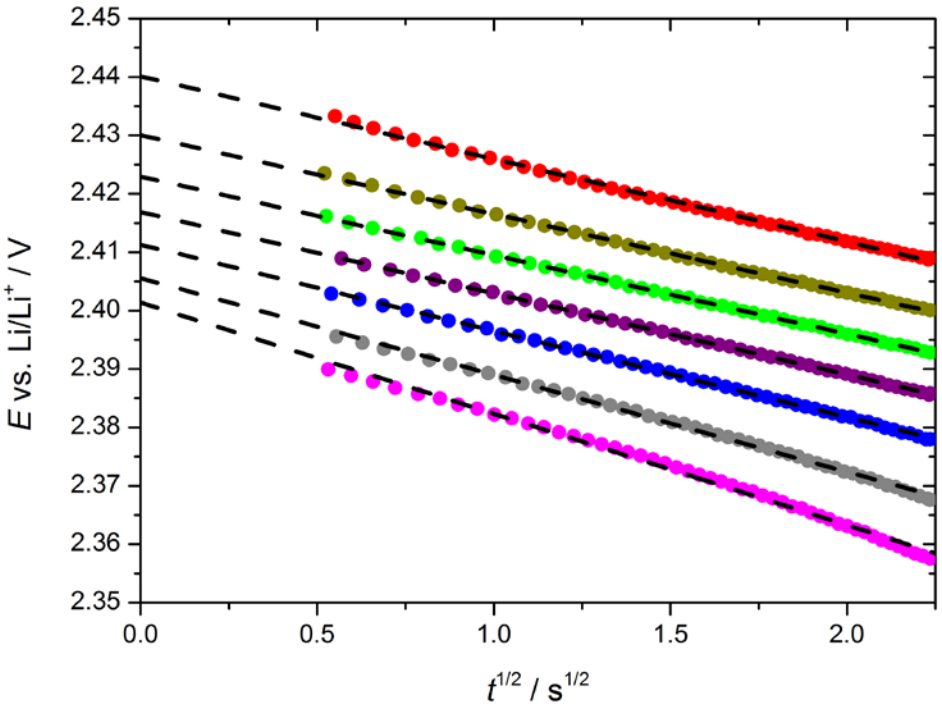


**Figure 6.3.25 –** Transient potential responses of $EtV^{2+}$ against the square root of time for 7 pulses (10% reduction ●●●, 15% reduction ●●●, 20% reduction ●●●, 25% reduction ●●●, 30% reduction ●●●, 35% reduction ●●●, 40% reduction ●●●).

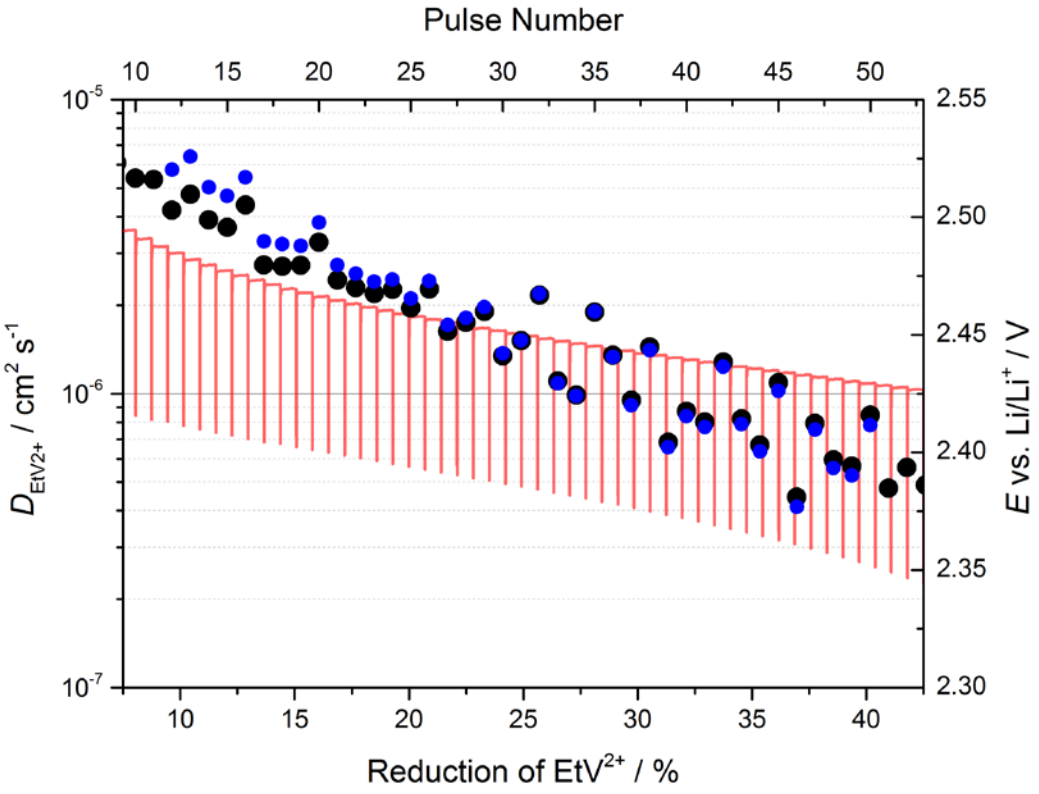


**Figure 6.3.26 –** The diffusion coefficient of $EtV^{2+}$ ($D_{EtV2+}$) measured using Equation 6.3.10 ●●● (same as Figure 6.3.23) and Equation 6.3.11 ●●●. The GITT data ─ has been included.

By only taking into account pulses which give a linear transient potential response against the square root of time and discounting any data points below 0.5 $s^{1/2}$ to remove deviations caused by internal cell resistance and capacitive effects, it is observed that the calculated values $D_{EtV2+}$ still vary continually throughout the GITT measurement as before and the values range by 1.5 orders of magnitude, between 7 x $10^{-6}$ cm$^2$ s$^{-1}$ and 4 x $10^{-7}$ cm$^2$ s$^{-1}$. It is unrealistic to assume that the actual value $D_{EtV2+}$ is changing so drastically as the reduction of $EtV^{2+}$ proceeds from 10% to 40%, since the model system being analysed is fairly dilute (5 mM), which means that the changing concentrations of $EtV^{2+}$ and $EtV^{+}$ should not affect the mobility of ions. However, on comparing the values of $D_{EtV2+}$ obtained using Equation 6.3.10 (black points) and Equation 6.3.11 (blue points), it is observed the best agreement occurs between 20 and 30% reduction of $EtV^{2+}$, with values ranging between 1.0 x $10^{-6}$ cm$^2$ s$^{-1}$ and 2.3 x $10^{-6}$ cm$^2$ s$^{-1}$ in this region. This range of values is much more reasonable and the value of $D_{EtV2+}$ obtained using cyclic voltammetry (2 x $10^{-6}$ cm$^2$ s$^{-1}$) falls within this range. Therefore, it is possible to conclude that the GITT equation can only be used if the transient potential response is truly linear, indicating that the change in potential is proportional to the change in concentration. This is a key

assumption used to derive the GITT equation (Equation 6.3.10). A simple method of determining whether the change in potential is proportional to the change in concentration is to plot the experimentally determined steady-state potentials as a function of the equilibrium concentration of $EtV^{2+}$ (Figure 6.3.27).

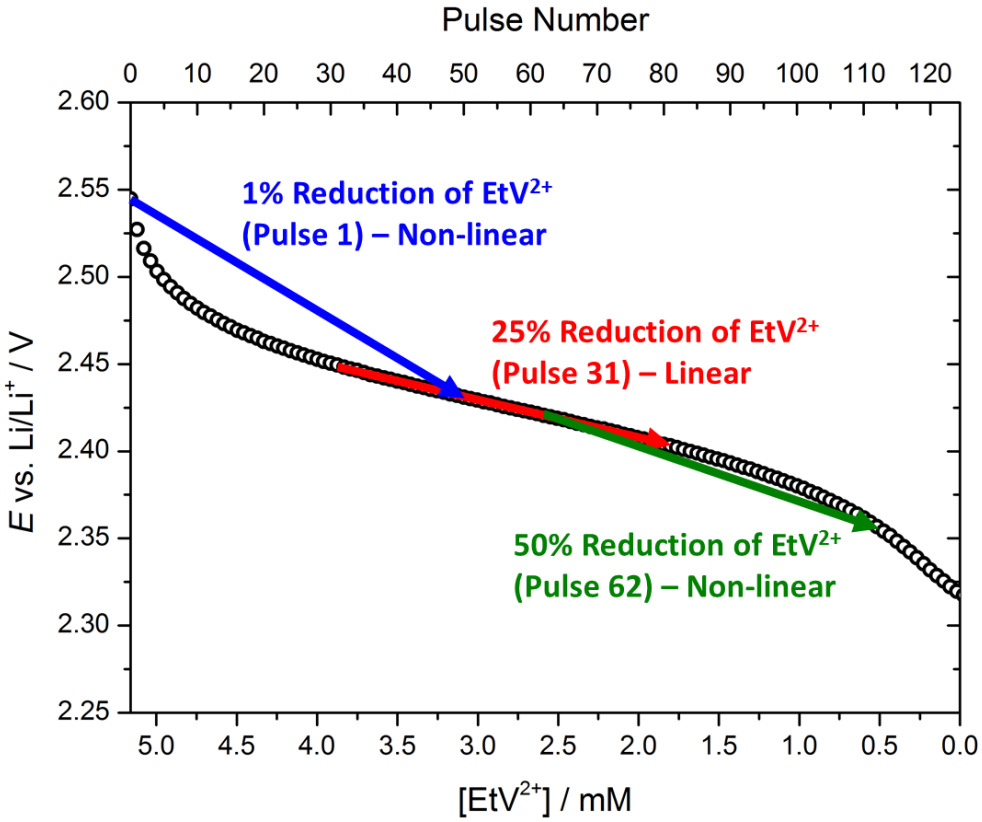


**Figure 6.3.27 –** An illustration of the expected linearity of three different pulses using the experimentally determined steady-state potentials measured using GITT (see Figure 6.3.20). Such a plot can be used to determine the pulses that should be used to determine values of diffusion coefficient when analysing GITT data. Each arrow represents a current pulse and indicates the expected start and end potential, assuming no IR drop.

In Figure 6.3.27, three arrows have been drawn, each representing a current pulse during the GITT measurement. The arrows each indicate the value of the potential before the current pulse begins (i.e. the steady-state potential) and the expected potential at the end of the current pulse (assuming no IR drop). Such a plot quickly illustrates whether or not a pulse will exhibit proportionality between change in potential and change in concentration and therefore, whether or not the transient potential response will be suitable for use with the GITT equation (Equation 6.3.10) to determine the diffusion coefficient.

In this chapter, it has been demonstrated that even when employing a model one-electron reversible solution-based redox system, using GITT to determine quantitative values of the diffusion coefficient must be performed with caution. Unrealistic values of diffusion coefficient can be easily obtained if the assumptions proposed by Weppner and Huggins are not fulfilled. In particular, it is important to ensure that proportionality exists between potential and concentration, which can be determined simply using the experimental steady-state potentials measured using GITT data. Through rigorous analysis of the GITT data, it was possible to determine a range for $D_{EtV2+}$ (between $1.0 \times 10^{-6}$ cm$^2$ s$^{-1}$ and $2.3 \times 10^{-6}$ cm$^2$ s$^{-1}$), which agrees with the value of $D_{EtV2+}$ obtained using cyclic voltammetry ($2 \times 10^{-6}$ cm$^2$ s$^{-1}$). This indicates that if approached cautiously, GITT measurements can be used to quantitatively determine diffusion coefficients for a model one-electron reversible solution-based redox system. However, using GITT to determine quantitative information regarding the mass transport of species present in a more complicated electrochemical system, such as Li-S batteries, will be even more challenging due to the presence of multiple redox species, which undergo multi-electron redox processes. Furthermore, the polysulfide species in a Li-S battery are present at high concentration (> 1 M) and precipitate is present on the electrode surface at different stages of cycling in the form of solid $S_8$ or solid $Li_2S$, exacerbating the analysis further.

## 6.4 – Conclusions and Further Work

During this chapter, GITT was investigated using a model redox system to determine its advantages and limitations, and to assess its potential application as a technique capable of determining quantitative information on the mass transport in Li-S batteries during cycling. The model redox system $EtV^{+}/EtV^{2+}$ was selected as this offered a reversible one-electron redox process at a suitable potential (~2.4 V vs. $Li/Li^{+}$), which avoids any possibility of DOL polymerisation. Furthermore, $EtV(OTf)_2$ was chosen to prepare the model solutions of $EtV^{2+}$ rather than using $EtVI_2$ as it prevented the incorporation of iodide, which is electrochemically active and could interfere with the measurements. The diffusion coefficient of $EtV^{2+}$ was determined to be $2 \times 10^{-6}$ $cm^2$ $s^{-1}$, using cyclic voltammetry and the Randles-Sevcik equation. However, since these experiments were not performed with IR correction or temperature control there is likely to be some error associated with the actual value of $D_{EtV2+}$. If time allowed, further experimentation could be performed to accurately determine $D_{EtV2+}$. Methods for reducing the effects of resistance include using IR corrected cyclic voltammetry or cyclic voltammetry using microelectrodes. Furthermore, an oil bath could be used to accurately control the temperature.

It was then demonstrated that the diffusion coefficient could be determined using constant current pulse techniques using both the U-cell and Swagelok cell configurations. Using the Sand equation, both cell configurations gave diffusion coefficients (U-cell = $2.3 \times 10^{-6}$ $cm^2$ $s^{-1}$ and Swagelok cell = $2.2 \times 10^{-6}$ $cm^2$ $s^{-1}$) consistent with that obtained using cyclic voltammetry ($2 \times 10^{-6}$ $cm^2$ $s^{-1}$). However, it should be noted that this agreement was only obtained when a specific method was used to measure the transition time (see $\tau_C$ in Figure 6.3.14). It is likely that the other methods suffer more from the effects of natural convection and double layer charging. Since the values obtained using the Sand equation varied between $2 \times 10^{-6}$ $cm^2$ $s^{-1}$ and $4 \times 10^{-6}$ $cm^2$ (using the $\tau_B$ and $\tau_C$ methods), it was not possible to precisely determine the actual value of $D_{EtV2+}$, although the determined range is satisfactory for the purpose of this study.

Once it had been demonstrated that constant current pulse techniques could be used to determine the diffusion coefficient of $EtV^{2+}$ using a Swagelok cell configuration, GITT was performed in order to determine whether it too could be used to determine the

diffusion coefficient when applied to a solution-based redox system. It was determined that the experimental steady-state potentials were consistent with the model values obtained using the Nernst equation and calculating the changes in the equilibrium concentrations of $EtV^{2+}$ and $EtV^{+}$ after each current pulse. Furthermore, the transient (or under current) potential was effectively analysed using the Sand equation to calculate the concentration of $EtV^{2+}$ close to the electrode surface. It was determined that the drop in the measured transient potentials observed at 60% reduction of $EtV^{2+}$ were caused by the concentration of $EtV^{2+}$ reaching 0 mM close to the surface of the electrode surface during the current pulse. Therefore, subsequent analysis of the GITT data was restricted to pulses occurring before 60% reduction of $EtV^{2+}$ (i.e. pulses 1 – 74).

Using the GITT equation (Equation 6.3.10), it was determined that the values of $D_{EtV2+}$ varied hugely throughout the GITT measurement over several orders of magnitude. On plotting the transient potential responses against the square root of time, it was possible to observe that many of the current pulses analysed were non-linear, a key condition for using the GITT equation. On considering only the pulses where a linear transient potential response was observed (10 – 40% $EtV^{2+}$ reduction), the calculated diffusion coefficients varied over 1.5 order of magnitude. However, on comparing values of $D_{EtV2+}$ calculated using both the simplified GITT equation (Equation 6.3.10) and another equation, which only considers the linear regions of the transient potential response (Equation 6.3.11), it was possible to determine a range of values, which gave good agreement (20 – 30% $EtV^{2+}$ reduction). These values of $D_{EtV2+}$ ranged between $1.0 \times 10^{-6}$ $cm^2$ $s^{-1}$ and $2.3 \times 10^{-6}$ $cm^2$ $s^{-1}$, which agrees with the value of $D_{EtV2+}$ obtained using cyclic voltammetry ($2 \times 10^{-6}$ $cm^2$ $s^{-1}$). This indicates that if approached cautiously and considering the proportionality between potential and concentration, GITT measurements can be used to quantitatively determine diffusion coefficients for a model one-electron reversible solution-based redox system. However, using GITT to determine quantitative information regarding the mass transport of species present in a more complicated electrochemical system, such as Li-S batteries, will be even more challenging due to the presence of multiple redox species, which undergo multi-electron redox processes. Furthermore, the polysulfide species in a Li-S battery are present at high concentration (> 1 M) and precipitate is present on the electrode surface at different stages of cycling in the form of solid $S_8$ or solid $Li_2S$, exacerbating the analysis further.

Due to time constraints, the findings of this chapter have not yet been applied to analysing the Li-S battery system, in particular focusing on the mass transport of sulfur and the polysulfide species. To begin analysing these species using GITT, measurements should be performed on electrolytes containing dissolved sulfur at dilute concentrations (e.g. 1 mM), in order to reduce the issues associated with precipitation, before moving on to dilute polysulfide electrolyte solutions. Furthermore, EIS could be incorporated into the GITT technique at the end of each rest period to give a greater insight into the effects on the electrode interfaces during cycling.

## 6.5 – References


1. W. Weppner and R. A. Huggins, *J. Electrochem. Soc.*, 1977, **124**, 1569-1578.
2. P. P. Prosini, M. Lisi, D. Zane and M. Pasquali, *Solid State Ionics*, 2002, **148**, 45-51.
3. Y. Zhu and C. Wang, *J. Phys. Chem. C*, 2010, **114**, 2830-2841.
4. N. Ding, J. Xu, Y. X. Yao, G. Wegner, X. Fang, C. H. Chen and I. Lieberwirth, *Solid State Ionics*, 2009, **180**, 222-225.
5. Y. Zhu, Y. Xu, Y. Liu, C. Luo and C. Wang, *Nanoscale*, 2013, **5**, 780-787.
6. J.-J. Kim, H. S. Kim, J. Ahn, K. J. Lee, W. C. Yoo and Y.-E. Sung, *J. Power Sources*, 2016, **306**, 617-622.
7. S. Waluś, C. Barchasz, R. Bouchet, J. F. Martin, J. C. Leprêtre and F. Alloin, *Electrochim. Acta*, 2015, **180**, 178-186.
8. Z. Lin, Z. Liu, N. J. Dudney and C. Liang, *ACS Nano*, 2013, **7**, 2829-2833.
9. M. Cuisinier, P. E. Cabelguen, B. D. Adams, A. Garsuch, M. Balasubramanian and L. F. Nazar, *Energ. Environ. Sci.*, 2014, **7**, 2697-2705.
10. M. R. Busche, P. Adelhelm, H. Sommer, H. Schneider, K. Leitner and J. Janek, *J. Power Sources*, 2014, **259**, 289-299.
11. J. W. Park, K. Yamauchi, E. Takashima, N. Tachikawa, K. Ueno, K. Dokko and M. Watanabe, *J. Phys. Chem. C*, 2013, **117**, 4431-4440.
12. M. J. Lacey, K. Edstrom and D. Brandell, *Chem. Commun.*, 2015, **51**, 16502-16505.
13. M. J. Lacey, *ChemElectroChem*, 2017, **4**, 1997-2004.
14. E. I. Rogers, D. S. Silvester, L. Aldous, C. Hardacre and R. G. Compton, *J. Phys. Chem. C*, 2008, **112**, 6551-6557.

15. C. L. Bentley, A. M. Bond, A. F. Hollenkamp, P. J. Mahon and J. Zhang, *J. Phys. Chem. C*, 2014, **118**, 22439-22449.

16. W. H. Reinmuth, *Anal. Chem.*, 1961, **33**, 485-487.

# 7 – Conclusions and Further Work

## 7.1 – Conclusions

The use of different cell designs were found to significantly affect cycling performance. On testing three designs (metal cell, Nylon cell and Swagelok cell), the Swagelok cell afforded the largest discharge capacities (over 700 mA h $g_S^{-1}$ after 20 cycles), as well as reduced capacity fading on cycling. The Swagelok test cell design offers several other advantages, including its primary use of metal components, which aids in the exclusion of air/moisture without resorting to O-rings, as well as the use of an FEP film to line the internal cell wall, which is disposed of after each use to prevent any undesired contamination. Furthermore, the Swagelok cell configuration is widely used in Li-S battery research, which enables the results obtained in this project to be more accurately compared to those in the literature.[1-6] It was also determined that the Swagelok cell offers good reproducibility and it was decided that the Swagelok test cell design would be used throughout the majority of this work when using stacked cell geometry. Using the Swagelok cell design, the effects of using $LiNO_3$ as an electrolyte additive were investigated. It was determined that using $LiNO_3$ greatly improves the Coulombic efficiency of the cell from 85 – 79% (without $LiNO_3$, excluding first cycle) to a consistent 100% (with $LiNO_3$, excluding first cycle). According to the literature, this is likely due to the formation of an SEI layer on the lithium metal negative electrode, reducing the effect of the shuttle mechanism.[7-11] To a lesser extent, $LiNO_3$ may improve the overall discharge capacity and reduce capacity fading on cycling, although this is inconclusive. These results agree with Barchasz *et al.* who reported a similar study, doping $LiNO_3$ (0.1 M) into 1 M LiTFSI in 1:1 TEGDME:DOL electrolyte and found that whilst the Coulombic efficiency improved significantly, the discharge capacity and capacity fading were unaffected.[12]

The effect of varying the salt concentration in an electrolyte was analysed with respect to its physicochemical properties and cycling performance. Preparing electrolytes using different concentrations of LiTFSI dissolved in DOL, it was determined that the saturation concentration of LiTFSI in DOL is slightly over 3 M (approximately 3 molecules of DOL per molecule of LiTFSI), and the density of LiTFSI increases from 1.334 g $cm^{-3}$ (powder) to 2.07 g $cm^{-3}$ on dissolution in DOL (increase of 35%). Additionally, it was determined that increasing the LiTFSI concentration causes the

viscosity to increase exponentially from 0.56 mPa s (pure DOL) to 23.1 mPa s (3 M LiTFSI in DOL). From 0.2 M to 1.5 M LiTFSI in DOL, the molar conductivity increases with increasing the LiTFSI concentration, despite the increase in viscosity. This is possibly due to enhanced $Li^+$ ion mobility caused by either a reduced DOL solvation sphere surrounding the $Li^+$ ions as the LiTFSI concentration increases, or more likely, a change in ion formation from neutral LiTFSI ion pairs to charged triple ions. After 1.5 M, the molar conductivity decreases linearly with LiTFSI concentration, likely caused by the increase in viscosity. Using the Walden plot, it was determined that highly concentrated LiTFSI in DOL electrolytes act like ionic liquids and possess 'superionic' behaviour, where the exponent $\gamma = 0.75$ ($\Lambda\eta^{\gamma} = C$).

Using DSC, it was observed that increasing the concentration of LiTFSI in DOL resulted in the presence of different LiTFSI solvate phase transitions that could be associated the with different ion structures. Most notably, a peak attributed to the melting of an LiTFSI solvate in the form of neutral ion pairs was observed between -54 °C and -49 °C for all concentrations. However, for electrolytes with LiTFSI concentrations of 1.5 M and higher, another peak attributed to the crystallisation/melting of an LiTFSI solvate in the form of charged triple ions was observed at -60 °C. The size of the peak associated with charged triple ions increased with respect to the peak associated with neutral ion pairs, as LiTFSI concentration was increased, indicating that the ratio of triple ions present compared to ion pairs was increasing. In pure DOL, a peak attributed to the melting of DOL was observed at approximately -96 °C and this peak was also observed in the most dilute LiTFSI in DOL electrolytes (0.5 M and 1 M), indicating the presence of uncoordinated molecules of DOL. For electrolytes with LiTFSI concentrations of 1.5 M and higher, a peak attributed to the glass transition temperature was observed. This peak increased with increasing LiTFSI concentration, from -114 °C (1.5 M LiTFSI in DOL) to -88 °C (3 M LiTFSI in DOL), which can be correlated with increasing viscosity. This agrees with the observations made by Suo et al, who studied the effect of LiTFSI concentration dissolved in DOL/DME.[13] On analysing the polysulfide solubility, it was determined that the polysulfides prepared in a ratio to give $Li_2S_6$ with a concentration of 1 M [S] fully dissolved in the LiTFSI in DOL electrolytes with LiTFSI concentrations of 2 M and lower. However, the polysulfides did not fully dissolved in the 3 M LiTFSI in

DOL electrolyte solution, indicating lower polysulfide solubility. Unfortunately, the polysulfide concentration used was too small to evaluate their solubility any further.

It has been demonstrated that increasing the LiTFSI concentration in DOL improves the cycle life when used as an electrolyte in Li-S batteries. Increasing the LiTFSI concentration from 0.2 M to 2 M enhances the cycle life from approximately 60 cycles (40 mA h $g_S^{-1}$) to at least 200 cycles (385 mA h $g_S^{-1}$). All electrolytes containing LiTFSI concentrations of 2 M and higher performed similarly when cycling was limited to 200 cycles, all achieving capacities over 385 mA h $g^{-1}$. The Coulombic efficiency was also improved on increasing the LiTFSI concentration, with the highest concentration (3 M LiTFSI in DOL) performing the best (over 98% throughout). On disassembling these cycled cells and performing SEM on the lithium metal electrodes, it was observed that increasing the LiTFSI concentration in the electrolyte resulted in smoother less degraded lithium surfaces.

Two simple and reliable methods have been successfully designed that quantitatively analyse polysulfide composition in prepared polysulfide electrolyte solutions. A gravimetric analysis technique has been developed to measure the concentration of total dissolved sulfur $[S]_T^{sol.}$ and a UV-vis spectroscopic redox titration has been developed to measure the average oxidation state of the dissolved sulfur ($S^{m-}$). The gravimetric analysis method utilises the low solubility of $BaSO_4$ and it was precisely able to determine the concentration of total dissolved sulfur $[S]_T^{sol.}$ in a prepared 1 M $[S]_T^{sol.}$ $Li_2S_6$ polysulfide electrolyte to be 1.03 ± 0.02 M $[S]_T^{sol.}$. This method avoids the use of thorin indicator, which is a highly toxic arsenic compound. The UV-vis spectroscopic redox titration utilises the high redox potential of ferrocene/ferrocenium ($Fc/Fc^+$, ~ 3.2 V vs. $Li/Li^+$) to quantitatively oxidise the polysulfides to sulfur. On adding aliquots of a prepared polysulfide electrolyte solution to a solution of $Fc^+$, the change in $Fc^+$ concentration can be used to determine the 'dissolved sulfide' concentration [$S^{2-}$]. The change in $Fc^+$ concentration is determined by measuring the change in a characteristic $Fc^+$ absorption peak at 620 nm in the UV-vis absorption spectrum. Using this method, the concentration of 'dissolved sulfide' present [$S^{2-}$] in a prepared 1 M $[S]_T^{sol.}$ $Li_2S_6$ polysulfide electrolyte was measured to be 0.163 ± 0.006 M, which gave an average oxidation state of the dissolved sulfur ($S^{0.33-}$) and an average polysulfide chain length of

$Li_2S_{6.1}$. Once these methods had been successfully developed, concentrated polysulfide electrolyte solutions were analysed (*experimental data in Section 5.3.3 was obtained by John W. Smith*) in order to determine the polysulfide composition when the electrolyte (1 M LiTFSI in DOL) was fully saturated with polysulfides, i.e. the congruent solution. The solutions analysed were prepared as 10 M $[S]_T^{sol.}$ $Li_2S_8$, 20 M $[S]_T^{sol.}$ $Li_2S_8$, 10 M $[S]_T^{sol.}$ $Li_2S_6$ and 20 M $[S]_T^{sol.}$ $Li_2S_6$ in an attempt to achieve saturation. Using the developed methods, it was possible to determine that the congruent solution possessed a concentration of total dissolved sulfur $[S]_T^{sol.}$ of ~ 6 M and an average oxidation state of the dissolved sulfur ($S^{m-}$) of $S^{0.45-}$ corresponding to an average polysulfide chain length ($Li_2S_n$) of $Li_2S_{4.5}$. Using this data, it was possible to construct the first experimental ternary phase diagram of the $S_8$-$Li_2S$-electrolyte system, which has been used to rationalise the effect of changing the sulfur to electrolyte ratio on the Li-S battery equilibrium discharge profile. This was also able to explain the one equilibrium discharge plateau observed by Cuisinier *et al.* using non-solvents, which possess very low polysulfide solubility.[14] To improve the associated errors with extracting such small volumes of a viscous solution, a reverse titration could be performed. This was successfully demonstrated using a freshly prepared 20 M $[S]_T^{sol.}$ $Li_2S_6$ polysulfide electrolyte solution for which similar values of the average oxidation state of the dissolved sulfur ($S^{0.47-}$, previously $S^{0.48-}$) and the average polysulfide chain length ($Li_2S_{4.3}$, previously $Li_2S_{4.2}$) were measured when compared with the standard titration. The advantage of using the reverse titration method is that the volume of polysulfide electrolyte solution initially used can be much larger and can even exceed the volume required for complete reaction with the $FcBF_4$ in DOL.

A quantitative analysis of GITT was performed using a model redox system to determine its ability to measure the diffusion coefficients of a species dissolved in electrolyte with the view of investigating mass transport within Li-S batteries during cycling. The redox pair $EtV^+/EtV^{2+}$ was selected for use as the model redox system as this offered a reversible one-electron redox process with a suitable formal potential ($E_e^{0'}$ = ~2.4 V vs. $Li/Li^+$), which avoids any possibility of DOL polymerisation. The diffusion coefficient of $EtV^{2+}$ was determined to be 2 x $10^{-6}$ $cm^2$ $s^{-1}$, using cyclic voltammetry and the Randles-Sevcik equation. It was demonstrated that this diffusion coefficient could be reproduced using chronopotentiometry in both the U-cell and Swagelok cell configurations (U-cell = 2.3 x $10^{-6}$ $cm^2$ $s^{-1}$ and Swagelok cell =

2.2 x $10^{-6}$ $cm^2$ $s^{-1}$). However, it should be noted that this agreement was only obtained when a specific method ($\tau_C$) was used to measure the transition time. However, since the value of $D_{EtV2+}$ determined using cyclic voltammetry was not performed with IR correction or temperature control and the values obtained using the Sand equation varied between 2 x $10^{-6}$ $cm^2$ $s^{-1}$ and 4 x $10^{-6}$ $cm^2$ (using the $\tau_B$ and $\tau_C$ methods), it was not possible to precisely determine the actual value of $D_{EtV2+}$. It is likely that $D_{EtV2+}$ possesses a value in the range of 2 x $10^{-6}$ $cm^2$ $s^{-1}$ and 4 x $10^{-6}$ $cm^2$ $s^{-1}$, although to precisely determine the value of $D_{EtV2+}$, further experimentation is required.

After successfully demonstrating that constant current pulse techniques could be used to reproduce the diffusion coefficient of $EtV^{2+}$ in a Swagelok cell, GITT was performed in order to determine whether it too could be used to determine the diffusion coefficient when applied to a solution-based redox system. Using GITT, it was demonstrated that even when employing a model one-electron reversible solution-based redox system, determining quantitative values of the diffusion coefficient must be performed with caution. Unrealistic values of diffusion coefficient can be easily obtained if the assumptions proposed by Weppner and Huggins are not fulfilled.[15] In particular, it is important to ensure that proportionality exists between potential and concentration, which can be determined simply using the experimental steady-state potentials measured using GITT data. Through rigorous analysis of the GITT data, it was possible to determine a range for $D_{EtV2+}$ (between 1.0 x $10^{-6}$ $cm^2$ $s^{-1}$ and 2.3 x $10^{-6}$ $cm^2$ $s^{-1}$), which agrees with the value of $D_{EtV2+}$ obtained using cyclic voltammetry (2 x $10^{-6}$ $cm^2$ $s^{-1}$). This indicates that if approached cautiously, GITT measurements can be used to quantitatively determine diffusion coefficients for a model one-electron reversible solution-based redox system. However, using GITT to determine quantitative information regarding the mass transport of species present in a more complicated electrochemical system, such as Li-S batteries, will be even more challenging due to the presence of multiple redox species, which undergo multi-electron redox processes. Furthermore, the polysulfide species in a Li-S battery are present at high concentration (> 1 M) and precipitate is present on the electrode surface at different stages of cycling in the form of solid $S_8$ or solid $Li_2S$, exacerbating the analysis further.

## 7.2 – Further Work

Lithium metal protection is important not only for application in Li-S batteries but also other battery technologies, such as Li-ion and Li-air. Further methods of pre-treating the lithium metal electrode should be investigated in order to form an SEI layer capable of protecting the lithium. SEM should be used to observe the morphology of the lithium before and after cycling and electrochemical impedance spectroscopy (EIS) should be used to obtain information on interfacial resistance. The physicochemical properties of electrolytes with much lower LiTFSI concentrations in DOL should be studied (e.g. 0.1 – 200 mM) in order to obtain a better understanding of the ion structure within the electrolytes. In addition to this, other combinations of electrolyte salts (e.g. LiFSI, $LiNO_3$, LiOTf or LiI) and solvents (DME, TEGDME) should be investigated. It should be noted that it is unlikely that any one electrolyte will be suitable for all Li-S battery applications. Therefore, investigating a variety of electrolyte systems and performing thorough analysis of their physicochemical properties should be conducted, rather than focussing solely on cycling performance. The two techniques designed to quantitatively analyse the polysulfide composition in prepared polysulfide electrolyte solutions should be optimised to improve their precision. Notably, the viscous nature of the concentrated polysulfide electrolyte solutions makes it difficult to extract reliable volumes for analysis. To improve this, the density of each polysulfide electrolyte solution prepared could be measured so that any extracted volumes used can be weighed to determine the volumes reliably. In addition to this, the reverse titration method should be investigated further to enable the use of larger volumes of polysulfide electrolyte solution, reducing both volume and weighing errors. Additionally, more dilute polysulfide concentrations in the 1 M LiTFSI in DOL electrolyte system should be analysed in order to construct the phase boundaries between the one- and two-phase regions and complete the phase diagram. The congruent point in other commonly used electrolyte systems, such as LiTFSI in DOL/DME or DOL/TEGDME should be investigated. To begin analysing the mass transport of sulfur species present within a Li-S batteries using GITT, measurements should be performed on electrolytes containing dissolved sulfur at dilute concentrations (e.g. 1 mM), in order to reduce the issues associated with precipitation, before moving on to dilute polysulfide electrolyte solutions. Furthermore, EIS could be incorporated into the GITT technique at the end of each rest period to give a greater insight into the effects on the electrode interfaces during cycling.

## 7.3 – References


1. M. Safari, C. Y. Kwok and L. F. Nazar, *ACS Central Science*, 2016, **2**, 560-568.

2. L. A. Huff, J. L. Rapp, J. A. Baughman, P. L. Rinaldi and A. A. Gewirth, *Surf. Sci.*, 2015, **631**, 295-300.

3. M. U. M. Patel, I. Arčon, G. Aquilanti, L. Stievano, G. Mali and R. Dominko, *ChemPhysChem*, 2014, **15**, 894-904.

4. V. S. Kolosnitsyn, E. V. Kuzmina and S. E. Mochalov, *J. Power Sources*, 2014, **252**, 28-34.

5. N. A. Cañas, D. N. Fronczek, N. Wagner, A. Latz and K. A. Friedrich, *J. Phys. Chem. C*, 2014, **118**, 12106-12114.

6. X. Ji, K. T. Lee and L. F. Nazar, *Nat Mater*, 2009, **8**, 500-506.

7. I. Bauer, S. Thieme, J. Bruckner, H. Althues and S. Kaskel, *J. Power Sources*, 2014, **251**, 417-422.

8. J. Bruckner, S. Thieme, H. T. Grossmann, S. Dorfler, H. Althues and S. Kaskel, *J. Power Sources*, 2014, **268**, 82-87.

9. S. Walus, C. Barchasz, J. F. Colin, J. F. Martin, E. Elkaim, J. C. Lepretre and F. Alloin, *Chem. Commun.*, 2013, **49**, 7899-7901.

10. S. Z. Xiong, K. Xie, Y. Diao and X. B. Hong, *J. Power Sources*, 2014, **246**, 840-845.

11. G. Y. Xu, B. Ding, J. Pan, P. Nie, L. F. Shen and X. G. Zhang, *J. Mater. Chem. A*, 2014, **2**, 12662-12676.

12. C. Barchasz, J.-C. Leprêtre, F. Alloin and S. Patoux, *J. Power Sources*, 2012, **199**, 322-330.

13. L. Suo, Y.-S. Hu, H. Li, M. Armand and L. Chen, *Nat. Commun.*, 2013, **4**, 1481.

14. M. Cuisinier, P. E. Cabelguen, B. D. Adams, A. Garsuch, M. Balasubramanian and L. F. Nazar, *Energ. Environ. Sci.*, 2014, **7**, 2697-2705.

15. W. Weppner and R. A. Huggins, *J. Electrochem. Soc.*, 1977, **124**, 1569-1578.

# 8 – Appendices

## A1 – Iodometric Titration Analysis

To determine the accuracy and precision of undertaking standard iodometry in an organic solvent such as tetraglyme (TEGDME), a solution of iodine in TEGDME (25 mM, 5 mL) was titrated against sodium thiosulfate aqueous solution (25 mM) using starch (Vitex) as an indicator. For the iodometric titration to be useful, the end-point should be reached once twice the volume of sodium thiosulfate solution (25 mM) has been added to the iodine solution (25 mM) giving a $Na_2S_2O_3/I_2$ molar ratio of 2 (Equation A1.2). On analysing the results (Table A1.1), it can be seen that the titration end-point was consistently observed only after the $Na_2S_2O_3/I_2$ molar ratio had exceeded 2, with a broad range of results between 2.2 and 2.9. Another observation was that after ~30 seconds of reaching the end-point, the colourless solution turned yellow again. In order to determine whether or not these observations were a direct result of the TEGDME, the same titration performed (Table A1.2) but instead the iodine was dissolved in either water or dimethylsulfoxide (DMSO).

$$S_n^{2-} + I_2 \text{ (excess)} \rightarrow 2\ I^- + n\ S + I_2$$

**Equation A1.1 –** Overall reaction of excess iodine with polysulfides.

$$I_2 + 2\ Na_2S_2O_3 \rightarrow 2\ NaI + Na_2S_4O_6$$

**Equation A1.2 –** Overall reaction of iodometric titration.

| Trial | $I_2$ in TEGDME Concentration / M | $Na_2S_2O_3$ aqueous Concentration / M | Volume $Na_2S_2O_3$ added/mL | $Na_2S_2O_3/I_2$ Molar Ratio |
|---|---|---|---|---|
| 1 | 0.026 | 0.025 | 11.80 | 2.24 |
| 2 | 0.025 | 0.025 | 13.80 | 2.81 |
| 3 | 0.025 | 0.025 | 12.65 | 2.53 |
| 4 | 0.025 | 0.025 | 12.15 | 2.43 |
| 5 | 0.025 | 0.025 | 11.10 | 2.22 |
| 6 | 0.025 | 0.025 | 14.40 | 2.89 |

**Table A1.1 –** Iodometric titration in TEGDME, using 5 mL of the 25 mM $I_2$ in TEGDME solution.

| Trial | Solvent | $I_2$ Concentration / M | $Na_2S_2O_3$ aqueous Concentration / M | Volume $Na_2S_2O_3$ added / mL | $Na_2S_2O_3/I_2$ Molar Ratio |
|---|---|---|---|---|---|
| 7 | Water | 0.027 | 0.025 | 10.95 | 2.04 |
| 8 | Water | 0.026 | 0.025 | 10.40 | 2.03 |
| 9 | Water | 0.024 | 0.025 | 9.90 | 2.04 |
| 10 | DMSO | 0.027 | 0.025 | 7.90 | 1.47 |
| 11 | DMSO | 0.027 | 0.025 | 8.20 | 1.53 |

**Table A1.2 –** Iodometric titration in water and DMSO, using 5 mL of the 25 mM $I_2$ solutions for each titration.

On analysing the results (Table A1.2), it can be seen that for water, the titration end-point was observed once the $Na_2S_2O_3/I_2$ molar ratio had reached 2 and the range of results is relatively small. This indicates that the titration works as expected when iodine is dissolved in water i.e. the whole titration is performed in water. It can be seen that for DMSO, which was a solvent used by Rauh *et al.*, the titration end-point was observed once the $Na_2S_2O_3/I_2$ molar ratio had reached 1.5 and the range of results is relatively small.[1] This indicates that there is a strong relationship between the solvent used to dissolve the iodine and the $Na_2S_2O_3/I_2$ molar ratio at which the end-point is observed (Figure A1.1).

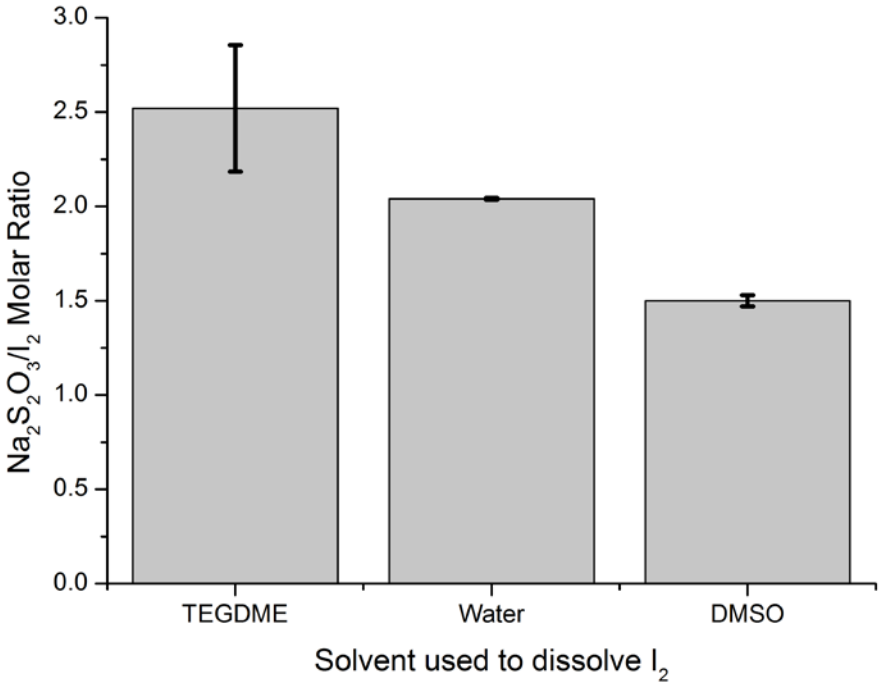


**Figure A1.1 –** Average $Na_2S_2O_3/I_2$ molar ratios obtained experimentally for each solvent.

It should be noted when using TEGDME as the solvent to dissolve iodine, that the results obtained have a large range (between 2.2 and 2.9, Figure A1.1) indicating that the end-point was difficult to determine. However, it was observed that the results obtained are consistently above 2. The only coloured species in the titration is iodine and in order to explain the poorly defined end-point and results consistently above the highest theoretical end-point, there are two possible scenarios. Firstly, the iodine may not be fully consumed in the titration, perhaps due to the mixed solvent system of TEGDME/water and the different solubility of species involved in the titration. Secondly, the TEGDME causes a side reaction to occur whereby iodine is reproduced after the initial reaction to iodide. To investigate the second possible scenario, various iodide salts were dissolve in TEGDME (Table A1.3). It was observed that the three iodide salts tested (lithium iodide, sodium iodide and potassium iodide) all turned yellow on dissolving in TEGDME, whereas both sodium iodide and potassium iodide were colourless when dissolved in water, and sodium iodide was also colourless when dissolved in DMSO. As these iodide salts should be colourless in solution, it was suspected that in TEGDME, the iodide was reacting to form the coloured iodine species. After adding lithium peroxide to the solution of sodium iodide in TEGDME and leaving for ~96 hours, the solution changed from yellow to colourless indicating that the iodine had been re-reduced to iodide (Equation A1.3).

$$Li_2O_2 + I_2 \rightarrow 2\ LiI + O_2$$

**Equation A1.3 –** Reduction of iodine to iodide.

| Salt | Solvent | Solubility | Appearance |
|---|---|---|---|
| Lithium Iodide | TEGDME | Soluble | Yellow |
| Sodium Iodide | TEGDME | Soluble | Yellow |
| Potassium Iodide | TEGDME | Soluble | Yellow |
| Sodium Iodide | Water | Soluble | Colourless |
| Potassium Iodide | Water | Soluble | Colourless |
| Sodium Iodide | DMSO | Soluble | Colourless |

**Table A1.3** – Solubility and appearance of iodide salt solutions.

Reports suggest that due to the relatively high donor and low acceptor numbers of ether solvents, it is likely that TEGDME solvates the iodide salts almost exclusively through solvent donor-cation interactions, effectively isolating the iodide anion (Figure A1.2).[2]

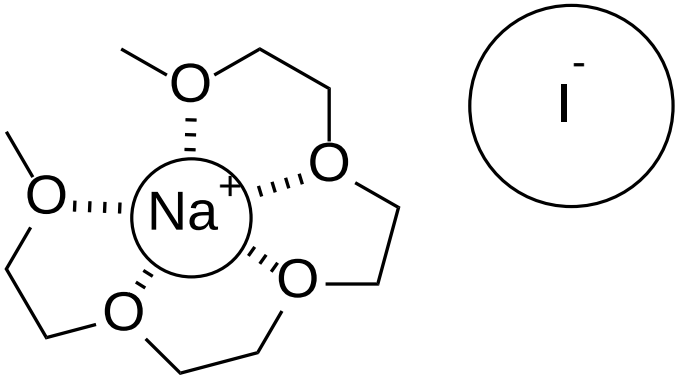


**Figure A1.2** – TEGDME chelation to sodium cation in sodium iodide.

The isolation of the iodide anion makes it less stable and thus more reactive, increasing its ability to reduce any contaminant in the solvent, such as oxygen, leading to the production of iodine (Equation A1.4). Reports suggest that the TEGDME-$H_3O^+$ complex is very stable and this could be a source of $H^+$.[3]

$$4\ I^- + O_2 + 4\ H^+ \rightarrow 2\ I_2 + 2\ H_2O$$

**Equation A1.4 –** Reduction of oxygen converting iodide to iodine.

This would explain why the iodometric titration was unsuccessful in TEGDME. The resulting sodium iodide produced in the titration (Equation A1.2) is unstable and readily reduces any contaminant species such as oxygen to give iodine. Therefore, much more sodium thiosulfate would be require to reach the observed end-point as the excess iodine would also need to be reduced. This explains the $Na_2S_2O_3/I_2$ molar ratio results for TEGDME which consistently exceeded the maximum theoretical ratio of 2. Furthermore, once the end-point is reached and all the iodine has been reduced to iodide (also after all initial oxygen dissolved in the solvent is exhausted), after a given period of time, the yellow colour may return as more oxygen dissolves in the solvent and re-oxidises the iodide to iodine. This explains the poorly defined end-point and the reoccurrence of the yellow colour after ~30 seconds of reaching the end-point (Figure A1.3).

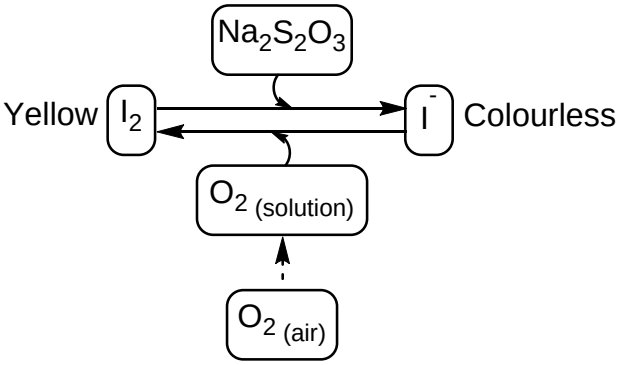


**Figure A1.3 –** Actual iodometric titration reaction in TEGDME.

In order to determine whether or not oxygen was the responsible oxidant in this reaction, anhydrous lithium iodide was dissolved in dried TEGDME in a glove box (under an inert argon atmosphere). The resulting solution still became yellow on dissolution of lithium iodide, although after leaving in the glove box for ~72 hours, the colour of the solution had become much fainter. Unfortunately, this experiment does not exclusively rule out oxygen being the oxidising species as small amounts oxygen could still be present in the dried TEGDME. Regardless of the oxidising species, it would appear that TEGDME is not compatible for use in an iodometric analysis that uses sodium thiosulfate dissolved in an aqueous media. Therefore, a different method is required to determine the *n* in the polysulfide solution (see Chapter 5.3.2 for UV-vis spectroscopic redox titration).

## A2 – Molar Extinction Coefficient of $FcBF_4$ in DOL

To calculate the molar extinction coefficient for $FcBF_4$ (95%, Sigma-Aldrich, dried) in DOL, various concentrations were prepared in an argon-filled glovebox.

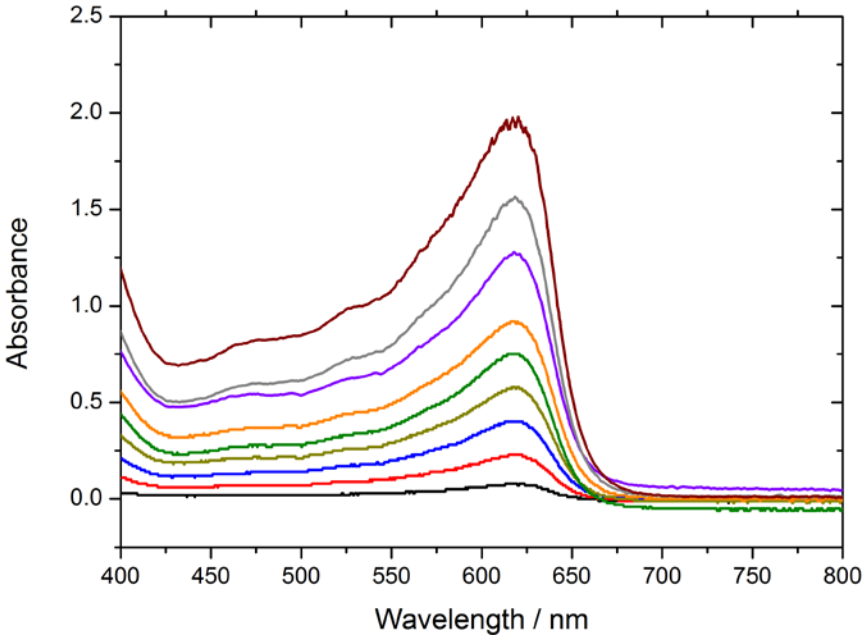


**Figure A2.1 –** UV-vis absorption spectrum of $FcBF_4$ dissolved in DOL using concentrations of **— 0.25** mM, **— 0.5** mM, **— 1.0** mM, **— 1.5** mM, **— 2.0** mM, **— 2.5** mM, **— 3.0** mM, **— 4.0** mM and **— 5.0** mM. Each solution was prepared individually by direct dilution.

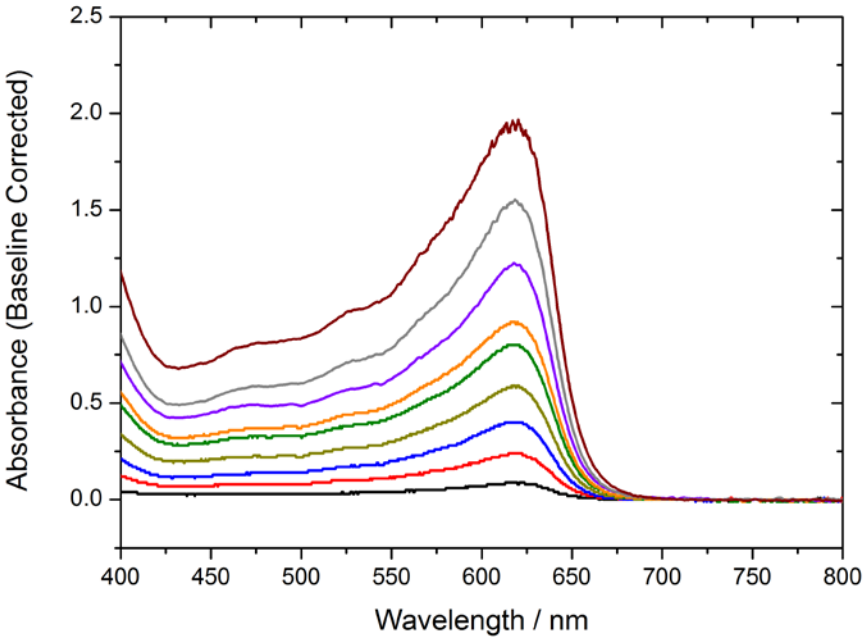


**Figure A2.2 –** UV-vis absorption spectrum of $FcBF_4$ dissolved in DOL corrected by subtracting baseline absorbance measured at 750 nm, where **— 0.25** mM, **— 0.5** mM, **— 1.0** mM, **— 1.5** mM, **— 2.0** mM, **— 2.5** mM, **— 3.0** mM, **— 4.0** mM and **— 5.0** mM. Each solution was prepared individually by direct dilution.

| Concentration of $Fc^+$ / mM | Absorbance at 620 nm | Baseline absorbance at 750 nm | Absorbance (Baseline Corrected) |
|---|---|---|---|
| 0.25 | 0.07 | -0.01 | 0.08 |
| 0.5 | 0.23 | -0.01 | 0.24 |
| 1.0 | 0.40 | 0.00 | 0.40 |
| 1.5 | 0.58 | -0.01 | 0.59 |
| 2.0 | 0.75 | -0.05 | 0.80 |
| 2.5 | 0.92 | 0.00 | 0.92 |
| 3.0 | 1.27 | 0.05 | 1.21 |
| 4.0 | 1.55 | 0.01 | 1.54 |
| 5.0 | 1.96 | 0.01 | 1.95 |

**Table A2.1 –** Absorbance data measured at 620 nm for the $FcBF_4$ in DOL solutions using the obtained UV-vis spectra (Figures A2.1 and A2.2).

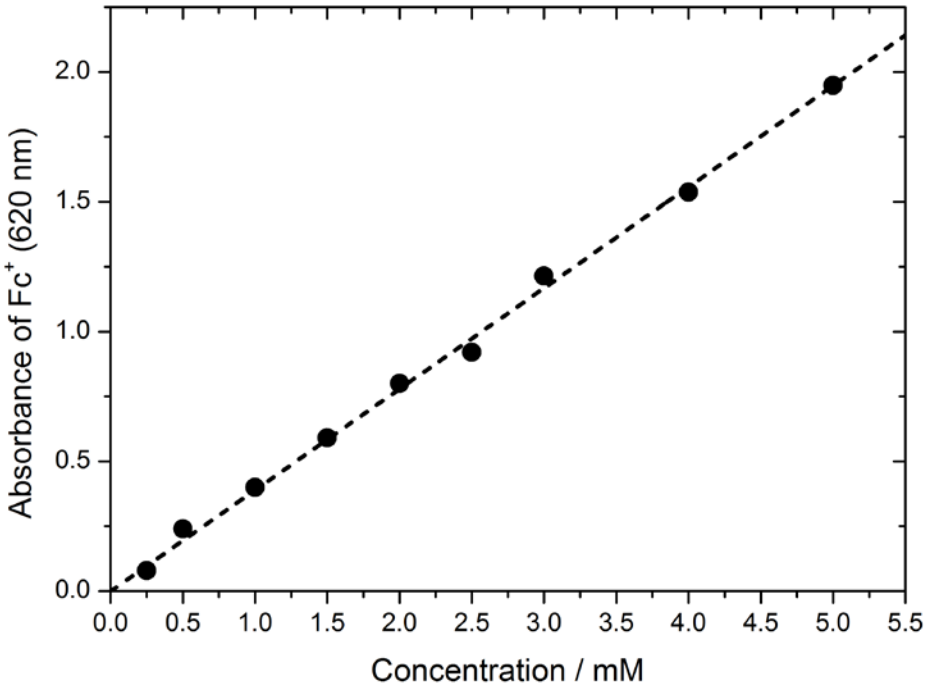


**Figure A2.3 –** Calculating the molar extinction coefficient ($\varepsilon_{Fc^+}^{620\ nm}$) of $FcBF_4$ in DOL absorbing at 620 nm. This plot uses the baseline corrected absorbance data from Figure A2.2 and Table A2.1 and the linear fit is plotted where the *y*-intercept has been fixed at 0. The slope is calculated to be 0.39 ± 0.01 $mM^{-1}$, where the error is calculated using linear regression and a 95% confidence limit.

The molar extinction coefficient is calculated using the Beer-Lambert law (Equation A2.1) and the slope obtained in Figure A2.3 ($0.39 \pm 0.01$ $mM^{-1}$).

$$A = \varepsilon c l$$

**Equation A2.1 –** The Beer-Lambert law, where $A$ = absorbance, $\varepsilon$ = molar extinction coefficient, $c$ = concentration and $l$ = cuvette cell path length (1 cm).

Since Figure A2.3 is a plot of absorbance ($A$) against the concentration ($c$), the slope is equal to the molar extinction coefficient ($\varepsilon$) multiplied by the cuvette cell path length ($l$, which is equal to 1 cm). Hence, the molar extinction coefficient ($\varepsilon_{Fc^+}^{620\ nm}$) is calculated to be $390 \pm 10$ $M^{-1}$ $cm^{-1}$.

## A3 – Concentrated Polysulfide Electrolyte UV-Vis Analysis

*Note: The experimental data presented in this section (Section A3) was obtained by John W. Smith, a fourth year undergraduate student (MChem), whom I mentored throughout his Master's project under the supervision of Professor John R. Owen and Dr Nuria Garcia-Araez (2015 – 2016). However, processing and analysis of the raw data has been performed by myself.*

In this section, the raw data discussed Section 5.3.3 is shown along with the analysis.

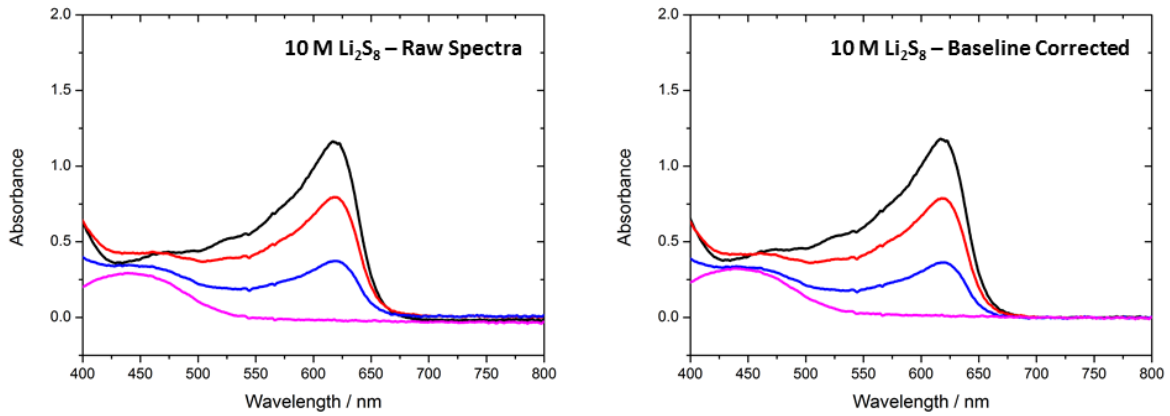


**Figure A3.1 –** UV-vis absorption spectra of 3 mM $FcBF_4$ dissolved in DOL, where per mL of $FcBF_4$ in DOL solution used either **— 0** µL, **— 0.6** µL, **— 1.2** µL or **— 1.8** µL of the 10 M $[S]_T^{mix.}$ $Li_2S_8$ in 1 M LiTFSI in DOL (filtered) were added.

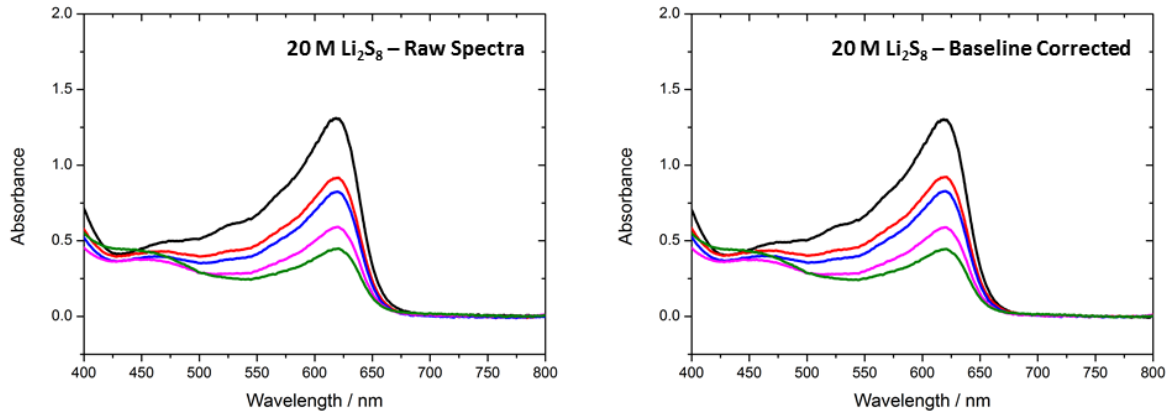


**Figure A3.2 –** UV-vis absorption spectra of 3 mM $FcBF_4$ dissolved in DOL, where per mL of $FcBF_4$ in DOL solution used either **— 0** µL, **— 0.5** µL, **— 0.67** µL, **— 0.83** µL or **— 1** µL of the 20 M $[S]_T^{mix.}$ $Li_2S_8$ in 1 M LiTFSI in DOL (filtered) were added.

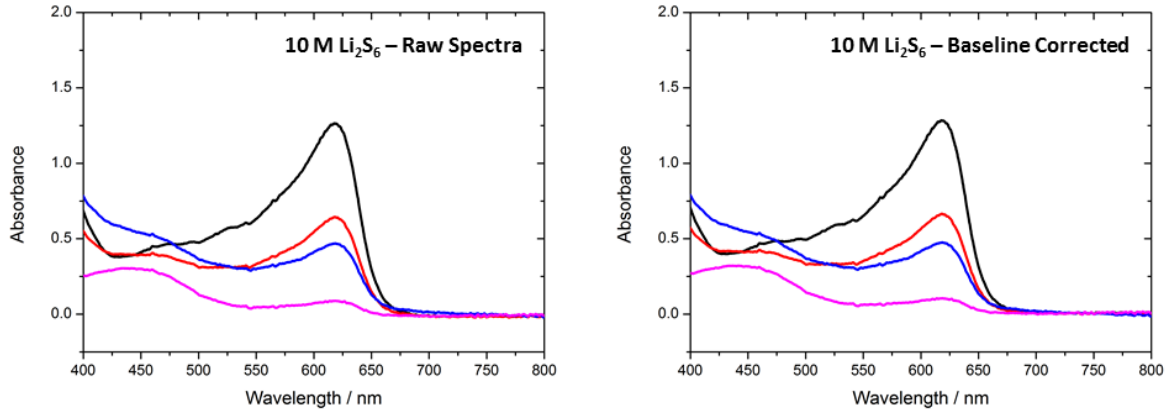


**Figure A3.3 –** UV-vis absorption spectra of 3 mM $FcBF_4$ dissolved in DOL, where per mL of $FcBF_4$ in DOL solution used either **— 0** µL, **— 0.6** µL, **— 0.9** µL or **— 1.2** µL of the 10 M $[S]_T^{mix.}$ $Li_2S_6$ in 1 M LiTFSI in DOL (filtered) were added.

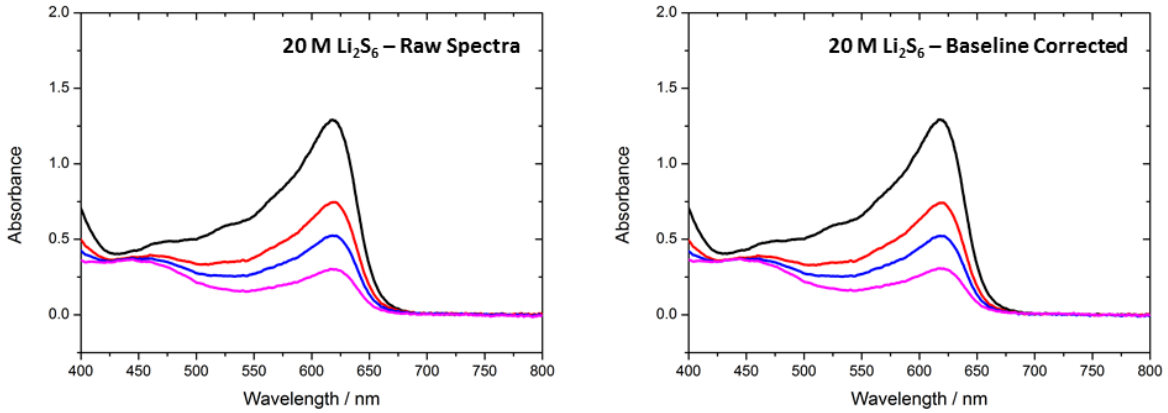


**Figure A3.4 –** UV-vis absorption spectra of 3 mM $FcBF_4$ dissolved in DOL, where per mL of $FcBF_4$ in DOL solution used either **— 0** µL, **— 0.5** µL, **— 0.67** µL or **— 0.83** µL of the 20 M $[S]_T^{mix.}$ $Li_2S_6$ in 1 M LiTFSI in DOL (filtered) were added.

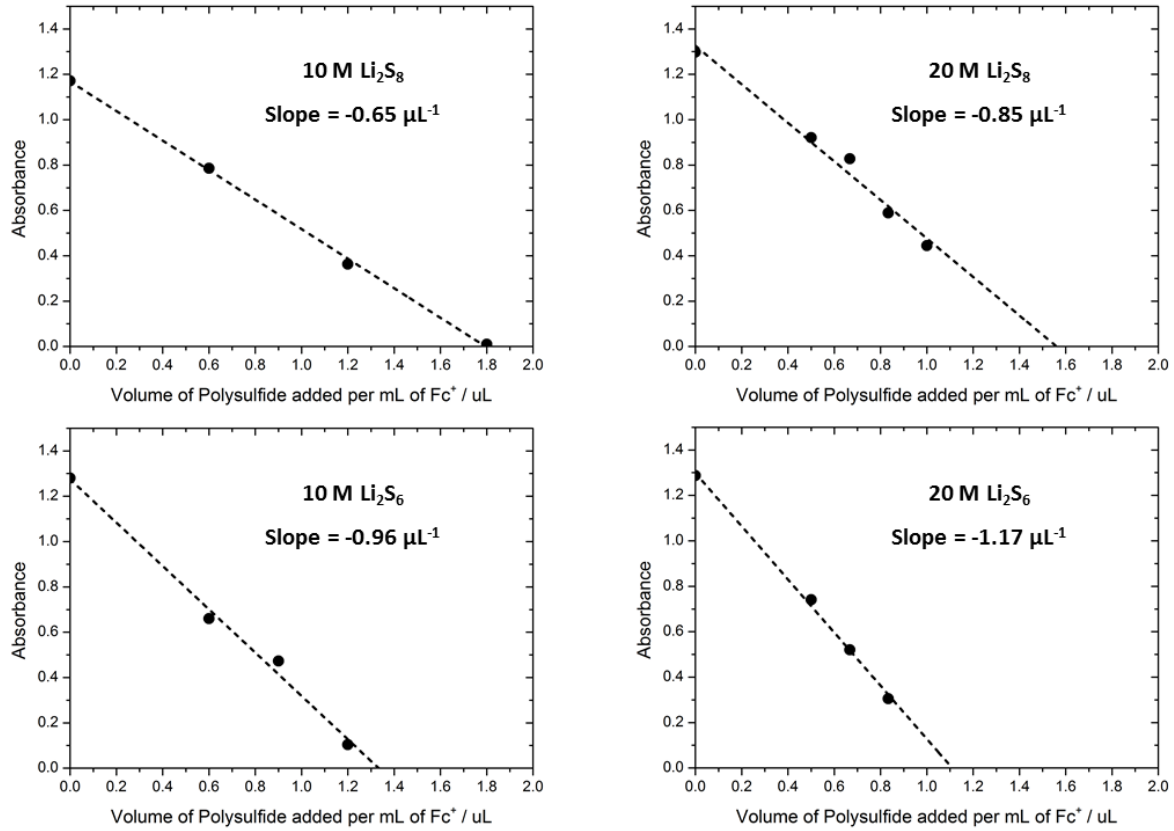


**Figure A3.5 –** Calculated slopes for each polysulfide electrolyte solution analysed when plotting absorbance measured at 620 nm against the volume of polysulfide electrolyte solution (filtered) added per mL of 3 mM $FcBF_4$ in DOL solution.

The calculations for each polysulfide electrolyte solution to determine the concentration of 'dissolved sulfide' $[S^{2-}]$, the average oxidation state of dissolved sulfur ($S^{m-}$) and the apparent average polysulfide chain length are shown (each has been calculated without round errors):

For $Li_2S_8$ (10 M $[S]_T^{mix.}$):

Slope = -0.65 $\mu L^{-1}$ = -650 $cm^{-3}$

$$[S^{2-}] = \frac{-\text{slope}\ V_{Fc^+}}{2\ l\ \varepsilon_{Fc^+}^{620\ nm}} = \frac{-(-650)\ cm^{-3}\ .\ 1\ cm^3}{2\ .\ 1\ cm\ .\ 390\ M^{-1}\ cm^{-1}} = \mathbf{0.83\ M}$$

$$m\ (S^{m-}) = \frac{2\ [S^{2-}]}{[S]_T^{sol.}} = \frac{2\ .\ (0.83)\ M}{4.1\ M} = \mathbf{0.40}\ (\mathbf{S^{0.40-}})$$

$$n\ (Li_2S_n) = \frac{2}{m\ (S^{m-})} = \frac{2}{0.40} = \mathbf{5.0}\ (\mathbf{Li_2S_{5.0}})$$

For $Li_2S_8$ (20 M $[S]_T^{mix.}$):

Slope = -0.85 $\mu L^{-1}$ = -850 $cm^{-3}$

$$[S^{2-}] = \frac{-\text{slope}\ V_{Fc^+}}{2\ l\ \varepsilon_{Fc^+}^{620\ nm}} = \frac{-(-850)\ cm^{-3}\ .\ 1\ cm^3}{2\ .\ 1\ cm\ .\ 390\ M^{-1}\ cm^{-1}} = \mathbf{1.10\ M}$$

$$m\ (S^{m-}) = \frac{2\ [S^{2-}]}{[S]_T^{sol.}} = \frac{2\ .\ (1.10)\ M}{5.3\ M} = \mathbf{0.41}\ (\mathbf{S^{0.41-}})$$

$$n\ (Li_2S_n) = \frac{2}{m\ (S^{m-})} = \frac{2}{0.41} = \mathbf{4.9}\ (\mathbf{Li_2S_{4.9}})$$

For $Li_2S_6$ (10 M $[S]_T^{mix.}$):

Slope = -0.96 $\mu L^{-1}$ = -960 $cm^{-3}$

$$[S^{2-}] = \frac{-\text{slope}\ V_{Fc^+}}{2\ l\ \varepsilon_{Fc^+}^{620\ nm}} = \frac{-(-960)\ cm^{-3}\ .\ 1\ cm^3}{2\ .\ 1\ cm\ .\ 390\ M^{-1}\ cm^{-1}} = \mathbf{1.22\ M}$$

$$m\ (S^{m-}) = \frac{2\ [S^{2-}]}{[S]_T^{sol.}} = \frac{2\ .\ (1.22)\ M}{5.9\ M} = \mathbf{0.41}\ (\mathbf{S^{0.41-}})$$

$$n\ (Li_2S_n) = \frac{2}{m\ (S^{m-})} = \frac{2}{0.41} = \mathbf{4.8}\ (\mathbf{Li_2S_{4.8}})$$

For $Li_2S_6$ (20 M $[S]_T^{mix.}$):

Slope = -1.17 $\mu L^{-1}$ = -1170 $cm^{-3}$

$$[S^{2-}] = \frac{-\text{slope}\ V_{Fc^+}}{2\ l\ \varepsilon_{Fc^+}^{620\ nm}} = \frac{-(-1170)\ cm^{-3}\ .\ 1\ cm^3}{2\ .\ 1\ cm\ .\ 390\ M^{-1}\ cm^{-1}} = \mathbf{1.50\ M}$$

$$m\ (S^{m-}) = \frac{2\ [S^{2-}]}{[S]_T^{sol.}} = \frac{2\ .\ (1.50)\ M}{6.3\ M} = \mathbf{0.48}\ (\mathbf{S^{0.48-}})$$

$$n\ (Li_2S_n) = \frac{2}{m\ (S^{m-})} = \frac{2}{0.48} = \mathbf{4.2}\ (\mathbf{Li_2S_{4.2}})$$

## A4 – Calculating Mole Fractions and Plotting the Ternary Phase Diagram

*Note: The experimental data presented in this section (Section A4) was obtained by John W. Smith, a fourth year undergraduate student (MChem), whom I mentored throughout his Master's project under the supervision of Professor John R. Owen and Dr Nuria Garcia-Araez (2015 – 2016). However, processing and analysis of the raw data has been performed by myself. Furthermore, this Section has been adapted from the supporting information in article:* J. W. Dibden, J. W. Smith, N. Zhou, N. Garcia-Araez and J. R. Owen, *Chem. Commun.*, 2016, **52**, 12885-12888.[4] *Permission from the Royal Society of Chemistry not required.*

The number of moles of $Li_2S$, S and electrolyte were calculated for 1 mL (0.001 $dm^3$) of each polysulfide electrolyte solution. As described in Section 5.3.2, the term 'dissolved sulfide' is used as all of the negative charge associated with the polysulfide is effectively provided by the initial $Li_2S$ added. Therefore, the number of moles of 'dissolved sulfide' present in 1 mL of the polysulfide electrolyte solution can be calculated using the determined concentrations of 'dissolved sulfide' (Equation A4.1).

$$\text{moles}_{S^{2-}} = 0.001\ \text{dm}^3\ [S^{2-}]$$

**Equation A4.1 –** Calculating the moles of 'dissolved sulfide' ($\text{moles}_{S^{2-}}$) in 1 mL of polysulfide electrolyte solution using the determined concentration of 'dissolved sulfide'.

Once the moles of 'dissolved sulfide' have been calculated, the moles of 'dissolved sulfur' can be calculated, since it can be assumed that the remaining sulfur in the polysulfide electrolyte solution has no charge and cannot be attributed to sulfide (Equation A4.2).

$$\text{moles}_{S^0} = \left(0.001\ \text{dm}^3\ [S]_T^{\text{sol.}}\right) - \text{moles}_{Li_2S}$$

**Equation A4.2 –** Calculating the moles of 'dissolved sulfur' ($\text{moles}_{S^0}$) in 1 mL of polysulfide electrolyte solution using the determined total concentration of dissolved sulfur species $[S]_T^{\text{sol.}}$ and the moles of 'dissolved sulfide' ($\text{moles}_{S^{2-}}$).

Then, an estimate of the volume of electrolyte present in 1 mL of each of the polysulfide electrolyte solutions can be made through deducting the volume taken by the moles of 'dissolved sulfide' and 'dissolved sulfur' (Equation A4.3).

$$V_{electrolyte} = 0.001\ cm^3 - \left(\frac{moles_{S^{2-}}\ RMM_{Li_2S}}{density_{Li_2S}}\right) - \left(\frac{moles_{S^0}\ RMM_S}{density_S}\right)$$

**Equation A4.3 –** Calculating the moles of volume of electrolyte in 1 mL of polysulfide electrolyte solution, where $moles_{S^{2-}}$ and $moles_{S^0}$ have already been calculated, $RMM_{Li_2S}$ = 45.95 g mol$^{-1}$, $RMM_S$ = 32.06 g mol$^{-1}$, $density_{Li_2S}$ = 1.66 g cm$^{-3}$ and $density_S$ = 2.07 g cm$^{-3}$.

The total number of 'moles of electrolyte' can then be calculated taking into account the volume of electrolyte present that will be occupied by LiTFSI and DOL (Equation A4.4). Obviously, this is an approximation necessary to make when preparing a phase diagram based on number of moles present and using electrolyte as one single component. However, this only affects the position of points on the 'y-axis' and a concentration axis has been included for clarity and accuracy.

$$moles_{electrolyte} = moles_{LiTFSI} + moles_{DOL}$$

$$= \left(\frac{volume_{electrolyte}\left(\frac{volume_{LiTFSI}}{volume_{LiTFSI} + volume_{DOL}}\right) density_{LiTFSI}}{RMM_{LiTFSI}}\right)$$

$$+ \left(\frac{volume_{electrolyte}\left(\frac{volume_{DOL}}{volume_{LiTFSI} + volume_{DOL}}\right) density_{DOL}}{RMM_{DOL}}\right)$$

**Equation A4.4 –** Calculating the 'moles of electrolyte' (LiTFSI and DOL) in 1 mL of polysulfide electrolyte solution.

The calculated $moles_{electrolyte}$ was then divided by 5 in order to stretch the data points towards the bottom of the ternary phase diagram (Figure A4.5). This effectively scales the vertical concentration axis so that the data points can be seen clearer.

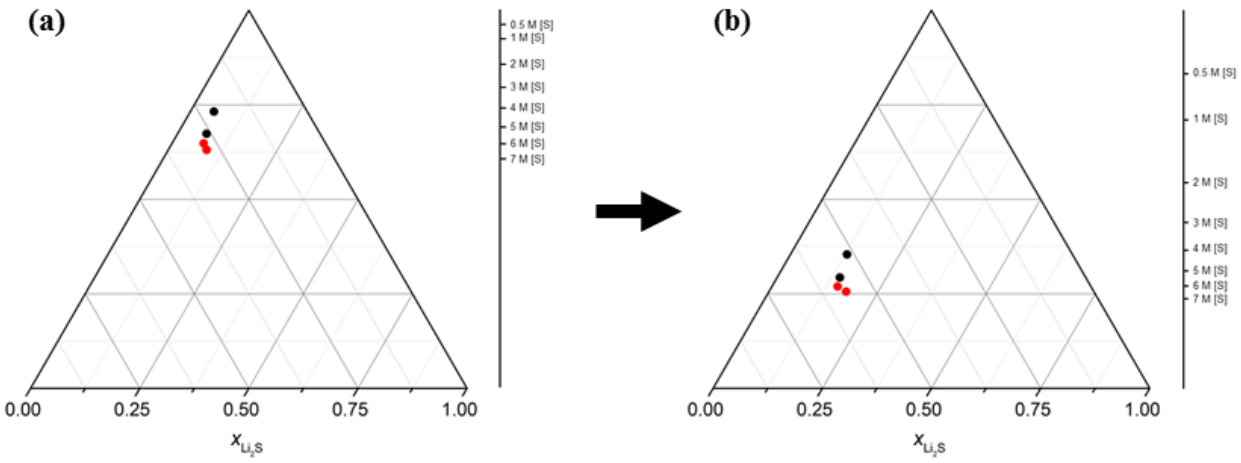


**Figure A4.5 –** (a) Ternary phase diagram without manipulating $moles_{electrolyte}$ and (b) ternary phase diagram with the $moles_{electrolyte}$ divided by 5 to stretch data towards bottom.

## A5 – References for Appendices A1 – A4

1. R. D. Rauh, F. S. Shuker, J. M. Marston and S. B. Brummer, *J. Inorg. Nucl. Chem.*, 1977, **39**, 1761-1766.

2. W. A. Henderson, N. R. Brooks and V. G. Young, *Chem. Mater.*, 2003, **15**, 4685-4690.

3. R. Neumann and I. Assael, *J. Chem. Soc. Chem. Comm.*, 1989, DOI: 10.1039/c39890000547, 547-548.

4. J. W. Dibden, J. W. Smith, N. Zhou, N. Garcia-Araez and J. R. Owen, *Chem. Commun.*, 2016, **52**, 12885-12888.

## B1 – Electrochemical Characterisation of $EtV(OTf)_2$ using Cyclic Voltammetry

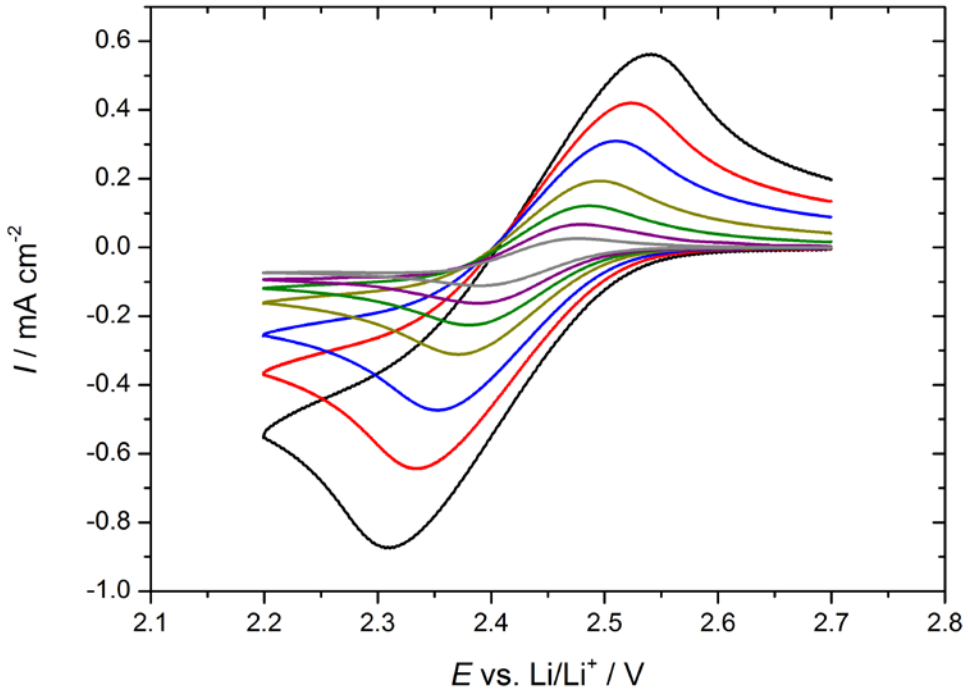


**Figure B1.1 –** Cyclic voltammetry measurements at scan rates of **— 200** mV $s^{-1}$, **— 100** mV $s^{-1}$, **— 50** mV $s^{-1}$, **— 20** mV $s^{-1}$, **— 10** mV $s^{-1}$, **— 5** mV $s^{-1}$ and — 2 mV $s^{-1}$ between the potential limits of 2.7 V and 2.2 V. The two-compartment U-cell consisted of a glassy carbon working electrode (Ø = 3 mm), 5 mM $EtV(OTf)_2$ dissolved in 1 M LiTFSI in DOL electrolyte in the working electrode compartment and 1 M LiTFSI in DOL electrolyte in the counter/reference electrode compartments and a lithium metal counter/reference electrode. First cycles at specified scan rates are shown. Between changing the scan rates, the potential of the working electrode was held at 2.7 V for at least 2 minutes.

| Scan rate / mV $s^{-1}$ | $E_{pc}$ vs. $Li/Li^+$ / V | $I_{pc}$ / mA $cm^{-2}$ | $E_{pa}$ vs. $Li/Li^+$ / V | $I_{pa}$ / mA $cm^{-2}$ | $\Delta E$ / mV |
|---|---|---|---|---|---|
| 200 | 2.31 | -0.87 | 2.54 | 0.61 | 232.5 |
| 100 | 2.33 | -0.64 | 2.53 | 0.50 | 192.4 |
| 50 | 2.35 | -0.47 | 2.51 | 0.38 | 158.8 |
| 20 | 2.37 | -0.31 | 2.50 | 0.26 | 126.2 |
| 10 | 2.38 | -0.23 | 2.49 | 0.19 | 105.9 |
| 5 | 2.38 | -0.16 | 2.48 | 0.14 | 99.6 |
| 2 | 2.39 | -0.11 | 2.48 | 0.10 | 87.1 |

**Table B1.1 –** Peak currents ($I_{pc}$ and $I_{pa}$), peak potentials ($E_{pc}$ and $E_{pa}$) and peak-to-peak separation ($\Delta E$) at scan rates 200, 100, 50, 20, 10, 5 and 2 mV $s^{-1}$. See Figure B1.1 for experimental details.

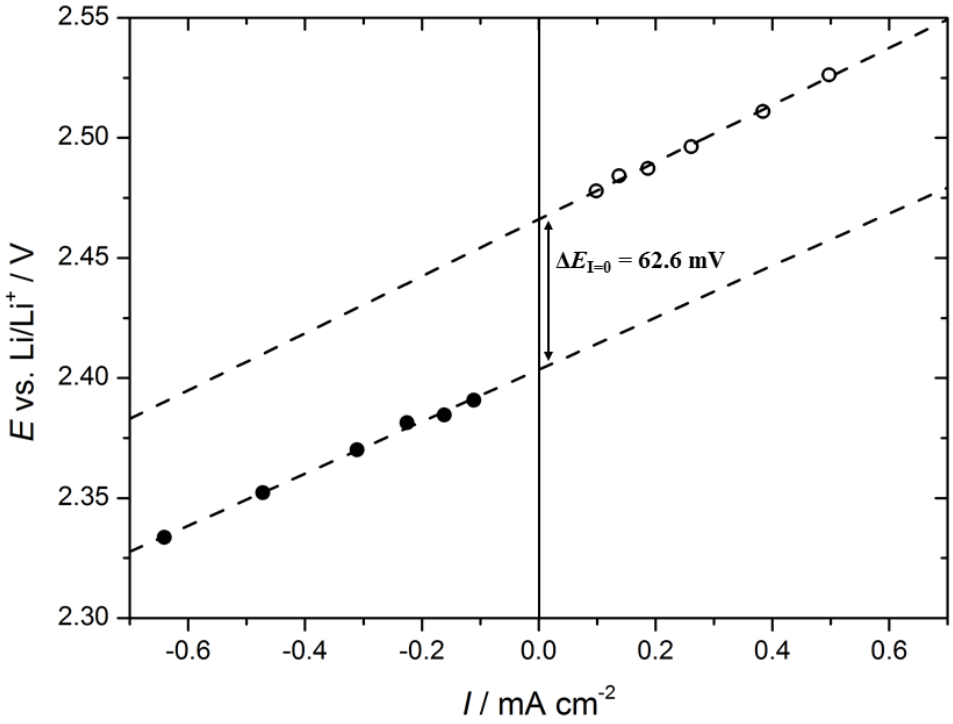


**Figure B1.2 –** Peak potentials ($E_{pc}$ and $E_{pa}$) plotted against the peak currents ($I_{pc}$ and $I_{pa}$) at different scan rates (100, 50, 20, 10, 5 and 2 mV $s^{-1}$). Linear trendlines have been used to determine the peak-to-peak separation at zero current ($\Delta E_{I=0}$). Reduction intercept = 2.4035 V and oxidation intercept = 2.4661 V.

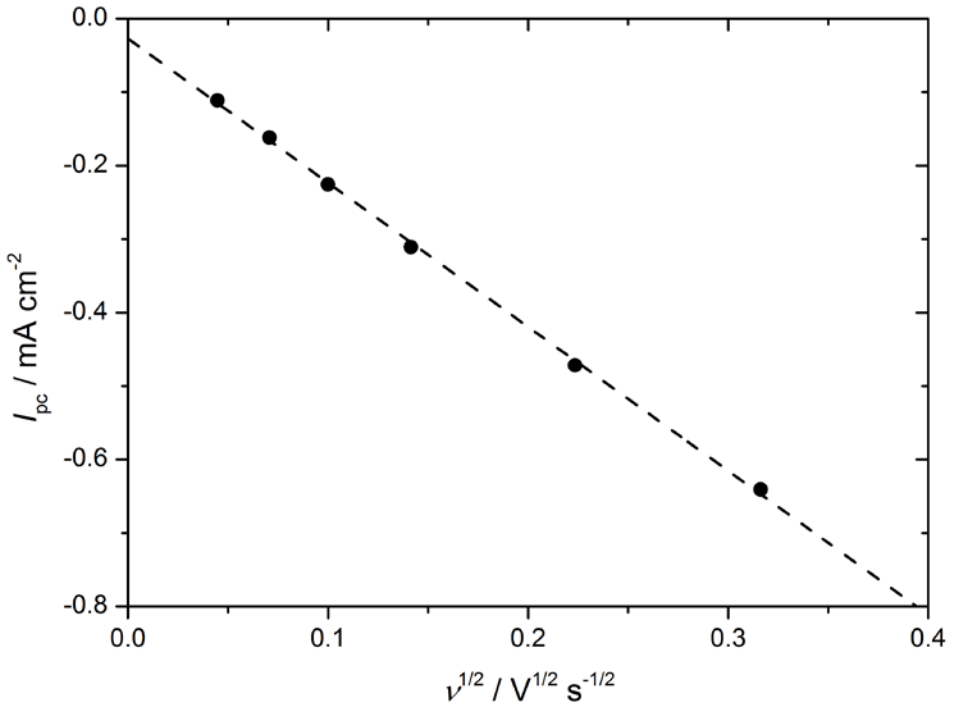


**Figure B1.3 –** Peak currents ($I_{pc}$) plotted against the square root of scan rate ($\nu^{1/2}$) at different scan rates (100, 50, 20, 10, 5 and 2 mV $s^{-1}$). A linear trendline has been plotted and the slope (-1.96 mA $cm^{-2}$ $V^{-1/2}$ $s^{1/2}$) used in the Randles-Sevcik equation to determine $D_{EtV2+}$.

## B2 – Calculating the Model Values of Steady-State Potential

$E_e^{0'}$ = 2.42 V, determined from the experimental steady-state potential for pulse 63, where theoretically $[EtV^{2+}] = [EtV^{+}]$

Example for Pulse 1:

Initial equilibrium concentration of $EtV^{2+}$ = 5.16 mM
Initial equilibrium concentration $EtV^{+}$ = 0 mM
Total volume of electrolyte = 250 μL

Charge per pulse = 5 s. 200 x $10^{-6}$ A = 0.001 A s

Change in moles per pulse = $\frac{0.001 \text{ A s}}{96485 \text{ A s mol}^{-1}}$ = 1.036 x $10^{-8}$ moles

Change in concentration per pulse = $\frac{1.036 \text{ x } 10^{-8} \text{ moles}}{250 \text{ x } 10^{-6} \text{ dm}^3}$ = 4.146 x $10^{-5}$ M = 0.04 mM

Equilibrium concentration of $EtV^{2+}$ after Pulse 1 = 5.16 mM – 0.04 mM = 5.12 mM
Equilibrium concentration of $EtV^{+}$ after Pulse 1 = 0.00 mM + 0.04 mM = 0.04 mM

Calculating the Model Steady-State Potential:

$$E_e = E_e^{0\prime} + \frac{RT}{nF} \ln \frac{[EtV^{2+}]}{[EtV^{+}]}$$

$$E_e = 2.42 \text{ V} + \frac{8.314 \text{ J K}^{-1}\text{mol}^{-1} \,.\, 298 \text{ K}}{1 \,.\, 96485 \text{ A s mol}^{-1}} \ln \frac{[5.12 \text{ mM}]}{[0.04 \text{ mM}]} = 2.544 \text{ V}$$

## B3 – Calculating the Internal Cell Resistance

To calculate the internal cell resistance, a method similar to that reported by Lacey was performed.[1] As described in Section 6.3.5, the pulses in the region of 20 – 30% reduction of $EtV^{2+}$ (pulses 25 – 37) gave most linear transient potential responses when plotted against the square root of time. These pulses were used to calculate the internal cell resistance, which was determined to be 168 ± 5 Ω. Since low concentrations of $EtV^{2+}$ were used and none of the products are insoluble, this value of resistance was considered constant throughout the entire GITT measurement. Therefore, this value of resistance is the only one used in calculating the diffusion coefficient.

Example for Pulse 30:

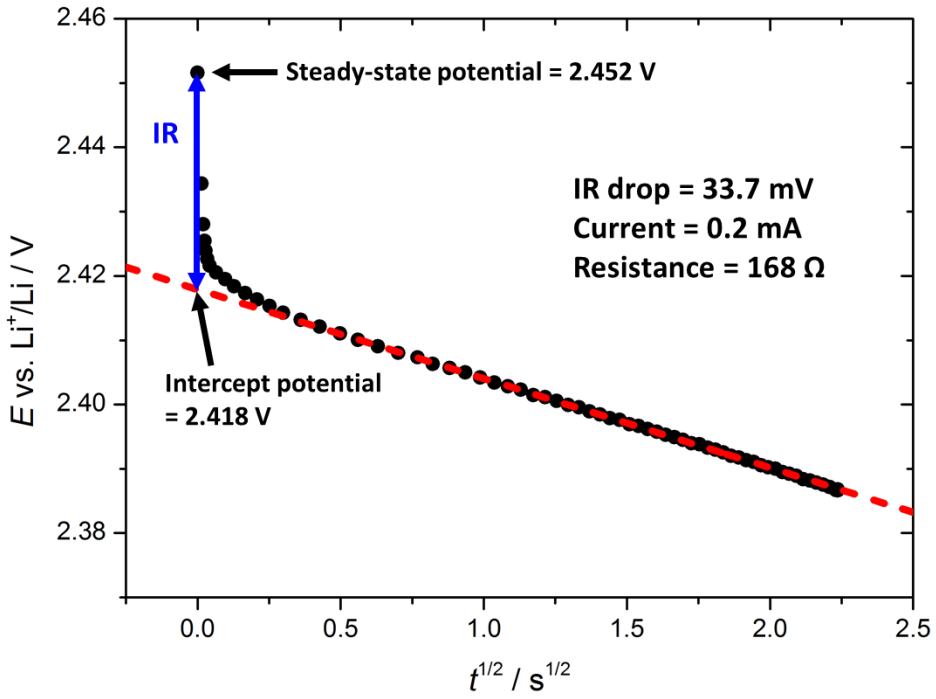


**Figure B3.1 –** Calculating the IR drop for pulse 30 (24% reduction of $EtV^{2+}$). Similar to the analysis in Section 6.3.5, the linear fit of the transient potential response against the square root of time is only considered for points above 0.5 $s^{1/2}$ to avoid effects of resistance and capacitance. Then the difference between the intercept of the linear fit (2.418 V) and the steady-state potential (2.452 V) can be used to calculate the IR drop (33.7 mV), which is used with the current (0.2 mA) to determine the resistance (168 Ω).

## B4 – Calculating the $\Delta E_s$, $\Delta E_t$ and $D_{EtV2+}$

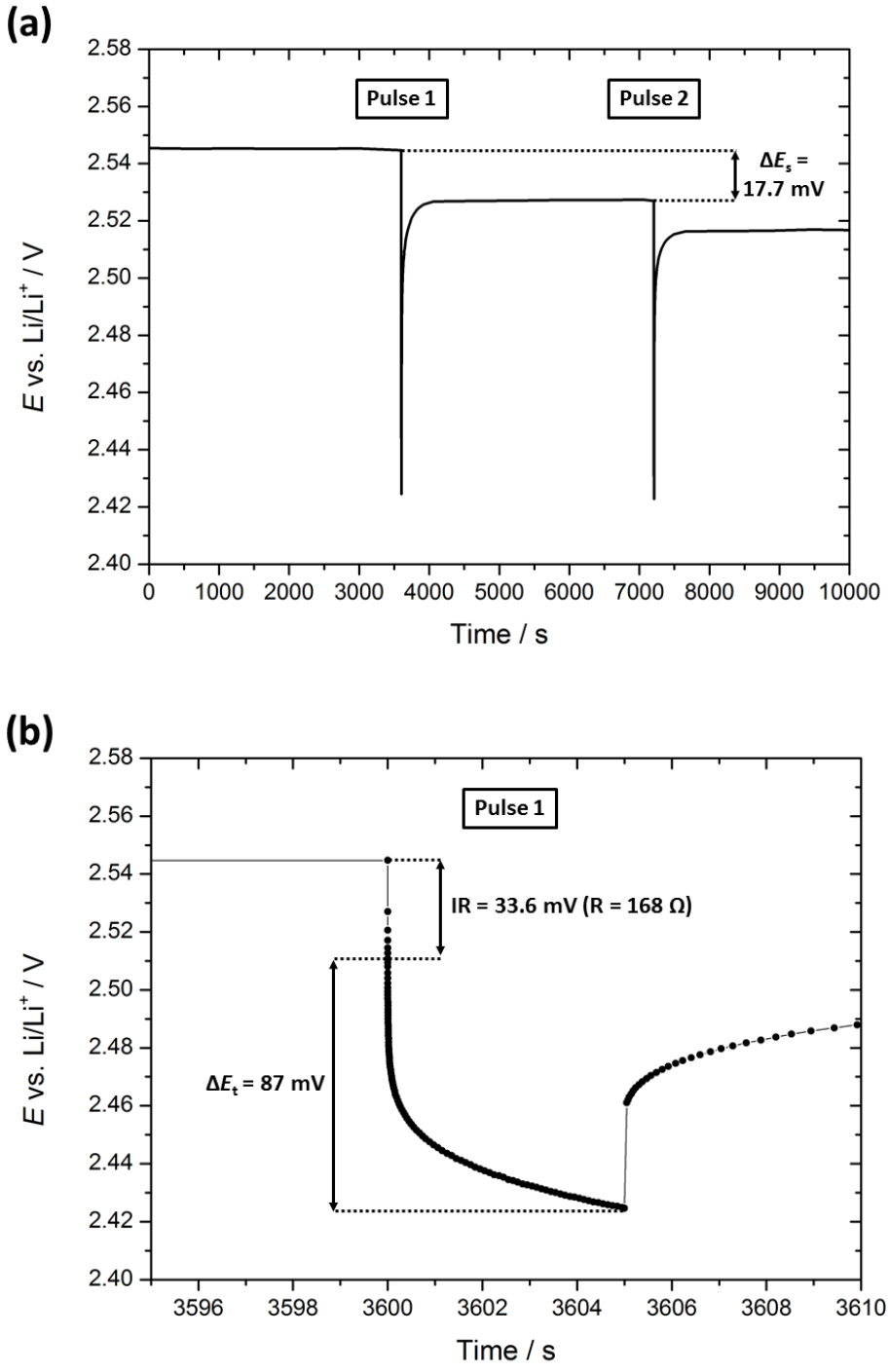


**Figure B4.1 –** Calculating the values of $\Delta E_s$ and $\Delta E_t$ for pulse 1. GITT discharge profile of a Swagelok cell consisting of a carbon coated aluminium foil working electrode (Ø = 15 mm), 2 x glass-fibre separators (GF/F, Ø = 18 mm), 5 mM $EtV(OTf)_2$ dissolved in 1 M LiTFSI in DOL electrolyte (250 µL), LICGC (Ohara Corporation, Ø = 25.4 mm), glass-fibre separator (GF/F, Ø = 25 mm), 1 M LiTFSI in DOL electrolyte (250 µL) and a lithium metal (Ø = 25 mm) counter/reference electrode. The cell was allowed to rest at OCP for 60 min, followed by 5 s discharge at -0.11 mA $cm^{-2}$, followed by a rest period of 60 min and so on.

$$D = \frac{4L^2}{\pi\tau}\left(\frac{\Delta E_s}{\Delta E_t}\right)^2$$

**Equation B4.1 –** Simplified equation for determining the diffusion coefficient (*D*), where *L* is the distance between where the electrochemical redox process occurs and the impermeable phase boundary (in this case, the distance between the electrode surface and the LICGC separator), $\tau$ is the duration of the current pulse, $\Delta E_s$ is the change in steady-state potential over a single current pulse and $\Delta E_t$ is the total change in potential during the current pulse, excluding *IR* drop.

Example for Pulse 1:

$\Delta E_s$ = 17.7 mV

$\Delta E_t$ = 87 mV

L = 0.07 cm (measured)

$\tau$ = 5 s

$$D = \frac{4L^2}{\pi\tau}\left(\frac{\Delta E_s}{\Delta E_t}\right)^2 = \frac{4.(0.07\text{ cm})^2}{\pi.5\text{ s}}\left(\frac{17.7\text{ mV}}{87\text{ mV}}\right)^2 = 5.2 \text{ x } 10^{-5}\text{ cm}^2\text{ s}^{-1}$$

## B5 – References for Appendices B1 – B4

1. M. J. Lacey, *ChemElectroChem*, 2017, **4**, 1997-2004.